

**Imaging Neuronal Pathways  
of the Rat Basal Ganglia System  
with  $^{52}\text{Mn}$  PET and MEMRI**

Dissertation

zur Erlangung des Grades eines  
Doktors der Naturwissenschaften

der Mathematisch-Naturwissenschaftlichen Fakultät

und

der Medizinischen Fakultät

der Eberhard-Karls-Universität Tübingen

vorgelegt

von

**Hanna Napieczyńska**

aus Posen, Polen

Oktober 2018

Tag der mündlichen Prüfung: 08.04.2019

Dekan der Math.-Nat. Fakultät: Prof. Dr. W. Rosenstiel

Dekan der Medizinischen Fakultät: Prof. Dr. I. B. Autenrieth

1. Berichterstatter: Prof. Dr. B. J. Pichler

2. Berichterstatter: Prof. Dr. Dr. F. Schick

Prüfungskommission: Prof. Dr. C. Schwarz

Prof. Dr. B. J. Pichler

Prof. Dr. Dr. F. Schick

Prof. Dr. C. la Fougère

**Erklärung / Declaration:**

Ich erkläre, dass ich die zur Promotion eingereichte Arbeit mit dem Titel: „Imaging Neuronal Pathways of the Rat Basal Ganglia System with <sup>52</sup>Mn PET and MEMRI“ selbständig verfasst, nur die angegebenen Quellen und Hilfsmittel benutzt und wörtlich oder inhaltlich übernommene Stellen als solche gekennzeichnet habe. Ich versichere an Eides statt, dass diese Angaben wahr sind und dass ich nichts verschwiegen habe. Mir ist bekannt, dass die falsche Abgabe einer Versicherung an Eides statt mit Freiheitsstrafe bis zu drei Jahren oder mit Geldstrafe bestraft wird.

*I hereby declare that I have produced the work entitled “Imaging Neuronal Pathways of the Rat Basal Ganglia System with <sup>52</sup>Mn PET and MEMRI”, submitted for the award of a doctorate, on my own (without external help), have used only the sources and aids indicated and have marked passages included from other works, whether verbatim or in content, as such. I swear upon oath that these statements are true and that I have not concealed anything. I am aware that making a false declaration under oath is punishable by a term of imprisonment of up to three years or by a fine.*

Tübingen, den .....

Datum / Date

.....

Unterschrift /Signature



To My Family



## Abstract

**Introduction:** The basal ganglia are components of neuronal circuits responsible for important functions, such as learning, memory, motor control and motivation. Disturbances of these functions are symptoms of neuropsychological diseases, including the Parkinson's disease, attention deficit hyperactivity disorder, depression and addiction. Since a changed neuronal activity in the involved pathways has been observed in all these diseases, it is important to develop a sensitive tool for functional studies of the neuronal tracts *in vivo*.

The present work proposes  $^{52}\text{Mn}$  for tracing neuronal pathways of the rat brain in an activity-dependent manner with positron emission tomography (PET). Several crucial aspects of this application, including the dosage, image quality and quantification, as well as pharmacological properties of the tracer, have been carefully evaluated.

**Methods:** Firstly, the relationship between the dose of non-radioactive  $\text{Mn}^{2+}$  injected into the ventral tegmental area (VTA), the signal enhancement it provides in magnetic resonance (MR) images and the dopaminergic toxicity, was assessed. Secondly, a  $^{52}\text{Mn}$  phantom study was conducted to evaluate the quality of the obtained PET images.

Next, a behavioral test and immunohistochemical staining techniques were used to evaluate the potentially harmful impact of the radioactivity doses in the range from 20 to 170 kBq on motor control system, dopaminergic neurons and the DNA damage. Having defined the non-toxic dose, [ $^{11}\text{C}$ ]methylphenidate and [ $^{11}\text{C}$ ]flumazenil PET measurements were performed to assess the effect of a single intracerebral injection of  $\text{Mn}^{2+}$  and  $^{52}\text{Mn}$  on the dopaminergic and GABAergic systems, respectively. Finally, the activity-dependence of the  $^{52}\text{Mn}$  neuronal transport was studied with pharmacological agents which modulate the neuronal activity.

Additionally, an experimental setup for PET with an online measurement of the radioactivity blood level with a blood sampler (BS) was established. It was subsequently used to investigate the impact of different techniques of obtaining the arterial input function (AIF) on the kinetic parameters (KPs) of [ $^{18}\text{F}$ ]fluorodeoxyglucose ([ $^{18}\text{F}$ ]FDG). The KPs estimated using the AIF derived from the manually collected and dispersion-corrected blood samples served as the reference approach.

**Results:** 45 nmol of  $\text{Mn}^{2+}$  provided a visible, although not statistically significant, change in the T1 maps 24 h after administration. However, it also caused a dopaminergic lesion at the injection site. The 0.5 nmol dose did not lead to the toxic effect, but it was not sufficient for MR imaging. Furthermore, 50 nmol of  $\text{Mn}^{2+}$  significantly reduced binding potential of [ $^{11}\text{C}$ ]flumazenil in the frontal cortex ipsilateral to the injected striatum at 2 days, but not at 4 weeks post-injection. There was no impact of the metal on the binding potential of [ $^{11}\text{C}$ ]methylphenidate.

24 h after the injection of 170 kBq of  $^{52}\text{Mn}$  into the VTA, the tracer was clearly visible along the mesolimbic and mesostriatal pathways in the PET images. The quantitative analysis confirmed its accumulation also in other expected brain areas. However, the dose led to an impaired rotation behavior and a dopaminergic lesion 4 weeks post-injection. These side effects were avoided by reducing the dose to 20 kBq. Moreover, 150 kBq of  $^{52}\text{Mn}$ , but not the 30 kBq dose, induced a substantial DNA damage.

The neuronal transport of  $^{52}\text{Mn}$  was not affected by any of the tested pharmacological agents, except for the non-radioactive  $\text{Mn}^{2+}$  which substantially reduced  $^{52}\text{Mn}$  concentration in the analyzed brain regions. However, different transport rates and distribution patterns of the tracer were observed depending on the injected subnucleus of the VTA.

In the BS study, the sensitivity of the device was 23 %. Using a non-corrected image-derived AIF resulted in large differences of the KPs from the reference values. The deviations of the KPs estimated with the BS-based approach were 3-5 % if 10 min of the BS recording was combined with one manually collected blood sample to obtain the AIF. However, using the  $\frac{\text{plasma}}{\text{whole blood}}$  activity ratio led to an 8 % overestimation of the  $k_3$ .

**Conclusions:** Imaging neuronal tracts of the rat brain with  $^{52}\text{Mn}$  PET is possible. In order to avoid harmful effects of the applied radioactivity, doses in the range of 20-30 kBq should be used. The activity-dependence of the  $^{52}\text{Mn}$  neuronal transport could not be confirmed and should be farther investigated.

The online recording of the radioactivity level with the BS assures an accurate measurement of the peak activity after a bolus injection and prevents a blood loss. The obtained AIF allows reliable kinetic modeling if one manual blood sample is included. However, the differences in the estimated KPs lower than 10 % should be interpreted carefully provided the  $\frac{\text{plasma}}{\text{whole blood}}$  ratio was used.



# Table of Contents

Abstract.....	7
List of Tables.....	17
List of Figures .....	18
Nomenclature and Acronyms.....	22
INTRODUCTION.....	23
1 Ventral Tegmental Area .....	25
1.1 Anatomy.....	25
1.2 Diversity of cell types .....	27
1.3 Projections and their functions .....	29
1.3.1 Mesolimbic pathway.....	29
1.3.2 Mesocortical pathway .....	32
1.3.3 Mesostriatal pathway.....	33
1.4 Disturbances in the neuronal circuits involving the VTA.....	33
1.5 Methods for <i>in vivo</i> studies of functional neuronal connectivity in experimental animals .....	36
2 Manganese.....	39
2.1 Biological relevance .....	39
2.2 Uptake mechanisms.....	40
2.3 Neuronal transport.....	41

---

2.4	Manganese neurotoxicity.....	43
3	Magnetic Resonance Imaging .....	46
3.1	MRI principles.....	46
3.2	Image weighting.....	48
3.3	Signal location and image formation.....	50
3.4	MRI contrast agents .....	50
3.5	Manganese-enhanced MRI .....	51
4	Positron Emission Tomography .....	56
4.1	PET physics .....	56
4.1.1	Beta decay.....	56
4.1.2	Annihilation .....	58
4.2	Pure and non-pure positron emitters.....	59
4.3	Interactions of photons with matter .....	60
4.4	PET instrumentation and data acquisition .....	61
4.5	Corrections.....	63
4.6	Image reconstruction .....	65
5	Manganese-52 as a PET Tracer .....	67
5.1	Characteristics of $^{52}\text{Mn}$ .....	67
5.2	Production and separation methods.....	69
5.3	Current applications of $^{52}\text{Mn}$ PET.....	70
6	Motivation and Objectives .....	73

---

7	Small Animal PET with Online Blood Sampling.....	75
	MATERIALS AND METHODS .....	77
8	Description of the Studies .....	78
8.1	Study 1: Relationship between Mn <sup>2+</sup> doses, signal enhancement in MRI and dopaminergic toxicity.....	78
8.2	Study 2: <sup>52</sup> Mn phantom measurements.....	78
8.3	Study 3: Impact of different radioactivity doses of <sup>52</sup> Mn on the dopaminergic system.....	80
8.3.1	Experiment 1: Impact of the 170 kBq dose on the dopaminergic system .....	80
8.3.2	Experiment 2: Impact of the 30 kBq and 150 kBq doses on the DNA strand breaks.....	81
8.3.3	Experiment 3: Impact of the 20 kBq dose on the dopaminergic system.....	81
8.4	Study 4: Interactions of Mn <sup>2+</sup> with the dopaminergic and GABAergic neurotransmitter systems.....	82
8.5	Study 5: Activity-dependence of <sup>52</sup> Mn neuronal transport and dosimetry.....	83
9	PET tracers.....	85
9.1	Production of <sup>52</sup> Mn .....	85
9.2	Separation of <sup>52</sup> Mn.....	85
9.3	Production of <sup>11</sup> C .....	88
9.4	Synthesis of [ <sup>11</sup> C]methylphenidate .....	88
9.5	Synthesis of [ <sup>11</sup> C]flumazenil.....	89

---

10	Animals and Stereotactic Injection.....	90
10.1	Animals.....	90
10.2	Stereotactic injection.....	90
11	Imaging Procedures.....	94
11.1	PET measurements.....	94
11.2	MRI measurements.....	95
12	Image Coregistration and VOIs.....	97
13	Quantitative Image Analysis.....	100
14	Dosimetry.....	102
15	Rotameter Test.....	103
16	TH-Staining.....	105
17	$\gamma$ H2AX-Staining.....	107
18	PET with Online Recording of Blood Radioactivity.....	109
18.1	Experimental setup.....	109
18.2	Experimental protocol.....	110
18.3	Dispersion.....	112
18.4	Data analysis.....	113
	RESULTS.....	117
19	Study 1.....	118
20	Study 2.....	122
21	Study 3.....	126
21.1	Experiment 1.....	126

---

21.1.1	Purity of the tracer solution.....	126
21.1.2	PET.....	126
21.1.3	Rotameter test.....	129
21.1.4	TH-staining.....	130
21.2	Experiment 2.....	131
21.3	Experiment 3.....	134
21.3.1	Purity of the tracer solution.....	134
21.3.2	PET.....	135
21.3.3	Rotameter test.....	137
21.3.4	TH-staining.....	138
22	Study 4 .....	140
23	Study 5 .....	144
23.1	Dependence of the $^{52}\text{Mn}$ distribution on the pharmacological treatment.....	144
23.2	Dosimetry.....	159
24	PET with Online Recording of Blood Radioactivity .....	161
24.1	Evaluation of the experimental protocol .....	161
24.2	Impact of the technique of obtaining the AIF on 2TCM-KPs .....	164
DISCUSSION.....		168
25	$\text{Mn}^{2+}$ for Tracing Neuronal Pathways with MEMRI vs Toxicity of the Metal .....	169
26	$^{52}\text{Mn}$ PET as an Alternative Method for Tracing Neuronal Tracts.....	174
26.1	Dosage .....	174

26.2	Advantages of the method and potential applications.....	181
26.3	Activity-dependence of the <sup>52</sup> Mn neuronal transport .....	187
26.4	Limitations and technical considerations .....	189
27	Small Animal PET with Online Recording of the Blood Radioactivity using a Blood Sampler.....	191
	CONCLUSIONS AND OUTLOOK.....	194
	Work Contribution and Acknowledgements.....	198
	Bibliography .....	201

## List of Tables

Table 4.1. Properties of selected PET isotopes.....	58
Table 10.1. Summary of the injection procedures used in the <i>in vivo</i> studies .....	92
Table 11.1. Parameters of the MRI sequences used in Studies 1 and 3 .....	95
Table 11.2. Parameters of the MRI sequences used in Study 4 and 5 .....	96
Table 21.1. $^{52}\text{Mn}$ content in brain regions 24 h after injection into the VTA.....	128
Table 21.2. $^{52}\text{Mn}$ content in brain regions 24 h after injection into the STR .....	128
Table 23.1. The numbers of the rats injected into different subregions of the dopaminergic midbrain.....	146
Table 24.1. KPs of the 2TCM .....	164

## List of Figures

Figure 1.1.	Location and subdivision of the VTA in the rat brain .....	26
Figure 1.2.	Dopaminergic nuclei in the rat brain.....	27
Figure 1.3.	Neuronal input onto and output of the VTA .....	30
Figure 3.1.	Physics principles of MRI.....	47
Figure 3.2.	Differences in the relaxation times between fat and water.....	49
Figure 3.3.	T1W MEMR images .....	52
Figure 4.1.	Positron emission and annihilation .....	59
Figure 4.2.	Coincidence detection.....	62
Figure 4.3.	Sinogram formation .....	63
Figure 5.1.	Scheme of the decay of $^{52}\text{Mn}$ .....	68
Figure 8.1.	Resolution phantom.....	79
Figure 8.2.	Time line of Study 4.....	82
Figure 9.1.	Synthesis of [ $^{11}\text{C}$ ]methylphenidate .....	89
Figure 9.2.	Synthesis of [ $^{11}\text{C}$ ]flumazenil.....	89
Figure 10.1.	Stereotactic injection .....	91
Figure 12.1.	VOIs used in Studies 1 and 3 .....	98
Figure 12.2.	VOIs used in Study 5.....	99
Figure 14.1.	VOIs used for dosimetry .....	102
Figure 15.1.	Rotameter test – experimental setup .....	104
Figure 17.1.	Semi-quantitative analysis of the $\gamma\text{H2AX}$ -staining .....	108
Figure 18.1.	Experimental setup for PET with BS recording.....	109

---

Figure 18.2. Blood sampler .....	110
Figure 18.3. Setup for dispersion measurement .....	112
Figure 18.4. Plasma vs whole blood ratio .....	115
Figure 19.1. Normalized T1W MR images.....	118
Figure 19.2. Quantitative results of the T1 mapping .....	119
Figure 19.3. TH-stained brain tissue of rats treated with Mn <sup>2+</sup> .....	120
Figure 20.1. PET Images of the resolution phantom.....	122
Figure 20.2. PET images of the volume phantoms.....	123
Figure 20.3. Profiles of the volume phantoms PET images .....	124
Figure 21.1. Quantification of the <sup>52</sup> Mn distribution in PET images (Experiment 1).....	127
Figure 21.2. <sup>52</sup> Mn distribution in PET images (Experiment 1).....	127
Figure 21.3. Results of the rotameter test (Experiment 1).....	129
Figure 21.4. Results of the TH-staining (Experiment 1).....	130
Figure 21.5. Results of the γH2AX staining – 90 min .....	132
Figure 21.6. Results of the γH2AX staining – 24 h .....	133
Figure 21.7. Semi-quantitative results of the γH2AX staining .....	134
Figure 21.8. <sup>52</sup> Mn distribution in PET images (Experiment 3) .....	135
Figure 21.9. Quantification of the <sup>52</sup> Mn distribution (Experiment 3).....	136
Figure 21.10. Results of the rotameter test (Experiment 3) .....	137
Figure 21.11. Results of the TH-staining (Experiment 3) .....	138
Figure 22.1. <sup>52</sup> Mn in the right STR 29 days after the administration .....	140
Figure 22.2. Results of the kinetic modelling of [ <sup>11</sup> C]methylphenidate and [ <sup>11</sup> C]flumazenil PET studies.....	141

Figure 22.3. Left-right differences in the BPnd of [ <sup>11</sup> C]methylphenidate and [ <sup>11</sup> C]flumazenil after an intrastriatal Mn <sup>2+</sup> injection.....	142
Figure 22.4. Mn <sup>2+</sup> neuronal transport 24 h after the intrastriatal injection.....	143
Figure 23.1. Identification of the injection location .....	144
Figure 23.2. Injection locations identified based on the MR images .....	145
Figure 23.3. Mn <sup>2+</sup> impact on the neuronal transport of <sup>52</sup> Mn.....	148
Figure 23.4. <sup>52</sup> Mn transport to the main output regions of the VTA – <i>Cold Mn</i> group.....	149
Figure 23.5. <sup>52</sup> Mn transport to the main output regions of the VTA – <i>AMPA</i> group.....	151
Figure 23.6. <sup>52</sup> Mn transport to the main output regions of the VTA – <i>TTX</i> group.....	152
Figure 23.7. <sup>52</sup> Mn transport to the main output regions of the VTA – <i>NMDA</i> and <i>AP5</i> groups .....	153
Figure 23.8. <sup>52</sup> Mn distribution in the VTAR-PBP and PN-PIF – injected rats .....	154
Figure 23.9. <sup>52</sup> Mn distribution in the VTAR-PBP and RN – injected rats .....	155
Figure 23.10. <sup>52</sup> Mn transport to the VTA output regions in the rats grouped based on the injection location – part 1.....	156
Figure 23.11. <sup>52</sup> Mn transport to the VTA output regions in the rats grouped based on the injection location – part 2.....	157
Figure 23.12. <sup>52</sup> Mn transport to the VTA output regions in the rats grouped based on the injection location – part 3.....	158
Figure 23.13. First step of the dosimetry estimation.....	160
Figure 24.1. Physiological parameters of a rat during the PET experiment with the BS measurement .....	161
Figure 24.2. <i>Wb</i> TACs recorded by the BS, MS, and PET in one rat.....	162
Figure 24.3. The TACs fitting procedure and the dispersion correction.....	163

Figure 24.4. KPs of the 2TCM .....165

Figure 26.1. The main neuronal projections of the rat basal forebrain.....184

## Nomenclature and Acronyms

Manganese occurs in the form of several isotopes and different ions. In the present work the following symbols are used to distinguish them:

**Mn** – refers to the metal in general, without specifying the isotope and the ionic form,

**Mn<sup>2+</sup>** – refers to the divalent ion of the stable manganese isotope, <sup>55</sup>Mn,

**Mn<sup>3+</sup>** – refers to the trivalent ion of the stable manganese isotope, <sup>55</sup>Mn,

**<sup>52</sup>Mn** – refers to the divalent ion of the radioactive manganese isotope, <sup>52</sup>Mn. The most proper acronym would be <sup>52</sup>Mn<sup>2+</sup>. However, for the sake of simplicity, <sup>52</sup>Mn is used.

Additionally, if any other symbol of an element is used (*e.g.* Na, Ca, Cr) without specifying the oxidation state, it simply denotes the name of the element.

<b>AIF</b>	arterial input function	<b>FDG</b>	fluorodeoxyglucose
<b>AMG</b>	amygdala	<b>fMRI</b>	functional magnetic resonance imaging
<b>APD</b>	avalanche photodiode	<b>GABA</b>	γ-aminobutyric acid
<b>BOLD</b>	blood oxygenation level dependent	<b>GP</b>	globus pallidus
<b>BS</b>	blood sampler	<b>γH2AX</b>	γ-phosphorylated 2AX histone protein
<b>bw</b>	body weight	<b>HIPP</b>	hippocampus
<b>CER</b>	cerebellum	<b>IF</b>	interfascicular nucleus
<b>CLi</b>	caudal linear nucleus		
<b>DA</b>	dopamine		

<b><i>i.p.</i></b>	intraperitoneal	<b>PN</b>	paranigral nucleus
<b>IPN</b>	interpeduncular nucleus	<b>RLi</b>	rostral linear nucleus
<b><i>i.v.</i></b>	intravenously	<b>RN</b>	red nucleus
<b>MEMRI</b>	manganese-enhanced magnetic resonance imaging	<b>RRF</b>	retrosubthalamic field
<b>Mn</b>	manganese (regardless of its molecular form)	<b>SNC</b>	substantia nigra pars compacta
<b>Mn<sup>2+</sup></b>	divalent manganese ion of the non-radioactive isotope ( <sup>55</sup> Mn)	<b>STR</b>	striatum
<b><sup>52</sup>Mn</b>	divalent ion of the radioactive manganese isotope ( <sup>52</sup> Mn)	<b>TH</b>	tyrosine hydroxylase
<b>MRI</b>	magnetic resonance imaging	<b>THL</b>	thalamus
<b>MS</b>	manual sampling	<b>tVTA</b>	tail of the VTA
<b>NAc</b>	nucleus accumbens	<b>VP</b>	ventral pallidum
<b>OB</b>	olfactory bulb	<b>VTA</b>	ventral tegmental area
<b>OT</b>	olfactory tubercle	<b>VTAR</b>	rostral part of the VTA
<b>PBP</b>	parabrachial nucleus	<b>VTGX</b>	ventral tegmental decussation
<b>PET</b>	positron emission tomography		
<b>PD</b>	Parkinson's disease		
<b>PFC</b>	prefrontal cortex		
<b>PIF</b>	paraintrafascicular nucleus		
<b>PMT</b>	photomultiplier tube		

# **INTRODUCTION**

# 1 Ventral Tegmental Area

## 1.1 Anatomy

The ventral tegmental area (VTA) is a symmetric brain structure located at the base of the midbrain and extending in the rostral-caudal direction from -4.68 mm to -6.84 mm from the bregma [16]. Although there is no common agreement on the subdivision of the VTA, several nuclei are usually assigned to compose the region. These include: parabrachial pigmented nucleus (PBP), paranigral nucleus (PN), rostral and caudal linear nuclei (RLi and CLi, respectively) and interfascicular nucleus (IF). In more recent publications the tail of the VTA (tVTA) is also included (Figure 1.1) [15, 17].

This division is slightly different in the Paxinos Atlas, the most commonly used anatomical template of the rat brain. Firstly, the tVTA is not distinguished. Secondly, an additional small group of cells, the paraintrafascicular nucleus (PIF), is identified bilaterally to the IF, ventromedially to the PBP, and dorsally to the PN. Moreover, the very anterior part of the PBP is distinguished as the rostral part of the VTA (VTAR). Finally, the IF and the R/CLi are not directly adjacent to each other, but the area between them is referred to as the VTA decussation (VTGX) [16]. In order to be able to use the Paxinos Atlas for the data analysis and to reference to other works, which often utilized this template, the Paxinos nomenclature is used throughout this work, with an exception for the tVTA which will be sporadically mentioned in this chapter.

Together with the neighboring substantia nigra pars compacta (SNc) and the retrorubral field (RRF), the VTA is considered the source of the dopaminergic cells in the brain. These

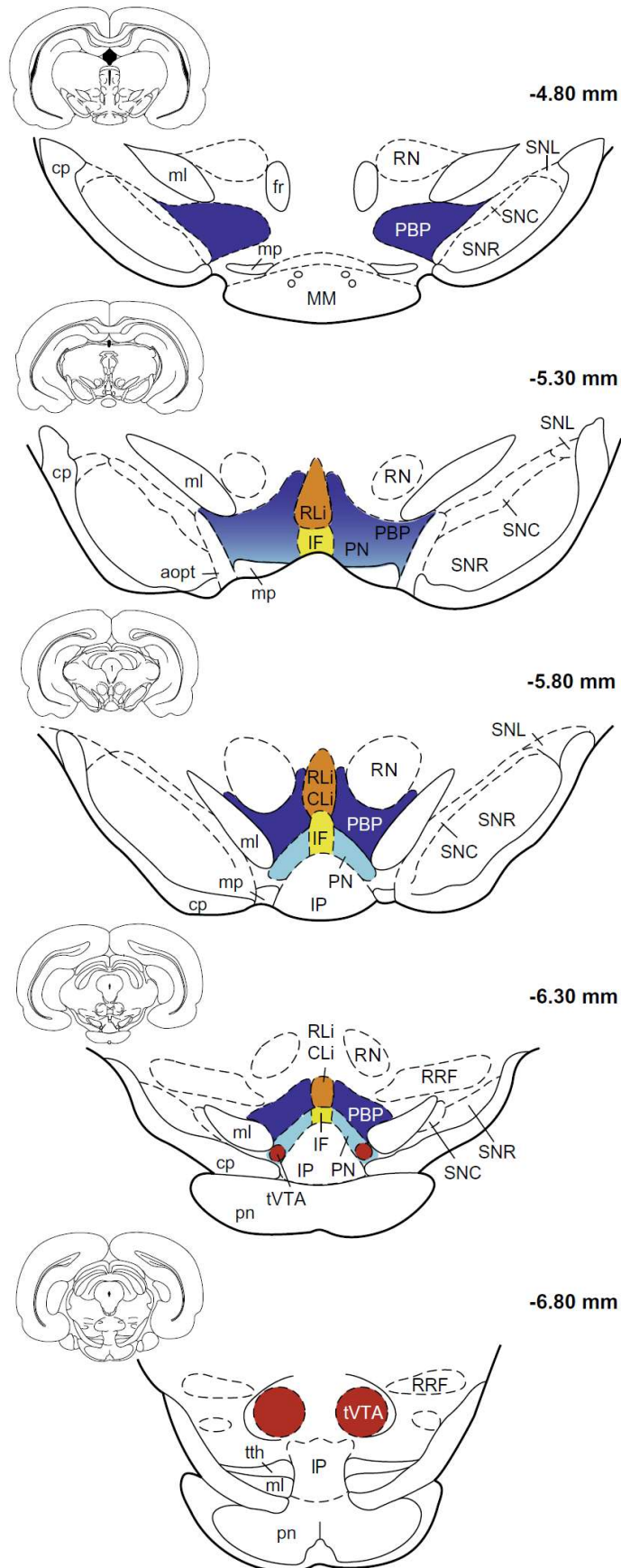


**Figure 1.1. Location and subdivision of the VTA in the rat brain**

The VTA is located at the ventral surface of the midbrain. The nuclei that compose the VTA include: PBP, PN and tVTA. The IF, RLi and CLi are usually also assigned as parts of the region. Abbreviations: aopt - accessory optic tract, cp - cerebral peduncle, fr - fasciculus retroflexus, IP - interpeduncular nucleus, ml - medial lemniscus, MM - medial mammillary nucleus, mp - mammillary peduncle, pn - pontine nuclei, RN - red nucleus, RRF - retrorubral field, SNR/SNC/SNL - substantia nigra reticulata/ compacta/ lateral, tth - trigeminothalamic tract. The numbers in the upper right corners indicate the distance from the bregma. Adapted from [13].

nuclei are often referred to as the A10, A8, and A9 cell groups, respectively [18], and they are three out of seventeen dopaminergic cell groups identified in the brain [9]. The nine major ones are depicted in Figure 1.2.

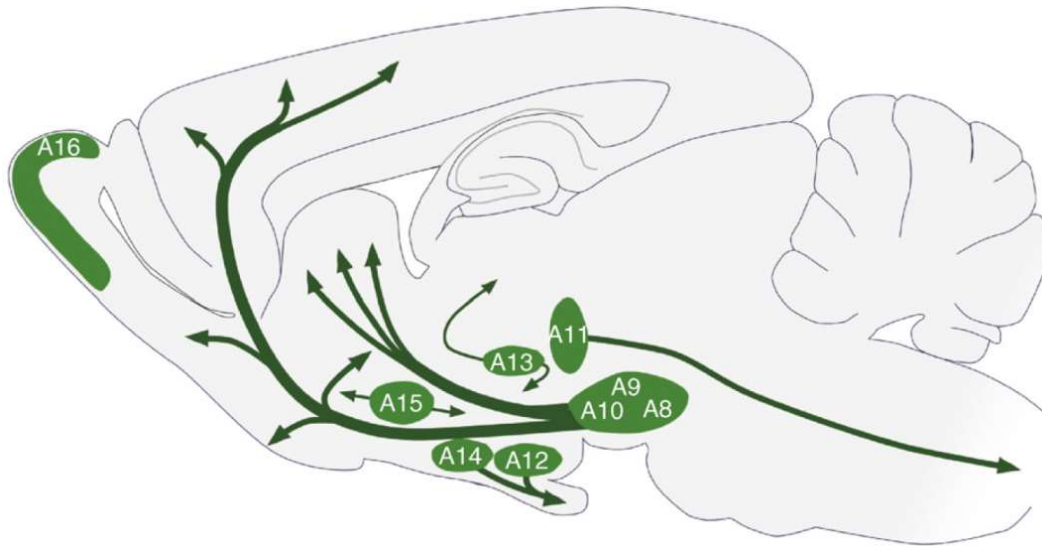


**Figure 1.2. Dopaminergic nuclei in the rat brain**

Nine out of seventeen identified groups of dopaminergic cells are shown. They are mostly located in the midbrain. The A8, A9, and A10 groups are situated within the RRF, SNC, and VTA, respectively. The main projection pathways are also schematically depicted. The mesocorticolimbic and the mesostriatal pathways target forebrain areas, but the rubrospinal tract, which is more prominent in rodents than in primates, projects in the caudal direction. Adapted from [9].

## 1.2 Diversity of cell types

The dopaminergic cells are not the only type of neurons present in the VTA. In fact, they comprise only approximately 65 % of the VTA neurons. The remaining portion is composed of cells releasing  $\gamma$ -aminobutyric acid (GABA) (~ 30 %) and glutamate (~ 5 %). It is said that the dopaminergic neurons are most densely present in the PN and PBP, the GABAergic cells in the rostral cluster and in the tVTA, while the glutamatergic neurons in the rostromedial part [17]. However, it is important to notice that the classification of the VTA neurons based on the neurotransmitter they release might be a simplification.

In fact, it has been recognized that some dopaminergic VTA neurons co-release glutamate [19, 20] or GABA [21, 22], and that the latter one can be also co-released by some glutamatergic VTA cells [23]. Interestingly, although it had been initially proposed that the co-release of dopamine (DA) and glutamate occurred from the same synaptic vesicles [24], more recent findings indicate that the two neurotransmitters are actually stored in separate vesicle pools within an axon, at least in the rat nucleus accumbens (NAc) [25]. In contrast, a vesicular coexistence of DA and GABA has been shown [26].

Additionally to the three main neurotransmitters, different VTA neurons also express a diverse peptides and proteins, such as cholecystokinin, parvalbumin, calretinin, and neurotensin [15, 27], which have a modulatory effect on the neuronal activity. Moreover, opioid and cannabinoid receptors have been also found in the region and their agonists are known to exert a significant impact on the VTA cells [28-31]. This diversity in the chemical composition shows that the VTA is not a homogenous nucleus. Its complexity is also reflected in distinct patterns of the electrophysiological activity.

Conventional dopaminergic VTA neurons (identified as tyrosine hydroxylase (TH)-positive) are characterized by phasic and tonic discharge patterns and these types of the neuronal activity play a role in so called reward-prediction error and uncertainty signaling [32-34]. However, a clearly different pattern has been identified in a substantial portion of the VTA neurons. Those cells “fired action potentials at a significantly higher frequencies in a sustained fashion” [35]. Therefore, the heterogeneity of the VTA neurons can be described at the level of expressed neurotransmitters and neuromodulators, as well as at the level of physiological properties. These differences also correlate with the differences in the cell morphology [35, 36]. Crucially, it has been recently recognized that neurons with similar

characteristics tend to be localized within specific subregions and project to particular brain areas [35, 37, 38].

### **1.3 Projections and their functions**

Multiple brain regions provide neuronal input to the VTA and many are innervated by projections originating in the area. In rats, majority of the VTA neurons have been found to innervate only a single site [39], but in a more recent study in mice a separate population of the VTA cells which target forebrain as well as midbrain structures was distinguished [40]. The confirmed connections of the VTA are schematically depicted in Figure 1.3. Additionally to the long-range targets, there exists a dense net of local interconnections within the VTA [15].

Complexity of the entire system indicates that the VTA is involved in intense neuronal processing and that it plays a role in numerous functions. Among all the known neuronal tracts involving the VTA, the mesolimbic, mesocortical, and mesostriatal pathways have been studied most extensively and their biology as well as roles in behavior have been understood to some extent.

#### ***1.3.1 Mesolimbic pathway***

The mesolimbic neuronal tract leads from the VTA to the ventral striatum, which is composed of the NAc and the olfactory tubercle (OT). The NAc, in turn, is composed of two subregions, the core and the shell. The VTA projections originating from different subnuclei show some preferences in respect to the targeted areas. Specifically, neurons in the posteromedial part of the VTA, including CLi, IF, PN, and medial PBP, project mostly to the medial OT and medial shell of the NAc, while neurons in the lateral VTA project

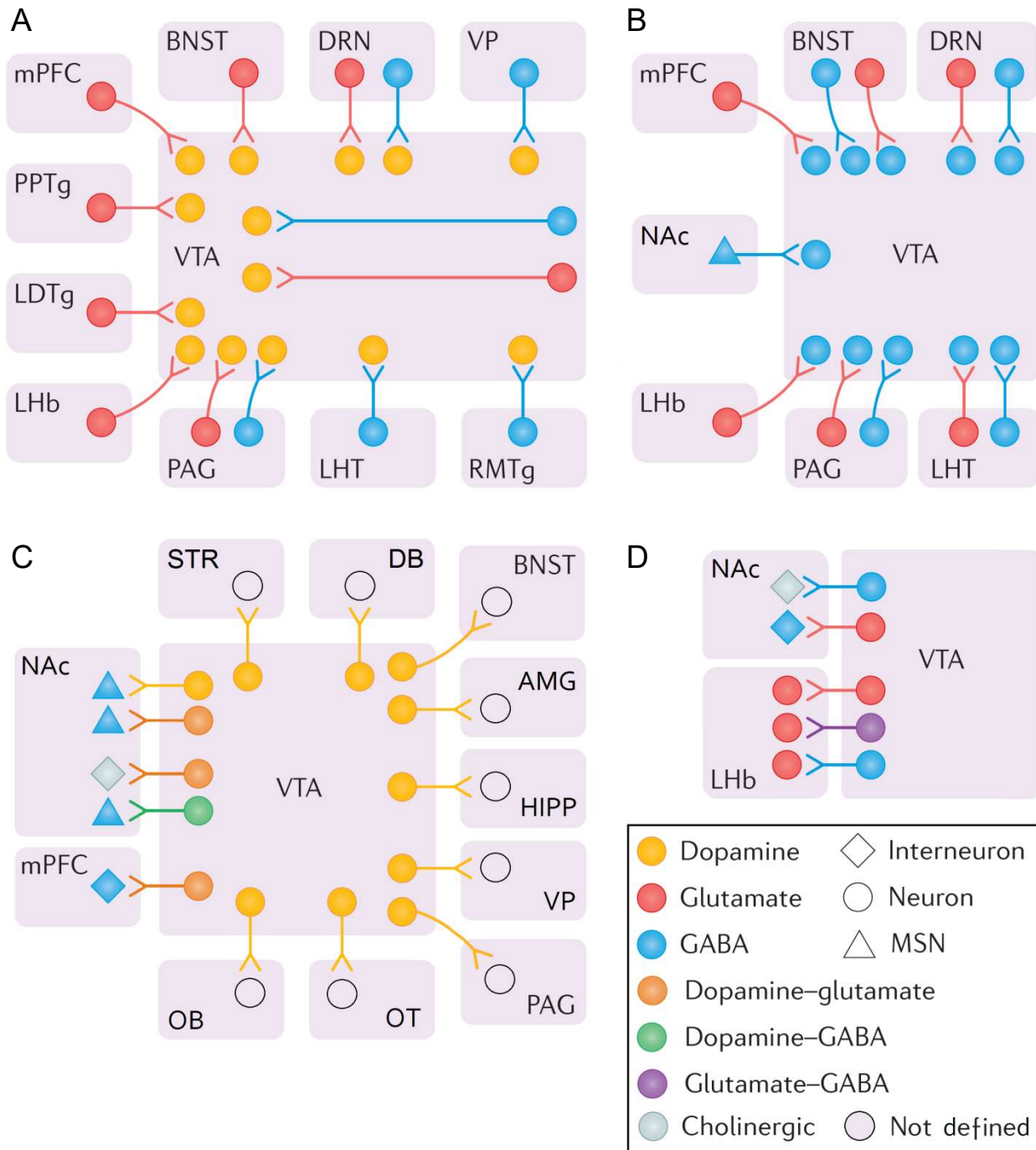


**Figure 1.3. Neuronal input onto and output of the VTA**

**A.** Dopaminergic neurons receive projections from: bed nucleus of the stria terminalis (BNST), dorsal raphe nucleus (DRN), laterodorsal tegmental nucleus (LDTg), lateral habenula (LHb), lateral hypothalamus (LHT), medial prefrontal cortex (mPFC), periaqueductal grey (PAG), pedunculo pontine tegmentum (PPTg), rostromedial mesopontine tegmental nucleus (RMTg), and ventral pallidum (VP). **B.** GABAergic neurons are innervated by some of the same regions: BNST, DRN, LHb, LHT, mPFC, PAG, and NAc. It is currently not known where the projections onto the glutamatergic cells derive from. **C.** The main output regions of the dopaminergic VTA neurons include: NAc, STR, mPFC, HIPP, and AMG, but many other targets have been also identified: OT, olfactory bulb (OB), PAG, and diagonal band (DB). **D.** The GABAergic and glutamatergic VTA neurons project onto the NAc and LHb. MSM – medium spiny neuron. Modified from [15].

preferentially to the lateral OT, lateral shell of the NAc and the NAc core [41].

The mesolimbic pathway is critically involved in reward and motivation systems of the brain which are closely linked to learning and aversive behavior. The roles of the mesolimbic pathway have been elucidated by numerous studies which found that the neurons increase their activity in response to an unpredicted rewarding stimulus. With training, the response of these neurons shifts to the stimuli that predict the reward and if the reward is not delivered within an expected time, their activity of the neurons drops to the below-baseline level [42].

The activity of the VTA neurons is subsequently transmitted onto the NAc. Electrical as well as pharmacological stimulation of the VTA neurons results in DA release in the NAc [43-45]. DA is an endogenous agonist of the dopaminergic receptors and an increase in the DA level or activation of the receptors have been linked to motivational or rewarding effects of food intake after a food deprivation [46], sexual arousal [47], and intake of addictive drugs, such as amphetamine or cocaine [48].

Nevertheless, although the DA release in the mesolimbic pathway is clearly the most important mediator in signaling the reward-related information, the entire neuronal circuit responsible for managing the motivational behavioral states is actually far more complicated [49]. In fact, the DA release in NAc is not only mediated by the VTA neurons, but also by the stimulation from the prefrontal cortex (PFC) [50]. Moreover, amygdala (AMG) and hippocampus (HIPPO) also modulate activity of the NAc neurons by dopaminergic signaling, although the latter acts via the VTA [51, 52]. Furthermore, not only NAc, but also other regions innervated by the VTA are involved in reward processing. For instance, the

lateral habenula receives GABAergic projections from a subpopulation of the VTA neurons and this inhibitory pathway is activated under rewarding conditions [53].

### ***1.3.2 Mesocortical pathway***

The mesocortical pathway leads from the VTA to the medial prefrontal, limbic and motor cortices and it is composed of dopaminergic fibers in only ~ 30 % [39, 54]. Activity of these dopaminergic neurons is under the glutamatergic control [55]. The remaining projections of the pathway are GABAergic, glutamatergic or mixed [54, 56]. The VTA neurons targeting cortical areas seem to be distributed across the entire region [57], although some studies have indicated that most of them originate from the rostromedial subregions, including VTAR, the rostromedial portions of the PBP and PN, the RLi, and the IF [39, 54, 58].

The mesocortical pathway is functionally linked to the mesolimbic pathway, as its involvement in reinforcement behaviors and emotional processing has been demonstrated. For instance, it has been shown that rats learn to self-administer addictive drugs, like cocaine, into the medial PFC (mPFC) [59, 60] and that a direct electrical stimulation of this site also acts as a reinforcement [61].

However, the PFC is probably responsible for processing different aspects of the reward-related information. It might be specifically involved in reward-guided learning and decision making and it has been proposed that distinct areas of the PFC are preferentially responsible for “selecting reward goals, choosing actions to obtain reward, and monitoring the potential value of switching to alternative courses of action” [62]. Therefore, the PFC controls more cognitive aspects of the reward-related actions.

### ***1.3.3 Mesostriatal pathway***

The mesostriatal pathway arises from the VTA-SNC complex and targets the dorsal striatum (STR). Since majority of the projections (~ 75 %) originate from the SNC [41], the pathway is also called nigrostriatal. Somas of the VTA-originating projections are located mostly within the PBP, but some also in the IF [41].

Interestingly, the VTA neurons projecting to the STR are very similar to those innervating the lateral shell of the NAc and to the SNC neurons which also target the STR. The similarities concern some aspects of molecular composition, electrophysiological activity, cell morphology, and site of origin in case of the VTA neurons. This set of characteristics is distinct from the characteristics of the VTA neurons projecting to the medial shell and core of the NAc, mPFC, and basolateral AMG and the differences between the two neuronal types may correspond to their involvement in different behavioral functions [35]. Therefore, in terms of the role of the VTA projections to the dorsal STR, it is difficult to differentiate it from the role of the SNC projections which target the same brain region.

One of the most important behavioral contributions of the mesostriatal pathway lies in maintaining motor control, motor coordination and sensorimotor integration [63, 64]. The dorsal striatal regions, innervated by the mesostriatal pathway, are also crucially involved in expressing goal-directed actions and habitual behavior, which are two stages of an evolutionary adaptive process of associative learning [65-68].

## **1.4 Disturbances in the neuronal circuits involving the VTA**

Based on the variety of the functions that the neuronal networks including the VTA are involved in, it can be easily predicted that disturbances in these networks may manifest

themselves with a wide spectrum of neurological and behavioral symptoms. Additionally, due to the mutual influences of different neuronal circuits on each other, a dysfunction of one pathway or a given cell type may affect the entire network. Consequently, the observed symptoms may be unspecific. Nevertheless, some neuropsychological diseases have been linked to particular pathological changes within the VTA networks.

One example is the Parkinson's disease (PD) which is caused by the degeneration of the nigrostriatal pathway. It affects approximately 7 mln people globally. The behavioral symptoms include: tremor, muscle rigidity, bradykinesia, and postural instability [64]. Additionally, PD patients may also suffer from disturbances in mood, sleep, cognitive functions, and others. The best currently available medication is the dopaminergic supplementation with L-DOPA, which however, is effective for only several years [69].

Another disorder that has been related to the malfunctioning of the mesostriatal, but also the mesolimbic, pathway is addiction. It has been proposed that the psychological component of addiction may be associated with disturbances in the gradual shift of the neuronal activity from the medial to lateral components of the thalamo-cortico-striatal circuits that normally occurs during associative learning and allows adaptive habit formation [70, 71]. Interestingly, some similarities in the brain activation patterns, including mesolimbic and prefrontal areas innervated by the VTA, have been found between drug and food addicts, imposing that similar treatment strategies might be efficient in both conditions [72].

Abnormalities in functioning of the mesolimbic and mesocortical pathways have been also found in other psychiatric disorders, including schizophrenia and depression [73, 74]. Regarding the former one, it has been proposed that the observed hyper-responsiveness of

the dopaminergic system [75-77] might be triggered by the neuronal hyperactivity in the anterior HIPP which projects to and overstimulates the VTA [78]. In case of depression, an opposite effect, *i.e.* an insufficient activity of the VTA neurons, was observed in animal models [79, 80]. The VTA hypoactivity may be presumably driven by the hyperactivity in the PFC [81] which stimulates the amygdala to activate the VP. The VP, in turn, exerts an inhibitory effect on the VTA [78].

The list of the neuropsychological disorders, briefly presented above, is certainly not complete. Post-traumatic stress disorder (PTSD) and attention-deficit hyperactivity disorder (ADHD) are yet another conditions which should be mentioned to demonstrate the wide range of diseases in which the VTA and the related neuronal circuits are disturbed [82, 83]. Interestingly, although the symptoms of the diseases are very diverse, and range from anhedonia and lack of motivation in depression, through abnormal anxiety reactions in PTSD and difficulties in focusing attention in ADHD, to hyperactivity or even hallucinations in schizophrenia – to name just a few – the dysregulation of the neuronal activity patterns is a common feature.

Therefore, monitoring neuronal activity of the VTA, its projections and the target areas, which together constitute complex neuronal networks, is an important element of studying brain connectivity in health and disease. It is also the key step in the development of efficient therapies for the diseases which currently affect millions of people worldwide, impairing every-day lives of the patients and their families and producing significant costs for the health-care systems [84]. In this regard, the development of adequate methods is crucial.

## 1.5 Methods for *in vivo* studies of functional neuronal connectivity in experimental animals

Currently available techniques for functional studies of the neuronal networks *in vivo* include relatively invasive electrophysiological recordings as well as minimally or non-invasive imaging methods. The first approach allows the most direct measure of the electrical activity of the neurons. It also provides the opportunity to correlate the neuronal activity with an unrestrained behavior of the experimental animal. Additionally, if the electrodes are inserted into two anatomically connected brain regions, one of them can be used for stimulation, while the other one for recording of the induced change in the activity. In this way, the strength of the neuronal connection between the brain regions can be measured [85-87].

However, not only is the electrophysiological recording an invasive technique, but also the neuronal connections of interest have to be known in advance in order to correctly implant the electrodes. Finally, recording the activity of several neuronal pathways spreading in different directions across the brain would require inserting multiple electrodes which would likely result in a significant brain damage.

A non-invasive approach, which allows recording of the neuronal activity also in humans, is electroencephalography (EEG). Besides its non-invasiveness, advantages of the technique include coverage of the entire brain and a high temporal resolution. However, EEG is also characterized by a relatively low spatial resolution or regional specificity. These characteristics could also describe magnetoencephalography (MEG), another brain imaging technique. One of the main problems associated with the functional brain mapping using

either of the methods is the volume conduction effect of the head [88]. Despite significant advancement in the technology as well as in data analysis procedures, the spatial resolution of EEG/MEG of the human brain remains in the cm range [89]. Additionally, detection and discrimination of the signals from deep brain structures are not straightforward [90].

Alternatively, a few functional magnetic resonance imaging (fMRI) methods, which are usually characterized by a superior spatial resolution, have been developed. The most commonly used in functional brain connectivity studies is the blood oxygenation level-dependent (BOLD) fMRI.

The technique is based on the relationship between the neuronal activity and the hemodynamic response of the blood vessels. It is quite well understood that an increase in the neuronal activity imposes an increased need of oxygen and other substrates, which results in a rise of the blood supply, mostly in the form of a higher cerebral blood flow. The increment actually exceeds the needs of the tissue resulting in the increase in the ratio of the oxygenated to deoxygenated hemoglobin. This, in turn, translates into an increased MR signal [91].

Although BOLD fMRI has significantly contributed to the better understanding of the human brain function, the fact that it is an indirect and relative measure of the neuronal activity is a drawback of the method. Additionally, the BOLD signal depends on several factors which are difficult to control. These factors include the local capillary density, the temperature and pH, as well as the so called draining vein problem which may lead to a misregistration of the true signal location [92].

Moreover, it is quite difficult to use fMRI in animal experiments. Despite being a completely non-invasive technique, which is a great advantage, MRI requires anesthetizing the animal in order to reduce its mobility in the scanner. This is a serious limitation due to the known impact of anesthetics on the neuronal activity, as well as on the hemodynamic parameters [93-96]. Although MRI studies in awake rodents have been conducted, the animals in those experiments were usually physically restrained [97, 98]. The restraining may not only impose a substantial stress, which in turn may affect the measurement, but it also precludes performing many behavioral tasks, which are often used in animal studies as measures of neurological functions.

One another MRI method which aims to measure the neuronal activity is manganese-enhanced MRI (MEMRI). The technique is based on a unique combination of biological and magnetic properties of the divalent manganese ion ( $Mn^{2+}$ ) and can be also used with the awake animal protocol. It is described in detail in the following chapters.

## 2 Manganese

### 2.1 Biological relevance

Manganese (Mn) belongs to trace elements essential for human health. The adequate intake for an adult man is 2.3 mg/day and for a woman it is 1.8 mg/day [99]. Manganese is a cofactor of many enzymes involved in tissue development and metabolism as well as in antioxidant processes. Its enzymatic activity is based on the cation forms, predominantly  $Mn^{2+}$  [100].

One of the best described roles of Mn is its participation in dismutation of the superoxide radical ( $O_2^-$ ) in mitochondria. The process is catalyzed by superoxide dismutase (SOD2) and it relies on the conversion of the free radical into hydrogen peroxide and oxygen [101].

Another enzyme, for which Mn acts as a cofactor, is glutamine synthetase. In fact, the enzyme contains approximately 80 % of  $Mn^{2+}$  in the brain [102]. It catalyzes the conversion of glutamate into glutamine in astrocytes [103]. Glutamine, in turn, is further converted into  $\gamma$ -aminobutyric acid (GABA) which is the key inhibitory neurotransmitter of the central nervous system (CNS).

Considering the importance of glutamate and GABA in the CNS, it is not surprising that Mn dietary deficiency may lead to disturbances in the brain function. For instance, higher susceptibility to seizure has been found in experimental Mn-deficient rats [104] and the Mn level in the blood was lower in epileptic patients than in healthy people [105, 106].

Further disturbances that have been associated with Mn deficiency include poor skeletal development and growth as well as impaired reproduction in animals [107]. However, Mn deficiency in humans is very rare [108].

## 2.2 Uptake mechanisms

Mn can enter the CNS from the blood either across the capillary endothelium or via the choroid plexus. The first mechanism dominates at the normal plasma level of the metal, while the second one plays a bigger role when the Mn concentration in the plasma is elevated [109, 110]. Crossing the blood brain barrier (BBB) by  $Mn^{2+}$  is restricted by the extensive binding ( $\geq 70\%$  in the rat) of the ion to plasma proteins. However,  $Mn^{2+}$  would enter the CNS readily from protein-free saline and the free ion is the most probable form which is actually taken up. Complexes with  $HCO_3^-$ , citrate, phosphate and other solutes constitute less than 40% of the  $Mn^{2+}$  uptake [110].

The relatively high uptake level of Mn ions suggests an existence of mechanisms that facilitate the transport. In fact, it has been shown *in vivo* that Mn crosses the BBB in a transferrin-dependent manner and that the protein binds the trivalent ion,  $Mn^{3+}$  [111]. Furthermore, divalent metal transporter 1 (DMT1) and ZIP8 protein are also involved in  $Mn^{2+}$  transport across cell membranes [112, 113], although their roles in facilitating the transport through the BBB have not been demonstrated.

Moreover,  $Mn^{2+}$  can also enter excitable cells through non-specific mechanisms. The most important one being via voltage gated calcium channels (VGCC) [114, 115]. Additionally, it can cross the cell membrane of erythrocytes through Na/Ca exchanger [116] and Na/Mg antiporter [117]. Finally, the intracellular  $Mn^{2+}$  uses the Ca uniporter mechanism to enter

mitochondria [118]. Most importantly, however, it has been recently demonstrated that the  $Mn^{2+}$  uptake into neurons correlates with the neuronal activity. This was measured using electrophysiological recording and Ca imaging and it provided the first direct evidence that the  $Mn^{2+}$  neuronal uptake may be used as a tool to monitor the neuronal function [119].

## 2.3 Neuronal transport

Interestingly, Mn ions which have been taken up by neurons are subjected to axonal transport. Although the involvement of microtubules and, more specifically kinesins, in this process has been demonstrated [120, 121], more detailed mechanisms are not fully understood. Nevertheless,  $Mn^{2+}$  transport along different neuronal tracts has been studied in experimental animals. For instance, one day after a direct administration into the rat striatum,  $^{54}Mn^{2+}$  was transported to the ipsilateral thalamus, hypothalamus, medial forebrain bundle (MFB) and substantia nigra, as visualized in autoradiograms. Some portion of the tracer was also found in the cortical areas and the amygdala [120].

Many other neuronal pathways, including the olfactory and visual tracts [120, 122-124], as well as pathways connecting deep brain nuclei and the cortex [125, 126], have been also investigated. Interestingly, different transport rates of  $Mn^{2+}$  have been estimated for the olfactory neurons (2-5 mm/h) [123] and for the neurons of the visual pathway (1 mm/h) [122], which may suggest that different molecular mechanisms of the transport are available in different types of neurons.

Majority of the studies utilizing Mn neuronal transport were conducted with manganese enhanced magnetic resonance imaging (MEMRI) which will be described in detail in the next chapter. However, it is important to mention herein that  $Mn^{2+}$  does not only enter

neurons and is transported by the neuronal projections, but it also crosses synapses. This unique characteristic allows using the ion for tracing multi-synaptic neuronal circuits, which is not possible with other divalent metal ions [124].

For example,  $^{54}\text{Mn}^{2+}$  administration to the olfactory epithelium resulted in the tracer uptake in the olfactory bulbs and its further migration via the secondary and tertiary olfactory pathways. Six weeks after the application, the metal was detected in many other brain areas as well as in the spinal cord [127]. Similarly,  $\text{Mn}^{2+}$  injected into the eye could be detected in the retinal ganglion cells, their projections to the midbrain and projections of the next order leading up to the primary and secondary visual cortices [123, 128-130].

A crucial characteristic of the  $\text{Mn}^{2+}$  transport along axons is its partial dependence on the neuronal activity. A rigorous study has demonstrated that following an intravitreal injection of  $\text{Mn}^{2+}$  in mice genetically deprived of photoreceptors, which resulted in no electrical response of the neurons to the light stimulation, the contrast agent reached the midbrain area slower than in the wild type controls [131]. In another study, a pharmacological blockade of neuronal activity with tetrodotoxin (TTX), or with a combination of TTX and  $\text{Ni}^{2+}$ , attenuated an AMPA-induced increase in the  $\text{Mn}^{2+}$  transport along the habenulo-mesencephalic pathway, although it did not abolish the basal transport level [132].

However, in the visual pathway of the mice with the retinal blindness mentioned above,  $\text{Mn}^{2+}$  was not able to cross synapses. Therefore, while the axonal transport of the tracers is only partially dependent on the neuronal activity, the transsynaptic transport depends on the activity completely [131].

## 2.4 Manganese neurotoxicity

Despite the interesting electrophysiological properties of the divalent Mn ion, which could drive novel applications in the field of biomedical research, toxicity of the metal imposes a serious limitation. Although it is not common, Mn intoxication may occur as a consequence of an environmental overexposure to the element, liver cirrhosis, or an abuse of a not purified psychostimulant drug, ephedron. The resultant condition, called manganism, is characterized by neurological and behavioral symptoms which resemble, but are not exactly the same as, the symptoms of the Parkinson's disease (PD) [133].

Specifically, the affected patients suffer from muscle weakness and rigidity which result in disturbed gait, mask-like facial expression and drooling. Moreover, emotional and mood changes have been reported. One of the features that differentiate Mn intoxication from the PD is the lack of resting tremor, although action or postural tremors may occur. Additionally, conversely to the PD, there is no responsiveness to the L-DOPA treatment in manganism [133].

The similarity of the symptoms of the two conditions is not surprising taken into account that similar brain regions are affected in both diseases. In humans, Mn accumulates mostly in the basal ganglia, including globus pallidus, caudate, putamen, and substantia nigra and the accumulation can be readily visualized with MRI [133]. The basal ganglia, and the previously described mesostriatal pathway, are DA-rich areas involved in motor control and movement coordination [134]. Neurodegeneration of the neurons in the substantia nigra pars compacta and their striatal projections is the source of the PD.

The briefly described behavioral symptoms of manganism observed in human patients have been replicated in studies with non-human primates exposed to Mn overdoses [135-138]. Importantly, the animal experiments have provided additional information about molecular effects of the intoxication. The studies often focused on the dopaminergic system and, in fact, a decrease in the striatal and/or midbrain DA, as well as its metabolite, dihydroxyphenylacetic acid (DOPAC), levels have been reported following an exposure to the total Mn doses of hundreds of mg [135, 136, 139, 140]. However, the DA concentrations were not affected in other studies, some of which used lower Mn doses (below 100 mg) [138, 141, 142].

Also concentrations of DA transporter (DAT) and DA receptors in the caudate or putamen were reduced in monkeys, as measured with neurochemistry or neuroimaging techniques [137, 143]. Nevertheless, other studies reported no changes in the DAT and DA receptor levels [133, 141, 144]. The reasons for the discrepancy in the results are not fully understood. Potentially, the total accumulated dose and the differences between the monkey species may be relevant.

The impact of Mn intoxication on other neurotransmitter systems has been studied to a lesser extent. However, a decrease in GABA and 5-hydroxyindoleacetic acid, the main metabolite of serotonin, have been observed in the pallidum, and a decrease in the norepinephrine concentration in the caudate of monkeys subchronically treated with  $MnSO_4$  or  $MnO_4$  [135, 142]. Moreover, enzymatic activity of DOPA decarboxylase in the putamen and acetyltransferase in the globus pallidus were reduced upon a longitudinal exposure to the metal [136].

It is, therefore, clear that substantial amounts of Mn accumulated in the brain after a long-term exposure may interact with several neurotransmitter systems. The neurotransmitters, their receptors and transporters, as well as the enzymes involved in their synthesis or breakdown assure proper brain functioning. Consequently, if the biological properties of  $Mn^{2+}$  shall be used as an experimental tool, it is crucial to ensure that Mn doses do not lead to the toxic effects.

It is worth noting that the toxic effects may be different, or may not occur at all, following a single administration. Although this aspect has been studied to a limited extent only, it is known that a systemic administration of 16-80 mg/kg of  $MnCl_2$  induced a reduction in the motor activity in rats [145], while a 50 nmol dose injected directly into the vitreous body of a mouse eye disturbed electrical activity measured in the visual cortex [121]. Additionally, 40 nmol of  $Mn^{2+}$  unilaterally administered into the rat VTA significantly affected the morphology of the cells [146]. Finally, an intracerebral application of the 8 nmol dose did not cause neuronal toxicity, although this was verified in the cortex, and not in the basal ganglia which are most vulnerable to Mn [147].

In summary, Mn toxicity is a crucial aspect of any application involving systemic as well as local administration. Thus, before Mn ions are used for a biological experiment, the potential toxic effects should be carefully evaluated.

## 3 Magnetic Resonance Imaging

MRI is one of the most widely used biomedical imaging modalities whose development was initiated in the 1970s. It provides images of high spatial resolution and with a very good soft tissue contrast. These features make the technique a very useful diagnostic and research tool.

### 3.1 MRI principles

The method is based on magnetic properties of hydrogen atoms which constitute almost 50 % of biological tissues [148]. Other isotopes, including  $^{13}\text{C}$ ,  $^{19}\text{F}$  and  $^{17}\text{O}$ , can also be imaged, although this is not commonly done. Due to the imbalanced number of protons and neutrons, the nuclei of these isotopes are characterized by a non-zero angular momentum, *i.e.* a spin. When a spinning nucleus is placed in an external magnetic field, its axis of rotation tends to be aligned with the direction of the field [5].

The alignment of the hydrogen spins can be parallel or antiparallel to the lines of the applied magnetic field (Figure 3.1.A-B). The former orientation requires less energy than the latter one and thus, more nuclei are positioned in this way. The difference in the number of the parallel and antiparallel-oriented spins provides the net magnetic moment which depends on the strength of the magnetic field. In a high field more nuclei join the anti-parallel population [5].

Whether the nucleus is in the parallel or antiparallel orientation, it precesses around the direction of the applied magnetic field with a characteristic frequency. This frequency (also called the Larmor frequency) depends on the strength of the magnetic field and on the

gyromagnetic ratio which is characteristic for a given nucleus (Figure 3.1.C). The Larmor frequency of hydrogen nuclei at the magnetic field strengths used in clinical MRI systems corresponds to the radio frequency (RF) range. Therefore, in order to provide energy to the hydrogen nuclei by means of the nuclear magnetic resonance, an RF pulse is applied. This is done with a transmitter coil of the MRI scanner. As a result, some low-energy nuclei join the

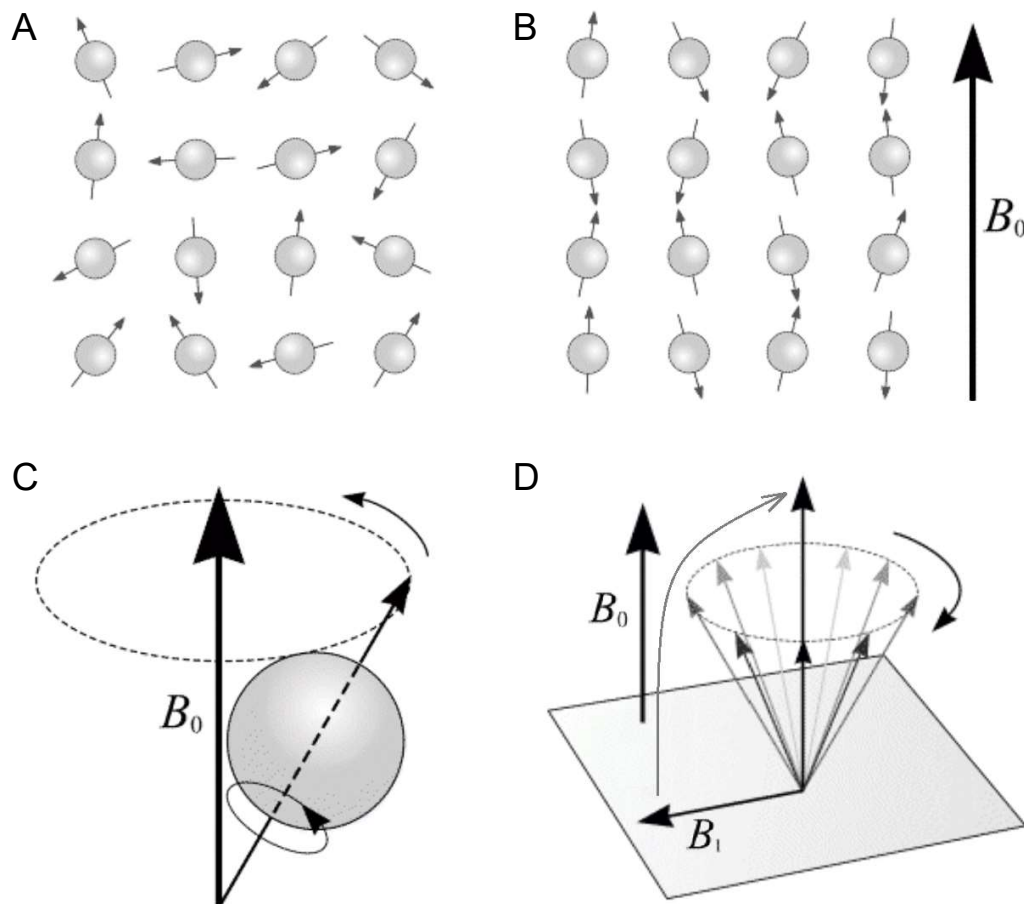


**Figure 3.1. Physics principles of MRI**

**A.** Without an external magnetic field nuclear spins are oriented in random directions. **B.** When the external field is applied, the spins become aligned with its direction ( $B_0$ ). **C.** An individual nucleus rotates around its own axis and it precesses around the direction of the  $B_0$  at a specific frequency (the precession pathway is depicted by the dashed line). **D.** Following an application of an energy pulse, the net magnetization vector (NMV) is flipped into a direction which depends on the magnitude and duration of the pulse. Here, the NMV was flipped by  $90^\circ$  ( $B_1$ ). After the energy pulse is removed, the NMV gradually returns to its original orientation (T1 relaxation). At the same time, the precessional movements of individual spins become desynchronized (T2 decay), which is depicted by different shades of grey of the arrows. Adapted from [12].

high-energy population which is associated with a change in the direction of the net magnetization vector (NMV). Simultaneously, the precessional movement of the individual spins becomes synchronized [5].

After the RF pulse is removed, the NMV gradually returns to its original orientation (Figure 3.1.D), so the longitudinal (or T1) magnetization will be recovered. This process is associated with giving up the energy, which the nuclei had gained, to their surrounding and it is called spin-lattice relaxation. The rate of the T1 relaxation has an exponential course and the time required for the recovery of 63 % of the original longitudinal magnetization is referred to as the T1 relaxation time [5].

Simultaneously with the longitudinal relaxation, the precession of individual spins gradually becomes incoherent due to the interactions of the nuclei with each other. This process is called spin-spin relaxation and results in a decay of the transverse magnetization (or T2 decay) (Figure 3.1.D). The time after which 37 % of the transverse magnetization has been lost is called the T2 relaxation time [5].

According to the Faraday's law of electromagnetic induction, the moving nuclear spins will induce a voltage in a conductive loop if such a loop is placed nearby. This phenomenon is exactly the mechanism by which the signal is recorded by a receiver coil in the MRI scanner.

## **3.2 Image weighting**

The excellent contrast of soft tissues that is achieved in MRI results from different magnetic properties of the tissue molecules. For instance, water molecules are characterized by a long T1 time, while the T1 time of fats is short. This is a consequence of different bonds of hydrogen atoms with other atoms in the molecules. The T2 times of the two substances

differ as well - the T2 time of water is long, while the T2 time of fats is short. By an appropriate adjustment of parameters of MR sequences, these differences can be visualized in the images.

The most important parameters include the time between the consecutive applications of the RF pulses (*i.e.* the repetition time, TR) and the time when the MR signal is read out following the RF pulse (*i.e.* the echo time, TE). In order to expose the differences in the T1, *i.e.* to obtain a T1-weighted (T1W) image, typically a short TR and a short TE are set. If a T2-weighted (T2W) image is desired, the TR and the TE should be long (Figure 3.2) [5].

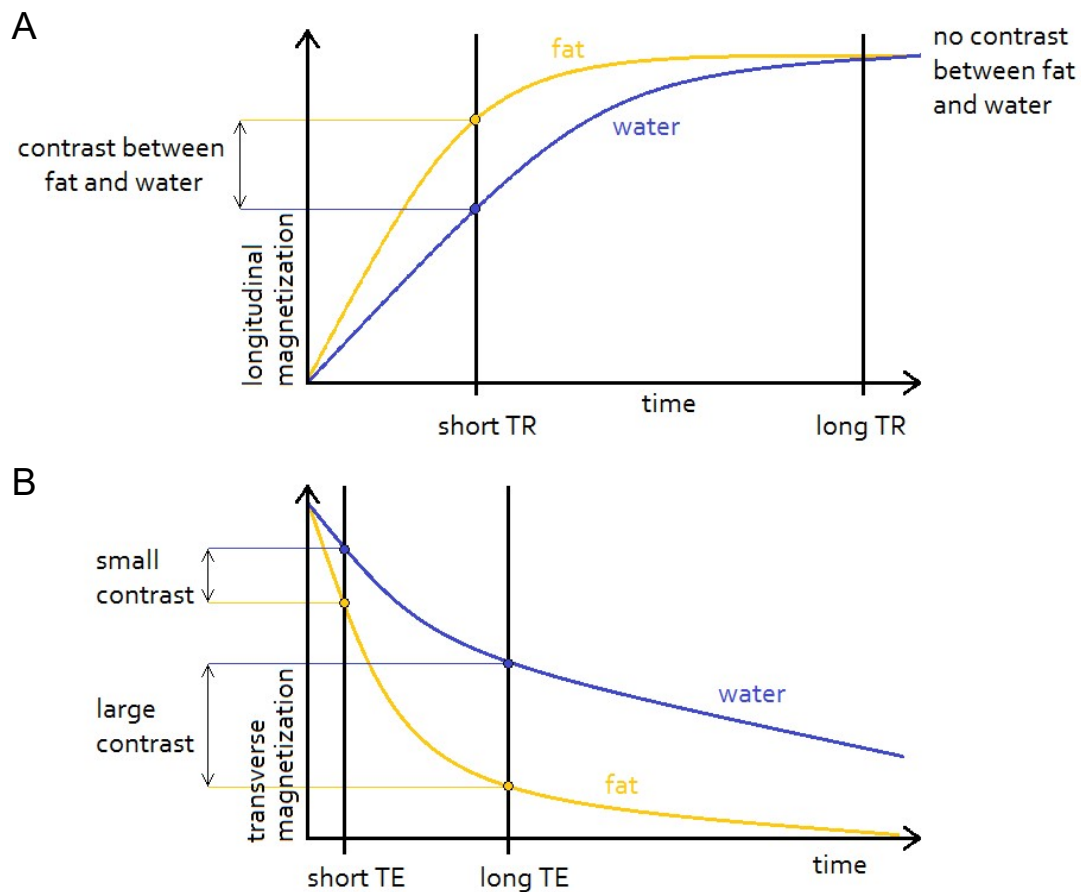


**Figure 3.2. Differences in the relaxation times between fat and water**

**A.** T1 relaxation of fat and water. **B.** T2 relaxation of fat and water. Image weighting depends on the duration of TR and TE. Adapted from [5].

### 3.3 Signal location and image formation

The previously mentioned receiver coil registers the signal, but it cannot localize its origin. Therefore, an additional mechanism is necessary to obtain three-dimensional images. In fact, every MRI scanner is equipped with a set of gradient coils which are positioned in three dimensions. Their task is to temporarily modify the uniform magnetic field along all the axes in a controlled manner.

The first gradient is applied in the  $z$  dimension of the scanner to provide slice selection. The second and the third gradients are consecutively applied to modify the frequency and phase of the spinning hydrogen protons. Thus, the nuclei from a given slice will be characterized by a specific frequency and phase depending on their position along the  $x$  and  $y$  directions. This information is later used during the process of image formation [5].

The signal recorded by the receiver coil after an application of each RF pulse, which is followed by the application of the three gradients, is saved as one data point in a spatial frequency domain, called K-space. During the entire scanning time, the polarity and the slope of the gradients change resulting in the gradual filling of the entire K-space. Finally, a mathematical operation called fast Fourier transform is used to convert the information of the K-space into an image [5].

### 3.4 MRI contrast agents

Although MRI provides a very good contrast for most of the soft tissue types, there are cases, *e.g.* certain pathologies, when the intrinsic contrast is not sufficient. In order to increase the contrast, substances with specific magnetic properties can be used. These are usually compounds whose molecules contain atoms with unpaired electrons. The unpaired

electrons are responsible for a positive susceptibility of the substances (paramagnetism). When placed in an external magnetic field, spins of these electrons align parallel with the field, which results in its local enhancement. As the T1 and T2 times of the tissue depend on the magnetic field in which the tissue is situated, the relaxation parameters will be affected in the presence of the contrast medium [5].

For instance, the long T1 of water molecules is related to the fact that their tumbling rate is much faster than the Larmor frequency of the hydrogen protons. However, if the magnetic field is enhanced by the presence of the contrast agent, the tumbling rate of the molecules becomes closer to the Larmor frequency and the T1 relaxation is more efficient. The shortened T1 time will result in higher signal intensity in the T1W image [5].

The most commonly used contrast media are gadolinium (Gd)-based. Although, the Gd ion alone is nephron- and hepatotoxic, it can be chelated with other molecules which assure a safe use. In this form the contrast agent can be administered to a patient via an intravenous injection [149].

### **3.5 Manganese-enhanced MRI**

Mn divalent ion also poses paramagnetic properties. It strongly reduces the T1 and T2 times of water and hence, can serve as an MRI contrast agent. Although, Mn-based contrast media are not commonly used, several compounds have been tested, including Mn bicine complex [150], Mn citrate, Mn *N*-(2-hydroxyethyl)iminodiacetic acid (HIDA) [151], and *N,N'*-dipyridoxylethylenediamine-*N,N'*-diacetate 5,5'-bis(phosphate) (DPDP). The latter one is used for pancreas imaging in animal models [152] as well as in patients [153-155].

The free  $Mn^{2+}$ , administered in the form of  $MnCl_2$ , has been also used in animal research. The studies utilized it to image myocardial infarction [156-158], as well as brain structure and function. In those studies  $MnCl_2$  was administered systemically as a bolus injection or as an infusion, resulting in excellent contrast enhancement (example is shown in Figure 3.3).

However, due to the poor penetration through the BBB, relatively high doses of  $Mn^{2+}$  are required to achieve the desired contrast enhancement in the brain. For instance, to obtain the enhancement effect shown in Figure 3.3, the animals were injected with 90-180 mg/kg. The high doses may potentially lead to toxic effects, as previously described (section 2.4). Unfortunately, the toxicity aspect has not been carefully investigated in many MEMRI studies. Nevertheless, a robust dose-dependent decrease in motor activity, resembling the typical symptoms of Mn intoxication, has been observed following a single subcutaneous (*s.c.*) injection of 16-80 mg/kg in rats. Although the lowest dose resulted in minimal adverse effects, it was not sufficient for brain mapping [145].

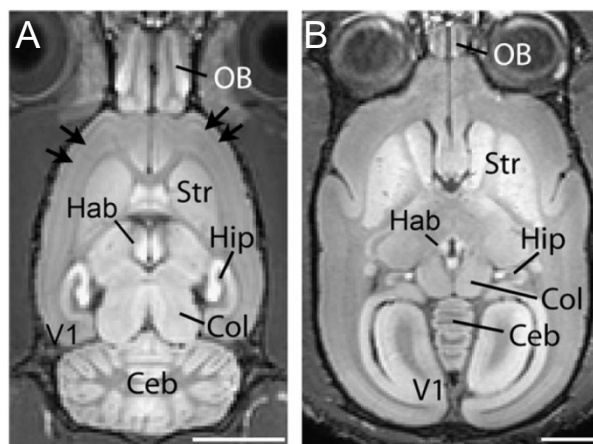


**Figure 3.3. T1W MEMR images**

**A.** An image of a rat brain. Arrows indicate cortical layers. **B.** An image of a marmoset brain. The scale bars correspond to 5 mm. OB – olfactory bulb, Hab – habenula, Str – striatum, Hip – hippocampus, Col – colliculus, Ceb – cerebellum, V1 – primary visual cortex. Reproduced from [7].

Alternatively, a cumulative dose of 80 mg/kg, which is adequate for imaging purposes, could be delivered by means of a continuous infusion using an intraperitoneally (*i.p.*) implanted osmotic pump. This procedure did not produce any behavioral side effects, but the required administration time was 7 days [145]. This may be not optimal for some studies.

Besides imaging the brain anatomy, yet another interesting application of MEMRI has been developed in the field of neuroscience. Starting from 1998 [123], the technique has been widely used for tracing neuronal connections. The olfactory and visual pathways of the rat brain were imaged in the first place [123], but the focus of the studies rapidly spread onto other neuronal tracts, including cortical as well as deep brain circuits [126, 146, 159, 160]. The intense studies have been driven by the unique properties of  $Mn^{2+}$  as an MRI contrast agent, which allow visualization of multi-synaptic neuronal connections in a living brain.

As previously described, the  $Mn^{2+}$  neuronal uptake and crossing the synapses dependent on the neuronal activity completely, while the axonal transport is partially activity-dependent. These mechanisms are associated with increased opening of Ca channels during electrical activity of the neurons which results in more Mn ions entering the cells [119]. Consequently, the active brain areas exhibit increased signal intensity in T1W MR images [132]. This unique property of  $Mn^{2+}$  has been widely used for studying brain function and plasticity in rodents [125, 161-163], birds [164, 165] and monkeys [166].

For example, activation of the pain pathway after application of an electrical stimulus and a subsequent reduction in the activation following an administration of morphine could be visualized using MEMRI in rats [167]. In another interesting experiment, the technique was used to study seasonal plasticity of the neuronal pathway between two song-control brain

nuclei in songbirds. The study revealed structural as well as functional differences between male and female birds [164]. Further functional MEMRI studies in the field of neuroscience included investigations of auditory pathway in mice [168], brain circuitry involved in novel stress response [169] and the conditioned taste aversion in rats [125], as well as many others.

Besides investigations of the normal brain function, the technique has been also used to study brain dysfunctions in various disease models. Animal models of neurodegenerative diseases, like the Alzheimer's disease (AD) and PD, were widely investigated [119, 170-172], but usefulness of MEMRI for studying disturbances in different neurotransmitter systems, including specifically the DA, norepinephrine and serotonin transporters, has been also proved [163, 173, 174]. In summary, the diversity of the topics that have been studied with MEMRI illustrates how universal the method is.

One of the biggest advantages of using MEMRI for tracing neuronal pathways relies on the possibility to image the brain function without affecting it with anesthesia. Although currently it is not a typical approach,  $Mn^{2+}$  can be injected into a specific brain region of an awake experimental animal via a guide cannula previously fixed on the skull. The freely moving animal can then undergo a behavioral procedure, while the tracer will be gradually transported along the neuronal tracts being involved in the activity.

The fact that the animal can be unrestrained and freely perform the task, being it an exploration of a new territory or pressing a lever, is crucial for many experimental paradigms used in neurological and neuroscientific studies. Moreover, the relatively low neuronal transport rate of  $Mn^{2+}$  allows sufficient time for the experimental procedure.

Once the task has been completed, the animal is anesthetized and placed in the MRI scanner to read out the tracer distribution in the brain. Therefore, not only the influence of the anesthetics on the neuronal activity, but also the distress of the animal associated with being in the scanner, is avoided during the behavioral performance. In fact, this procedure has been successfully used in one study in rats [125].

The only limiting factor for MEMRI procedures is Mn toxicity. Especially if dopaminergic neurons, like the basal ganglia, or longitudinal studies involving multiple administrations of the tracer are of interest, this aspect should be carefully evaluated. As previously mentioned, tens of nmol of  $Mn^{2+}$  are commonly used for tracing neuronal pathways which may lead to toxic effects. Doses lower than 10 nmol have been reported not to cause toxicity after a single administration into the cortex, but the results could be different in the more vulnerable dopaminergic areas. Additionally, the low doses impose that the scanning procedure is either performed directly after the injection [131, 147], or it takes several hours [175]. Therefore, sensitivity of the MRI systems is a serious limitation for MEMRI experiments in which avoiding the toxicity effects is desired [8].

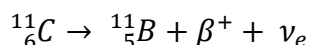
## 4 Positron Emission Tomography

The development of positron emission tomography (PET) was initiated in the 50s and 60s of the XX century. Further works led to an introduction of first tomographs in the mid-70s [176, 177]. Since then, a tremendous progress has been achieved in the concepts of PET data acquisition and processing, image reconstruction algorithms, as well as in the design and synthesis of various radioligands. Consequently, PET has become a powerful molecular imaging modality characterized by a very high sensitivity [178]. It is currently widely used for research as well as for clinical purposes in several biomedical disciplines.

### 4.1 PET physics

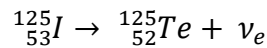
#### 4.1.1 Beta decay

A nucleus of an atom consists of positively charged protons and not charged neutrons which are held together by the nuclear force. The nucleus is stable if the numbers of protons and neutrons are balanced. If there is an excess of one of the nucleons, the nucleus becomes unstable and tends to convert the excessive nucleon into the other one in the process called beta ( $\beta$ ) decay. A conversion of a neutron into a proton is associated with an emission of an electron, and hence it is called  $\beta^-$  decay. However, PET imaging is based on the opposite transition, *i.e.* a conversion of a proton into a neutron, called  $\beta^+$  decay. This process is associated with an emission of a positron and an electron neutrino. As a result, a different chemical element, with the number of protons reduced by one, is formed [179]. For example,  $^{11}\text{C}$  decays to  $^{11}\text{B}$  through  $\beta^+$  decay:



During  $\beta^+$  decay, the mass-energy of the system, *i.e.* of the parent and daughter nuclei, the positron, and the neutrino, has to be conserved. Therefore, the reaction is only possible if the energy difference between the initial and the resultant nuclei is at least twice the equivalent of the electron mass, *i.e.* 1.022 MeV. The exact energy of the emitted positron depends on the parent and the daughter nuclei. Consequently, different PET isotopes are characterized by different positron energy which, in turn, influences the distance the positrons can penetrate the tissue, called the positron range [1, 180].

Alternatively to  $\beta^+$  decay, proton-rich nuclei may also decay through another process which results in the reduction in the number of protons, namely electron capture (EC). Electron capture relies on absorbing an orbital electron by the nucleus which allows the conversion of a proton into a neutron. This is also associated with a release of a neutrino [179]. As an example,  $^{125}\text{I}$  decays to  $^{125}\text{Te}$  via the EC:



Importantly, the process does not necessarily lead to a stable nuclide. An outer electron may fill the vacancy that was left after the absorbed electron, resulting in an emission of X-rays, or if the nucleus is in an excited state, it may further decay to the ground state by emitting  $\gamma$ -rays [179].

Whether a radionuclide decays through positron emission or electron capture depends on the energy difference between the parent and the daughter nuclei. In general, the higher the difference, the higher the probability of  $\beta^+$  decay. However, for larger nuclei with a very high energy difference, more decay pathways are possible and the  $\beta^+$  branching fraction

may be quite low [180]. Table 4.1 summarizes physical properties of the positron emitters most commonly used in PET.

**Table 4.1. Properties of selected PET isotopes**

Adapted from [1-3].

Isotope	$E_{\text{mean}}$ (MeV)	$E_{\text{max}}$ (MeV)	Range in water (mm)		$\beta^+$ branching (%)	Half-life (min)
			mean	max		
$^{11}\text{C}$	0.386	0.960	1.2	4.2	99.8	20.4
$^{18}\text{F}$	0.250	0.634	0.6	2.4	96.9	109.8
$^{15}\text{O}$	0.735	1.738	3.0	8.4	99.9	2.0
$^{13}\text{N}$	0.492	1.732	1.8	5.5	99.8	10.0
$^{64}\text{Cu}$	0.278	0.653	0.7	2.5	17.5	762.1
$^{89}\text{Zr}$	0.396	0.902	1.3	3.8	22.7	4704.6
$^{68}\text{Ga}$	0.890	1.899	2.9	8.9	87.7	67.8

### 4.1.2 Annihilation

After a positron is emitted from the nucleus, it penetrates the surrounding tissue for a distance dependent on its energy. However, due to numerous interactions with the surrounding matter, the positron's path is very tortuous [1]. As it passes through the tissue, the positron also loses its kinetic energy and finally, when it is already almost at rest, it combines with an electron creating a positronium. All this happens very rapidly and the positronium exists for only about  $10^{-10}$  s before annihilation occurs [179].

Annihilation is a process in which the masses of the interacting positron and electron are converted into energy according to the Einstein's mass-energy equivalence. It results in an emission of electromagnetic radiation and the most probable form of it is an emission of two 511 keV  $\gamma$ -rays (Figure 4.1). Because not only the energy, but also momentum has to be conserved, the photons are emitted in an opposite direction [1].

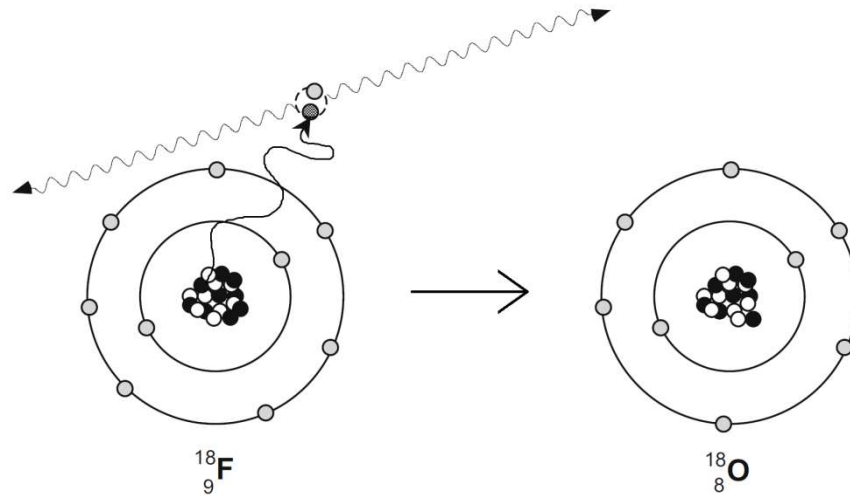


**Figure 4.1. Positron emission and annihilation**

A positron is ejected from a  $^{18}\text{F}$  nucleus resulting in its transition into an  $^{18}\text{O}$  nucleus. The emitted proton passes through the surrounding tissue losing its kinetic energy until it combines with an electron in the process of annihilation. This results in two 511 keV photons being emitted in an opposite direction. Adapted from [1].

The properties of the emitted photons are crucial for PET. The energy of 511 keV is high enough to allow the  $\gamma$ -rays to leave the body and be detected outside. Moreover, the fact that they are always emitted with the  $180^\circ$  angle allows for a precise localization of the annihilation event [179].

## 4.2 Pure and non-pure positron emitters

As these are the annihilation photons, and not the ejected positron, that are detected in PET, any other photons with similar energy that simultaneously hit the detectors during the measurement may induce artificial signals. Thus, isotopes which decay without emission of additional  $\gamma$ -rays (*i.e.* “pure” positron emitters) are traditionally preferred for PET imaging.  $^{11}\text{C}$ ,  $^{15}\text{O}$ ,  $^{13}\text{N}$  and  $^{18}\text{F}$  are all examples of pure emitters (Table 4.1). The small fraction of the decays of these isotopes that occurs via EC lead to stable isotopes and thus, no additional photons are emitted. Also  $^{64}\text{Cu}$  is considered a pure positron emitter, even though its  $\beta^+$

branching fraction is only 17.5 %. Neither the relatively high  $\beta^-$ , nor the EC branching fractions (38.5 % and 44 %, respectively) have a significant impact on PET data acquisition. Only about 0.5 % of the decays is associated with an emission of  $\gamma$ -rays, which may be neglected [3].

However, non-pure positron emitters can be also used in PET. For instance, 3.2 % of the  $^{68}\text{Ga}$  decays are associated with an emission of 1.077 MeV  $\gamma$  photons, some of which may scatter generating  $\gamma$ -rays of lower energy, detectable by the PET scanner [3]. Nevertheless, the isotope is widely used in research, as well as in clinical applications, for imaging different types of cancer [2]. Another example is  $^{124}\text{I}$  which decays through the  $\beta^+$  emission in only 22.4 % and through  $\gamma$  radiation in 74.1 % [3].  $^{124}\text{I}$  is used for imaging of thyroid diseases [181].

### **4.3 Interactions of photons with matter**

There are three main mechanisms by which photons interact with matter and their probability depends on the photon's energy. Radiation with the energy lower than approximately 100 keV predominantly interacts via the photoelectric effect and radiation with the energy between 100 keV and 2 MeV via Compton scattering. Additionally, if the photon carries at least 1.022 keV, it may spontaneously convert into a positron and an electron, which is called pair production. In respect to the annihilation photons, the Compton scattering is the most relevant type of the interactions [1].

This effect relies on the energy transfer from a photon to a free or loosely bound electron which results in ejecting the electron from its original position and in scattering the photon off from its original path. After the interaction, the energy of the photon is reduced by the

binding energy of the electron and its acquired kinetic energy [179]. The consequences of these events for PET are twofold. Firstly, the annihilation event is detected at a wrong location, and secondly, the detected signal is attenuated.

The decay  $\gamma$  rays of non-pure positron emitters interact with matter in the same way as the 511 keV photons. Therefore, not only may they induce spurious signal by directly hitting a detector, but also they contribute to the scattering effect. Moreover, if the energy is high enough and the pair production occurs, the created positron will undergo annihilation resulting in an emission of two detectable photons. This will add on to the artificial signal. Also a combination of different types of the  $\gamma$  radiation interaction with matter is possible depending on the energy of the photons [3].

#### **4.4 PET instrumentation and data acquisition**

The 511 keV photons generated in the annihilation process travel through the surrounding until they reach a detector. The detector converts the amount of the energy deposited by the photon into an electrical signal. This is usually achieved based on the process called scintillation. It relies on absorbing the energy of the photons by electrons in the detector crystal, which brings them to an excited state, and subsequent returning to the ground state by releasing the energy in the form of light. The scintillation light is emitted isotropically and its amount is proportional to the amount of the energy absorbed in the first place. Therefore, the energy of the annihilation photons deposited in the detector can be measured [1, 179].

In order to provide a high signal to noise ratio (SNR), the detector should absorb as much of the incident photons as possible. Therefore, dense materials, like bismuth germanate or

lutetium oxyorthosilicate (LSO) are used. Furthermore, the brightness of the scintillator (*i.e.* the number of the photons produced following an absorption of one 511 keV photon), as well as its timing and energy resolution, are important factors [1].

The next step of the PET signal detection involves converting the scintillation light into an electrical signal. This is usually achieved with photomultiplier tubes (PMTs). The PMTs not only release photoelectrons upon a deposition of the energy of the scintillation photons on a photocathode, but also amplify the signal of the released electrons. The PMTs are typically arranged in  $4 \times 4$  blocks coupled with  $8 \times 8$  arrays of the scintillation crystals which is a cost-effective design [179].

In order to detect an annihilation event, both the emitted photons have to be detected. Therefore, in PET scanners the detector blocks are arranged in a ring (or rings). If the photons are registered by any two detector elements of the ring within a designated timing window, a coincidence is detected (Figure 4.2). The path between the two activated detectors is called a line of response (LOR) and a set of all parallel LORs in one angle is called a projection. During PET data acquisition the signal from the projections in all possible angles is recorded to form a sinogram (Figure 4.3) [10]. The sinogram is the basis

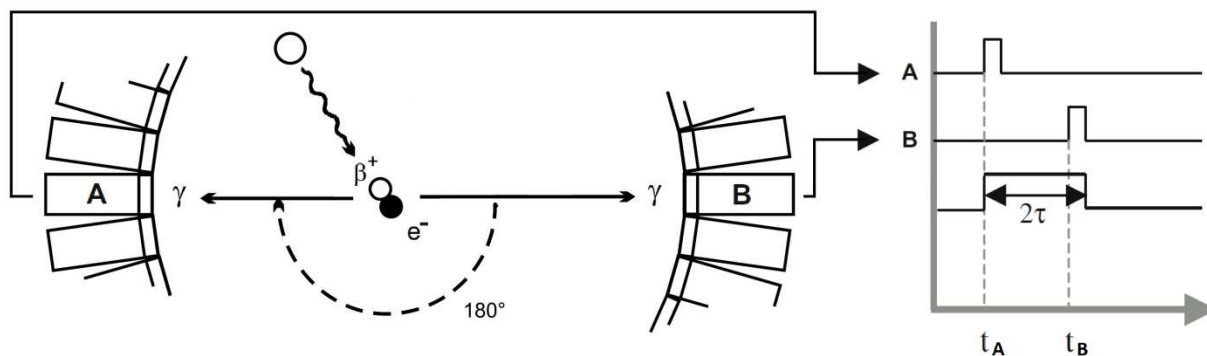


**Figure 4.2. Coincidence detection.**

As a result of the annihilation process, two  $\gamma$  photons are emitted in opposite directions. If the photons are registered by two detectors within the timing window ( $2\tau$ ), a coincidence is recorded. Modified from [1, 14].

for the image reconstruction.

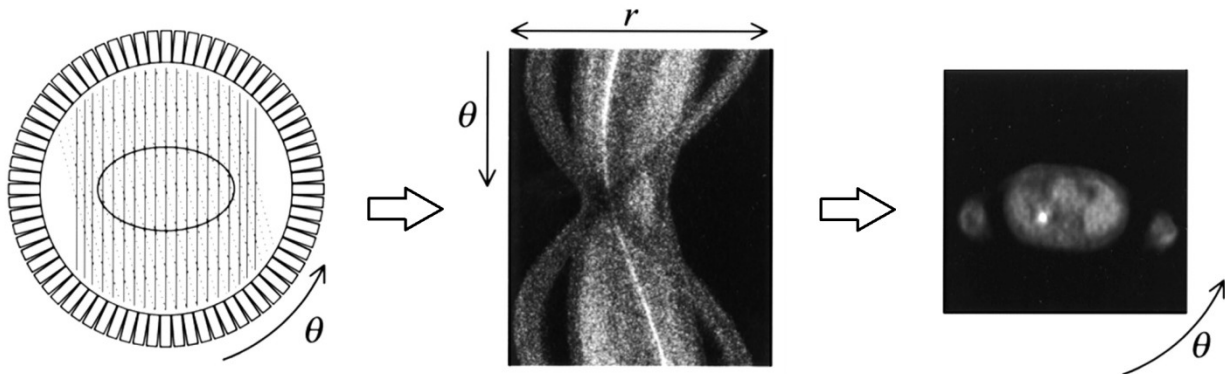


**Figure 4.3. Sinogram formation**

A set of LORs in a given angle  $\theta$  is depicted with solid lines (left). Similar projections are acquired in all other angles and the complete set of all the projections makes a sinogram (middle, “ $r$ ” denotes the distance of the LOR from the center of the field of view). In the sinogram, the signal integrated from one LOR in a given angle is represented by the brightness of the corresponding pixel. A PET image (right) is reconstructed from the sinogram. Modified from [10].

## 4.5 Corrections

Before a PET image is reconstructed from the sinogram, several data preprocessing steps are usually applied. The steps include: normalization, attenuation correction, dead time correction, scatter correction, and correction for random coincidences. If these are not applied, the pixel values in the reconstructed image may not reflect the tracer concentration accurately.

Normalization is necessary because the detector elements are not perfect in terms of their dimensions, geometry and the associated electronics. This results in variability in the responses of individual detectors to the same excitation. Normalization relies on applying appropriate multiplication factors on each pair of the detectors to correct for the nonuniformities [179].

As previously mentioned, due to the interactions of the photons with the surrounding matter, some portion of the signal that should be recorded by the detectors is lost. Attenuation correction is applied in order to take this effect into account. It relies on multiplying the signal from each LOR by a factor that depends on the thickness and density of the material along the LOR. These factors can be obtained by calculating the reduction of the signal originating in an external rotating source that occurs when an object (or a subject) is placed in the field of view (FOV) of the scanner. This approach has been used in the present work.

Besides signal attenuation, interactions of photons with matter also lead to scattering them off from the original trajectory. Consequently, the annihilation event may be attributed to an incorrect location. Unfortunately, correcting for this effect is not straightforward. One approach which reduces the problem relies on limiting the energy window. Scattering a photon by a large angle is associated with a large reduction in its energy. Therefore, only photons that have been scattered by a relatively small angle will be accepted in the narrow energy window [179].

Another type of events that contribute to the inaccuracy in the detected signal is a random coincidence. This is a coincidental detection of two photons that do not originate from the same annihilation. Events of this type occur with a uniform probability across the scanned object and their contribution to the recorded signal can be estimated. This is done either based on the number of singles recorded by each detector, or by including an additional coincidence circuit in which the logic pulse from one of the two detectors in each pair is delayed. Then, none true coincidence can fit within the timing window and if an event is

detected it must be accidental. The estimated amount of randoms is subsequently subtracted from the measured data [179].

Finally, the dead time correction needs to be applied to account for the time the scintillation crystals decay after an excitation. The correction can be done by modelling the dead time behavior of the system at different activity concentration levels [179].

## 4.6 Image reconstruction

There are two main approaches to the reconstruction of PET images from the sinogram data. In the first of them, called backprojection, an image matrix is defined in the first place. Then, a value is attributed to each pixel of the matrix based on the corresponding data from the sinogram. This, however, may sometimes result in attributing values outside of the scanned object, which is a drawback of the simple backprojection algorithm. Implementation of the projection slice theorem allows for taking this inaccuracy into account. Based on the theorem, the Fourier transform and the inverse Fourier transform operations can be used to accurately calculate the radioactivity distribution within the image [179].

A further improvement in the PET image reconstruction has been achieved by implementation of a filtering step. The filter function is applied on the Fourier transform of the sinogram data and the inverse Fourier transform is taken from the output. Depending on the filter, the final image is characterized by a trade-off between a higher spatial resolution and an improved SNR. A big advantage of the filtered-backprojection algorithm (FBP) is its low computational demand. The fact that the real geometry of the detectors is not accounted for and neglecting the noise belong to the disadvantages of the method [179].

The FBP algorithm was used to reconstruct the images in the blood sampler study, as will be described in section 18.4.

The second of the two approaches covers a number of iterative methods of the PET image reconstruction. The general idea behind all of them is to produce an “initial guess” of the image, calculate the projections of the assumed image, and finally compare them to the true projections. The two sets will differ in the first comparison, but based on the obtained differences, the “initial guess” will be modified and the entire process repeated. With an increasing number of such cycles, the predicted projection set will become more similar to the true one. The iterative process will stop when no further improvement can be achieved [182].

A variety of techniques has been developed to implement this idea. One of the currently widespread methods is the ordered subsets expectation maximization (OSEM) algorithm. It was developed as an improvement of the expectation maximization algorithm. The improvement has been achieved by using only a subset of the entire dataset for each iteration, which allows reducing the computational time significantly. In order to further amend the reconstructed image, a maximum *a posteriori* (MAP) function can be used. As the name suggests, the function uses *a priori* information to enforce certain desired conditions (*e.g.* that the tracer concentration is non-negative) [183].

The biggest drawback of the iterative methods is the relatively high computational demand, especially in regard to 3-dimensional images, which translates into the long reconstruction time. This is the price that has to be paid for the improved SNR and higher spatial resolution. The OSEM3D-MAP algorithm was used in the present work for the reconstruction of almost all the  $^{52}\text{Mn}$  PET images, as will be described in section 8.2.

## 5 Manganese-52 as a PET Tracer

### 5.1 Characteristics of $^{52}\text{Mn}$

Among over twenty characterized isotopes of Mn, three positron-emitters,  $^{52}\text{Mn}$ ,  $^{52\text{m}}\text{Mn}$ , and  $^{51}\text{Mn}$ , are potentially suitable for PET. The isotopes differ in regard to their half-lives (5.591 days for  $^{52}\text{Mn}$ , 21.1 min for  $^{52\text{m}}\text{Mn}$ , and 46.2 min for  $^{51}\text{Mn}$ ) and positron energy. Although the half-lives of  $^{51}\text{Mn}$  and  $^{52\text{m}}\text{Mn}$  are closer to the half-lives of commonly used PET isotopes, the high positron energies of these isotopes (970.2 keV and 1179 keV, respectively) translate into long distances the positrons may penetrate the tissue (4.275 mm and 5.288 mm, respectively). Consequently, a worse image quality can be expected.

In contrast, the positron energy and range in tissue of  $^{52}\text{Mn}$  are much more favorable. The mean and maximal energies are 244.6 keV and 575.8 keV, and the corresponding ranges in water are 0.63 mm and 2.461 mm, respectively [184]. The relatively long half-life allows more time for radiochemistry, transportation of the tracer and performance of the experiment. Moreover, a long-term monitoring is possible after a single tracer administration.

Nevertheless, PET imaging with  $^{52}\text{Mn}$  is also associated with some disadvantages. Not only is the  $\beta^+$  branching fraction (29.6 %) relatively low compared to traditional PET isotopes, but also the decay scheme includes multiple  $\gamma$  rays (Figure 5.1), some of which may interfere with PET data acquisition. Specifically,  $\gamma$  rays with the energies of 744.2 keV, 935.5 keV, and 1434.0 keV occur with high probability (90.0, 94.5, and 100.0 % per decay,

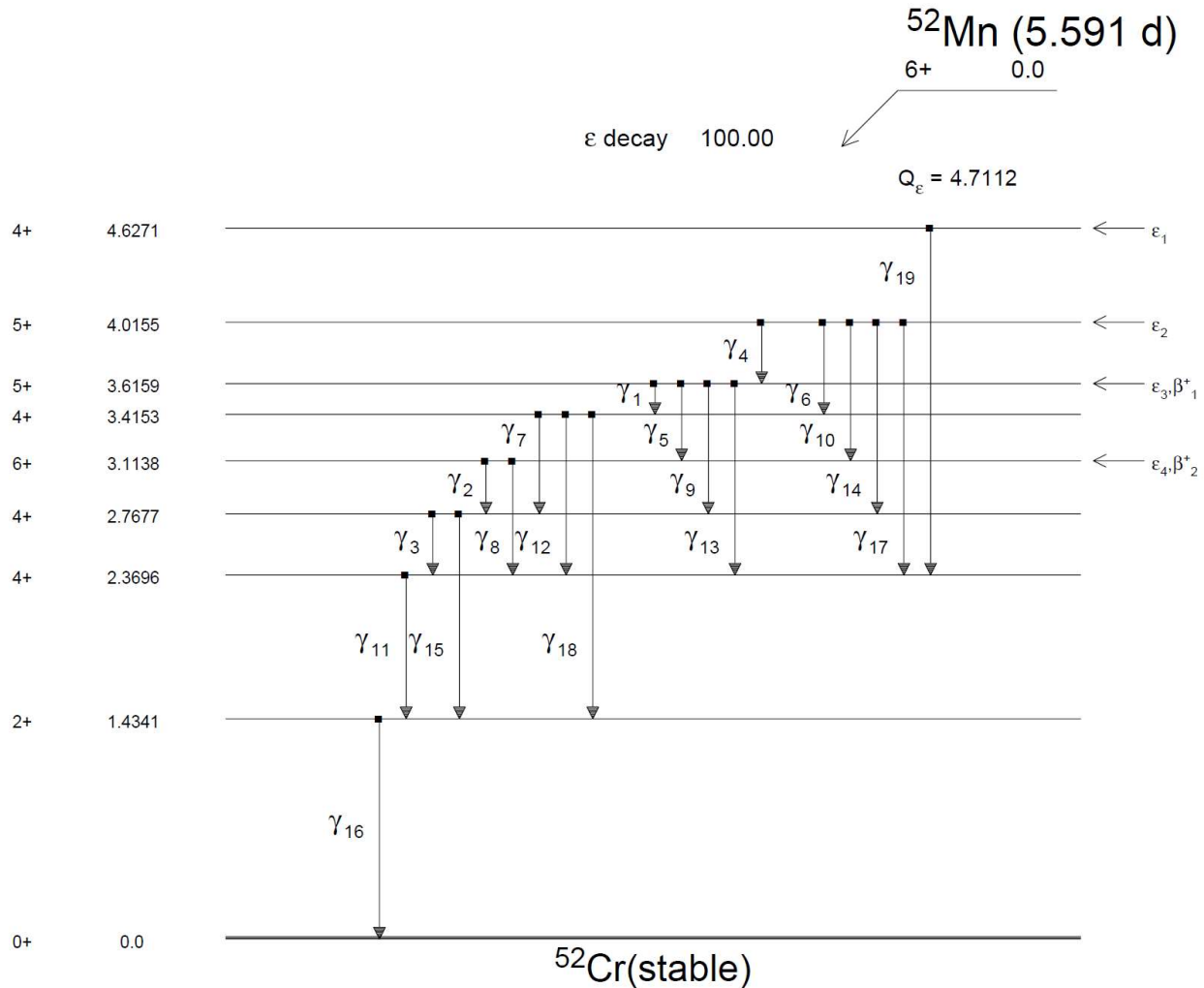


**Figure 5.1. Scheme of the decay of  $^{52}\text{Mn}$**

Source: [4].

respectively) and may be recorded by the detectors. Although narrowing the energy window during the measurement should eliminate a direct detection, these  $\gamma$  rays may interact with the surrounding matter losing some of their energy. The scattered  $\gamma$  rays may be potentially captured by the PET system [185].

The undesired  $\gamma$  radiation, along with the relatively long half-life of  $^{52}\text{Mn}$ , also contributes to the increased radiation exposure for all the persons involved in the study. Finally, for safety reasons, a prolonged time of waste storage is required [180].

## 5.2 Production and separation methods

In order to use  $^{52}\text{Mn}$  for any PET application, the production method has to be well established. In fact, a tremendous improvement has been achieved in the production as well as the separation techniques over the past several years [186-191].

$^{52}\text{Mn}$  can be obtained from chromium (Cr) of high chemical purity (99.95-99.99 %) by proton irradiation, according to the nuclear reaction:  $^{52}\text{Cr}(p,n)^{52}\text{Mn}$ . Due to the small amounts of  $^{53}\text{Cr}$  in Cr, the reaction may also proceed with the production of 2 neutrons:  $^{53}\text{Cr}(p,2n)^{52}\text{Mn}$ . Finally, a bombardment of  $^{54}\text{Cr}$ , which is also present in the substrate, will result in the production of  $^{54}\text{Mn}$ :  $^{54}\text{Cr}(p,n)^{54}\text{Mn}$  [191]. Due to its long half-life (312 days),  $^{54}\text{Mn}$  will contaminate the obtained product. Contribution of the different reaction channels depends on the energy of the applied proton beam [186]. It has been shown that using 16 MeV protons allows achieving at least 99.55 % purity of  $^{52}\text{Mn}$  [188, 189].

The nuclear reaction described above can be conducted on a small medical cyclotron. The target is usually pressed onto a silver disk with a mechanical press and, subsequently, irradiated at the proton beam current of 20-60  $\mu\text{A}$  for 1-5 h. The silver disc is cooled with water from the backside [8, 188, 189, 191]. After the irradiation, several hours should be allowed for the decay of  $^{52\text{m}}\text{Mn}$  (half-life 21 min) [8].

The most difficult part of the tracer preparation is separation of  $^{52}\text{Mn}$  from the Cr matrix. This step is necessary for any biomedical application due to the toxicity of Cr [192]. However, the separation process may be challenging because both, Mn and Cr, can be present at many oxidation states. Moreover,  $\text{Mn}^{2+}$  and  $\text{Cr}^{3+}$  are difficult to separate by

chromatographic methods [189]. Nevertheless, a few techniques have been recently proposed.

The currently preferable method was introduced by Graves and colleagues [188] and it relies on so called “trap-and-release” mechanism. After irradiation, the target is first dissolved in HCl and subsequently diluted with ethanol. The produced ionic complexes of  $^{52}\text{Mn}$  chlorides can be extracted by an anion-exchange resin. In the same conditions  $\text{Cr}^{3+}$  is hydrated and passes through the column. Subsequently, the eluent is changed to a fully aqueous HCl solution which elutes  $^{52}\text{Mn}$  from the resin bed. The entire cycle is repeated three times [188].

This separation technique can be further improved by using pure ethanol and by conducting an additional rising on a small column, which allows a removal of metallic impurities, such as Zn, Fr, Co and Cu, and consequently, improves the specific activity (SA) of the final product [191].

### **5.3 Current applications of $^{52}\text{Mn}$ PET**

Although  $^{52}\text{Mn}$  was used in autoradiography or  $\gamma$ -counting biodistribution studies already in the 1960s [193, 194], only very recently has it entered the field of preclinical PET imaging. The first trial was reported in 2013 [185]. In that study, one rat was injected with approximately 600 kBq of the tracer *i.p.* and scanned 1 and 2 days afterwards, demonstrating that  $^{52}\text{Mn}$  PET is feasible. The second rat was injected *i.v.* and with a higher dose which resulted in a better penetration of the tracer throughout the body and an improved image quality. 5 min after the administration, the tracer was detected in the liver, kidneys, throat, bladder and testicles. However, the penetration through the BBB was very

poor. Finally, a long-term distribution was monitored in the third rat. Except for the abdominal organs, the tracer accumulation in the bones and spinal cord was also observed.

After this first proof-of-principle work, only four other application studies involving *in vivo*  $^{52}\text{Mn}$  PET were conducted, have been reported until now. In the first of them, the tracer was used to track DMT1 – overexpressing human stem cells which had been transplanted into the striatum of two rats [189]. Although penetration of  $^{52}\text{Mn}$  via the BBB was very poor following the systemic administration, the tracer could be detected in the brain in an *ex vivo* PET measurement, as well as in autoradiography.

In the second study, two mice were injected *i.v.* with  $^{52}\text{Mn}$  and the distribution pattern of the tracer known from the previous reports was replicated [195].

A very interesting application of  $^{52}\text{Mn}$ , with a potential to be translated into the clinical level, has been described in the third article. In that work the tracer was used for functional imaging of pancreatic  $\beta$  cells in mice. Importantly, not only an uptake by the pancreas in healthy animals was shown once again, but also a pharmacological manipulation of the uptake could be demonstrated. Namely, the pancreas standardized uptake value (SUV) of  $^{52}\text{Mn}$  was reduced following an administration of nifedipine or diazoxide, both of which block the ability of Ca to stimulate insulin release. Conversely, the SUVs were increased after an administration of glibenclamide which increases the level of intracellular Ca [196]. Therefore, the known mechanism of the intracellular  $^{52}\text{Mn}$  uptake, *i.e.* via the VGCCs, was once again confirmed.

Finally, based on a part of the data from the present doctoral thesis,  $^{52}\text{Mn}$  was used for tracing neuronal pathways in rats [8].

In summary,  $^{52}\text{Mn}$  PET is a very novel tool in the field of preclinical imaging. It allows longitudinal monitoring of the Mn biodistribution, as well as imaging of specific targets that the tracer has an affinity to. Due to the unique biological properties of the divalent Mn ion, as well as the physical properties of the isotope, many other applications are potentially possible. However, since only a handful of studies utilizing  $^{52}\text{Mn}$  have been reported, many aspects require further investigations. Among those are dosimetry issues and a description of the tracer's behavior in the CNS.

## 6 Motivation and Objectives

As it has been discussed in the previous sections,  $Mn^{2+}$  is characterized by unique biological properties which make it a very interesting tool for tracing neuronal pathways. If it was possible to avoid the toxicity effects associated with the doses required for MEMRI, the technique could be safely applied in many studies focusing on the relationship between the brain function and behavior in experimental animals. Since PET is a much more sensitive imaging method than MRI, and using Mn doses of 2-3 orders of magnitude lower should be possible, the main goal of this work was to introduce  $^{52}Mn$  as a PET tracer for functional imaging of neuronal tracts in preclinical studies. This objective was divided into several steps which were realized in separate studies.

In the first study (Study 1), the relationship between the doses of  $Mn^{2+}$ , the changes in the T1 relaxation time the doses provide, and the dopaminergic toxicity they may induce, was investigated. The goal was to verify whether the dose which does not lead to a dopaminergic lesion following a direct administration into the VTA would suffice for MRI.

The second study (Study 2) focused on the image quality that can be achieved with  $^{52}Mn$  PET. The goals of the performed phantom measurements were to select the most optimal image reconstruction algorithm, which would be subsequently used in *in vivo* experiments, and to assess a potential influence of prompt  $\gamma$  rays emitted during the  $^{52}Mn$  decay process on the obtained image.

Subsequently (Study 3), the effect of different radioactivity doses of  $^{52}Mn$  on motor control, on the VTA dopaminergic neurons, and on the DNA integrity in this nucleus was evaluated.

This was accomplished by means of a behavioral test as well as immunohistochemical staining methods in total of three experiments. The primary goal was to define the radioactivity dose of the tracer which could be safely administered into the rat brain.

The aim of the next study (Study 4) was to investigate the possible impact of  $^{52}\text{Mn}$  on the dopaminergic and GABAergic neurotransmitter systems. Specifically, the short- and long-term effects of the intrastriatal administration of the PET tracer on the non-displaceable binding potential (BP<sub>nd</sub>) of [ $^{11}\text{C}$ ]methylphenidate and [ $^{11}\text{C}$ ]flumazenil were to be assessed. For comparison, a similar assessment of potential effects of non-radioactive  $\text{Mn}^{2+}$ , at the dose relevant for MEMRI, was also carried out.

This study was important because DA, as well as GABA, may affect neuronal activity [197, 198]. If Mn ions change the DA or GABA neurotransmission, they may indirectly modify the neuronal activity, which would be highly undesired.

Finally (Study 5), in order to demonstrate the activity-dependence of the  $^{52}\text{Mn}$  neuronal transport, several pharmacological agents, known to influence the neuronal activity, were co-injected with the PET tracer into the VTA. It was expected to detect an increased or reduced  $^{52}\text{Mn}$  concentration in the VTA output regions depending on whether a stimulant or an inhibitor of the neuronal activity was used. A positive result of this study would strongly support the idea of using  $^{52}\text{Mn}$  for functional imaging of the neuronal activity.

## 7 Small Animal PET with Online Blood Sampling

Although this work focuses predominantly on tracing neuronal pathways following a direct injection of  $^{52}\text{Mn}$  into the brain, this is not a standard route of administration of a PET tracer. In human patients, as well as in experimental animals, PET tracers are normally injected intravenously (*i.v.*) and they reach the target organ with the blood stream. The subject undergoes a PET scan after a defined uptake time which should be sufficient for the tracer to reach a constant level in the region of interest (ROI). Subsequently, the tracer concentration can be extracted from the PET image ( $C_{\text{img}}$ ) to quantify the result. This is commonly done using the standardized uptake value (SUV) which is the  $C_{\text{img}}$  normalized by the injected dose (ID) and the body weight of the subject (BW):

$$SUV = C_{\text{img}} * \frac{BW}{ID}$$

Using the SUV is a convenient approach but it has some limitations. Specifically, the SUV may substantially depend on the image resolution, noise level, and the method of ROI definition [199].

An alternative quantification method, kinetic modeling, can be used if dynamic data are available. In this approach, PET is conducted directly after the tracer administration and gradual accumulation of the tracer in the ROI is recorded. The time activity curve (TAC) from the ROI is then used to estimate rate constants of the processes predefined by the applied model. Consequently, the very general concept of the tracer “uptake” is decomposed into several steps, which provides more precise characterization of the tracer

pharmacokinetics and, ultimately, of the biological processes under investigation [200, 201]. This is especially important when a novel PET tracer is developed.

However, in order to use a full, and not a simplified, kinetic model, it is necessary to know the distribution of the tracer in the arterial blood and in the plasma over time, *i.e.* the arterial input function (AIF). The AIF may be obtained from blood samples collected during the PET measurement, which is relatively easy to perform in humans. However, manual blood sampling (MS) in small animals is much more challenging due to the limited blood volume. In order to avoid the blood loss, the blood radioactivity level can be recorded with a blood sampler (BS) in an arterial-venous shunt. This procedure also assures an accurate capturing of the peak activity after a bolus injection [202].

An interesting design of an MR-compatible BS was proposed several years ago [203] but, despite its excellent performance, the device has been never used in a routine small animal PET study. Therefore, an additional goal of the present work was to establish an experimental protocol for PET with online blood sampling using a very similar BS in rats. The established procedure should be applicable for experiments with any PET tracer, including potential  $^{52}\text{Mn}$ -labeled compounds. The specific aim of this study was to evaluate the impact of the technique of the AIF recording on the kinetic parameters (KPs) of [ $^{18}\text{F}$ ]fluorodeoxyglucose ([ $^{18}\text{F}$ ]FDG).

# **MATERIALS AND METHODS**

## 8 Description of the Studies

Total of five studies were carried out in order to evaluate different aspects of using non-radioactive  $Mn^{2+}$  and the positron-emitting  $^{52}Mn$ , for tracing neuronal pathways in rats. Most of them were *in vivo* studies and only Study 2 was a phantom measurement.

### 8.1 Study 1: Relationship between $Mn^{2+}$ doses, signal enhancement in MRI and dopaminergic toxicity

Twelve rats underwent a baseline MRI scan, in which T1W images and T1 maps were acquired. 2-3 days later, they were stereotactically injected into the right VTA with Mn-bicine chelate solution. The Mn-bicine complex is a low affinity chelate and at the pH of 7.4, which was used, 10 % of the metal is present as free ions [150]. The amount of  $MnCl_2$  to be dissolved in the bicine solution was calculated to provide 0.5 nmol ( $n = 4$ ) or 45 nmol ( $n = 4$ ) of free  $Mn^{2+}$  ions in the injected volume. The control group ( $n = 4$ ) was treated with the bicine solution alone.

The second MRI measurement was carried out at 24 h post-injection. The obtained T1W images allowed verification of the injection site and visualization of the distribution of the contrast agent. The T1 maps were used for a quantitative VOI-based analysis.

The rats were sacrificed 4 weeks after the injection and their brains were used for the TH-staining.

### 8.2 Study 2: $^{52}Mn$ phantom measurements

Three phantoms were used in this study. The first one was an Ultra Micro Hot Spot Phantom (Data Spectrum Corporation, Durham, NC, USA) which contains 6 sets of rod

volumes with different diameters ranging from 0.75 mm to 2.40 mm. Its geometry is depicted in Figure 8.1.

The phantom was filled with  $^{52}\text{Mn}$  solution (2.92 MBq in approximately 6 mL) and positioned in the center of the FOV of the PET scanner. The acquisition was performed with the energy window of 350-650 keV and it lasted 20 min. The images were reconstructed with different algorithms and matrix sizes. Those were: the FBP algorithm and the matrix size of  $128 \times 128$  (i), the OSEM2D algorithm (4 iterations) and the matrix size of  $128 \times 128$  (ii), the OSEM3D (2 iterations) – MAP (18 iterations) algorithm and the matrix size of  $128 \times 128$  (iii), and the OSEM3D-MAP algorithm but the  $256 \times 256$  matrix size (iv). The obtained images were visually compared.

The second phantom was a 1.5 mL Eppendorf tube completely filled with  $^{52}\text{Mn}$  solution (0.8 MBq). It was placed in the centre of the FOV of the PET scanner and the acquisition was performed 4 times without moving the phantom. Each time one of the following energy windows was used: 350-650 keV, 400-650 keV, 450-650 keV, or 450-600 keV. Each acquisition lasted 20 min and was reconstructed as a single frame using the OSEM3D-MAP

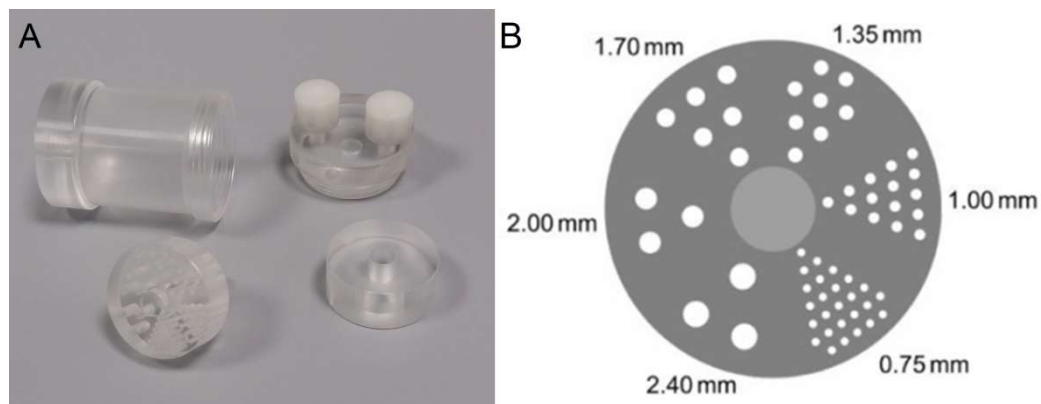


**Figure 8.1. Resolution phantom**

**A.** Elements of the resolution phantom. **B.** A schematic cross-section through the phantom showing the arrangement and diameters of the rod volumes. Adapted from [6].

algorithm and the  $256 \times 256$  matrix size.

The third phantom was a 1 mL plastic syringe partially filled with  $^{52}\text{Mn}$  solution (23 kBq) and with the opening closed with plasticine. The entire syringe was closed in a water-filled 15 mL Falcon tube. The water surrounding was meant to imitate a biological tissue. The phantom was positioned in the centre of the FOV of the PET scanner and 4 acquisitions were performed using the same energy windows as for the previous phantom. Due to the little activity available, each acquisition lasted 30 min.

### **8.3 Study 3: Impact of different radioactivity doses of $^{52}\text{Mn}$ on the dopaminergic system**

#### ***8.3.1 Experiment 1: Impact of the 170 kBq dose on the dopaminergic system***

Twelve rats were used in this experiment. Eight of them were stereotactically injected with  $169 \pm 24$  kBq (mean  $\pm$  sd, further denoted as 170 kBq) of  $^{52}\text{Mn}$  into the right VTA (*VTA* group,  $n = 4$ ) or right STR (*STR* group,  $n = 4$ ). The remaining four rats were injected also into the right VTA but approximately 3 months later. The time delay assured full decay of the injection solution (*VTA decayed* group).

Static PET (20 min acquisition) and MRI measurements were carried out on the animals from the *VTA* and *STR* groups 24 h post-injection in order to evaluate the tracer distribution in the brain. 4 weeks post-injection all the animals underwent the rotameter test. 1 day later, the rats were sacrificed and the brains were removed for the TH-staining.

### ***8.3.2 Experiment 2: Impact of the 30 kBq and 150 kBq doses on the DNA strand breaks***

Since a dopaminergic lesion, not likely caused by the metal, was observed in some animals in Experiment 1, Experiment 2 aimed at assessing a possible contribution of the ionizing radiation to the observed toxic effect. Thus, eight rats were unilaterally injected into the VTA with either  $149 \pm 10$  kBq (further denoted as 150 kBq,  $n = 4$ ) or  $28 \pm 6$  kBq (further denoted as 30 kBq,  $n = 4$ ) of  $^{52}\text{Mn}$ . The control group ( $n = 4$ ) was injected with saline solution. Two animals from each group were sacrificed at 90 min and two at 24 h post-injection. The brain tissues from all the rats were used for immunohistochemical staining against  $\gamma$ -phosphorylated histone protein H2AX ( $\gamma\text{H2AX}$ -staining) which detects DNA breaks.

### ***8.3.3 Experiment 3: Impact of the 20 kBq dose on the dopaminergic system***

Total of twenty four rats were used in this experiment. Eighteen of them were stereotactically injected with the reduced dose of  $^{52}\text{Mn}$  ( $20 \pm 5$  kBq) into the right VTA. Six rats were injected with a buffered saline solution to serve as a control group. 24 h after the injection, the  $^{52}\text{Mn}$ -treated rats underwent static PET (60 min acquisition) and MRI. All the animals underwent the rotameter test at the following time points: 3 days post-injection (six  $^{52}\text{Mn}$ -injected rats), 14 days post-injection (another six  $^{52}\text{Mn}$ -treated rats), and 28 days post-injection (six  $^{52}\text{Mn}$ -treated rats and six control animals). 1 day after the rotameter test, the animals were sacrificed and the brains were removed. Three brains from each group were used for the TH-staining.

## 8.4 Study 4: Interactions of $Mn^{2+}$ with the dopaminergic and GABAergic neurotransmitter systems

Three groups of rats were stereotactically injected into the right STR with 1  $\mu$ L of non-radioactive  $MnCl_2$  solution containing 50 nmol of  $Mn^{2+}$  (*Cold Mn* group,  $n = 8$ ), the solution containing  $29 \pm 13$  kBq of  $^{52}Mn$  (*Hot Mn* group,  $n = 8$ ), or 0.9% NaCl solution (*Control* group,  $n = 8$ ). On the following day, the rats underwent anatomical MRI and [ $^{11}C$ ]methylphenidate PET. At 48 h post-injection the [ $^{11}C$ ]flumazenil PET was performed. After 4 weeks, the MRI, as well as the [ $^{11}C$ ]methylphenidate and [ $^{11}C$ ]flumazenil PET measurements were repeated on 2 consecutive days to evaluate the long-term effects. The study design is depicted in Figure 8.2.

In case of the *Hot Mn* group, the systemic injections of the [ $^{11}C$ ]-tracers were preceded by 60 min static scans in order to acquire the signal from the  $^{52}Mn$  still present in the brain. The [ $^{11}C$ ]-tracer was administered directly afterwards without changing the animal's position on the bed. With the assumption that during the time of these PET acquisitions, the  $^{52}Mn$  distribution in the brain does not change, it was planned to subtract the static  $^{52}Mn$  images from the subsequently acquired dynamic images containing the mixed signal of

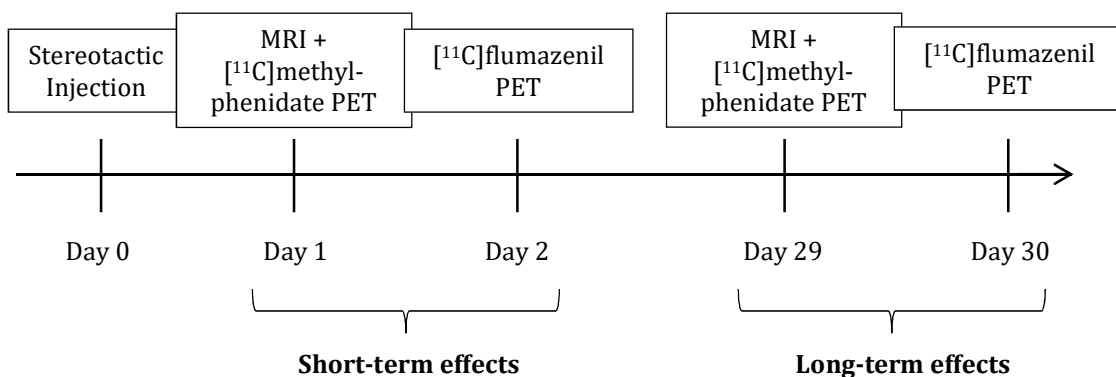


Figure 8.2. Time line of Study 4

$^{52}\text{Mn}$  and the  $[^{11}\text{C}]$ -tracer. The following framing was used to reconstruct the dynamic images:  $12 \times 5$  s,  $6 \times 10$  s,  $6 \times 30$  s,  $5 \times 60$  s,  $10 \times 300$  s.

Unfortunately, due to the difficulties associated with the subtraction procedure in the *Hot Mn* group, the images containing the  $^{11}\text{C}$  signal alone could not be recovered. Therefore, the data of this group could not be analyzed.

## 8.5 Study 5: Activity-dependence of $^{52}\text{Mn}$ neuronal transport and dosimetry

Six groups of rats were treated with different pharmacological agents known to stimulate or inhibit the neuronal activity. These agents were stereotactically co-injected with  $27 \pm 8$  kBq (mean  $\pm$  sd) of  $^{52}\text{Mn}$  solution in  $2 \mu\text{L}$ , directly into the right VTA. The following pharmacological agents were used:

- $100 \mu\text{M}$  2-amino-3-(3-hydroxy-5-methyl-isoxazol-4-epropionic acid (AMPA, Alomone Labs Ltd., Jerusalem, Israel) – *AMPA* group,  $n = 7$ ;
- tetrodotoxin (TTX, Alomone Labs Ltd.) – *TTX* group,  $n = 10$ ;
- *N*-Methyl-D-aspartic acid or *N*-Methyl-D-aspartate (NMDA, Alomone Labs Ltd.) – *NMDA* group,  $n = 10$ ;
- 2-amino-5-phosphonopentanoic acid (AP-5, Alomone Labs Ltd.) – *AP5* group,  $n = 5$ ;
- Manganese (II) chloride tetrahydrate ( $\text{MnCl}_2 \times 4\text{H}_2\text{O}$ , Sigma-Aldrich Chemie GmbH, Munich, Germany) – *Cold Mn* group,  $n = 4$ ;
- The control group (*CTRL*) was injected with  $^{52}\text{Mn}$  solution alone;  $n = 9$ .

After the stereotactic injection and suturing of the wound, the animal was transferred to the PET scanner and the acquisition started  $26 \pm 3$  min (mean  $\pm$  sd) after the end of the

injection. It lasted 6 h and the images were reconstructed as 12 × 30 min frames which allowed visualization of the gradual transport of  $^{52}\text{Mn}$  from the injection site to different brain regions. The injection location was verified based on the T2W MR images.

The PET data from the *CTRL* rats were additionally used for dosimetry estimates, which will be described in details later.

## 9 PET tracers

$^{52}\text{Mn}$  was produced by Dr Gregory Severin and Dr Jesper Fonslet at The Hevesy Laboratory, Technical University of Denmark. Since the present work focuses on potential applications of this PET tracer, its production and separation methods are described in detail.

$[^{11}\text{C}]$ methylphenidate and  $[^{11}\text{C}]$ flumazenil were used in Study 4. These tracers were synthesized by Ramona Stumm and Dr Andreas Maurer at the Werner Siemens Imaging Center. The radiosynthesis procedures of these substances are also described.

### 9.1 Production of $^{52}\text{Mn}$

$^{52}\text{Mn}$  was produced from Cr powder (200 mg, 99.99%, 100-325 mesh, Alfa Aesar, Thermo Fisher GmbH, Karlsruhe, Germany). Cr was mechanically pressed onto a silver disc (0.5 cm thick  $\times$  2.7 cm diameter) and covered with an Al foil. The irradiation of the target (20  $\mu\text{A}$  protons at 15.4 MeV, degraded by the foil from the nominal 16.0 MeV, for 4.8 h) was performed on a PETtrace cyclotron (General Electric, Boston, Massachusetts, USA). During this process, the silver disc was being cooled with water from the backside.

Following the irradiation, several hours were allowed for a decay of  $^{52\text{m}}\text{Mn}$  ( $T_{0.5} = 21$  min) contaminating the product. Subsequently, the silver disk was immersed in 12 M HCl overnight. The obtained mixture was directed for a chemical separation [191].

### 9.2 Separation of $^{52}\text{Mn}$

Two different methods were used. *Method 1* (used only for Experiment 1 in Study 3) was adapted from Lahiri *et al.* [204]. *Method 2*, adapted after Graves *et al.* [188], was used for all

the other studies. *Method 2* was preferred as it resulted in a reduced content of metallic impurities and in an improved specific activity (SA).

### Method 1

The obtained solution was first diluted with water to the approximate HCl concentration of 7.6 M, and subsequently separated into two falcon tubes. 0.5 M trioctylamine in cyclohexane (Sigma Aldrich Chemie GmbH, Copenhagen, Denmark) was added to each of them. The vials were shaken for 5 min and then spun in a centrifuge (4400 rpm, 5 min, radius of approximately 20 cm). As a result, three phases were formed in the tubes with the green Cr being mostly present in the bottom one. The two upper phases from both tubes were pooled and the centrifugation was repeated. A small amount of the aqueous Cr phase formed once again at the bottom of the tube. The upper phases were decanted and centrifuged for the final 10 min. The separated Cr phase was removed with a syringe.

Afterwards, the  $^{52}\text{Mn}$  phase was back-extracted into 2 mL of aqueous 0.1 mM  $\text{NH}_4\text{OH}$  solution (Sigma Aldrich Chemie GmbH) by vigorous shaking and centrifugation (5 min). The formed aqueous phase was pipetted out into a glass vial for drying (130 °C under Ar flow). The obtained purple residue was dissolved in 12 M HCl and then diluted with neat ethanol. The solution was passed over a 400 mg AG 1 × 4 anion exchange resin (Bio-Rad Laboratories, Copenhagen, Denmark). The following solutions were sequentially used in the resin: 6 M HCl (5 mL), 2 M HCl (5 mL), water (5 mL), 6 M HCl (5 mL), and 2 M HCl (5 mL). 12 M HCl in ethanol (5 mL) was used as the mobile phase. This was followed by passing the mobile phase, repassing the active sample and final washing with the mobile phase. 4 mL of 0.1 M HCl were used to elute  $^{52}\text{Mn}$  from the column.

The solution was subsequently dried at 130°C under Ar. Then, 1 mL of 0.1 M HCl was added to the vial to redissolve the activity. 350 µL of the solution was again taken to be dried under Ar at 130 °C. Finally, 50 µL of 10 mM Na (L+) ascorbate in normal saline (0.9 % NaCl) was passed through a sterile filter into the vial. 10 mM Na (L+) ascorbate in normal saline was used as a buffer also in all future preparations of  $^{52}\text{Mn}$  used in this work.

### Method 2

The obtained solution was first dried at 130 °C, then reconstituted in 3.0 mL of 12 M HCl, and finally diluted with neat ethanol to 60 mL. This was passed over a 725 mg AG 1 × 8 column and 2 M HCl, 6 M HCl and ethanol were sequentially used for rinsing. This was followed by 97:3 ethanol:aq. 12 M HCl which trapped  $^{52}\text{Mn}$ .

The column was subsequently washed with 97:3 ethanol:12 M HCl (22 mL) and  $^{52}\text{Mn}$  was eluted in 1 mL of 0.1 M HCl. The obtained solution was dried at 130 °C. The dried substance was redissolved in 0.5 mL of HCl, then diluted with ethanol to 10 mL, and subsequently passed over a second AG 1 × 8 column (697 mg). The washing and eluting steps, as well as the following drying and redissolving, were exactly the same as in the first run. Finally, the entire column procedure was conducted for the third time on a small 89 mg AG 1 × 8 anion exchange resin.  $^{52}\text{Mn}$  was eluted in 0.1 M HCl, dried under Ar, and redissolved in 10 mM Na (L+) ascorbate in normal saline.

Regardless of the  $^{52}\text{Mn}$  separation method, a sample of the final solution was evaluated with Inductively Coupled Plasma Optical Emission Spectroscopy (ICP-OES, Thermo Fischer Scientific, Waltham, MA, USA) versus Ag, Cr, Ni, Cu, Fe, Mn, Ca and Zn standards.

### 9.3 Production of $^{11}\text{C}$

$^{11}\text{C}$  was produced on a PETtrace cyclotron (GE Healthcare, Munich, Germany) from  $^{14}\text{N}$ , according to the nuclear reaction:  $^{14}\text{N}(p,\alpha)^{11}\text{C}$ . For this purpose,  $\text{N}_2$  gas with 1 %  $\text{O}_2$  was irradiated with 70  $\mu\text{A}$  protons at 16.5 MeV for 30 min.  $[^{11}\text{C}]\text{CO}_2$  was created as the reaction product. Subsequently, the product was catalytically reduced to  $[^{11}\text{C}]$ methane, which was then reacted with iodine to obtain  $[^{11}\text{C}]$ iodomethane.  $[^{11}\text{C}]$ iodomethane was used to synthesize the tracers.

### 9.4 Synthesis of $[^{11}\text{C}]$ methylphenidate

The synthesis occurs in two steps, as depicted in Figure 9.1. Its precursor is D-threo-N-NPS-ritalinic acid, 2 mg of which are dissolved in a mixture of 500  $\mu\text{L}$  dimethylformamide (DMF) with 2  $\mu\text{L}$  NaOH 2 M. In the first step of the synthesis,  $[^{11}\text{C}]$ iodomethane is dissolved in the mixture. The methylation reaction is performed at 83  $^\circ\text{C}$  for 8 min. After cooling to 30  $^\circ\text{C}$ , hydrolysis of the NPS protecting group is performed as the second step. It relies on adding 150  $\mu\text{L}$  of HCl 1M and 2.5  $\mu\text{L}$  of thioglycolic acid to the reaction mixture with a subsequent incubation at 30  $^\circ\text{C}$  for 3.5 min.

Separation of the final product is conducted with high performance liquid chromatography (HPLC). The purified  $[^{11}\text{C}]$ methylphenidate is trapped on a solid-phase extraction cartridge (Strata-X, Phenomenex), eluted with ethanol and subsequently diluted with phosphate-buffered saline and sterile filtered (0.22  $\mu\text{m}$ ).

In Study 4,  $24 \pm 3$  MBq (mean  $\pm$  sd) of the tracer was administered *i.v.* as a bolus injection.

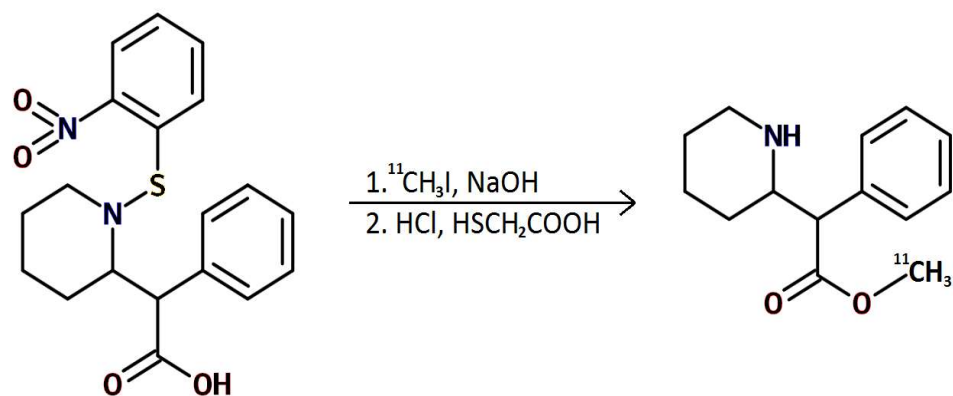


Figure 9.1. Synthesis of [ $^{11}\text{C}$ ]methylphenidate

## 9.5 Synthesis of [ $^{11}\text{C}$ ]flumazenil

[ $^{11}\text{C}$ ]iodomethane is combined with 2 mg of the precursor, desmethylflumazenil, in 300  $\mu\text{L}$  of dimethylformamide and 3  $\mu\text{L}$  of 0.5 M NaOH. The reaction is performed at 70  $^\circ\text{C}$  for 5 min (Figure 9.2). After cooling to 30  $^\circ\text{C}$ , the mixture is diluted with 1.5 mL of the HPLC eluent and directed to the HPLC for the separation of the final product. [ $^{11}\text{C}$ ]flumazenil is trapped on a solid-phase extraction cartridge (Strata-X, Phenomenex), eluted with ethanol and subsequently prepared for injections by dilution with phosphate-buffered saline and by sterile filtration (0.22  $\mu\text{m}$ ).

In Study 4,  $26 \pm 2$  MBq (mean  $\pm$  sd) of [ $^{11}\text{C}$ ]flumazenil was administered *i.v.* as a bolus injection.

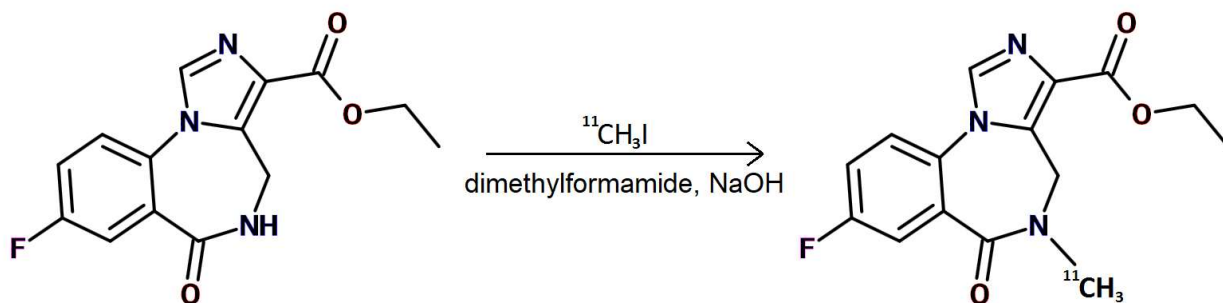


Figure 9.2. Synthesis of [ $^{11}\text{C}$ ]flumazenil

## 10 Animals and Stereotactic Injection

### 10.1 Animals

All the animal procedures were performed in accordance with international standards for the care and use of laboratory animals and were approved by the local Animal Welfare and Ethics Committee of the Country Commission Tübingen, Germany (Animal Licenses No R05/2013, R02/16 and R01/2017). In all the *in vivo* studies, male Lister Hooded rats were used. They were housed in individually ventilated cages in groups of up to 4 per cage. Food and tap water were provided *ad libitum*. The temperature and humidity in the animal facility were  $22 \pm 1^\circ\text{C}$  and  $55 \pm 2\%$  RH, respectively. The light was always turned on at 7 am and turned off at 7 pm.

The number of animals used for each study is provided in the respective section.

### 10.2 Stereotactic injection

Prior to the surgery, the rats were anesthetized by one of the following methods:

- Medetomidine (Domitor, Orion Corporation, Espoo, Finland) / midazolam (Midazolam-hameln, Hameln Pharma Plus GmbH, Hamelin, Germany) / fentanyl (Fentadon, Albrecht GmbH, Aulendorf, Germany) mixture in saline (0.15/2.0/0.005 mg/kg bw, *i.p.*) – used in Studies 1 and 3. After the surgery, the flumazenil (Fresenius Kabi, Bad Homburg, Germany) / atipamezole mixture (0.75/0.20 mg/kg bw, *s.c.*) was administered as an antidote.
- Isoflurane (Isoflurane CP, CP-Pharma Handelsgesellschaft mbH, Burgdorf, Germany) – oxygen (Hans Mast GmbH, Tuebingen, Germany) mixture (2.5 % for induction and

app. 1.7 % for maintenance) – used in Studies 4 and 5. In this case, fentanyl was additionally administered for analgesia (5 µg/kg bw, *i.p.*)

The intracerebral injections were performed on a stereotactic frame (Stoelting Europe, Dublin, Ireland), where the animal's head was fixed with ear and tooth bars. The body temperature was maintained by a heating mat. In order to expose the skull surface, the skin was incised with a scalpel. Subsequently, a small hole was drilled in the skull at the location determined based on the rat brain atlas [16] (Figure 10.1). The following coordinates were used:

- for the VTA injections in small rats (200-250g, Studies 1 and 3): 5.20 mm posterior, 2.00 mm lateral to the bregma, and -8.00 mm ventral from the skull surface;
- for the VTA injections in bigger rats (350-450g, Studies 4 and 5): 5.40 mm posterior, 2.05 mm lateral to the bregma, and 8.05 mm ventral from the skull surface;
- for the intrastriatal injections (Studies 3 and 5): 0.7 mm anterior, 3.2 mm lateral to the bregma, and -5.15 mm ventral from the skull surface.

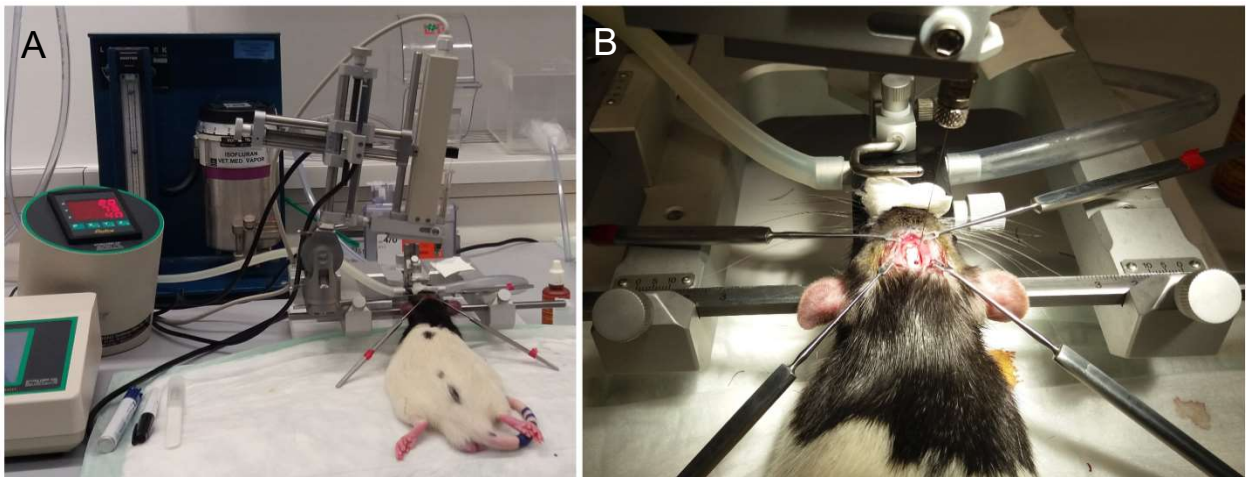


**Figure 10.1. Stereotactic injection**

**A.** The stereotactic frame connected to the automatic infusion pump allows for a direct and precise administration of the tracer solution into the designated brain location. **B.** A small hole in the skull is drilled before insertion of the needle.

**Table 10.1. Summary of the injection procedures used in the *in vivo* studies**

Study	Group	N	Injection solution	Target region; inj. vol ( $\mu$ L); inj. rate ( $\mu$ L/min)
1	<i>0 nmol</i>	4	100 mM bicine	Right VTA; 0.05; 0.05
	<i>0.5 nmol</i>	4	5 nmol of MnCl <sub>2</sub> in 100 mM bicine	
	<i>45 nmol</i>	4	50 nmol of MnCl <sub>2</sub> in 100 mM bicine	
3 Exp. I	<i>VTA</i>	4	169 $\pm$ 24 kBq of <sup>52</sup> Mn in buffer*	Right VTA or STR; 1.00; 0.25
	<i>STR</i>	4		
	<i>VTA decayed</i>	4	the same, but decayed solution	
3 Exp. II	<i>Control – 90 min</i>	2	0.9 % NaCl	Right VTA; 1.50; 0.25
	<i>Control – 24 h</i>	2		
	<i>30 kBq – 90 min</i>	2	28 $\pm$ 6 kBq of <sup>52</sup> Mn in buffer	
	<i>30 kBq – 24 h</i>	2		
	<i>150 kBq – 90 min</i>	2	149 $\pm$ 10 kBq of <sup>52</sup> Mn in buffer	
	<i>150 kBq – 24 h</i>	2		
3 Exp. III	<i>3 days</i>	6	20 $\pm$ 5 kBq of <sup>52</sup> Mn in buffer	Right VTA; 1.50; 0.25
	<i>14 days</i>	6		
	<i>28 days</i>	6		
	<i>Control</i>	6	buffer	
4	<i>Control</i>	8	0.9 % NaCl	Right STR; 1.00; 0.25
	<i>Cold Mn</i>	8	50 mM MnCl <sub>2</sub> in 0.45% NaCl**	
	<i>Hot Mn</i>	8	<sup>52</sup> Mn in buffer	
5	<i>CTRL</i>	9	<sup>52</sup> Mn in buffer	Right VTA; 2.00; 0.25
	<i>AMPA</i>	7	<sup>52</sup> Mn in buffer with 100 $\mu$ M AMPA	
	<i>NMDA</i>	10	<sup>52</sup> Mn in buffer with 1 mM NMDA	
	<i>AP-5</i>	5	<sup>52</sup> Mn in buffer with 1mM AP-5	
	<i>TTX</i>	10	<sup>52</sup> Mn in buffer with 5 $\mu$ M TTX	
	<i>Cold Mn</i>	4	<sup>52</sup> Mn in buffer with 25 mM Mn <sup>2+</sup>	

\*Throughout this table, “buffer” refers to 10 mM Na (L+) ascorbate-buffered normal saline, even though the bicine solution used in Study 1 also served as a buffering agent.

\*\*Reduced concentration of the NaCl was used in order to achieve the final osmolality of 304 mOsm/L, which is close to the physiological value.

The injections were done using a 5  $\mu$ L syringe with a 26 G needle (Hamilton Robotics, Bonaduz, Switzerland). The needle was inserted into the rat brain at an angle of 8 ° for the VTA injections, or at 0 ° for the intrastriatal injection. An automated pump (Stoelting) was used to deliver the solution into the target location. The injected volumes and infusion rates differed between the studies and are specified in Table 10.1. The table also summarizes all the pharmacological agents used for the stereotactic injections.

After the end of the injection, the solution was allowed to diffuse over 7-8 min to prevent its backflow into the needle. Then, the needle was withdrawn at the approximate rate of 1 mm/min. Finally, the hole in the skull was sealed with wax and the skin was sewn.

In case of  $^{52}\text{Mn}$  administration, the radioactivity in the syringe was measured in a well counter (CRC-25R Dose Calibrator, Capintec Inc., Pittsburgh, PA, USA) before and after the injection.

# 11 Imaging Procedures

## 11.1 PET measurements

All the PET measurements were performed on  $\mu$ PET scanners (Inveon dedicated PET, Siemens Healthineers, Knoxville, TN, USA) which are characterized by the  $10 \times 10 \times 12 \text{ cm}^3$  FOV. The Inveon Acquisition Workplace software (v.1.5.0.28, Siemens) was used for data acquisition which was performed with the energy window of 360-650 keV. Only in the phantom measurements different energy windows were used, as described in section 8.2.

During the *in vivo* measurements, the rats were anaesthetized with the isoflurane (CP-Pharma Handelsgesellschaft mbH) – oxygen (Hans Mast GmbH) mixture (2.5 % isoflurane for induction and 1.7 % for maintenance) and the body temperature was kept at  $37 \pm 0.5 \text{ }^\circ\text{C}$  by a rectal probe and a heating mat with a feedback loop control system. If the heating system was insufficient, a red light lamp was used in addition.

The rats were scanned on individual MR-compatible beds (Bruker BioSpin) with the head fixed by tooth and ear bars. Additionally, a thin tube filled with a diluted  $^{52}\text{Mn}$  solution was put around the neck of the rat for later coregistration of the PET and MR images. Directly after the PET acquisition, the animal was transferred to the MRI scanner on the same bed. Only in Study 4, two rats were positioned head-to-head on the same bed for PET, while MRI was conducted individually for each animal.

The durations of the PET acquisitions varied and are specified for each study in chapter 8. Each acquisition, with an exception for two volume phantom measurements, was followed by a 10 min transmission scan performed with a rotating  $^{57}\text{Co}$  source which was later used

for attenuation correction. All the PET data were also normalized and corrected for the tracer decay and the dead time of the detectors.

All the PET images from the *in vivo* studies were reconstructed with OSEM3D (2 iterations)-MAP (18 iterations) algorithm and the  $256 \times 256$  matrix size. Different algorithms and matrix sizes were used in one phantom experiment, as described in section 8.2.

## 11.2 MRI measurements

In Studies 1 and 3, MRI was performed on a 7 T small animal MRI scanner (ClinScan, Bruker BioSpin, Ettlingen, Germany). Image acquisition was performed with Syngo MRI software (Siemens Medical Solutions, Erlangen, Germany). T2W and T1W images, as well as T1 maps, were obtained using the parameters presented in Table 11.1.

**Table 11.1. Parameters of the MRI sequences used in Studies 1 and 3**

Obtained image	T2W	T1W	T1 map
Sequence type	Spin Echo (SE)	Gradient Echo (GE)	Fast Low-Angle Shot (FLASH)
TR	3000 ms	50 ms	10 ms
TE	205 ms	3.65 ms	1.12 ms
FOV <sub>r</sub>	57 mm	40 mm	34 mm
FOV <sub>ph</sub>	35.625 mm	40 mm	34 mm
slice thickness	0.22 mm	0.31 mm	1 mm
Matrix size	$256 \times 256$	$128 \times 128$	$128 \times 128$
Flip angles	-----	-----	6° and 34°
Number of excitations (NEX)	1	1	2

**Table 11.2. Parameters of the MRI sequences used in Study 4 and 5**

Obtained image	T2W	T1W
Sequence type	Rapid Imaging with Refocused Echoes (RARE)	FLASH
TR	4264.78 ms	40 ms
TE	11 ms	3.65 ms
FOV <sub>r</sub>	32 mm	30 mm
FOV <sub>ph</sub>	35 mm	40 mm
slice thickness	0.8 mm	0.3125 mm
Matrix size	256 × 256	128 × 128
RARE factor	8	-----
NEX	1	1

Another small animal 7 T MRI scanner (BioSpec, Bruker BioSpin) was used in Studies 4 and 5. It was equipped with the ParaVision 6 acquisition software (Bruker Biospin). T2W and T1W images were acquired using the sequence parameters presented in Table 11.2.

Both the scanners were equipped with a rat brain receiver coil (Bruker BioSpin).

## 12 Image Coregistration and VOIs

PET and MR image analysis was performed with Pmod software v.3.2 (PMOD Technologies LCC, Zurich, Switzerland). For image analysis in Studies 1 and 3 (where smaller rats were used), the T1W (Study 1) and T2W (Study 3) images were first registered to the anatomical template. The template had been obtained by averaging T2W images of 5 rats of the same strain and similar body weight, not included in the present work. Subsequently, the T1 maps (Study 1) and the PET images (Study 3) were registered to their corresponding MR images.

Volumes of interest (VOIs), ipsilateral and contralateral to the injection side, were drawn on the template in the coronal plane according to the rat brain atlas [16] and, subsequently, copied onto the coregistered T1 maps (Study 1) or PET images (Study 3). The following VOIs were included in the analysis of the images of the VTA-injected rats: NAc, STR, PFC, OT, AMG, and cerebellum (CER). In Study 1, only the first 3 of them were used. For the intrastrially injected rats the following VOIs were included: GP, thalamus (THL), SN, and CER. The latter one served as a control region. The anatomical template and the VOIs are shown in Figure 12.1.

Larger rats were used in Study 4 and their brain size matched the anatomical template and the VOIs provided in the Pmod software. Therefore, the MR images were firstly coregistered to that template and the PET images were subsequently coregistered to their respective MR images. Then, TACs were obtained from: the ipsilateral STR, the contralateral STR and the CER for the [ $^{11}\text{C}$ ]methylphenidate images, and from: the ipsilateral PFC, contralateral PFC and the pons (PON) for the [ $^{11}\text{C}$ ]flumazenil images. The TACs were used for kinetic modelling which was also performed with Pmod using the simplified reference tissue model (SRTM) [205].

The [ $^{11}\text{C}$ ]methylphenidate data were modelled using the CER as the reference region and the [ $^{11}\text{C}$ ]flumazenil data were modelled using the PON as the reference region [206]. The estimated BPnd values were analyzed statistically, as will be described in the following chapter.

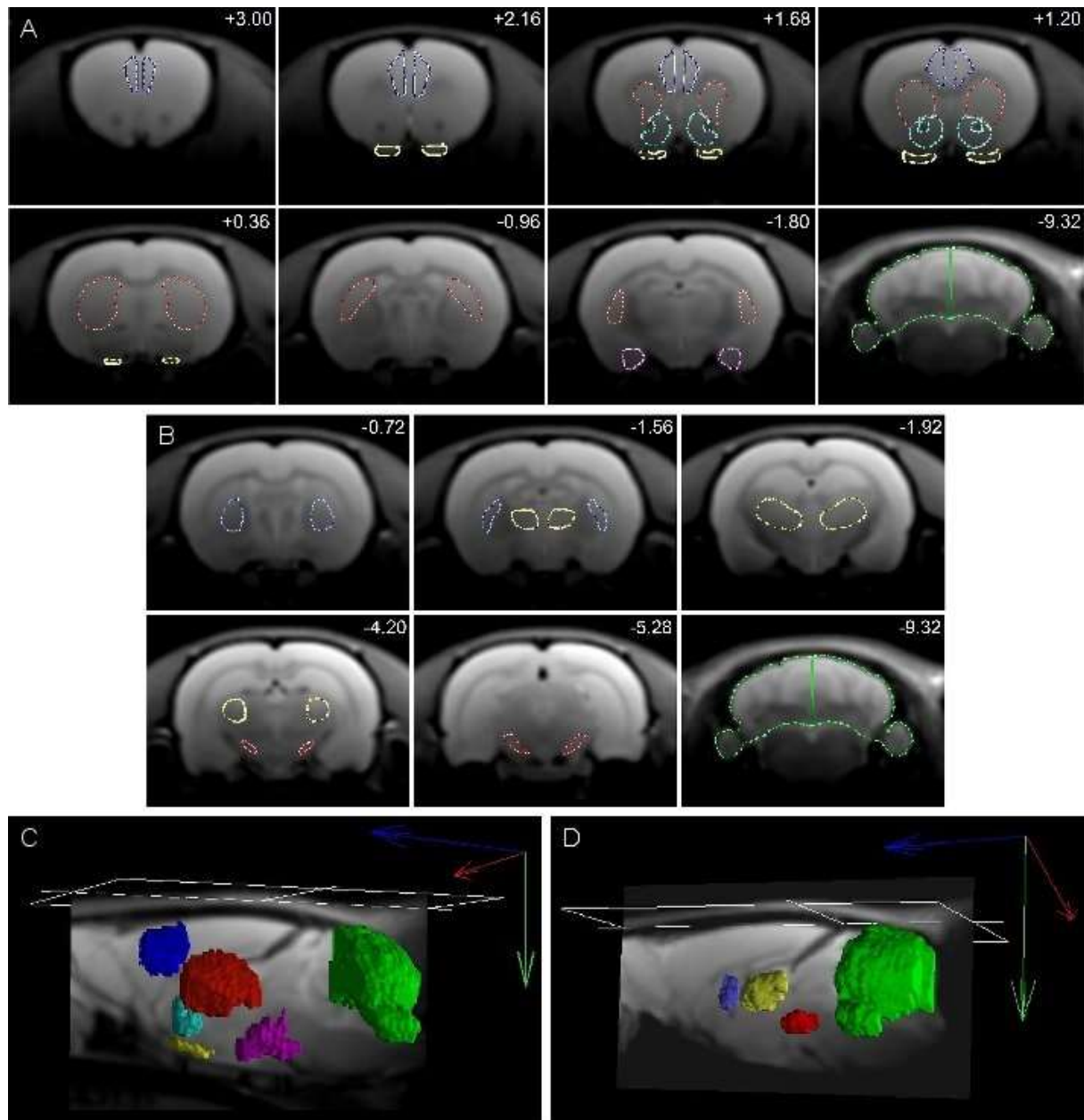


**Figure 12.1. VOIs used in Studies 1 and 3**

**A.** VOIs used for the image analysis of the rats injected into the VTA: PFC (blue), STR (red), NAc (turquoise), OT (yellow), AMG (pink), and CER (green). **B.** VOIs used for the image analysis of the rats injected into the striatum: GP (violet), THL (yellow), SN (red), CER (green). Numbers in the upper right corners indicate the distance from the bregma in mm. **C.** 3D rendering of the VOIs shown in A. **D.** 3D rendering of the VOIs shown in B. Adapted from [8].

Identification of the exact injection location was crucial in Study 5. Hence, the T2W MR images were coregistered to the rat brain atlas [16] which had been implemented in Pmod. This allowed identification of the injection location down to the subregion of the VTA. Subsequently, each of the 12 frames of the PET image was coregistered to its corresponding MR image. Before the coregistration, the MR and PET images were scaled by a factor of 0.05 in order to match the atlas dimensions.

The VOIs used in Study 5 were drawn based on the atlas and they are depicted in Figure 12.2. They included: ipsilateral and contralateral OB, anterior olfactory nucleus (AON), prelimbic cortex (PLC), STR, NAc, horizontal limb of the diagonal band and the magnocellular nucleus (HLDB&MCN), VP, OT, and medulla oblongata (MO). TACs from these regions were used for the data analysis.

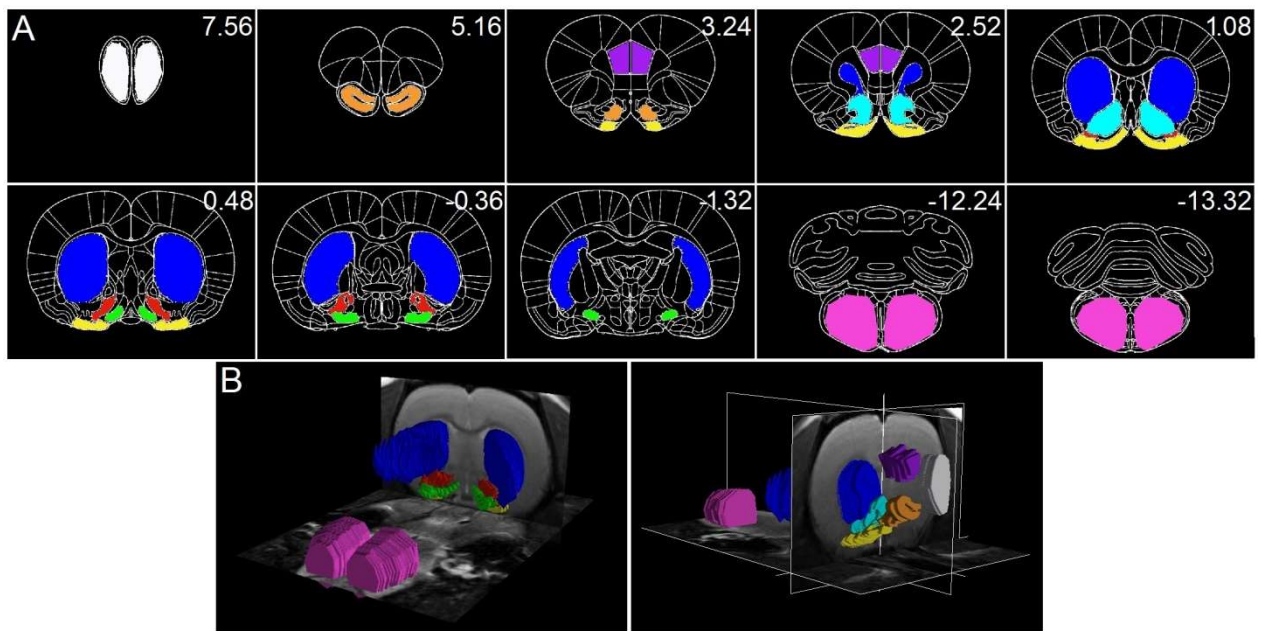


**Figure 12.2. VOIs used in Study 5**

**A.** The VOIs were drawn in the coronal plane of the rat brain atlas. They included: OB (white), AON (orange), PLC (violet), STR (navy blue), NAc (light blue), HLDB&MCN (light green), VP (red), OT (yellow), and MO (purple). The numbers in the right upper corners indicate the distance from the bregma in mm. **B.** 3D renderings of the VOIs viewed from the caudal side (left) and from the rostral side (right). In the latter image, only the right VOIs are shown.

## 13 Quantitative Image Analysis

Statistical analysis was carried out using SPSS Statistics 2.2 software (IBM Corporation, Armonk, NY, USA). Normal distribution of the data was always verified with the Shapiro-Wilk test, homogeneity of variances with the Levene's test, and sphericity with the Mauchly's test.

In Study 1, the group mean T1 values of the ipsilateral NA, STR and PFC at the baseline measurement were compared to their corresponding mean T1 values at the 24 h-time point measurement using a post-hoc Tukey's test with the Bonferroni correction. The differences were considered significant for  $p < 0.05$ .

In Study 2, the images of the resolution phantom reconstructed with different algorithms were compared visually. In the analysis of the images of the volume phantoms, the profile values obtained in the coronal plane were compared visually.

In Study 3, the average concentration of the tracer in a given VOI in the PET image and the injected dose (ID) were used to express the results as [% ID]. The group means  $\pm$  standard deviations (sd) are presented graphically.

Additionally, the data from Experiment 3 were analyzed statistically. They were first log-transformed to achieve normal distribution, and then analyzed with a mixed-design ANOVA. "Brain side" (*ipsilateral* or *contralateral*) was considered a between-subject factor (BSF) and "brain region" (*NAc*, *OT*, *AMG*, *STR*, *PFC*, and *CER*) – a within-subject factor (WSF). The omnibus test was followed by the Tukey's post-hoc test. The differences were considered significant for  $p < 0.05$ .

In Study 4, the BPnd of the ipsilateral VOI (BPnd<sub>R</sub>) was subtracted from the BPnd of the contralateral VOI (BPnd<sub>L</sub>) for each individual animal. Then, the BPnd<sub>L</sub> – BPnd<sub>R</sub> differences of the *Cold Mn* group were compared to the BPnd<sub>L</sub> – BPnd<sub>R</sub> differences of the *Control* group using a 2-samples t-test. This was done separately for each tracer and each time point. In order to correct for these 4 comparisons, the p value of 0.0125 was used as the significance threshold.

Additionally, the possible effect of the injection procedure alone was verified with a 1-sample t-test performed on the BPnd<sub>L</sub> – BPnd<sub>R</sub> difference of the 24 h [<sup>11</sup>C]methylphenidate data and 48 h [<sup>11</sup>C]flumazenil data of the *Control* group. The p value of 0.05 was used for these tests.

In Study 5, an additional VOI, covering the entire brain, was drawn for the dosimetry calculations, which will be described in the following chapter. The concentration of the tracer in all the other VOIs was expressed as the % of the activity in the whole brain [% WB]. The gradual changes in these concentrations over the 6 h of the PET scanning are graphically presented for individual rats and the characteristic patterns of the changes are compared between the groups.

## 14 Dosimetry

OLINDA/EXM software (v.1.0, Vanderbilt University, Nashville, TN, USA) was used to estimate the absorbed dose ( $D$ ) of the whole rat brain following the  $^{52}\text{Mn}$  injection into the VTA. In the first step, the absorbed doses for the masses range from 0.01 g to 20 g were computed using the OLINDA "sphere model" and the physical half-life of  $^{52}\text{Mn}$ . The natural logarithms of the doses and masses were fitted with a third order polynomial function for the interpolation of the absorbed doses corresponding to the measured data.

The obtained coefficients were subsequently used to calculate the absorbed dose of the whole brain VOI (Figure 14.1.A) using its volume ( $1.98\text{ cm}^3$ ) as its mass (1.98 g) and the mean activity measured in the first frame of the PET images of three rats from the *Control* group, injected with 29.9, 30.6 and 31.8 kBq of  $^{52}\text{Mn}$ . The same was calculated for the injected VTAR-PBP region with  $1\text{ mm}^3$  volume (Figure 14.1.B).

No biological clearance of the tracer was assumed.

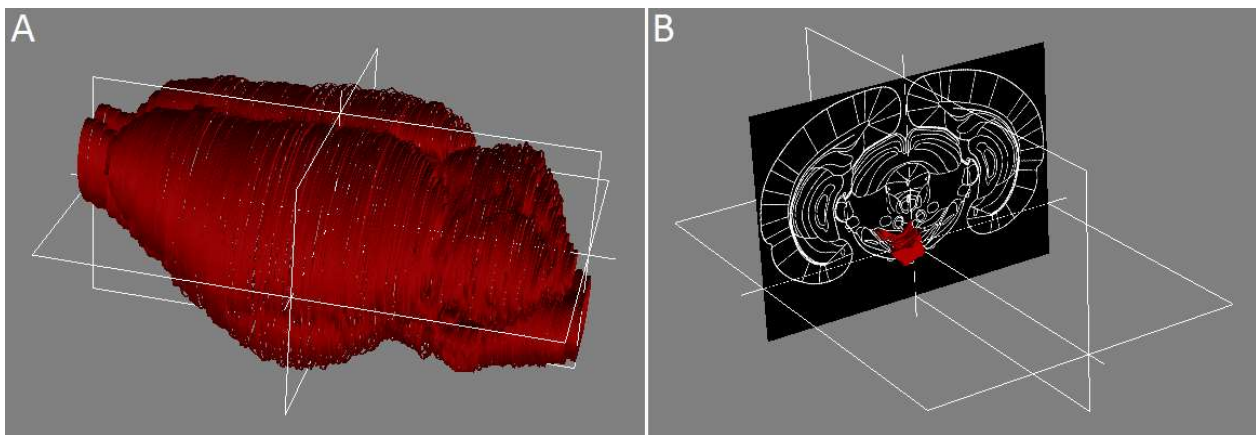


**Figure 14.1.** VOIs used for dosimetry

A. Whole brain. B. Right VTAR-PBP region shown from the rostral side.

## 15 Rotameter Test

This behavioral test was based on the original work of Ungerstedt and Arbuthnott [207]. It was conducted using an automated rotameter system, composed of four hemi-spheres (TSE Systems GmbH, Bad Homburg, Germany), as shown in Figure 15.1. The system records the number of clockwise and counterclockwise rotations the animal performs, registering a difference of 30° in its position.

During the test, a rat was placed in the hemi-sphere and wore a corral which was connected to the recording unit by a wire. Its length was adjusted such that the animal could reach the edge of the hemi-sphere but could not go beyond it. After the first 10 min (which was considered the *baseline*), the recording was paused for 1-2 min in order to administer apomorphine (apomorphine hydrochloride, 0.25 mg/kg bw, *s.c.*, Sigma Aldrich Chemie GmbH). Subsequently, it continued for 30 min, but the first 10 min recorded after the injection were considered the apomorphine uptake time and were not included in the analysis [208]. The remaining 20 min were divided into two 10 min bins and the number of the rotations performed during the two bins was averaged. This was considered the *test* measurement. The results are expressed as the ratio of the number of ipsilateral over contralateral rotations per 10 min (further referred to as “ipsilateral/contralateral rotations”).

In Experiment 1 of Study 3, individual *baseline* and *test* results are presented graphically. The data of the rats from Experiment 3 in that study were analyzed statistically with SPSS Software 2.2 (IBM Corporation), employing a mixed-design ANOVA. For the analysis, “group” (3 days, 14 days, 28 days, or 28 days-control) was considered a BSF and the



**Figure 15.1. Rotameter test - experimental setup**

“measurement” (*baseline* or *test*) a WSF. The assumptions of normal distribution and homogeneity of variances were tested with the Shapiro-Wilk test and the Levene’s test, respectively. The results were considered significant for  $p \leq 0.05$ .

## 16 TH-Staining

After dissection, brains were kept in 4 % paraformaldehyde solution (PFA) at 4 °C for 24 h, and then in 30 % glucose solution at 4 °C for at least 3 days. Subsequently, they were covered with TissueTek (VWR, Radnor, PA, USA) and stored at -20 °C until cutting on a cryotome (Leica Biosystems GmbH, Nussloch, Germany). From each brain, 20 µm sections were obtained in the coronal plane at the level of the injection (VTA-injected rats) or at the midbrain level (intrastriatally injected rats).

The sections were directly immersed in tris-buffered saline (TBS) and this washing step was repeated three times for 10 min. Subsequently, the solution was changed to TBS with 0.2 % triton and normal horse serum (NHS, Vector Laboratories Ltd., Peterborough, UK) and the preparation was placed on a shaker for 20 min. After this, the sections were incubated overnight in a bath composed of TBS, 0.2 % triton, NHS, and the primary monoclonal TH antibody (ImmunoStar, Inc., Hudson, NY, USA) which was used with the dilution of 1:1000.

The next steps consisted of: washing three times for 10 min in the TBS with 0.2 % triton solution and incubating with the secondary antibody (biotinylated anti-mouse IgG antibody, Vector Laboratories Ltd.), used with the dilution of 1:1000, in TBS with 0.2% triton and NHS solution over 90 min on the shaker. After another series of washing (3 × 10 min in TBS with 0.2% triton), the sections were incubated with an avidin-biotin complex (Vectastain Elite ABC-Kit, Vector Laboratories Ltd.) for 60 min. Subsequently, the slices were washed again (3 × 10 min in TBS) and stained with 3,3'-diaminobenzidine (DAB, DAB Substrate Kit, Vector Laboratories Ltd.). The reaction was stopped by adding 2 drops of 30 % H<sub>2</sub>O<sub>2</sub>

solution. Following the final washing in TBS, they were placed on microscopic glass slides and left overnight to dry.

NanoZoomer 2.0HT (Hamamatsu Photonics K.K., Hamamatsu, Japan) was used to analyze the stained tissue slices. Intensity of the staining of the injected VTA region (or the SN region in the STR-injected brains) was visually compared to the contralateral VTA (or SN).

## 17 $\gamma$ H2AX-Staining

The dissected brains were immersed in 4% PFA and kept at 4 °C for 24 h. Then, ethanol solutions of increasing concentration (50 %, 70 %, 90 %, 100 %) were used for dehydration and xylene solution for washing (3 × 20 min). Wet brains were embedded in paraffin. 3  $\mu$ m sections were cut in the coronal plane at the level of the injection using a Leica RM2235 microtome (Leica Biosystems GmbH). They were placed on glass microscopic slides and left at 37 °C for 48 h to dry. The following steps preceded the staining: deparafinization (xylene), rehydration (ethanol solutions of decreasing concentration: 100 %, 96 %, 70 %, 40 %), washing (phosphate-buffered saline, PBS), epitope retrieval (microwaving in a citrate buffer solution for 30 min), cooling, and final washing (PBS).

The following agents were used in the staining procedure according to manufacturer's instruction: anti-phospho-histone H2AX (Ser139) clone JBW301 antibody (Merck Millipore, Darmstadt, Germany), Tyramide Signal Amplification Kit (Alexa Fluor 488, Life Technologies GmbH, Darmstadt, Germany), and 4',6-Diamidino-2-phenylindole dihydrochloride (DAPI) (Sigma Aldrich Chemie GmbH).

One section from each brain was used for a semi-quantitative analysis of the  $\gamma$ H2AX foci, which was performed with a Zeiss Axio Imager MI fluorescence microscope (Carl Zeiss AG, Oberkochen, Germany). The microscope was equipped with a AxioCam MRm monochrome digital camera (Carl Zeiss AG) and controlled by AxioVision 4.8 software (Carl Zeiss AG).

Three 230  $\mu$ m × 170  $\mu$ m “stack-images” were obtained from within the injected VTA region and three from the contralateral VTA. Each “stack-image” was composed of seven layers

acquired in different microscopic focus planes which were  $0.25\ \mu\text{m}$  away from each other. This is depicted in Figure 17.1. The seven layers were merged into a single 2D stack-image.

The semi-quantitative analysis relied on counting all the nuclei visible in the image (further referred to as “cells total”) and the nuclei containing at least 3  $\gamma\text{H2AX}$  foci (“cells with foci”). The result was expressed as the “cells with foci/cells total” ratio, and the three numbers obtained at each brain side were averaged. Hence, for every brain there was one value for the ipsilateral VTA and one for the contralateral VTA. These were used to calculate group means and sd.

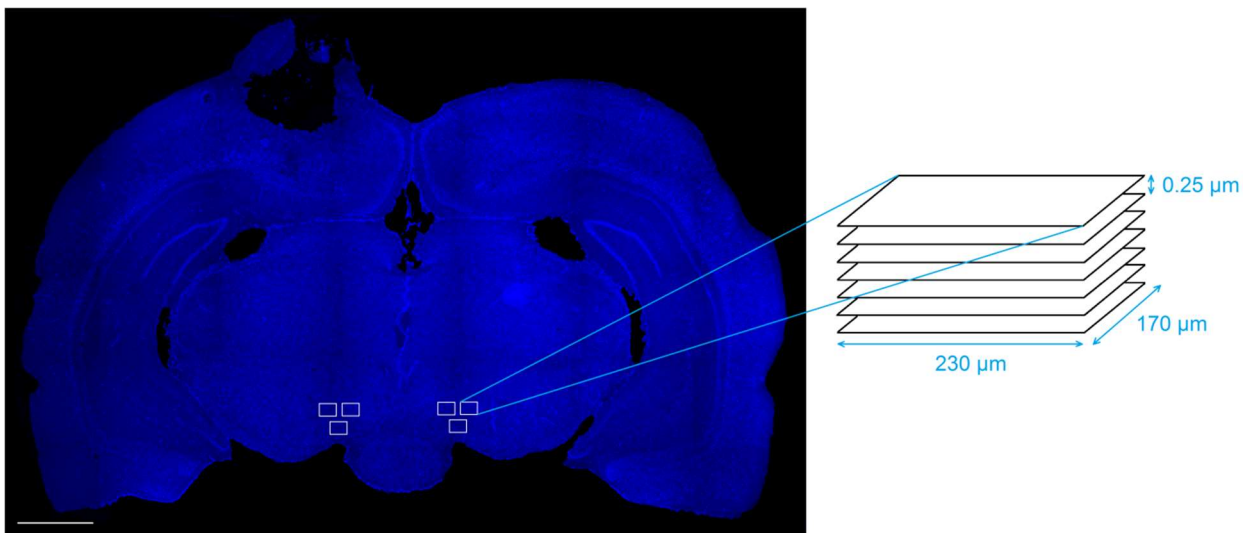


**Figure 17.1. Semi-quantitative analysis of the  $\gamma\text{H2AX}$ -staining**

Three stack-images were acquired from the injected VTA and three from the contralateral VTA. The brain regions were identified based on the anatomical features visible in the DAPI-stained tissue. A disruption of the tissue at the brain surface additionally marked the injection position.

Each stack-image was obtained by merging seven 2D images acquired at different microscopic focus planes. The results obtained from the three stack-images at each side were averaged and used to calculate the means and sd of the experimental groups. The scale bar in the lower left corner represents 1 mm. Adapted from[8].

# 18 PET with Online Recording of Blood Radioactivity

## 18.1 Experimental setup

The experimental setup (Figure 18.1) was composed of a  $\mu$ PET scanner (the same as previously described), a peristaltic pump (Ismatec REGLO Digital, Cole-Parmer GmbH, Wertheim, Germany), an infusion pump for a tracer administration (PHD 22/2000 Syringe Pump, Harvard Apparatus, Holliston, MA, USA), and a BS (Figure 18.2) which was build in-house based on the previously proposed design [203]. Its detector system was based on the Cerium-doped lutetium oxyorthosilicate (Ce:LSO) and avalanche photodiodes (APDs).

An arterial-venous shunt was surgically inserted into the left femoral artery and vein of a rat. It consisted of three pieces: the arterial piece (40 cm), the middle piece (30 cm), and the venous piece (25 cm). The former and the latter ones were made of a low density

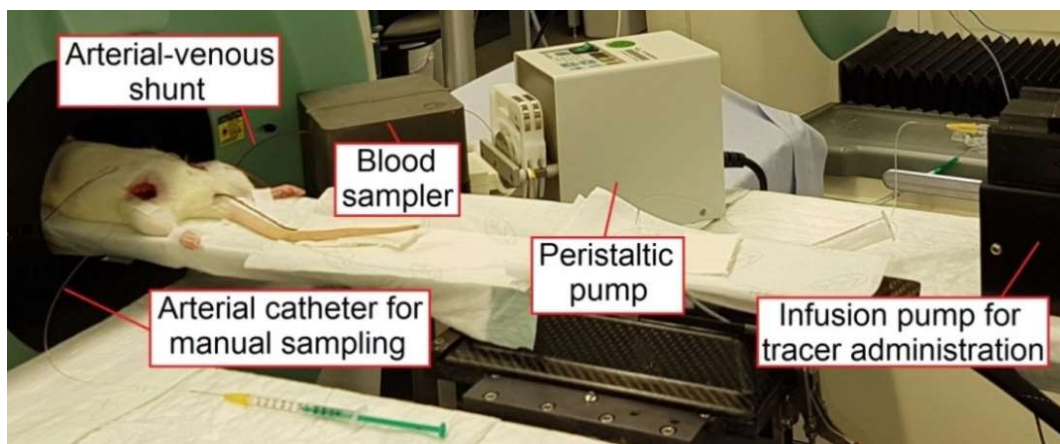


**Figure 18.1. Experimental setup for PET with BS recording**

The experiment was carried out on the PET scanner. The rat was positioned on its back and the arterial-venous shunt was inserted on the left side. The catheter passed the BS and the peristaltic pump. The second catheter was inserted into the right femoral artery for MS. The tracer was administered with an infusion pump via the tail vein catheter.



**Figure 18.2. Blood sampler**

The cassette with a groove for placing the catheter can be easily removed from and inserted in the BS.

polyethylene (LDPE) tube (ID = 0.4 mm, OD = 0.8 mm, Reichelt Chemietechnik GmbH, Heidelberg, Germany), while the middle piece was a Tygon tube (ID = 0.44 mm, OD = 2.26 mm, Ismatec). The three elements were connected with each other by steel connectors (1.5 cm long, ID = 0.3, OD = 0.63 mm, Ismatec).

Additionally, a 25 cm long catheter for MS was inserted into the right femoral artery and a 20 cm long catheter for the tracer injection into the tail vein. Both the catheters were made of the LDPE tube described above. Importantly, the length of the MS catheter was the same as the length of the shunt from the animal to the centre of the FOV of the BS.

The manual blood samples were collected to capillary tubes (Microvette CB 300 LH, Sarstedt, Nuembrecht, Germany).

## 18.2 Experimental protocol

Five rats were injected with approximately 60 MBq of [<sup>18</sup>F]FDG (0.5 mL over 25 s), which was directly followed by an injection of normal saline (0.1 mL over 5 s). The tracer

administration, the PET acquisition, and the BS recording began simultaneously (0 s time point). The MS started 3 s earlier and continued until 75 s. The next blood samples were taken at 3, 6, 10, 15, 25, 40, and 60 min. Each sample was approximately 75  $\mu\text{L}$  (3 drops) and this volume together with the number of samples collected during the first continuous sampling period were used to estimate the flow rate in the MS catheter.

From each manual sample, 10  $\mu\text{L}$  of the whole blood (*wb*) and 10  $\mu\text{L}$  of the separated plasma (*p*) (centrifugation at 4000 rpm, 5 min, 5 °C, 25 cm diameter) were measured with a  $\gamma$ -counter (2480 WIZARD<sup>2</sup>, Perkin Elmer, Waltham, MA, USA). The temperature and the breathing rate of the rat were monitored during the experiment.

The PET acquisition was followed by a 10 min transmission scan performed with a rotating <sup>57</sup>Co source which was later used for attenuation correction. After this, the venous piece of the shunt was cut and the coming out blood was collected to two Eppendorf tubes, each time for 30 s. The two volumes were measured by pipetting out and averaged. This was used to estimate the flow rate in the shunt.

After each experiment, the BS was cross-calibrated with the well-counter. Moreover, the background activity was recorded and later subtracted from the BS dataset. The BS data were also decay-corrected before any further analysis. Additionally a set of nine independent measurements was carried out to estimate the sensitivity of the device. These measurements relied on a 5-6 min recording of the radioactivity whose level had been first defined in the well counter.

## 18.3 Dispersion

The dispersion in the shunt was assessed in a separate measurement which was based on the previously proposed design [209]. The experimental setup (Figure 18.3) consisted of the BS, the peristaltic pump, and two cups filled with 16 mL of heparinized human venous blood. 0.45 mL of normal saline or of saline with 9.1 MBq of [ $^{18}\text{F}$ ]FDG was added to each of them. The cups were placed on magnetic stirrers which ensured proper mixing. All the components of the setup were connected by the same catheters which were used in the *in vivo* experiments.

By turning the pump on, the blood from one cup (without the activity) was drawn in the catheter. Then, the pump was briefly paused and the end of the tube was moved to the second cup. By turning the pump on again, the blood with the radioactivity filled the catheter which was registered by the BS. The recording lasted approximately 1 min. Subsequently, the catheter end was placed back to the first cup. The entire procedure was repeated four times with cleaning the tube in between the trials.

The decaying portions of the four recorded step functions were normalized to their

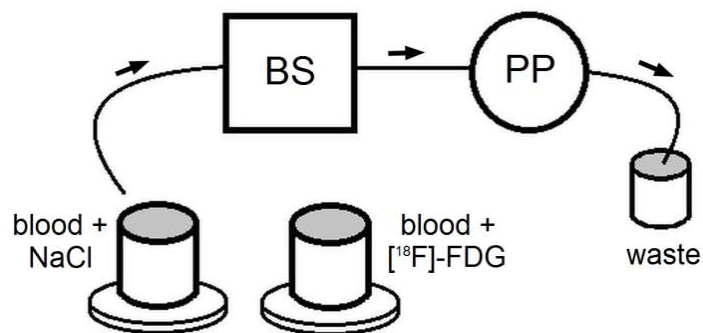


**Figure 18.3. Setup for dispersion measurement**

The setup consisted of two cups placed on magnetic stirrers, the BS, and the peristaltic pump (PP). The arrows indicate the direction of the blood flow in the catheter.

maximum values, and, as previously described [210], fitted with a monoexponential function:  $y = \exp\left(\frac{-t}{\tau}\right)$ , where  $\tau$  is the dispersion factor and  $t$  is the time. The average  $\tau$  value was used to model the impulse response function (IRF) of the setup according to the previously proposed method [210]. In this model the IRF is a monoexponential function:  $IRF = \frac{1}{\tau} \exp\left(-\frac{t}{\tau}\right)$ , which can be used to deconvolve the recorded TAC.

## 18.4 Data analysis

The decay, dead time, and attenuation corrections, as well as normalization, were applied to the PET data. The images were reconstructed with the FBP algorithm using the following framing:  $18 \times 5$  s,  $1 \times 30$  s,  $3 \times 60$  s,  $1 \times 180$  s,  $1 \times 120$  s,  $1 \times 300$  s,  $3 \times 900$  s. The two tissue compartment model (2TCM) assuming no dephosphorylation of FDG-6-phosphate ( $k_4 = 0$ ) [211], was used for the kinetic analysis of the right striatum. The analysis was performed nine times for each rat. Each time the AIF was obtained in a different way:

1. From the collected  $wb$  and  $p$  manual samples ("MS").
2. From the fitted manual samples ("MS-fit") – The previously described fitting procedure [212] was used and the obtained data ( $wb_{MS-}$  and  $p_{MS}$ ) were used as the AIF. This was done to verify whether the fitting procedure would influence the KPs.
3. From the fitted and dispersion-corrected manual samples ("MS-fit-dc") – The IRF, normalized to the area under the curve equal 1, was used to deconvolve the  $wb_{MS-f}$  and the  $p_{MS-f}$  obtained previously. The outcome of the deconvolution was used as the AIF. This approach was considered the reference one throughout the study.

4. From the fitted and dispersion-corrected manual samples, with  $p$  values calculated using the population-based  $\frac{p}{wb}$  ratio (“MS-fit-dc-calc”) – A biexponential function has been shown to accurately describe the  $\frac{p}{wb}$  ratio for [ $^{18}\text{F}$ ]FDG in rats [202]. Hence, for each rat the ratio was first calculated using his original  $p$  and  $wb$  data:

$$\frac{p}{wb} = A * \exp\left(\frac{-B}{t}\right) + C * \exp\left(\frac{-D}{t}\right) + E$$

where  $t$  denotes *time* and  $A$ - $E$  are the fit coefficients (Figure 18.4). To avoid a strong weighting by the many samples from the first 78 s, only the first-above-baseline ( $> 10$  kBq/mL) and the last data point from this period were used. Next, the  $A$ - $E$  coefficients obtained for each rat were averaged to provide group mean values ( $A_m$ - $E_m$ ). These mean coefficients were used to compute the  $p$  values from the dispersion-corrected  $wb_{MS-fit}$ :

$$p = wb_{MS-fit-d} * (A_m * \exp\left(\frac{-B_m}{t}\right) + C_m * \exp\left(\frac{-D_m}{t}\right) + E_m)$$

This procedure served to evaluate the effect of using the population-based  $\frac{p}{wb}$  ratio, rather than the true  $p$  data, to obtain the AIF on the KPs.

5. From the BS data (“BS-calc”) – The original BS  $wb$  data and the  $p$  values calculated from that using the  $A_m$ - $E_m$  coefficients, were used as the AIF.
6. From the fitted BS data (“BS-fit-calc”) – The original BS data were fitted using the previously mentioned procedure. The  $p$  values were calculated from the  $wb_{BS-fit}$  using the  $A_m$ - $E_m$  coefficients.

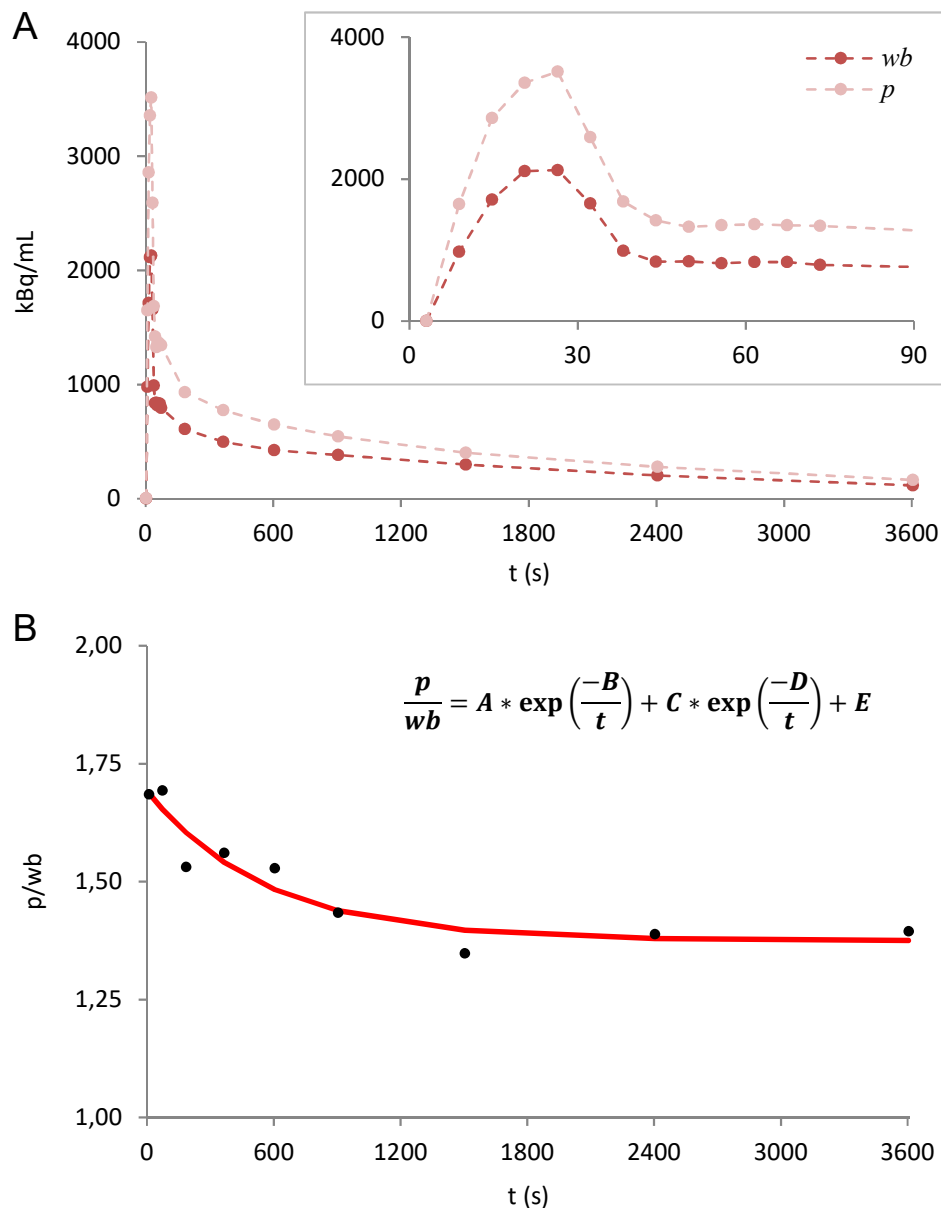


**Figure 18.4. Plasma vs whole blood ratio**

**A.** Example  $wb$  and  $p$  TAC as measured with the  $\gamma$ -counter from the manually collected blood samples. **B.** The  $\left(\frac{p}{wb}\right)$  ratio of the samples shown in A (black dots) and a biexponential fit to that data (red line).

- From the fitted and dispersion-corrected BS data (“BS-fit-dc-calc”) – The  $wb_{BS-fit}$  and  $p_{BS-fit}$  obtained in the previous step were corrected for dispersion in the same way as described for the MS data. The resultant  $wb_{BS-fit-dc}$  and  $p_{BS-fit-dc}$  were used as the AIF.

8. From the PET image (“ID-calc”) – A VOI was drawn on the left ventricle of the heart in the PET image and the extracted TAC, together with the  $A_m-E_m$  coefficients were used to calculate the  $p$  values.
9. From the fitted and dispersion-corrected combination of the BS and MS data (“BSMS-fit-dc-calc”) – The first 10 min of the BS recording was combined with one blood sample manually collected at 60 min. The combined data were fitted as previously described and the obtained  $wb_{BSMS-fit}$  was corrected for dispersion ( $wb_{BSMS-fit-dc}$ ). From this, the  $p$  values were calculated using the  $A_m-E_m$  coefficients.

The mean KPs of the five rats, estimated with the approaches described above, were compared to the KPs obtained with the reference method (“MS-fit-dc”).

# RESULTS

## 19 Study 1

The T1W MR images acquired 24 h after the stereotactic injections into the right VTA revealed a clear signal enhancement at the injection site in the brains treated with 45 nmol of  $Mn^{2+}$ . This effect was hardly visible in the images of the animals injected with the 0.5 nmol dose. No specific signal enhancement could be seen in the images of the *Control* group. Example images normalized to their maximum values are shown in Figure 19.1.A-B. After increasing the contrast in the images of the 45 nmol group, the mesolimbic pathway leading from the injected VTA to the ipsilateral nucleus accumbens could be recognized (Figure 19.1.C).

Besides the visualization of the  $Mn^{2+}$  distribution, the T1W images allowed verification of

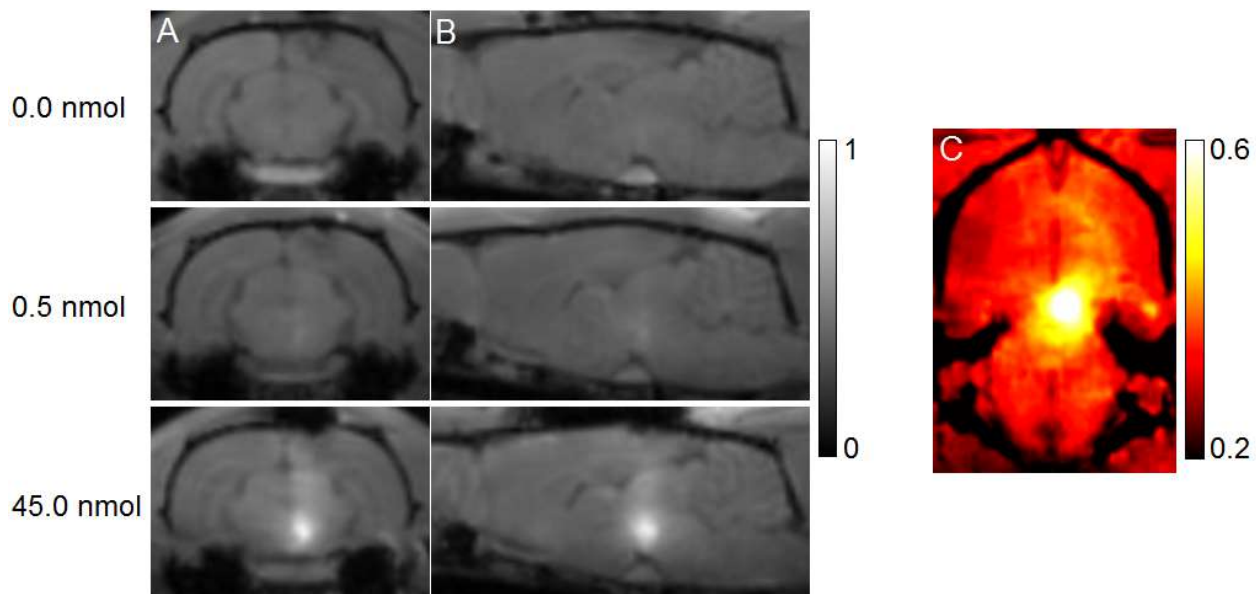


**Figure 19.1. Normalized T1W MR images**

24 h after the injection of 0, 0.5 or 45 nmol of  $Mn^{2+}$  into the right VTA, a relatively strong signal enhancement could be seen in the brains treated with the highest dose. This effect was very weak in the low-dose group. Typical images are shown in coronal (A) and sagittal (B) planes. An image of a rat injected with the 45 nmol dose is also shown in the horizontal plane in C. Increasing image contrast allowed visualization of the ipsilateral mesolimbic pathway leading from the VTA to the NAc (black arrow). Furthermore, a spot of an enhanced signal was noticed in the region corresponding to the right AMG (white arrow).

the injection location. In fact, a misinjection was recognized in one rat from each group. The data of these three animals were discarded from further analysis.

The T1 maps obtained before and 24 h after the injection were used to quantitatively analyze the effect of  $Mn^{2+}$  on the T1 relaxation values in three ipsilateral brain regions known to receive the neuronal input from the VTA. The results are graphically presented in Figure 19.2.

The largest change was observed in the NAc of the rats treated with the 45 nmol dose – the T1 dropped from  $2462 \pm 137$  ms to  $2196 \pm 160$  ms (mean  $\pm$  sd). A similar, although slightly weaker, effect was found in the STR of this group. Following the  $Mn^{2+}$  administration, the T1 values changed from  $2352 \pm 110$  ms to  $2179 \pm 179$  ms. Contrary, hardly any difference was observed in the PFC – the T1 at the baseline and at the 24 h time point were  $2077 \pm 116$  ms and  $2089 \pm 155$  ms, respectively.

In the 0.5 nmol group, much smaller and opposite changes were observed in the NAc and in

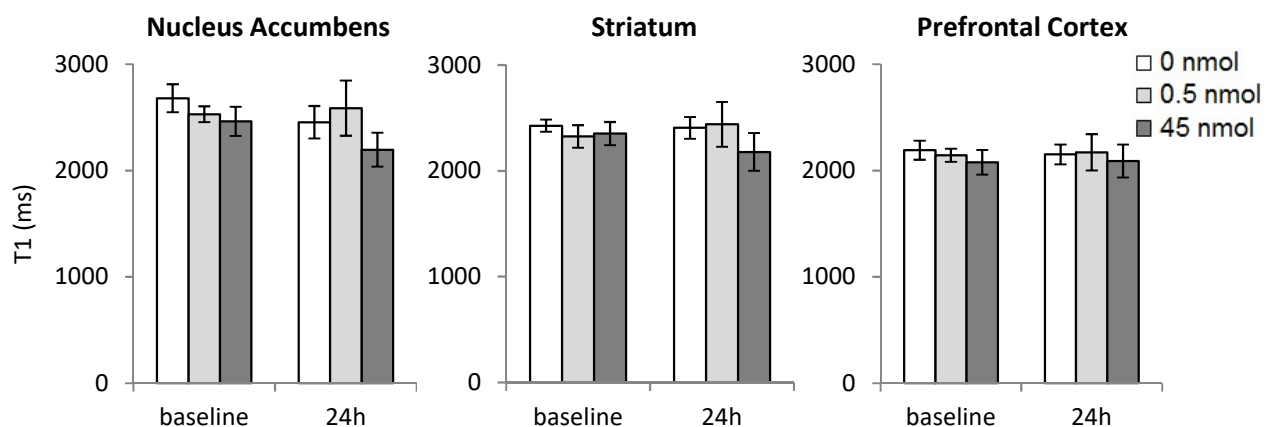


**Figure 19.2. Quantitative results of the T1 mapping**

Among the analyzed ipsilateral regions, the largest drop in the T1 value was observed in the NAc of the 45 nmol group. There were no substantial changes in any of the region in the 0.5 nmol group. The bars represent group mean  $\pm$  sd, n = 3 per group.

the STR. The T1 rose from  $2530 \pm 75$  ms to  $2587 \pm 259$  ms and from  $2324 \pm 107$  ms to  $2440 \pm 211$  ms, respectively. Similarly to the  $45$  nmol group, hardly any change was observed in the PFC. The T1 was  $2144 \pm 61$  ms at the baseline and  $2171 \pm 171$  ms at 24 h post-injection.

The T1 values in the *Control* group also hardly changed in the ipsilateral PFC as well as in the STR. The respective results were  $2191 \pm 90$  ms and  $2427 \pm 57$  ms at the baseline, and  $2152 \pm 93$  ms and  $2406 \pm 103$  ms at the 24 h time point. Somewhat surprisingly, a drop in the T1, from  $2680 \pm 132$  ms at the baseline to  $2454 \pm 153$  ms was found in the ipsilateral NAc.

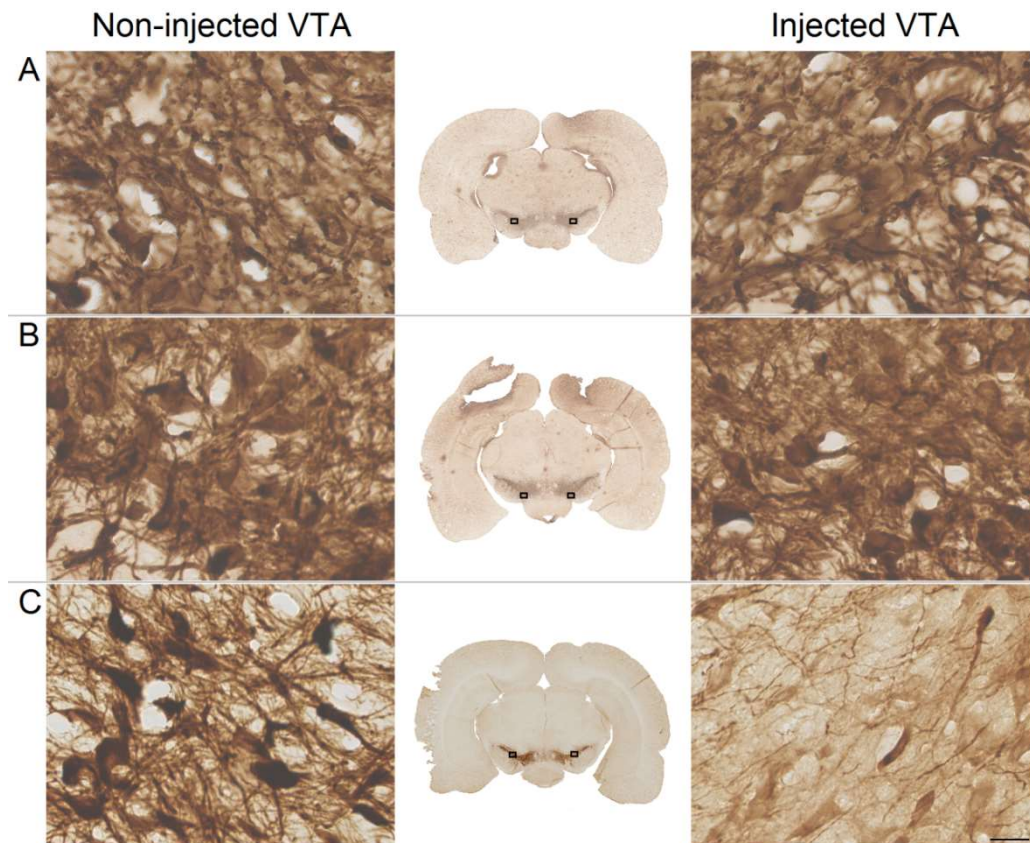


**Figure 19.3. TH-stained brain tissue of rats treated with  $Mn^{2+}$**

There was no sign of dopaminergic damage in the tissue slices from the *Control* group (A), neither from the  $0.5$  nmol group (B). In contrast, a clear reduction in the staining intensity was observed in the right VTA of the rats treated with the  $45$  nmol dose as compared to their contralateral VTA (C).

ANOVA was conducted in order to evaluate the data statistically. Although it did indicate a significant interaction between the *group*, the *region*, and the *time point* ( $F(4,12) = 3.58$ ,  $p = 0.04$ ), there was no significant difference between the groups at any time point and in any region in the post-hoc test.

The TH-staining of the brain tissues obtained 4 weeks after the  $Mn^{2+}$  injections revealed a dopaminergic lesion in the VTA treated with the highest dose. This was visible as a reduced staining intensity of the neurons within the right as compared to the left VTA. This effect was not found in any of the animals from the *0 nmol* or *0.5 nmol* groups Figure 19.3.

## 20 Study 2

The PET images of a  $^{52}\text{Mn}$ -filled resolution phantom were acquired and reconstructed with different algorithms and matrix sizes to evaluate the appearance of small volumes. This was important because brain regions such as VTA or SN, whose volumes are in the range of  $1\text{-}2\text{ mm}^3$ , would be possibly imaged in *in vivo* PET studies.

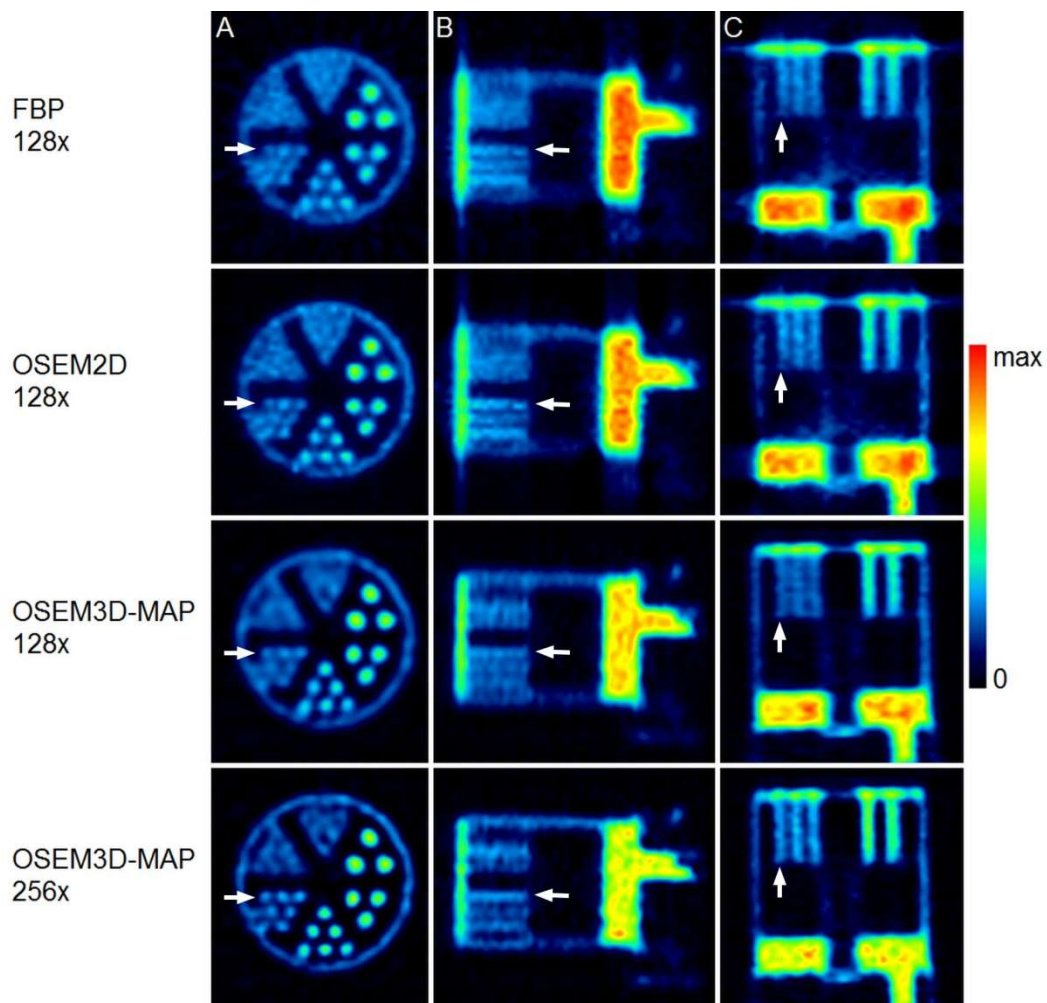


**Figure 20.1. PET Images of the resolution phantom**

The images of the phantom filled with the  $^{52}\text{Mn}$  solution are shown in the coronal (A), sagittal (B), and axial (C) planes. The smallest rod volumes that could be resolved in any of the images were the 1.35 mm diameter rods (pointed by the arrows). They appeared clearest in the images reconstructed with the OSEM3D-MAP algorithm and the matrix size of  $256 \times 256$  [8].

The 0.75 mm and 1.00 mm diameter rods of the phantom could not be resolved in any of the obtained images. However, the OSEM3D-MAP algorithm provided images in which the 1.35 mm diameter rods could be distinguished (Figure 20.1). Moreover, the edges of these rods appeared sharper and the spaces between them clearer, when the  $256 \times 256$  matrix size was applied. Therefore, the OSEM3D-MAP algorithm and the  $256 \times 256$  matrix size were used for reconstructing all the *in vivo* PET data.

Subsequently, two volume phantoms were used in order to verify the effect of the energy window used for the acquisition of the PET data. This was done by comparing the peak-normalized profiles of the values measured in the coronal plane of the images. The exact positions of the evaluated image planes are presented in Figure 20.2 and the profiles in

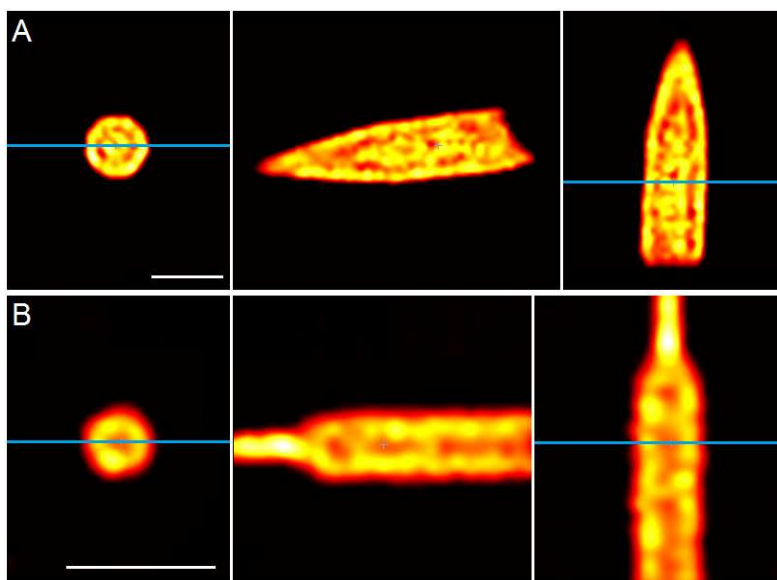


**Figure 20.2. PET images of the volume phantoms**

**A.** 1.5 mL Eppendorf tube filled with  $^{52}\text{Mn}$  solution. The phantom was surrounded by the air. **B.** A plastic syringe filled with  $^{52}\text{Mn}$  solution was closed inside a falcon tube filled with water. The water surrounding was meant to imitate a biological tissue. Both the phantoms are shown in the coronal (left), sagittal (middle) and axial (right) planes. The color scales were adjusted to visualize higher activity present by the walls of the phantoms. The blue lines indicate the position at which the image profiles were obtained. The scale bars represent 1 cm.

Figure 20.3.

For both phantoms, the image profiles acquired with 4 different energy windows were very similar to each other. The right wall of the phantom was located in the very center of the FOV and the values of the profiles corresponding to this location were exactly overlain. Despite the slightly larger distance from the center of the FOV, the values of the profiles

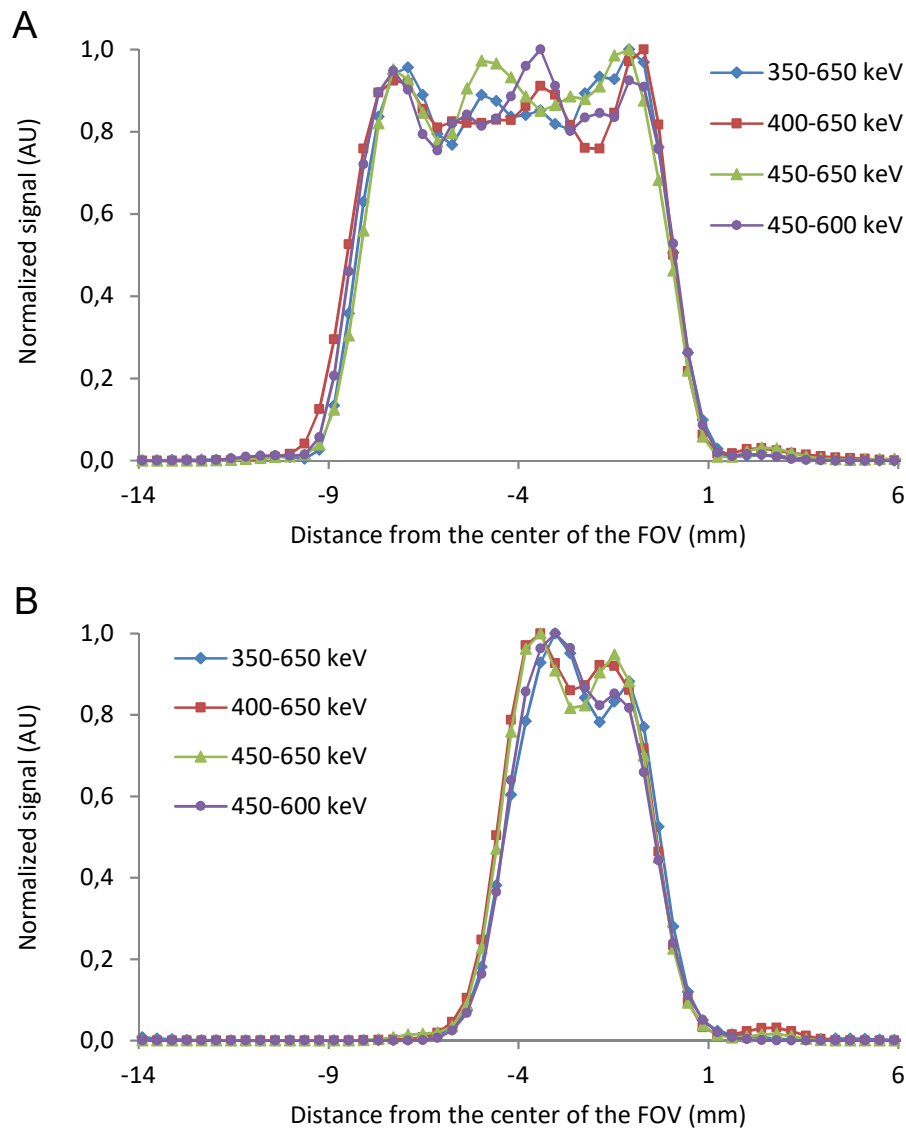


**Figure 20.3. Profiles of the volume phantoms PET images**

**A.** Profile of the Eppendorf tube phantom. **B.** Profile of the syringe phantom. For each phantom the image acquisition was performed with 4 different energy windows, as indicated in the legends.

corresponding to the other wall of the phantom were also close to each other. Therefore, it appeared that applying a narrower energy window than the standard 350-650 keV did not have a substantial effect, regardless of the surrounding environment (air or water). Thus, the standard energy window was used for all the *in vivo* studies.

## 21 Study 3

### 21.1 Experiment 1

#### 21.1.1 *Purity of the tracer solution*

The ICP-OES measurement of the metals in the tracer solution indicated presence of manganese, iron and chromium. The contents calculated per injected dose (1  $\mu$ L) were as follows:

- Mn: 2.1 ng (38.3 pmol)
- Fe: 0.9 ng (16.9 pmol)
- Cr: < 0.2 ng (< 3.8 pmol)

No other metal contaminants were detected. The specific activity (SA) at the injection times was 3.18-3.30 GBq/ $\mu$ mol.

#### 21.1.2 *PET*

24 h after the  $^{52}\text{Mn}$  injection into the right VTA, the mesolimbic and the mesostriatal pathways could be easily recognized in the acquired PET images (Figure 21.1.A). The highest content of the tracer was found in the ipsilateral NAc, confirming its transport along the mesolimbic tract. The second highest accumulation was detected in the ipsilateral STR consistently with the trace of  $^{52}\text{Mn}$  along the mesostriatal pathway observed in the images. A relatively high content was also found in the OT. The ipsilateral AMG and PFC accumulated lower amounts, and CER, used as a reference region, was characterized by the

lowest concentration. The exact quantitative results are presented in Figure 21.2.A and Table 21.1.

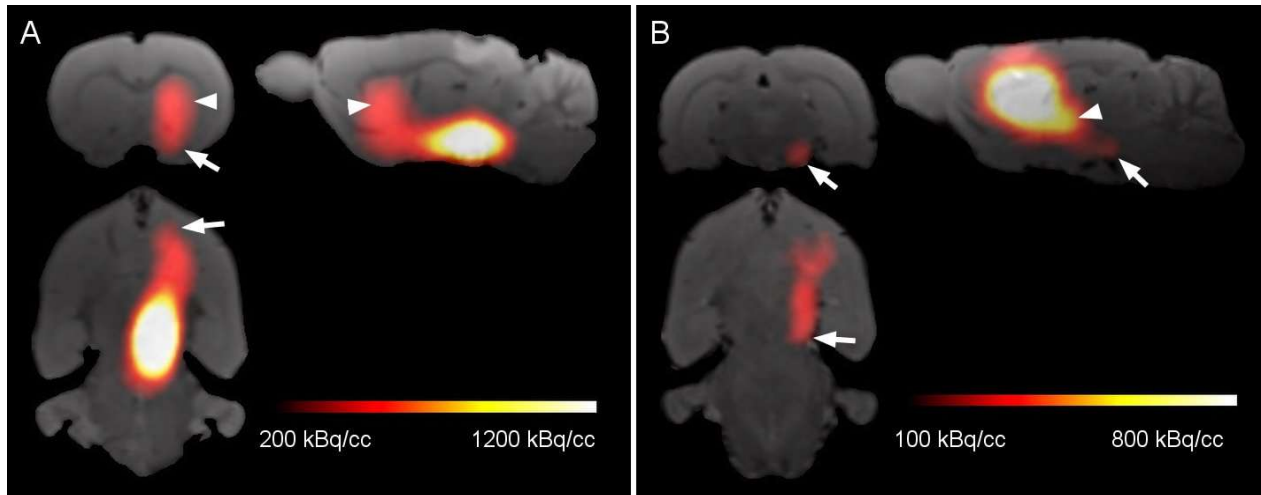


**Figure 21.1.**  $^{52}\text{Mn}$  distribution in PET images (Experiment 1).

**A.** Following injection into the VTA,  $^{52}\text{Mn}$  was transported along the mesolimbic and mesostriatal pathways. The arrow and arrowhead indicate the tracer accumulation in the NAc and the STR, respectively. **B.** After administration into the STR,  $^{52}\text{Mn}$  traced the striatonigral pathway, reaching the SN (arrow). Its accumulation in the THL was also prominent (arrowhead) [8].

Importantly, in all the analyzed brain areas but CER, there was more tracer detected on the ipsilateral than on the contralateral side.

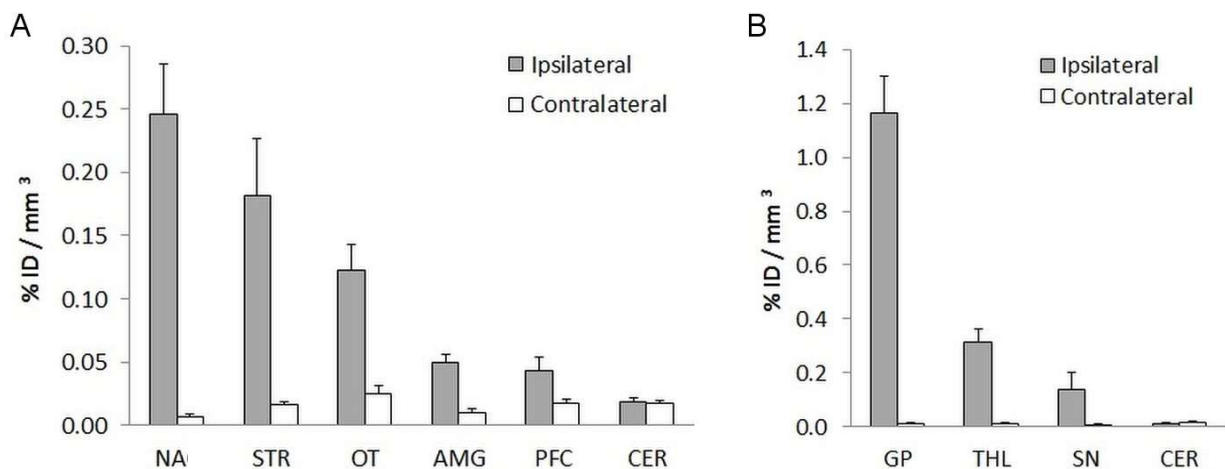


**Figure 21.2.** Quantification of the  $^{52}\text{Mn}$  distribution in PET images (Experiment 1).

**A.** 24 h after  $^{52}\text{Mn}$  injection into the right VTA, the highest content of the tracer was found in the ipsilateral NAc, STR, and OT. A lower signal was detected in the AMG and PFC. In all the analyzed regions, except for the CER, there was higher  $^{52}\text{Mn}$  accumulation on the ipsilateral than the contralateral side. **B.** After injection into the right STR the tracer content in the adjacent GP, THL, and the ipsilateral SN was higher than in the respective contralateral areas. This was not the case for the CER. Bars represent mean + sd, n = 4, [8].

In the PET images of the rats injected into the STR, the striatonigral pathway, leading to the ipsilateral SN, was clearly delineated by  $^{52}\text{Mn}$  (Figure 21.1.B). The tracer accumulation was, once again, always higher in the ipsilateral than in the contralateral region for all the analyzed areas, except for the CER (Figure 21.2.B). As could be expected, the GP, situated adjacently to the injection site, was characterized by the highest content of the tracer, but a substantial amount of  $^{52}\text{Mn}$  accumulated also in the THL. Most importantly, SN, the target region of the direct striatonigral pathway, also contained a relatively high  $^{52}\text{Mn}$  amount.

Similarly to the first group, the smallest fraction of the injected dose was found in the CER.

The exact values are presented in Table 21.2.

**Table 21.1.  $^{52}\text{Mn}$  content in brain regions 24 h after injection into the VTA**

The values represent group means  $\pm$  sd, n = 4.

Region	Ipsilateral [%ID/mm <sup>3</sup> ]	Contralateral [%ID/mm <sup>3</sup> ]
Nucleus accumbens	0.25 $\pm$ 0.04	0.04 $\pm$ 0.01
Striatum	0.18 $\pm$ 0.05	0.02 $\pm$ 0.00
Olfactory tubercle	0.12 $\pm$ 0.02	0.02 $\pm$ 0.01
Amygdala	0.05 $\pm$ 0.01	0.01 $\pm$ 0.00
Prefrontal cortex	0.04 $\pm$ 0.01	0.02 $\pm$ 0.00
Cerebellum	0.02 $\pm$ 0.00	0.02 $\pm$ 0.00

**Table 21.2.  $^{52}\text{Mn}$  content in brain regions 24 h after injection into the STR**

The values represent group means  $\pm$  sd, n = 4.

Region	Ipsilateral [%ID/mm <sup>3</sup> ]	Contralateral [%ID/mm <sup>3</sup> ]
Globus pallidus	1.16 $\pm$ 0.14	0.01 $\pm$ 0.00
Thalamus	0.31 $\pm$ 0.05	0.01 $\pm$ 0.00
Substantia nigra	0.14 $\pm$ 0.06	0.01 $\pm$ 0.00
Cerebellum	0.01 $\pm$ 0.01	0.01 $\pm$ 0.01

### 21.1.3 Rotameter test

The animals' performance in the rotameter test was examined 4 weeks after the intracerebral administration of  $^{52}\text{Mn}$ . All the rats rotated approximately equally to both directions during the baseline measurement, which resulted in the average "ipsilateral/contralateral rotation" of  $0.9 \pm 0.1$  in the *VTA* group,  $1.0 \pm 0.2$  in the *STR* group, and  $1.2 \pm 0.2$  in the *VTA decayed* group.

However, two animals from the *VTA* and two from the *STR* group exhibited 2-7 times increase in the measured parameter following dopaminergic stimulation with apomorphine (test). This indicated an imbalance of the dopaminergic system involved in the motor

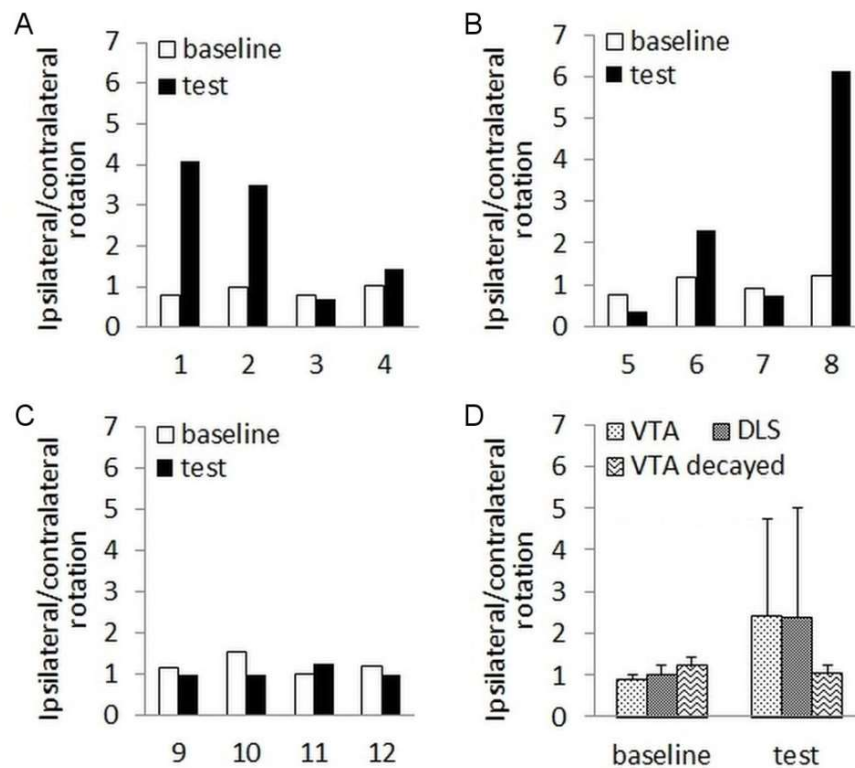


**Figure 21.3. Results of the rotameter test (Experiment 1)**

The ratio of the ipsilateral vs contralateral rotations was at least 2 times higher after the dopaminergic stimulation with apomorphine (test) than during the baseline measurement in two rats injected into the ventral *VTA* (A) and two rats injected into the *STR* (B). This effect was not present in any of the rats treated with the decayed solution (C). The average results of the three groups are compared in D. Bars represent mean + SD,  $n = 4$ , [8].

control. Crucially, this effect was not present in any of the rats from the *VTA decayed* group (Figure 21.3).

### 21.1.4 TH-staining

The TH-staining was performed on the brain tissue from all the rats. In some animals from the *VTA* and *STR* groups, the staining intensity at the injection side was reduced as compared to the contralateral region (Figure 21.4.A-B). This indicated a lesion of the dopaminergic neurons. In contrast, both VTAs were stained approximately equally in the rats treated with the decayed solution (Figure 21.4.C).

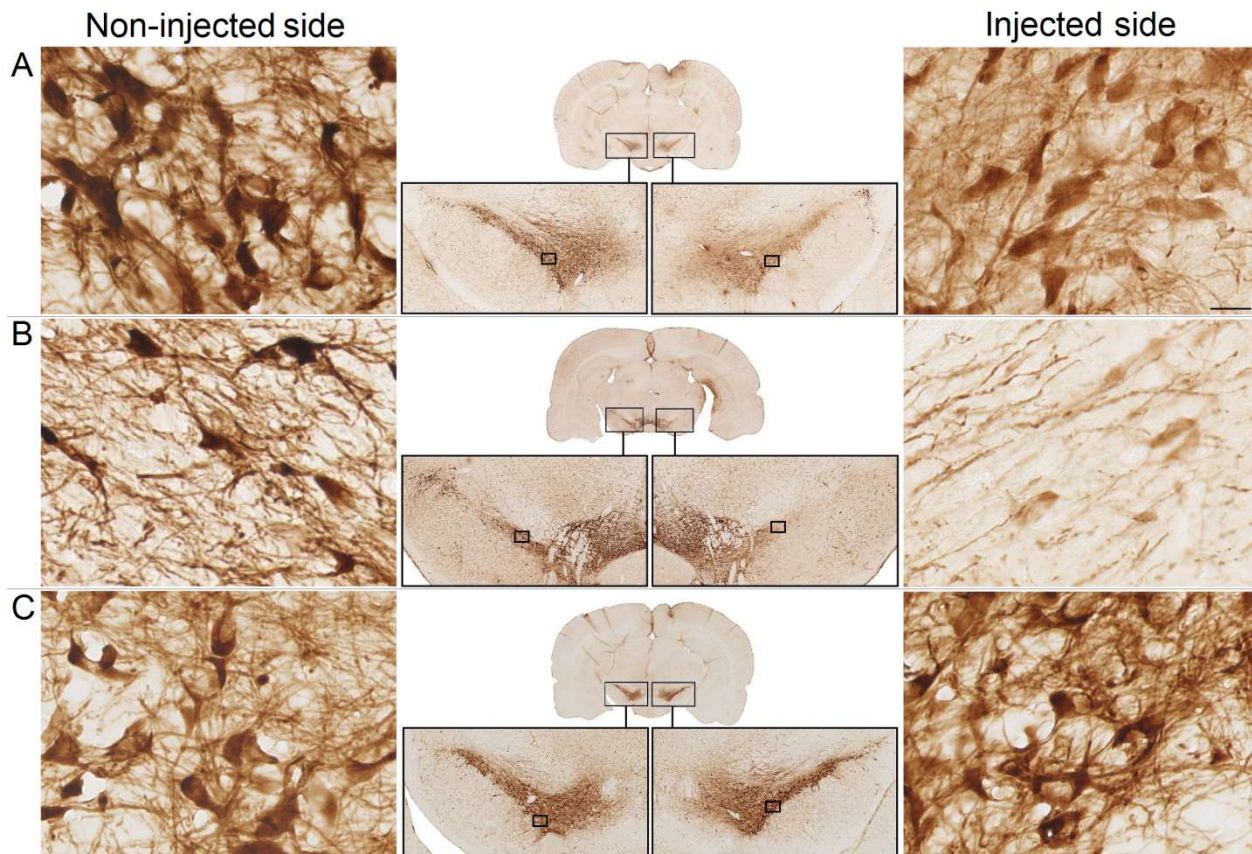


**Figure 21.4. Results of the TH-staining (Experiment 1)**

Example tissue sections of a rat from the *VTA* group (A), from the *STR* group (B), and from the *VTA decayed* group (C) are shown in the middle. The small rectangles in each image indicate the locations of the higher magnification sections shown sidewise. Staining intensity of the neurons within the injected VTA and the SN ipsilateral to the injected STR were reduced in some rats as compared to the contralateral regions. This was not found in any of the brains treated with the decayed solution. The scale bar in A corresponds to 20  $\mu\text{m}$  and applies to all the high magnification images [8].

This result was in line with the outcomes of the rotameter test and suggested that the observed dopaminergic lesion was not caused by the metal contaminants present in the solution, but rather by the radiation dose. Further investigation of the impact of the radioactivity doses was conducted in Experiment 2.

## 21.2 Experiment 2

$\gamma$ H2AX staining was performed on the brain tissue sections of the rats injected with either 30 kBq or 150 kBq of  $^{52}\text{Mn}$  and sacrificed 90 min or 24 h after the injection.

The results evaluated at the 90 min time point are presented in Figure 21.5. The increased number of foci, visible as green spots and clusters, is clear in the image of the VTA injected with the higher dose (Figure 21.5.E) as compared to the contralateral side (Figure 21.5.F) or to the VTA treated with the lower dose (Figure 21.5.C). Only sparse foci were present in the latter one, which was similar to the result in the control group (Figure 21.5.A). In the contralateral VTA of the 30 kBq and control groups, hardly any foci were found (Figure 21.5.B and D).

The semi-quantification of the images supported the qualitative results, showing an approximately 7 times higher fraction of cells with foci in the high dose group than in the low dose and *Control* groups. The number of the cells with foci vs the total number of cells in the contralateral VTA of the *150 kBq* group was also elevated (Figure 21.7.A).

In the tissue sections evaluated 24 h after the  $^{52}\text{Mn}$  injection, it appeared that the highest concentration of the foci was once again in the ipsilateral VTA of the *150 kBq* group, although the foci were not as abundant as at 90 min post-injection (Figure 21.6.E and F).

The images of the *30 kBq* and the *Control* groups were similar to those from the first time point, although some more foci could be seen in the controls (Figure 21.6.A-D).

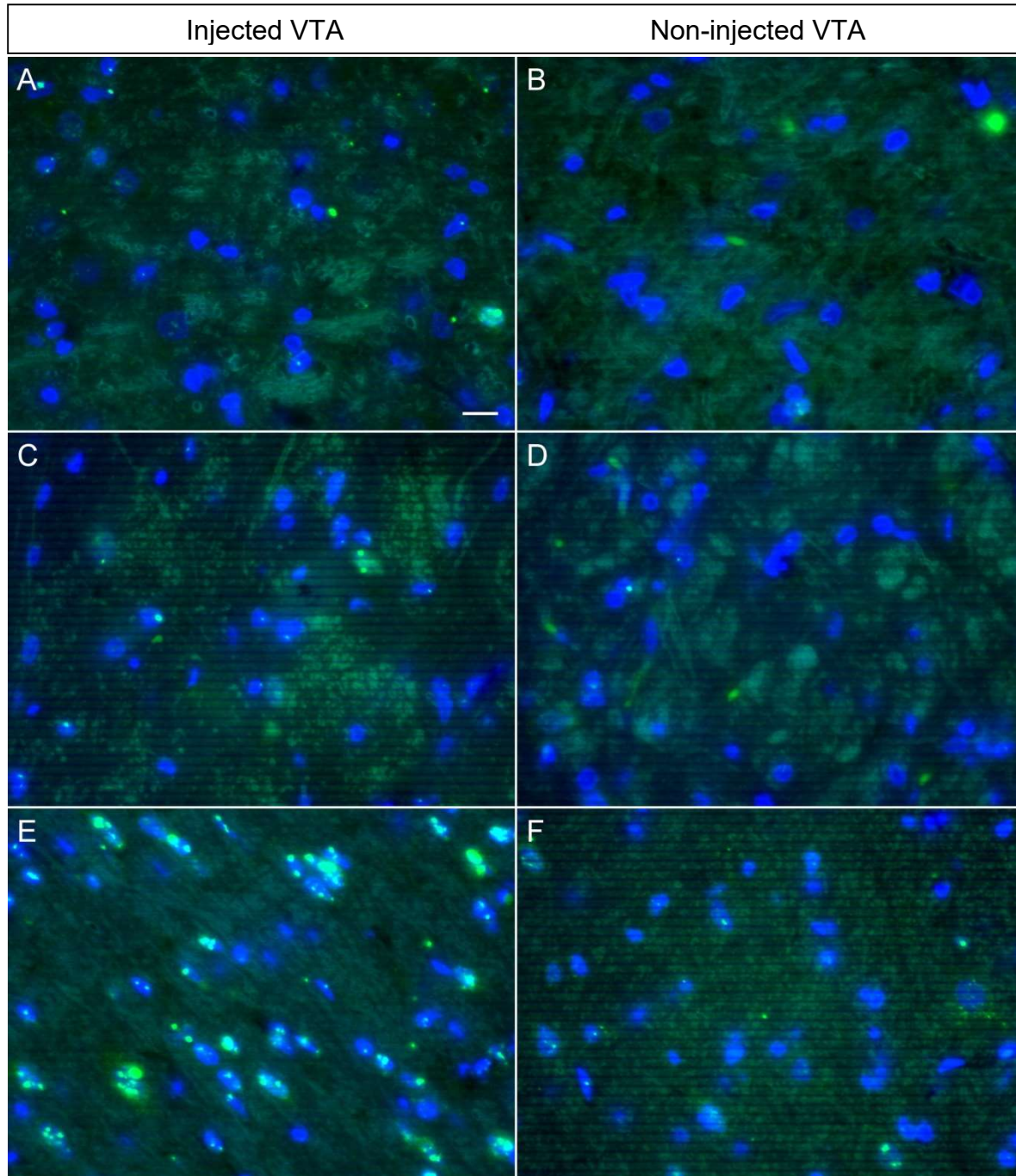


**Figure 21.5. Results of the  $\gamma$ H2AX staining - 90 min**

Example microscopic images of the brain tissue sections of: a rat from the *Control* group (A, B), from the *30 kBq* group (C, D), and from the *150 kBq* group (E, F). An increased number of foci was apparent in the images of the VTA injected with the highest radioactivity dose. This was in contrast to the tissues treated with the 0 or 30 kBq doses. The scale bar in A represents 10  $\mu$ m and applies to all the images, [8].

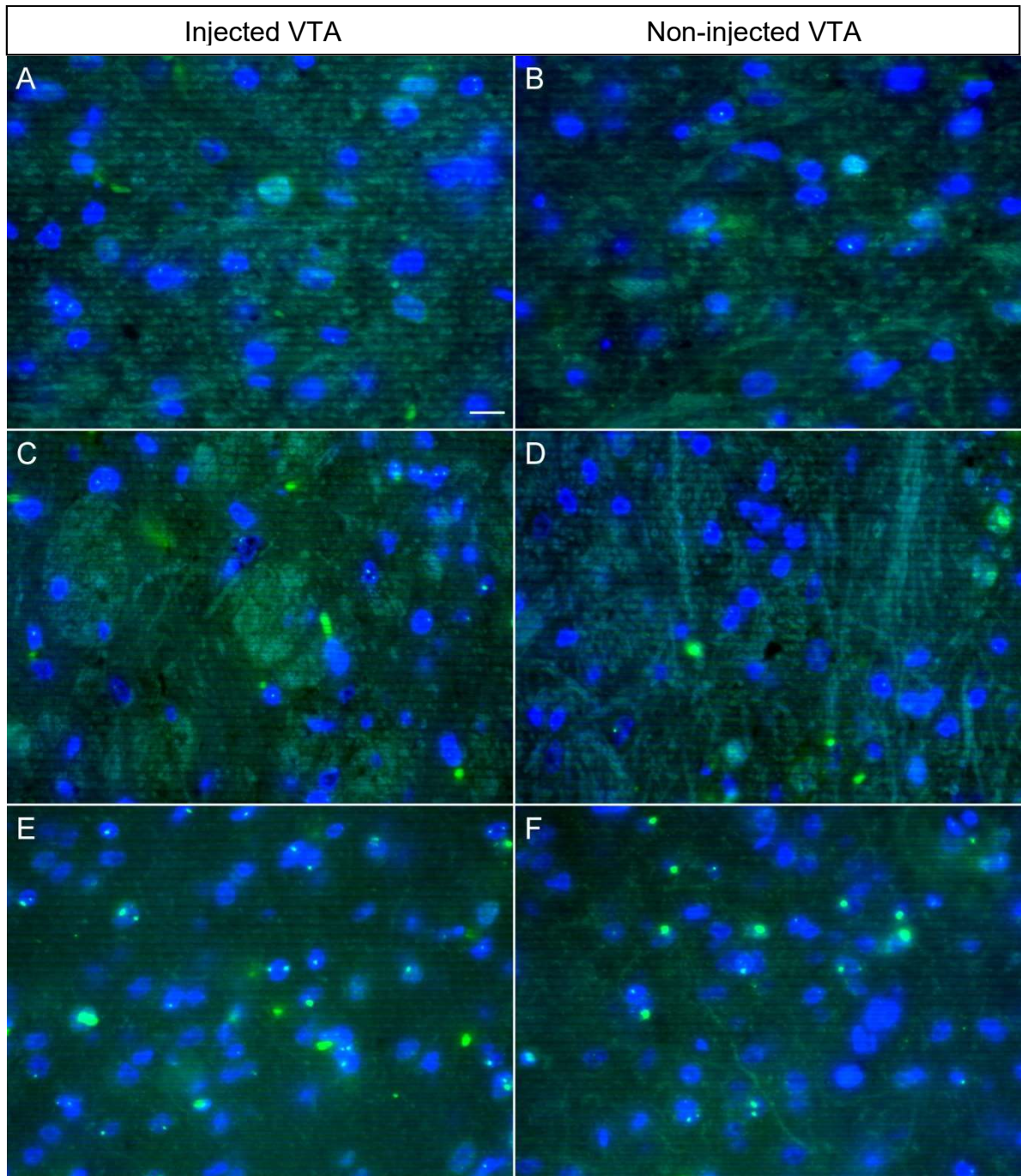


**Figure 21.6. Results of the  $\gamma$ H2AX staining - 24 h**

Example microscopic images of the brain tissue sections of a rat from the *Control* group (A, B), from the *30 kBq* group (C, D), and from the *150 kBq* group (E, F). An increased number of foci in the VTA injected with the highest dose was less apparent than at 90 min post-injection. Moreover, more foci were present in the contralateral VTA of this group as compared to the first time point. The number of foci in both the VTAs of the *Control* and *30 kBq* groups appeared unchanged. The scale bar in A represents 10  $\mu$ m and applies to all the images, [8].

This more homogenous distribution of the foci across the groups observed at the 24 h time point was reflected in the semi-quantitative results. They showed that the average “cells with foci/cells total” ratio in the VTAs treated with 150 kBq of  $^{52}\text{Mn}$  was only twice higher than in the VTAs of the control rats (Figure 21.7.B).

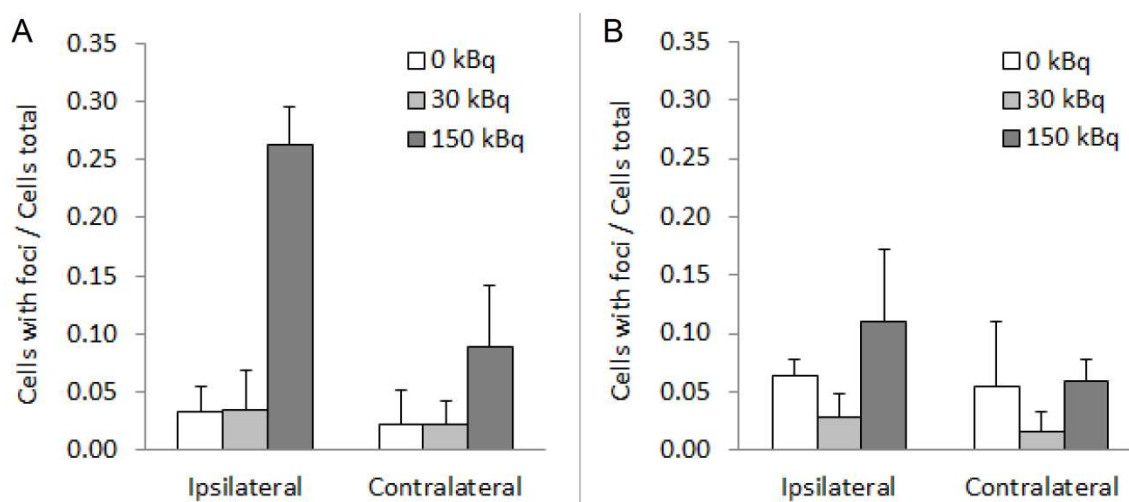


**Figure 21.7. Semi-quantitative results of the  $\gamma\text{H2AX}$  staining**

**A.** 90 min post-injection, the fraction of the cells with foci at the injection site was clearly highest in the 150 kBq group. It was also increased in the contralateral VTA of this group as compared to the Control and the 30 kBq groups. **B.** 24 h after the  $^{52}\text{Mn}$  administration, the fraction of the cells with foci was still highest in the 150 kBq group, although this effect was as strong as at the first time point. The bars represent mean + sd,  $n = 2/\text{group}/\text{time point}$ , [8].

## 21.3 Experiment 3

### 21.3.1 Purity of the tracer solution

Among the metals tested for with the ICP-OES, only Mn and Cr were detected. There was 0.1 ng (1.6 pmol) of the former element, and < 0.14 ng (< 2.7 pmol) of the latter one in the injection volume (1.5  $\mu\text{L}$ ).

The SA at the injection times was 21.3-23.8 GBq/ $\mu\text{mol}$ , *i.e.* it was approximately 7 times higher than in Experiment 1.

### 21.3.2 PET

Following the outcomes of Experiments 1 and 2, the feasibility of imaging the neuronal pathways with a reduced dose of  $^{52}\text{Mn}$  ( $\sim 20$  kBq) was tested in 18 rats injected into the right VTA. The tracer distribution pattern in the PET images acquired 24 h post-injection closely resembled the one observed in Experiment 1. Once again, the ipsilateral mesolimbic and nigrostriatal pathways were clearly delineated (Figure 21.8).

The results obtained by the VOI-based quantification of the images were also similar to those from Experiment 1. Namely, the highest  $^{52}\text{Mn}$  content was found in the ipsilateral NAc ( $0.17 \pm 0.05$  %ID/mm<sup>3</sup>). The OT and STR accumulated  $0.11 \pm 0.04$  and  $0.10 \pm 0.03$  %ID/mm<sup>3</sup>, respectively, while the AMG and PFC accumulated lower amounts ( $0.05 \pm 0.01$  and  $0.03 \pm 0.01$  %ID/mm<sup>3</sup>, respectively). Similarly to Experiment 1,  $^{52}\text{Mn}$  content in the

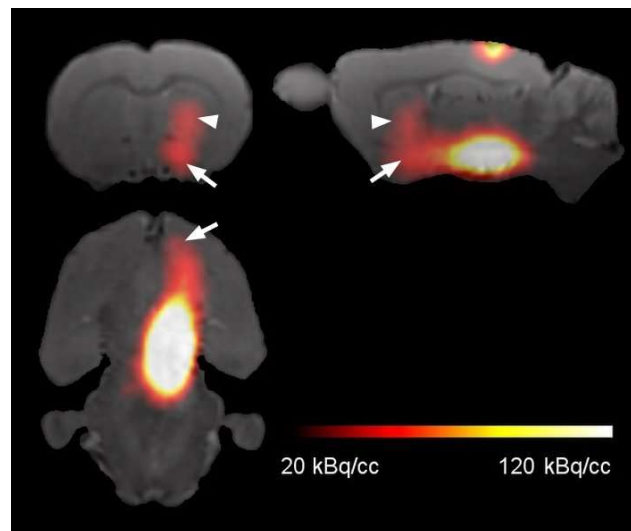


**Figure 21.8.**  $^{52}\text{Mn}$  distribution in PET images (Experiment 3)

The tracer transport from the injected VTA to the ipsilateral NAc (arrow) and STR (arrowhead) was clearly visible in the PET images following administration of the reduced  $^{52}\text{Mn}$  dose. This distribution pattern closely resembled the one observed in the PET images in Experiment 1, [8].

contralateral regions was always lower compared to the ipsilateral ones. Only the CER, which served as a control region, accumulated the same amounts on both sides ( $0.01 \pm 0.01$  %ID/mm<sup>3</sup>). This is shown in Figure 21.9.A.

Statistical analysis of the PET data with ANOVA showed a significant interaction between the “region” and the “brain side” factors ( $F(2.93, 99.44) = 61.00, p < 0.001$ ). The following

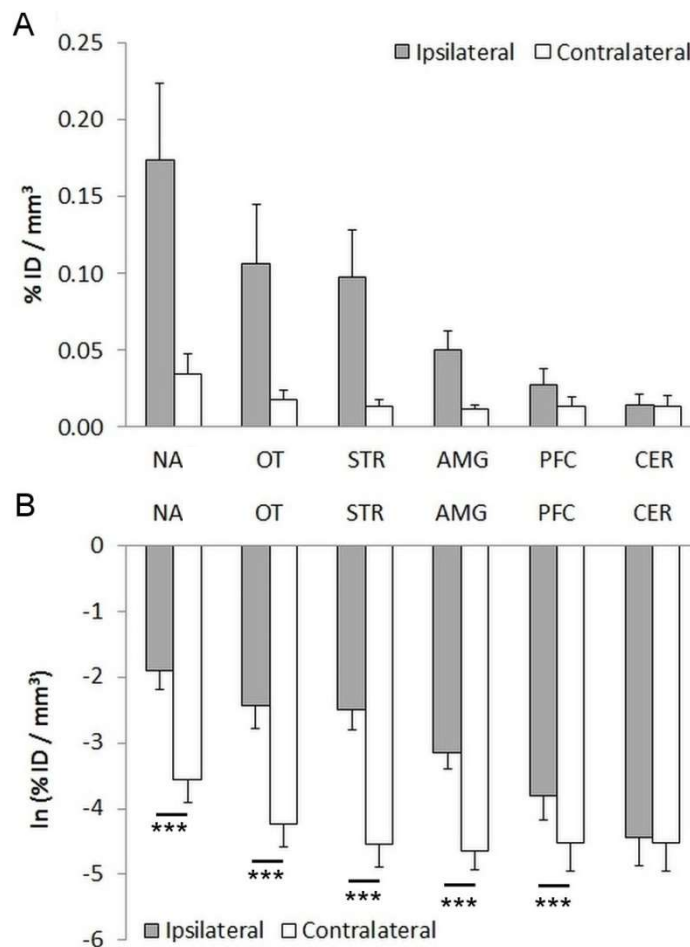


**Figure 21.9. Quantification of the <sup>52</sup>Mn distribution (Experiment 3)**

**A.** The VOI-based analysis revealed a very similar pattern of the tracer distribution to the one observed in Experiment 1. The tracer concentration was always higher in the ipsilateral than in the contralateral region, and this difference was not found only in the reference VOI, the CER. **B.** Statistical analysis of the log-transformed data confirmed that the observed differences were significant. Bars represent mean  $\pm$  sd,  $n = 18$ , \*\*\*  $p < 0.001$ , [8].

post-hoc test revealed a highly significant difference ( $p < 0.001$ ) between the ipsilateral and the contralateral side for all the regions but the CER ( $p > 0.05$ ) (Figure 21.9).

### 21.3.3 Rotameter test

The test was performed at different time points after the  $^{52}\text{Mn}$  injections. Six rats were tested at 3 days, six at 14 days and six at 28 days post-injection. The *Control* group was examined only at the 28 days-time point.

The average “ipsilateral/contralateral rotation” ratio was similar between the experimental groups during the baseline measurement. The exact scores were:  $0.9 \pm 0.1$  in the *3 days* group,  $1.1 \pm 0.4$  in the *14 days* group,  $1.2 \pm 0.4$  in the *28 days* group, and  $1.0 \pm 0.2$  for the *control* animals. The results obtained during the test measurement (*i.e.* after the administration of apomorphine) remained in the same range, yielding:  $1.0 \pm 0.7$  in the *3 days* group,  $1.2 \pm 0.5$  in the *14 days* group,  $1.1 \pm 0.8$  in the *28 group*, and  $0.8 \pm 0.6$  in the *controls*. These results are shown in Figure 21.10.

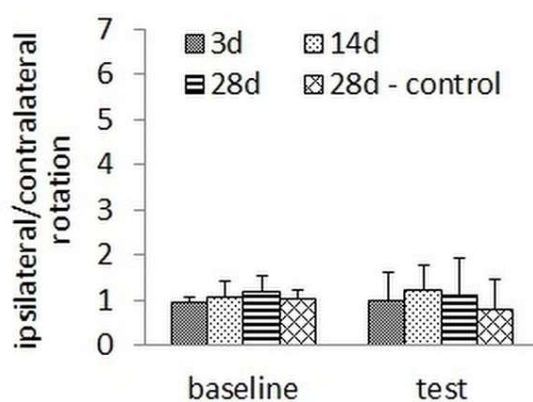


**Figure 21.10. Results of the rotameter test (Experiment 3)**

There was no significant difference between the groups neither at the baseline, nor at the test measurement. Bars represent mean + sd,  $n = 6$  per group, [8].

When compared statistically with ANOVA, neither the main effects ( $F(1, 20) = 0.05, p > 0.05$  for “measurement”,  $F(3, 20) = 0.62, p > 0.05$  for “group”), nor the interaction between the two factors ( $F(3, 20) = 0.59, p > 0.05$ ) were significant.

### 21.3.4 TH-staining

On the following day after the rotameter test, the rats were sacrificed and the brains were used for the TH-staining. There was no difference in the staining intensity between the injected and the contralateral VTA regions in any of the examined tissue sections (Figure

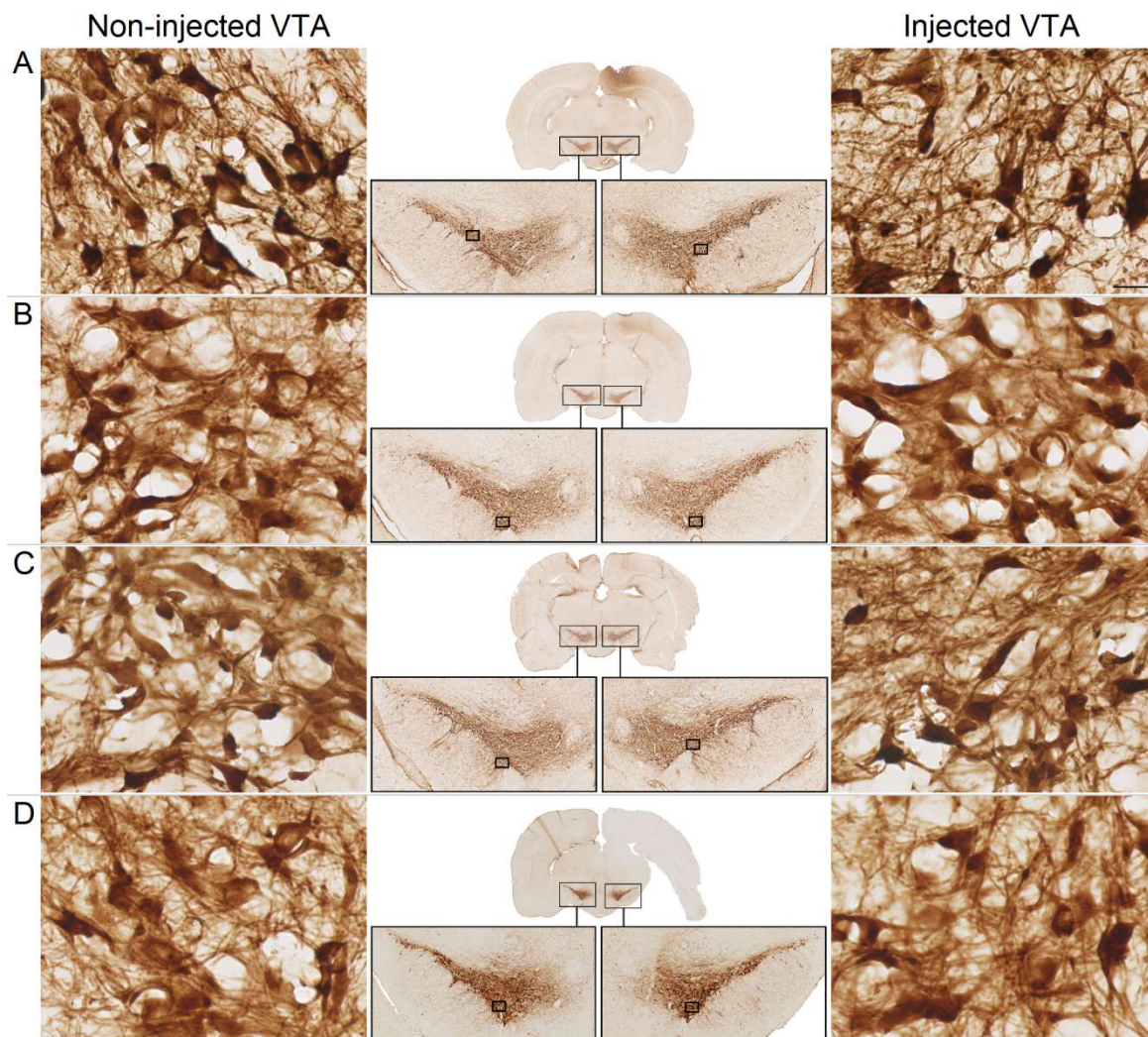


**Figure 21.11. Results of the TH-staining (Experiment 3)**

No differences in the staining intensity between the ipsilateral and contralateral VTAs were found at the examined time points: 3 days (A), 14 days (B), or 28 days (C) after the  $^{52}\text{Mn}$  injection. Similarly,, there was no effect in the *Control* group (D), [8].

21.11). Therefore, the ability of the dopaminergic neurons to synthesize tyrosine hydroxylase despite the treatment with ~20 kBq of  $^{52}\text{Mn}$  was confirmed for up to 4 weeks post-injection.

## 22 Study 4

This study aimed at verifying whether a single intrastriatal injection of non-radioactive  $Mn^{2+}$  or  $^{52}Mn$  could affect DAT or GABA<sub>A</sub> receptors (GABA<sub>AR</sub>), either shortly- (*i.e.* 24-48 h) or later (*i.e.* 4 weeks) after a direct intracerebral injection. Due to the difficulties associated with subtracting the  $^{52}Mn$  signal, still present at the injection site up to 1 month after the administration (Figure 22.1), from the image containing the “mixed” signal of  $^{52}Mn$  and the [ $^{11}C$ ]-tracer, the data of the *Hot Mn* group were not analyzed.

The SA of [ $^{11}C$ ]methylphenidate as well as of [ $^{11}C$ ]flumazenil varied substantially across the measurements. It ranged from 9.2 to 74.6 GBq/ $\mu$ mol for the first tracer, and from 19.9 to 66.8 GBq/ $\mu$ mol for the second one. The SA of [ $^{11}C$ ]flumazenil used for the measurement of the two rats from the *Cold Mn* group at 48 h was even beyond this range (233.6 GBq/ $\mu$ mol).

At the 24 h time point, the BPnd of [ $^{11}C$ ]methylphenidate in the right STR was  $0.99 \pm 0.09$  (mean  $\pm$  sd) in the *Control* group and  $1.01 \pm 0.11$  in the *Cold Mn* group, while the contralateral values were  $0.95 \pm 0.04$  and  $0.93 \pm 0.08$ , respectively. 4 weeks later, the BPnd of the injected STR was  $1.00 \pm 0.09$  in the control rats and  $1.00 \pm 0.15$  in the treated

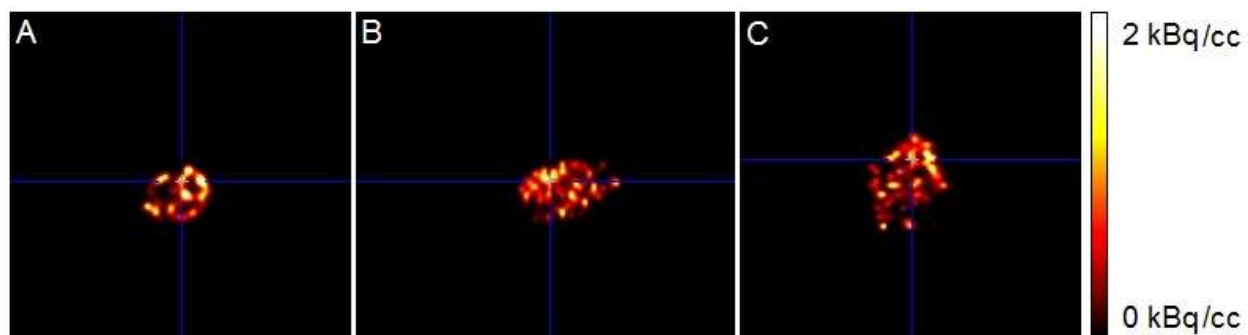


**Figure 22.1.**  $^{52}Mn$  in the right STR 29 days after the administration

The coronal (A), sagittal (B), and axial (C) views are shown. The blue lines in each image plane indicate the position of the two other planes. Due to this remaining  $^{52}Mn$  signal and the difficulties associated with subtracting it from the PET images of the [ $^{11}C$ ]-tracers, the data of the *Hot Mn* group were not evaluated.

animals, while the respective contralateral values were  $1.07 \pm 0.10$  and  $1.05 \pm 0.15$  (Figure 22.2.A).

The BPnd of [ $^{11}\text{C}$ ]flumazenil in the FC was estimated 2 and 30 days post-injection. In the *Control* group, it was  $0.87 \pm 0.10$  in the ipsilateral region and  $0.90 \pm 0.08$  on the contralateral side, while the corresponding values of the *Cold Mn* group were  $0.69 \pm 0.13$  and  $0.83 \pm 0.12$ . At the later time point, the BPnd in the control rats was  $0.97 \pm 0.13$  on the ipsilateral and  $0.97 \pm 0.14$  on the contralateral side, while in the rats treated with  $\text{Mn}^{2+}$ , the corresponding values were  $0.84 \pm 0.10$  and  $0.89 \pm 0.07$  (Figure 22.2.B).

In order to statistically analyze these results, the  $\text{BPnd}_L\text{-BPnd}_R$  differences were compared

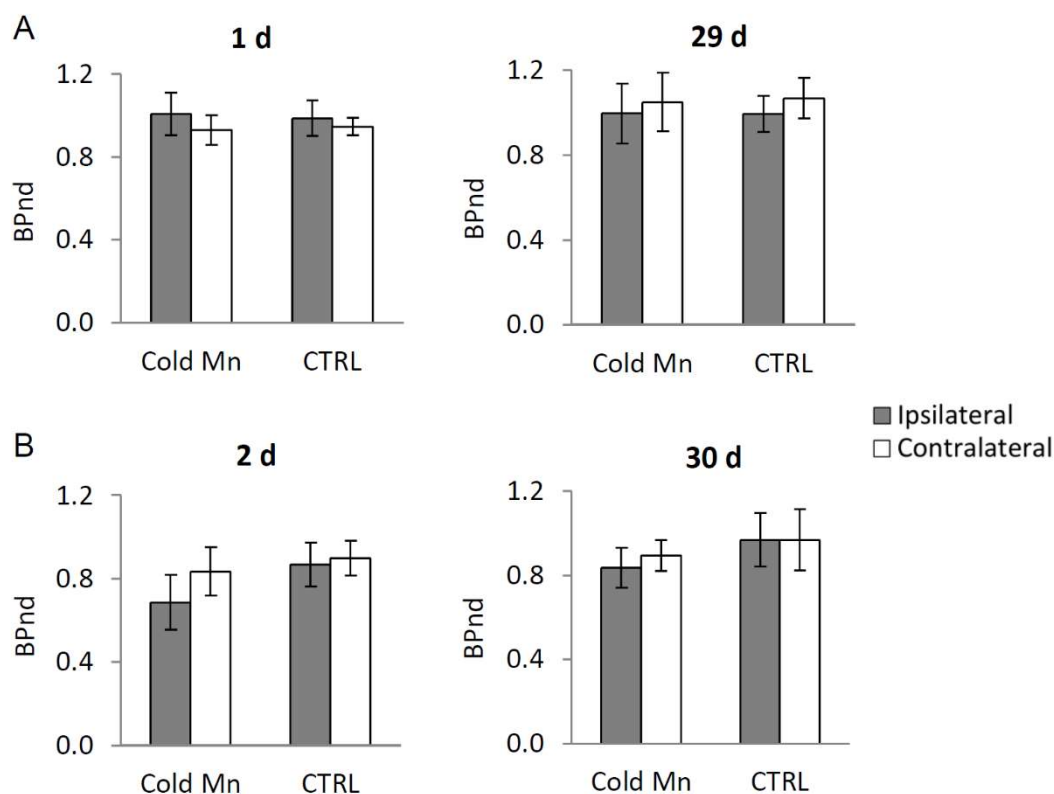


**Figure 22.2. Results of the kinetic modelling of [ $^{11}\text{C}$ ]methylphenidate and [ $^{11}\text{C}$ ]flumazenil PET studies**

**A.** BPnd of [ $^{11}\text{C}$ ]methylphenidate in the STR evaluated 1 and 29 days after the injection of  $\text{Mn}^{2+}$  (*Cold Mn* group) or normal saline (*CTRL*) into the right STR. **B.** BPnd of [ $^{11}\text{C}$ ]flumazenil in the FC estimated in the same animals 2 and 30 days post-injection. Bars represent mean  $\pm$  sd,  $n = 8$  per group.

between the *Cold Mn* group and the *Control* group. This was done separately for each tracer and each time point. The  $BPnd_L - BPnd_R$  differences of the [ $^{11}C$ ]methylphenidate data were not significantly different between the groups at any time point, indicating no effect of 50 nmol of  $Mn^{2+}$  on the DAT in the rat striatum (Figure 22.3.A). However, the right-left

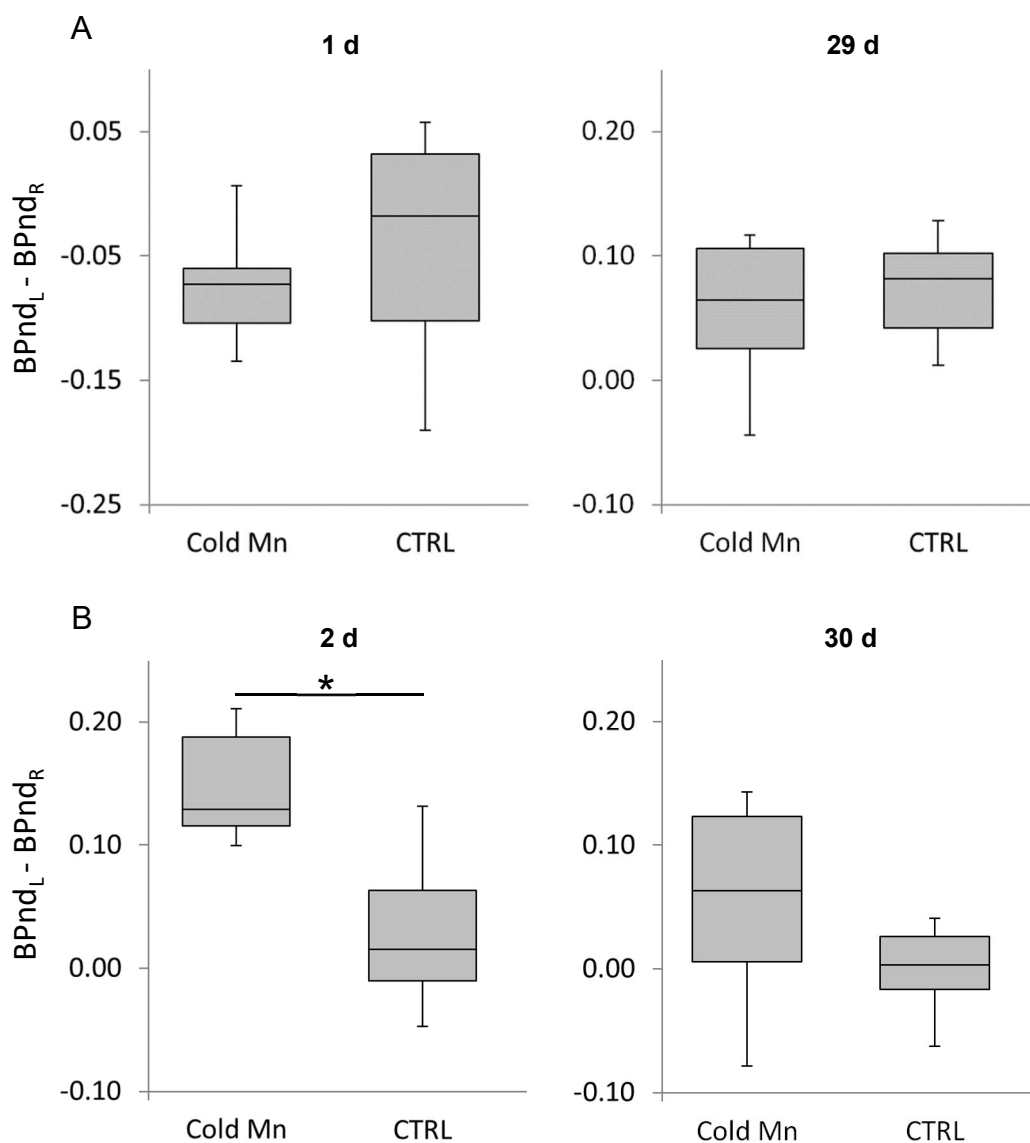


**Figure 22.3. Left-right differences in the BPnd of [ $^{11}C$ ]methylphenidate and [ $^{11}C$ ]flumazenil after an intrastriatal  $Mn^{2+}$  injection**

**A.** The  $BPnd_L - BPnd_R$  of [ $^{11}C$ ]methylphenidate measured in the STR were not significantly different between the experimental groups at any of the evaluated time points. **B.** The  $BPnd_L - BPnd_R$  of [ $^{11}C$ ]flumazenil measured in the FC were significantly larger in the *Cold Mn* group than in the control rats 2 days after the administration of  $Mn^{2+}$ . This difference was not significant anymore 30 days post-injection.  $N = 8$  per group,  $*p < 0.0125$ .

differences in the BPnd of [ $^{11}\text{C}$ ]flumazenil were significantly greater in the *Cold Mn* group than in the *Control* group at the first time point, indicating an impact of the intrastrially administered  $\text{Mn}^{2+}$  on the  $\text{GABA}_A$  receptors in the cortex. 30 days post-injection, this effect was not present anymore (Figure 22.3.B).

Interestingly,  $\text{Mn}^{2+}$  presence in the ipsilateral FC was clearly visible in the T1W MR images of the *Cold Mn* group 24 h post-injection (Figure 22.4).

In order to verify whether the intrastriatal sham injection had any effect on the DAT at 1 day, or on  $\text{GABA}_A\text{R}$  at day 2, the  $\text{BPnd}_L\text{-BPnd}_R$  differences of the *Control* group were analyzed with a 1-sample t-test. However, the tested mean differences were not significantly different from 0 ( $p > 0.05$ ), indicating no impact of the injection procedure.

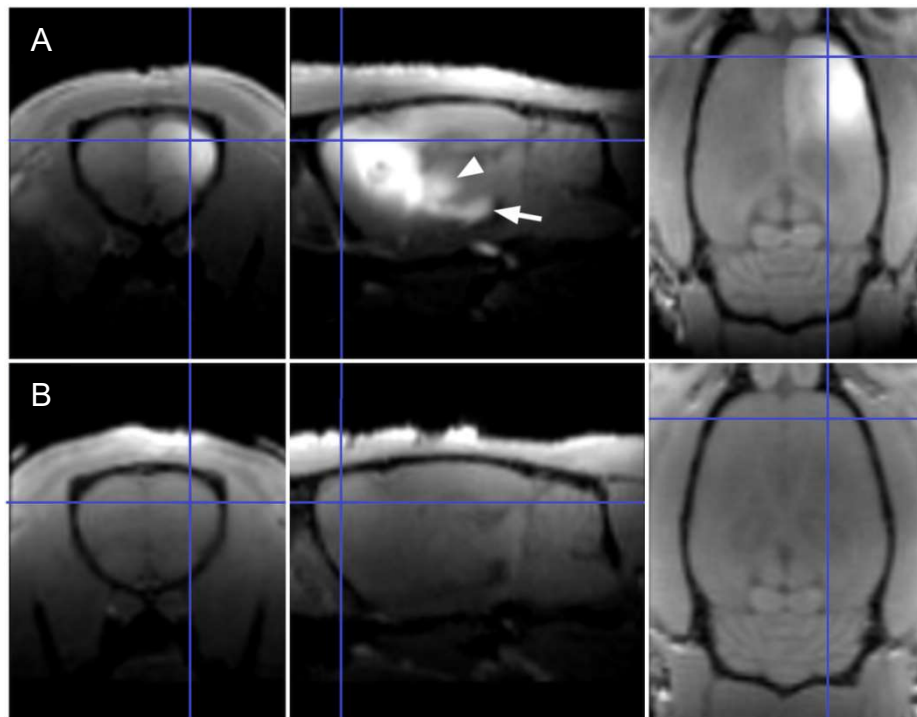


**Figure 22.4.  $\text{Mn}^{2+}$  neuronal transport 24 h after the intrastriatal injection**

**A.** An example T1W image of a rat from the *Cold Mn* group shown in the coronal (left), sagittal (middle) and axial (right) planes.  $\text{Mn}^{2+}$  transport to the SN (arrow) and THL (arrowhead) are clearly visible. The signal enhancement in the ipsilateral FC (cross-section of the blue lines) suggests that  $\text{Mn}^{2+}$  had reached also that area. **B.** An example T1W image of a *Control* rat at the same time point.

## 23 Study 5

### 23.1 Dependence of the $^{52}\text{Mn}$ distribution on the pharmacological treatment

The goal of this study was to investigate whether the distribution of  $^{52}\text{Mn}$  unilaterally injected into the VTA would be affected by a co-injection of a pharmacological agent known to influence neuronal activity. However, due to the numerous neuronal projections of the VTA originating from its different subregions, the tracer distribution pattern may also depend on the exact location of the injection. Therefore, the injection location was carefully evaluated in the first place. This could be readily done based on the T2W MR images which were coregistered to the anatomical atlas of the rat brain. The example of one rat is presented in Figure 23.1.

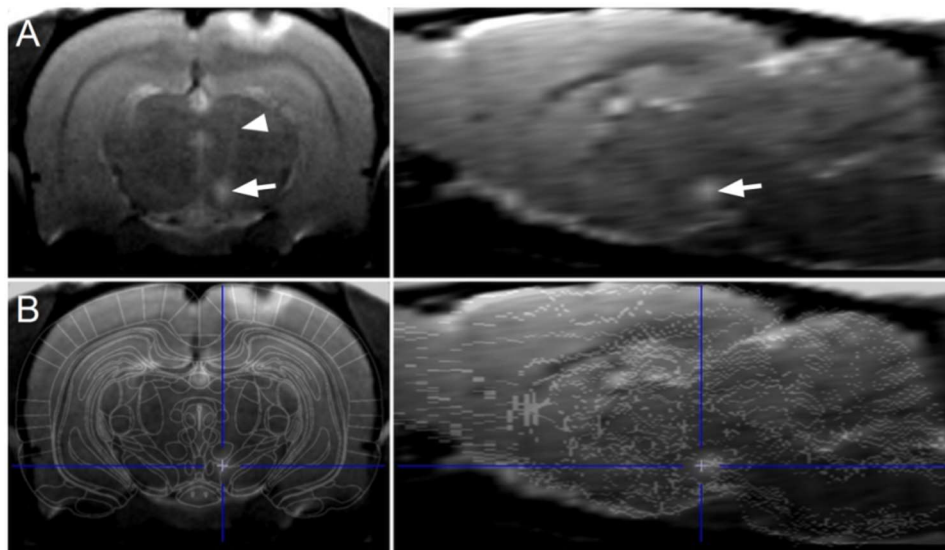


**Figure 23.1. Identification of the injection location**

**A.** The injection location (arrow) could be easily recognized in the coronal (left) and sagittal (right) plane. In many cases the needle track was also visible (arrowhead). **B.** The injection location was marked (intersection of the blue lines) and its anatomical position was read out from the overlaid brain atlas.

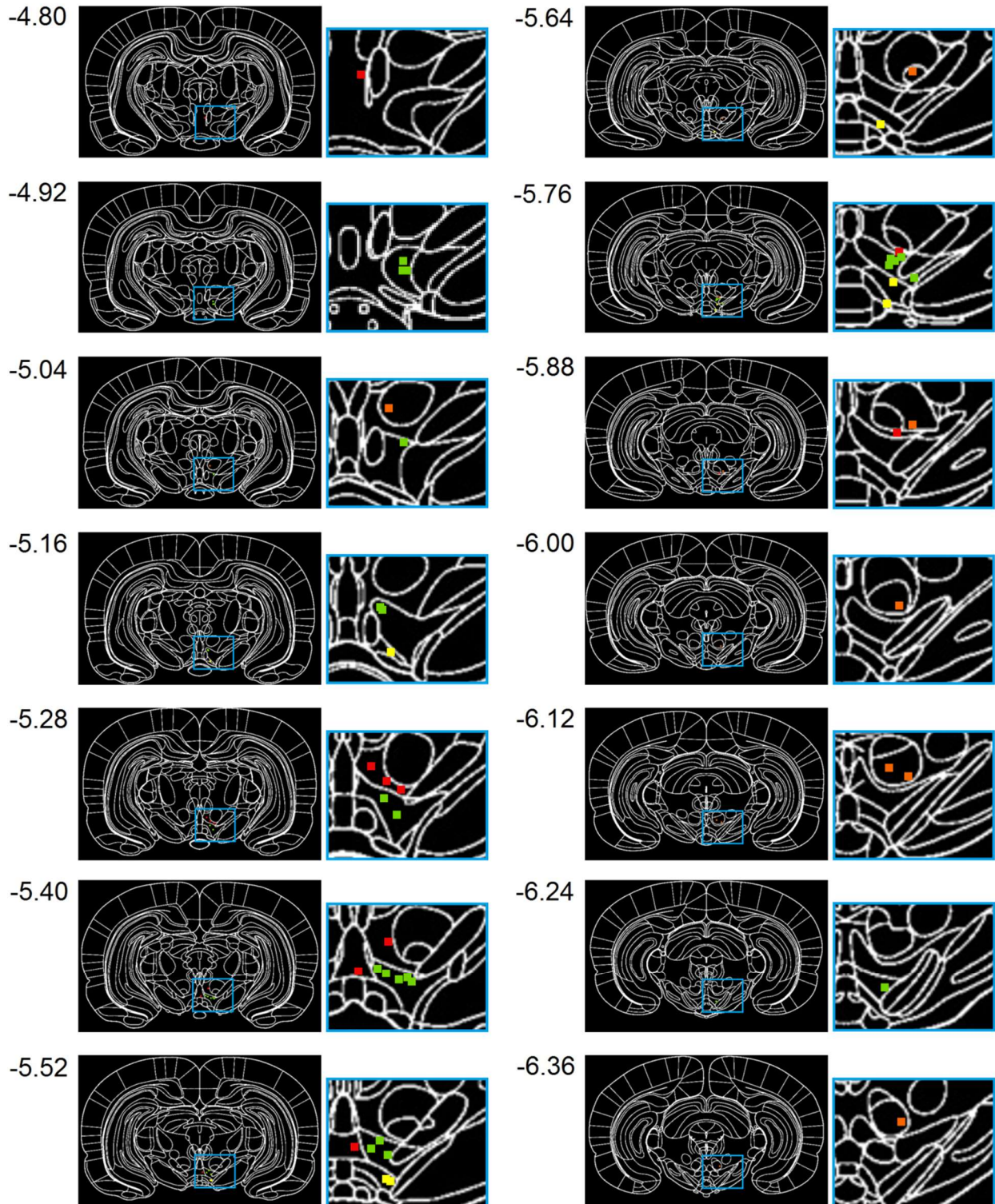


**Figure 23.2. Injection locations identified based on the MR images**

The identified locations are depicted on the rat brain atlas and the number on the left side indicates the distance from the bregma. The smaller images on the right side show a magnification of the injection area. Each dot in these images represents one animal. Injection locations identified within the VTAR or PBP are shown in green ( $n = 22$ ), the locations within the PN or the PIF of the VTA are marked in yellow ( $n = 6$ ), and the injection location within the RN are depicted in orange ( $n = 7$ ). All the injection sites identified in other regions were considered incorrect and are represented by the red dots ( $n = 9$ ).

In some images, the injection volume appeared relatively large and spread across a few slices. In those cases, the slice in which the needle track was visible was selected. In one animal from the NMDA group, a form of brain atrophy was identified. The data of that subject were rejected from further analysis.

Evaluation of the injection locations revealed that 28 rats were injected into the VTA, 7 were injected into the red nucleus (RN), which is located dorsally to the VTA, and the injection sites of the remaining 9 rats were identified in different locations around the VTA and RN. These 9 injection locations were considered incorrect and the data were excluded from further analysis. The incorrect injection sites are depicted as red dots in Figure 23.2.

Since the target region of a VTA neuron may depend on the subnucleus of the VTA in which its soma is situated [41], the 28 animals injected into the VTA were further subdivided. Namely, the rats whose injection location was identified within the rostral VTAR or the PBP were grouped together, as these nuclei are anatomically very close to each other. The rats

**Table 23.1. The numbers of the rats injected into different subregions of the dopaminergic midbrain**

Based on the identified injection location, the animals were assigned to one out of three groups: *VTAR-PBP*, *PN-PIF*, or *RN*. The remaining rats (*Other*) were rejected from further analysis.

Experimental group	Injection location			
	VTAR-PBP	PN-PIF	RN	Other
<i>CTRL</i>	4	1	1	3
<i>AMPA</i>	4	1	1	1
<i>TTX</i>	4	3	1	2
<i>NMDA</i>	4	1	3	1
<i>AP5</i>	2	0	1	2
<i>Cold Mn</i>	4	0	0	0
Total	22	6	7	9

injected into the PN or the PIF of the VTA were considered the second group. These two small nuclei are also adjacent to each other. They are located medially and caudally to the VTAR-PBP. The 7 rats injected into the RN constituted the third group. This is summarized in Table 23.1.

Only the data of the rats injected into the VTAR-PBP regions were included in the analysis of the effects of the pharmacological agents. There were 2-4 rats per a pharmacological agent in this group, which was sufficient for the comparison. Among the animals injected into the PN-PIF regions and into the RN, there were usually 0 or 1 rats per a pharmacological agent.

Firstly, based on the qualitative evaluation, no differences in the  $^{52}\text{Mn}$  distribution pattern was noticed between the PET images of the rats treated with almost any of the pharmacological agent and the images of the control rats. The only group in which the tracer appeared to have a distinctive distribution was the *Cold Mn* group. Specifically, while the mesolimbic and the mesostriatal pathways were clearly delineated by  $^{52}\text{Mn}$  in the images of the control animals, it was difficult to identify these neuronal tracts in the images of the *Cold Mn* group (Figure 23.3).

This blocking effect of non-radioactive  $\text{Mn}^{2+}$  could be clearly recognized also based on the image quantification. Among the three analyzed brain regions, the ipsilateral NAc and STR were characterized by a lower rate of increase in the  $^{52}\text{Mn}$  content over time in the rats from the *Cold Mn* group than in the control animals. This effect was not present in the ipsilateral PLC. In the contralateral NAc, STR, and PLC, the content of the tracer was not changing over time (Figure 23.4).

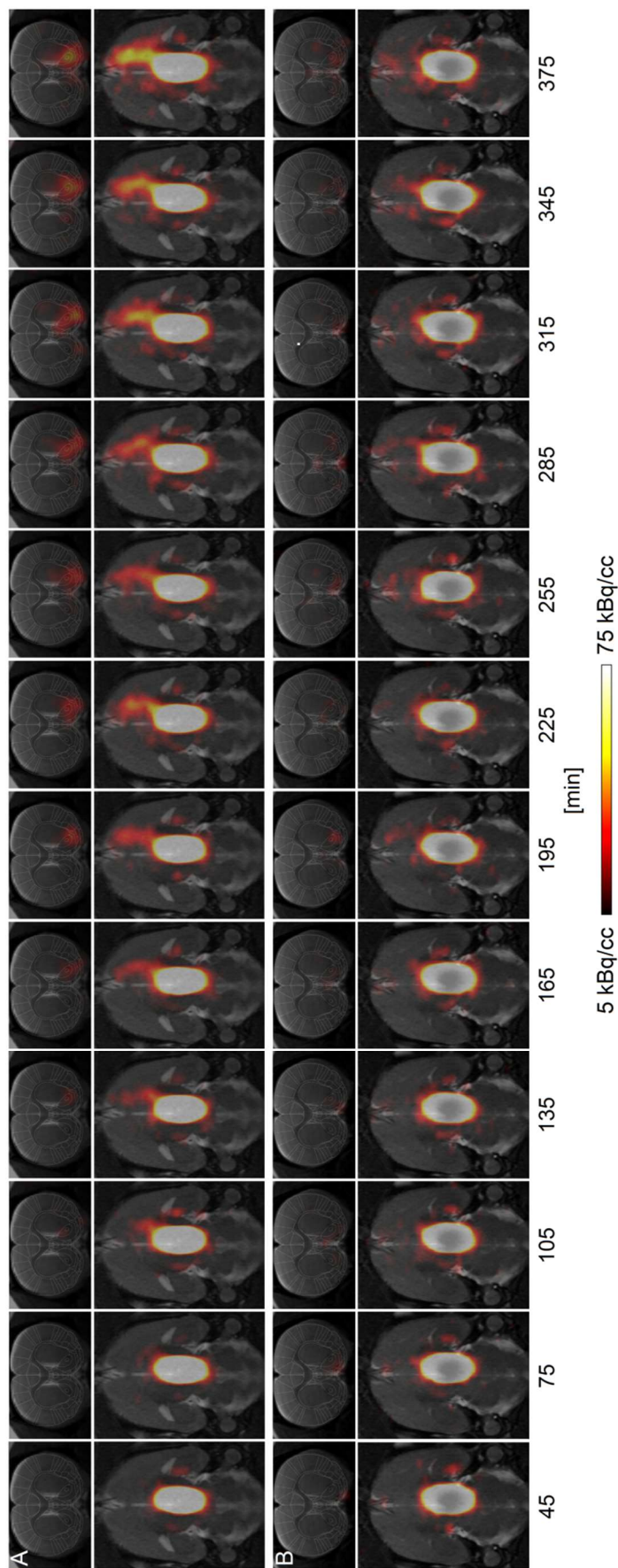


**Figure 23.3.  $\text{Mn}^{2+}$  impact on the neuronal transport of  $^{52}\text{Mn}$**

**A.** Twelve consecutive frames of the PET image acquired directly after the injection of  $^{52}\text{Mn}$  into the tight VTAR-PBP region are shown in the coronal (upper panel) and axial (lower panel) planes. In the former orientation, the gradual accumulation of the tracer in the ipsilateral NAc can be easily recognized. In the latter one, the transport along the mesolimbic pathway is visible. **B.** This neuronal transport was markedly reduced in the animals co-injected with 50 nmol of non-radioactive  $\text{Mn}^{2+}$ . This dose was also sufficient to affect the contrast in the MR image (darker area “shining” through the PET signal). The color scale of the PET images was adjusted to correct for the injected doses.

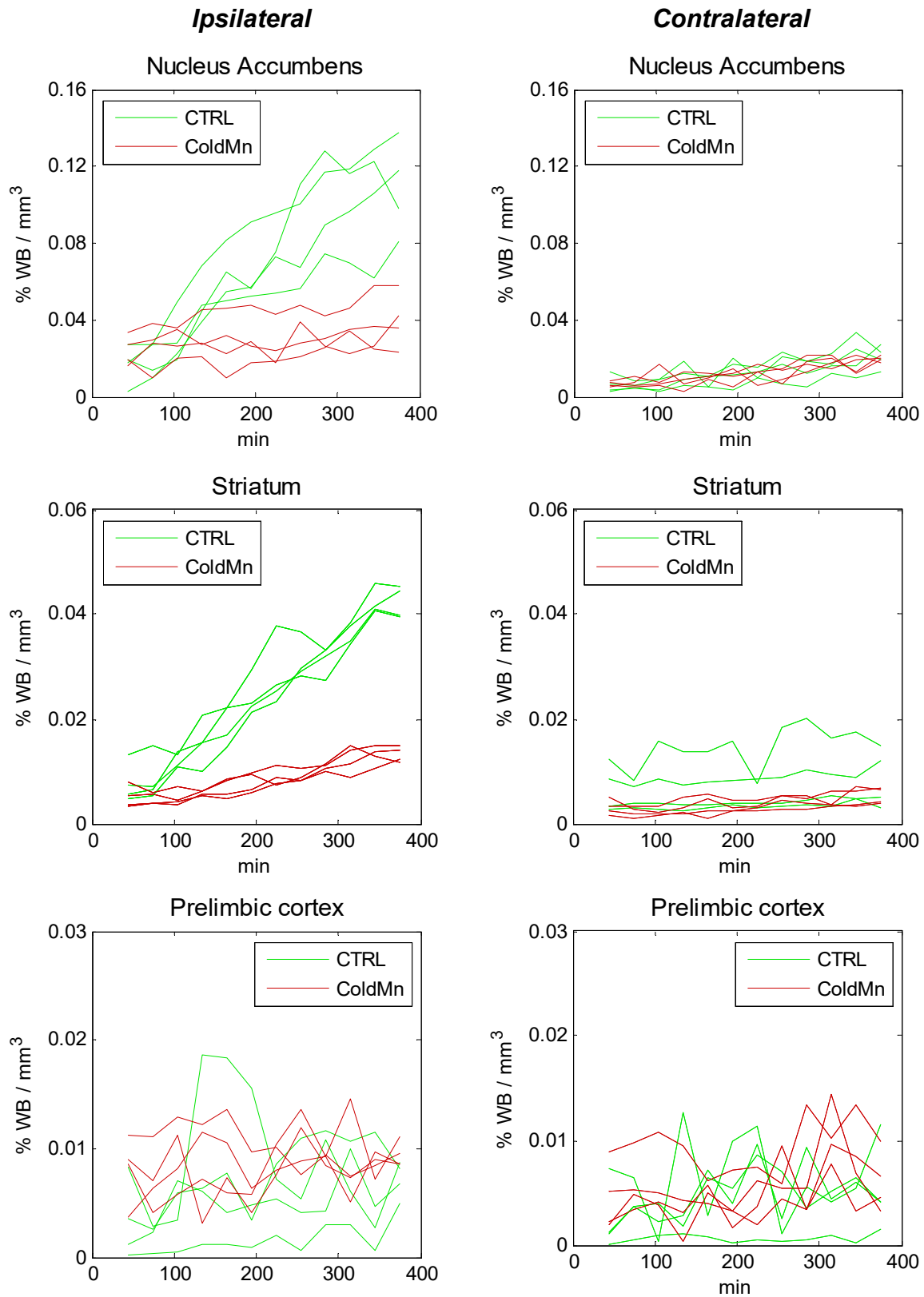


**Figure 23.4.**  $^{52}\text{Mn}$  transport to the main output regions of the VTA - *Cold Mn* group

The transport rate of the tracer was clearly lower in the ipsilateral STR and NAc in the rats co-injected with non-radioactive  $\text{Mn}^{2+}$  as compared to the control group. This effect was not visible in the PLC over the time of the measurement. Each line represents data of one animal.

Non-radioactive  $Mn^{2+}$  was the only tested pharmacological agent which had an impact on the spatial distribution of  $^{52}Mn$  in the rat brain. There were no obvious differences in the rate of the  $^{52}Mn$  accumulation and its distribution in any of the three analyzed VOIs between the *AMPA* group and the *CTRL* group (Figure 23.5), between the *TTX* group and the *CTRL* group (Figure 23.6), neither between the *AP5* or *NMDA* groups and the controls (Figure 23.7). In all these animals, the pattern of the PET tracer distribution resembled the pattern seen in the previous studies. Namely, a substantial transport of the tracer could be recognized in the ipsilateral NAc and STR (but not the PLC), the main output regions of the VTA, while only marginal changes were observed in the contralateral regions. Only one *NMDA* rat was characterized by a clearly higher  $^{52}Mn$  concentration in all the analyzed ipsilateral regions.

Since AMPA, NMDA, TTX, and AP5 appeared not to have an impact on the  $^{52}Mn$  distribution, all these rats (total of 18) could be grouped together based on the same injection location (VTAR-PBP) and compared to the six rats injected into the PN-PIF regions and to the seven rats injected into the RN. Two interesting observations were made in this comparison.

Firstly, a strong signal was visible along the neuronal tract leading from the midbrain to the OB in the very first frame of the PET images of the *PN-PIF* group. This was much weaker in the images of the rats from the *VTAR-PBP* group (Figure 23.8). Based on the registered anatomical atlas, the high signal was identified in the following ipsilateral regions: VP, OT, OB, AON, HLDB, and MPN.

The second characteristic pattern was noticed in the last frame of the PET images of the rats injected into the RN. The neuronal pathway delineated with  $^{52}Mn$  projected into the caudal direction crossing the midline of the brain. It extended along the contralateral MO.

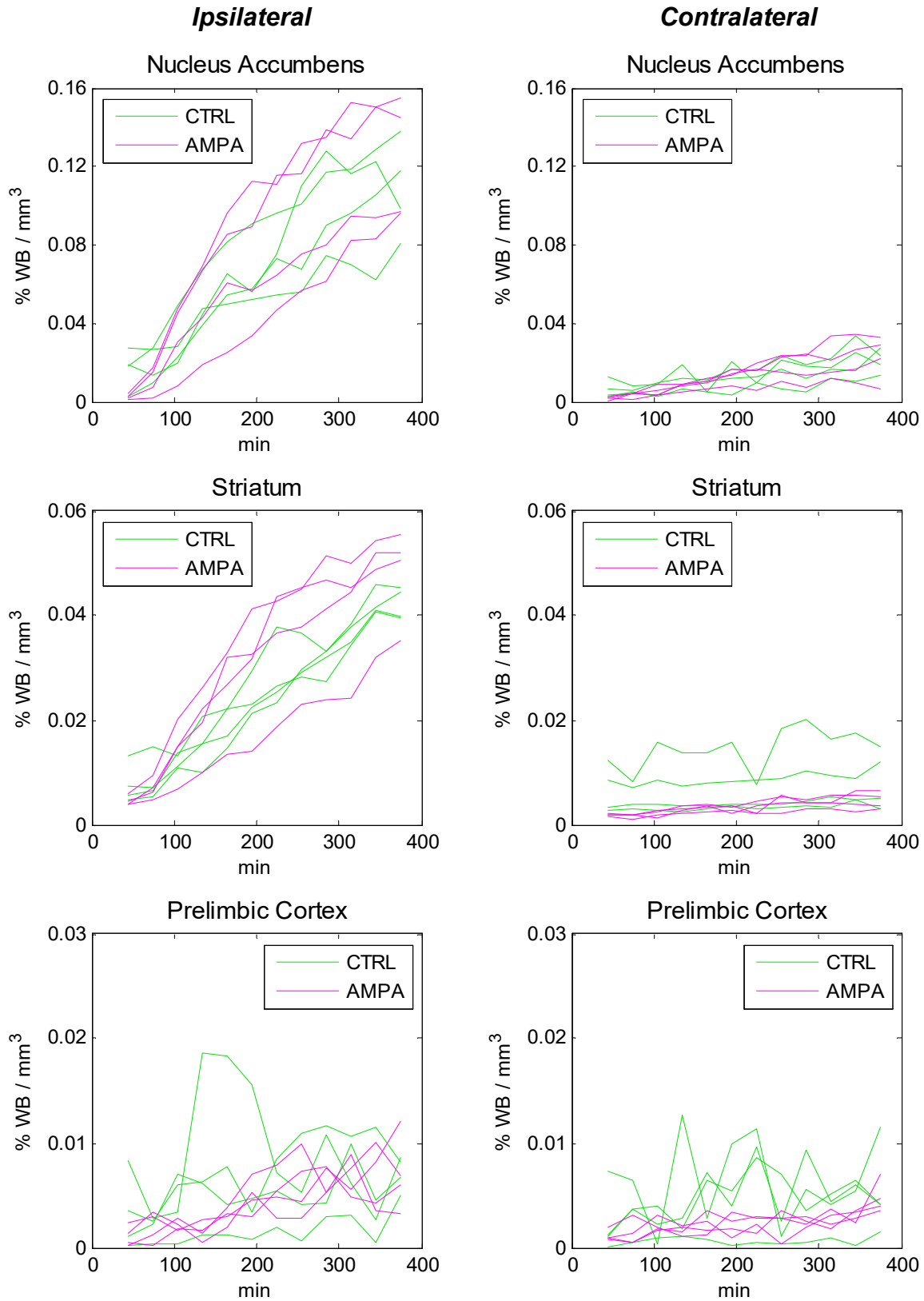


**Figure 23.5. <sup>52</sup>Mn transport to the main output regions of the VTA - AMPA group**

The gradual changes in the concentration observed in the AMPA group were very similar to the changes in the corresponding regions of the control group. Each line represents data of one animal.

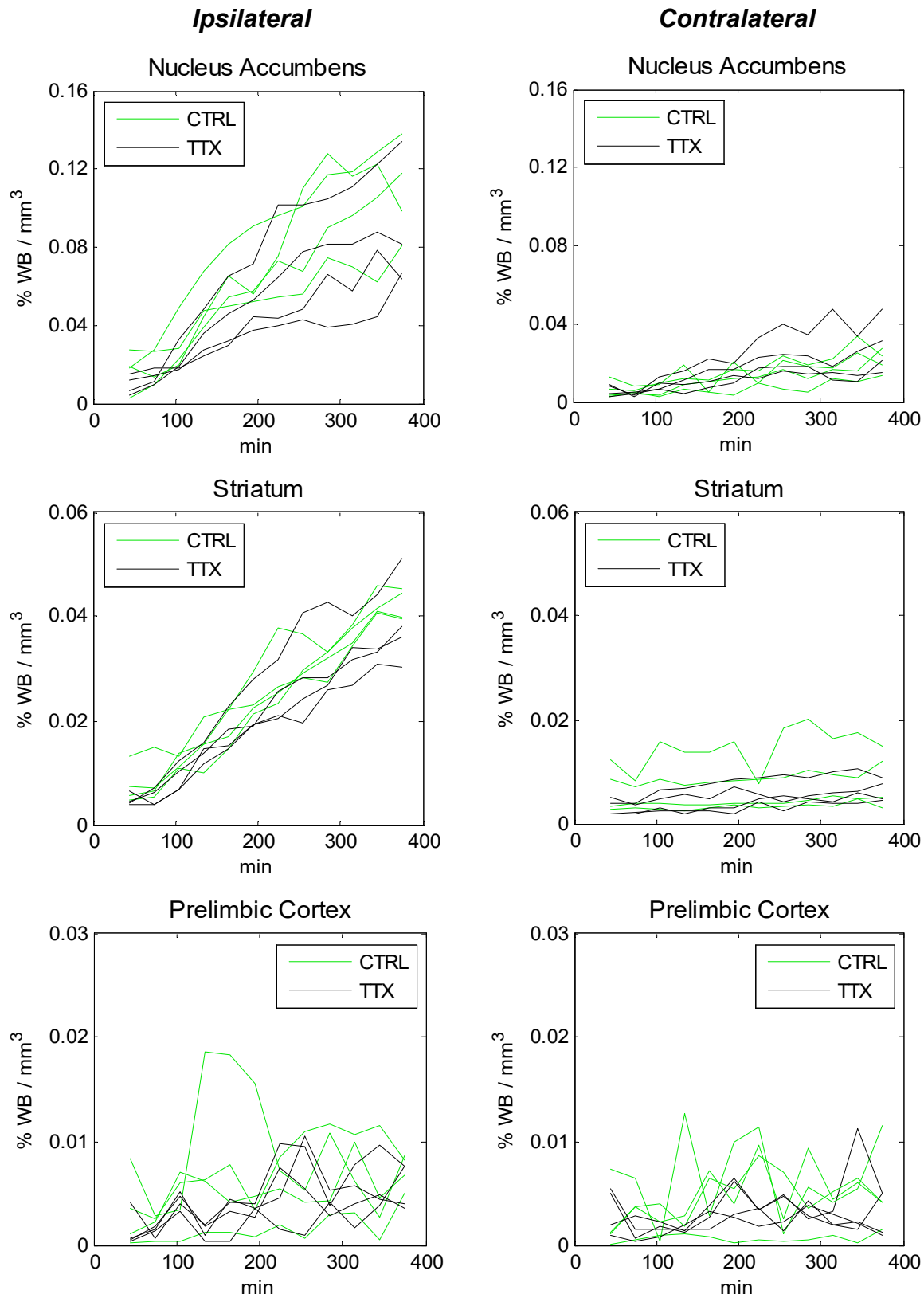


**Figure 23.6.** <sup>52</sup>Mn transport to the main output regions of the VTA - TTX group

The gradual changes in the concentration observed in the TTX group were very similar to the changes in the corresponding regions of the control group. Each line represents data of one animal.

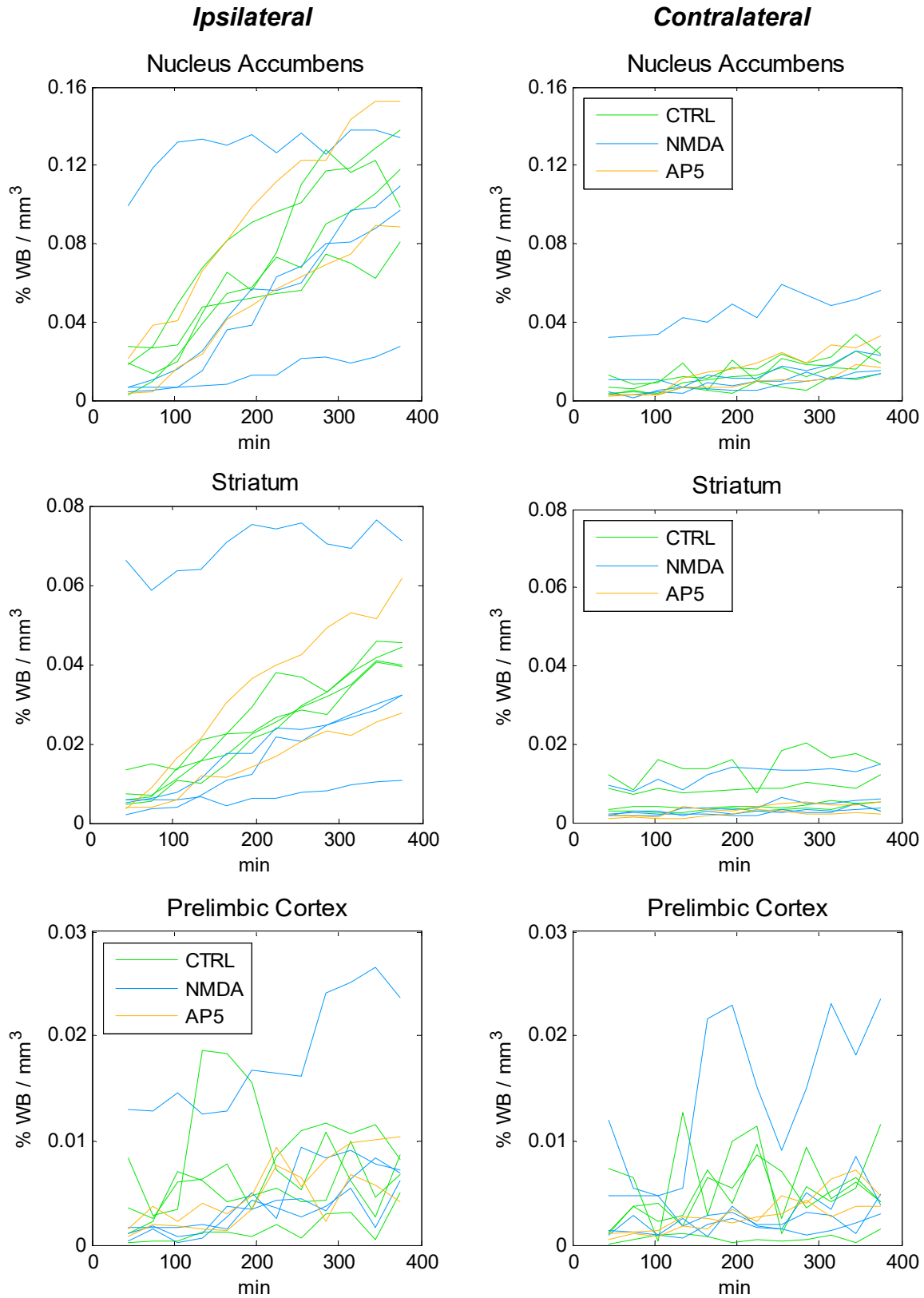


**Figure 23.7.**  $^{52}\text{Mn}$  transport to the main output regions of the VTA - *NMDA* and *AP5* groups  
 The changes in the concentration observed in the *AP5* group were similar to the changes in the corresponding regions of the control group. In the *NMDA* group, the data of two rats showed a different pattern in the ipsilateral STR and NAc. Each line represents data of one animal.

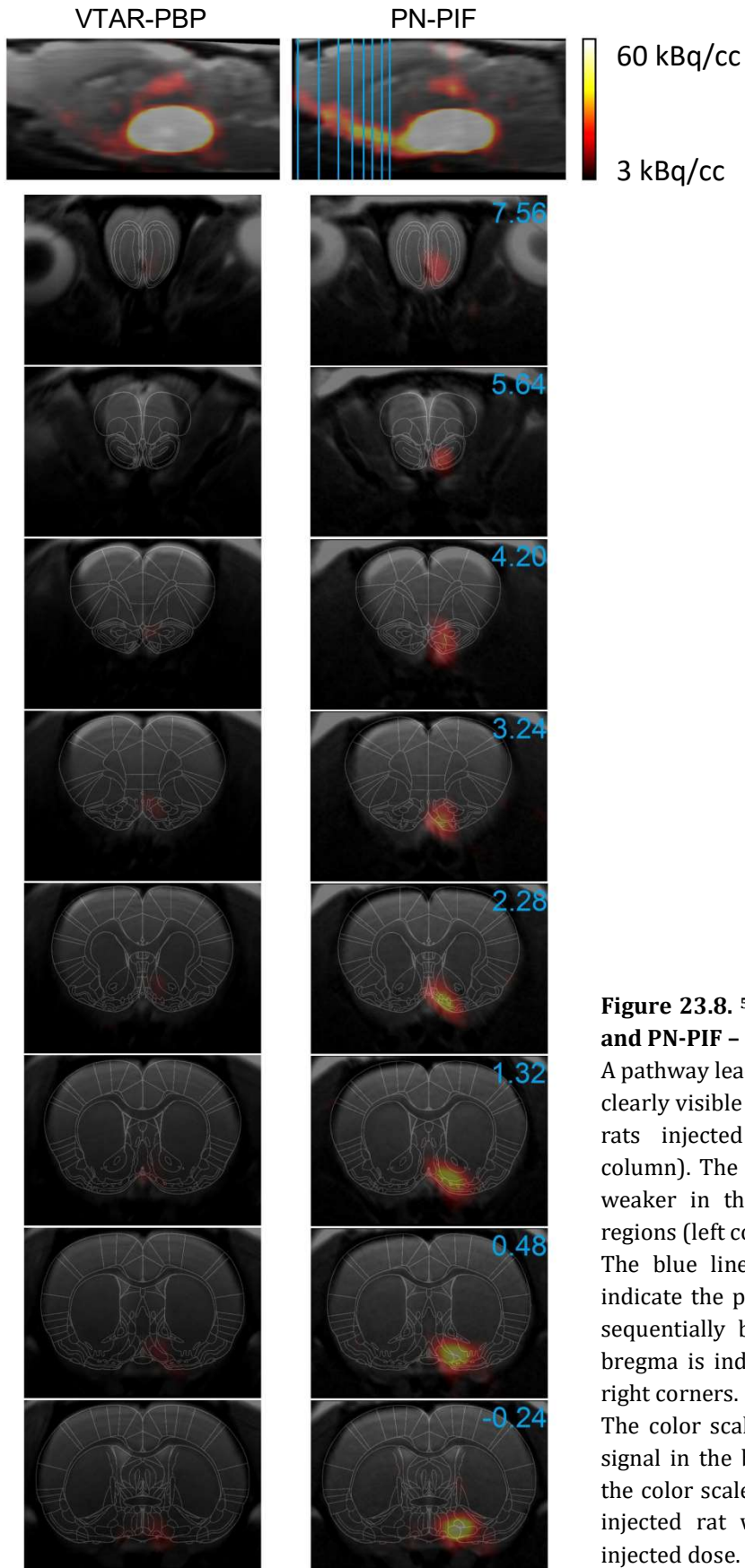


**Figure 23.8.  $^{52}\text{Mn}$  distribution in the VTAR-PBP and PN-PIF - injected rats**

A pathway leading from the midbrain to the OB was clearly visible in the first frame of the images of the rats injected into the PN-PIF regions (right column). The signal along this pathway was much weaker in the rats injected into the VTAR-PBP regions (left column).

The blue lines in the sagittal image at the top indicate the position of the coronal images shown sequentially below. The exact distance from the bregma is indicated by the numbers in the upper right corners.

The color scale was adjusted to visualize the PET signal in the brain of the PN-PIF-injected rat, and the color scale of the PET image of the VTAR-PBP-injected rat was adapted to that based on the injected dose.

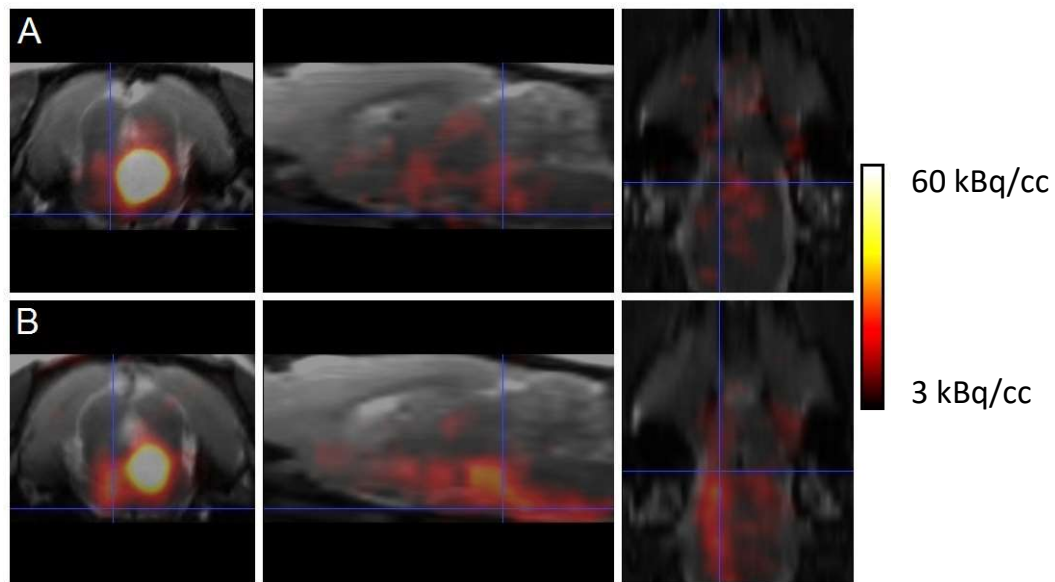


**Figure 23.9.**  $^{52}\text{Mn}$  distribution in the VTAR-PBP and RN - injected rats

The last frames of the PET images are shown. Even at this stage, there was not much signal in the contralateral MO in the rats from the *VTAR-PBP* group (A). In contrast, a pathway along the contralateral MO was clearly delineated in the *RN* group (B). This pathway was potentially the rubrospinal tract. In A, the same image as in Figure 23.8 is shown and the color scale of the image in B was adapted to it, based on the injected doses.

According to the overlaid rat brain atlas, this neuronal pathway could be the rubrospinal tract (Figure 23.9).

In order to quantitatively compare the  $^{52}\text{Mn}$  distribution between the groups based on the injection location, the mean concentrations of each group were computed. This was done not only for the three VOIs analyzed before (Figure 23.10), but also for six additional regions in which the tracer was visually localized in the PET images (Figure 23.11 and Figure 23.12). Some interesting features have been observed.

Firstly, a common characteristic observed across all the VOIs located rostrally to the VTA was that the mean  $^{52}\text{Mn}$  concentration of the *PN-PIF* group was always the highest among the three groups, and this was true for the ipsilateral as well as for the contralateral sides. Interestingly, this difference between the *PN-PIF* group and the other two groups was

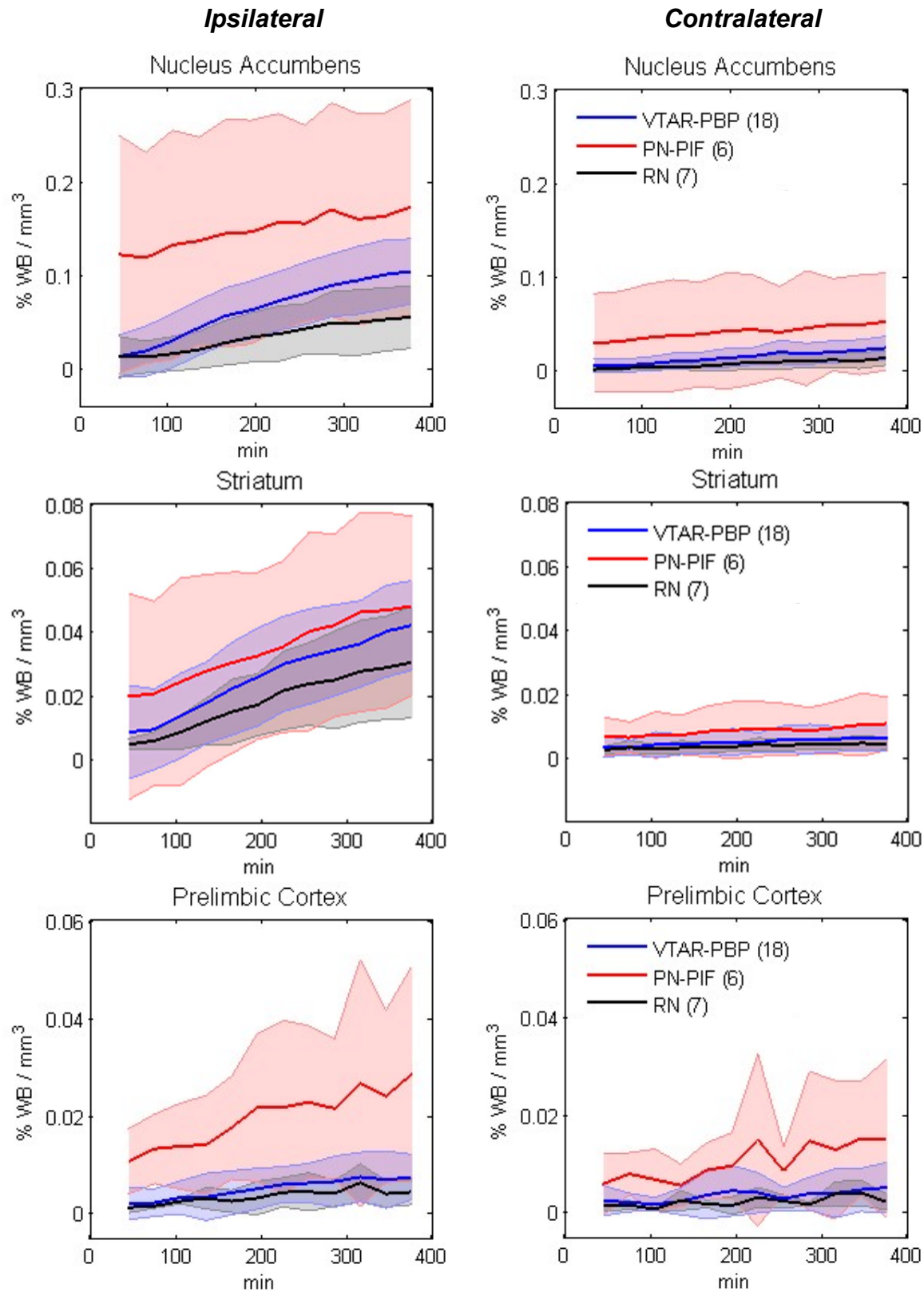


**Figure 23.10.** <sup>52</sup>Mn transport to the VTA output regions in the rats grouped based on the injection location - part 1

The thick lines represent the group means and the shaded areas are the standard deviations of the means.

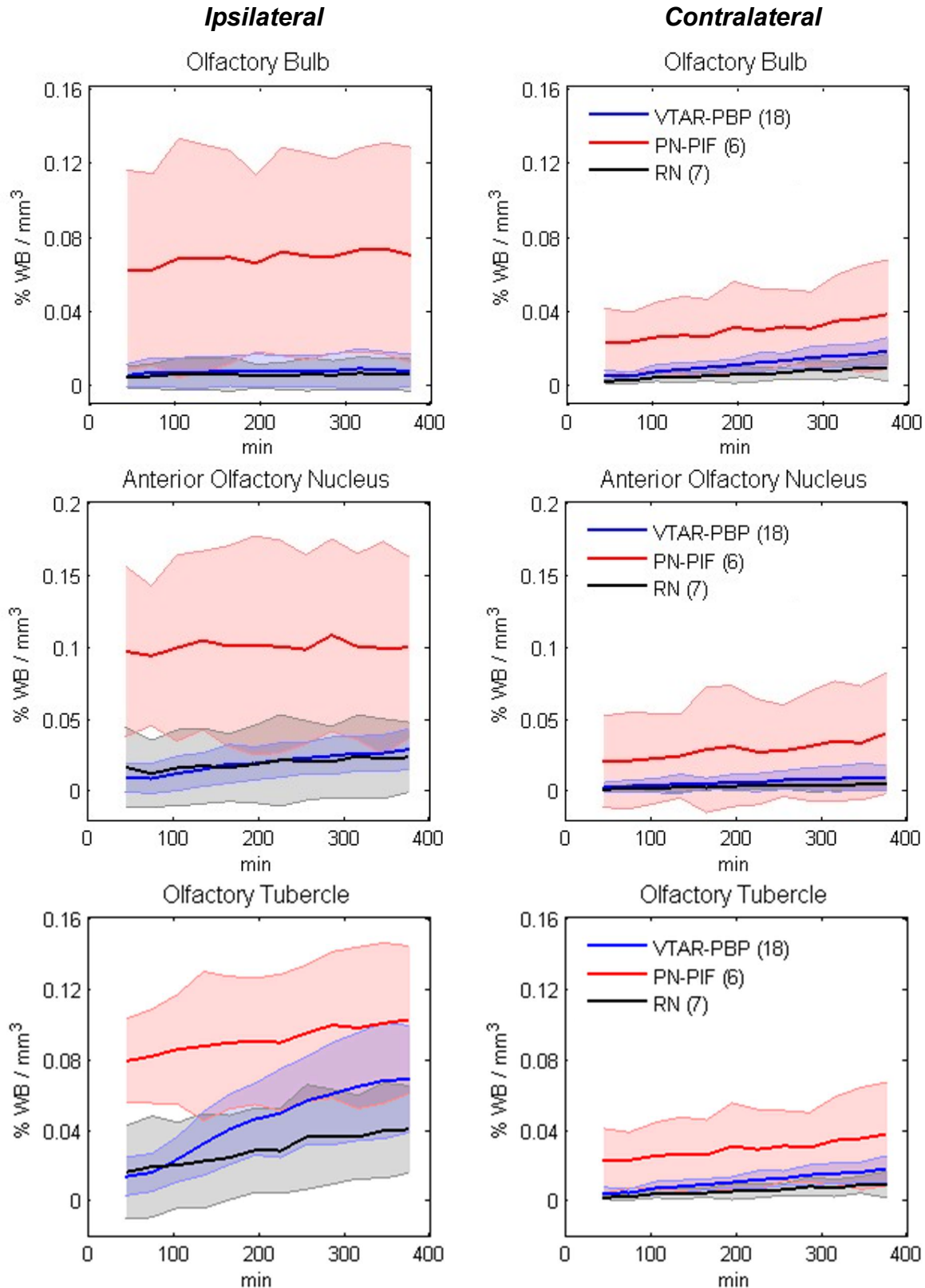


**Figure 23.11.** <sup>52</sup>Mn transport to the VTA output regions in the rats grouped based on the injection location - part 2

The thick lines represent the group means and the shaded areas are the standard deviations of the means.

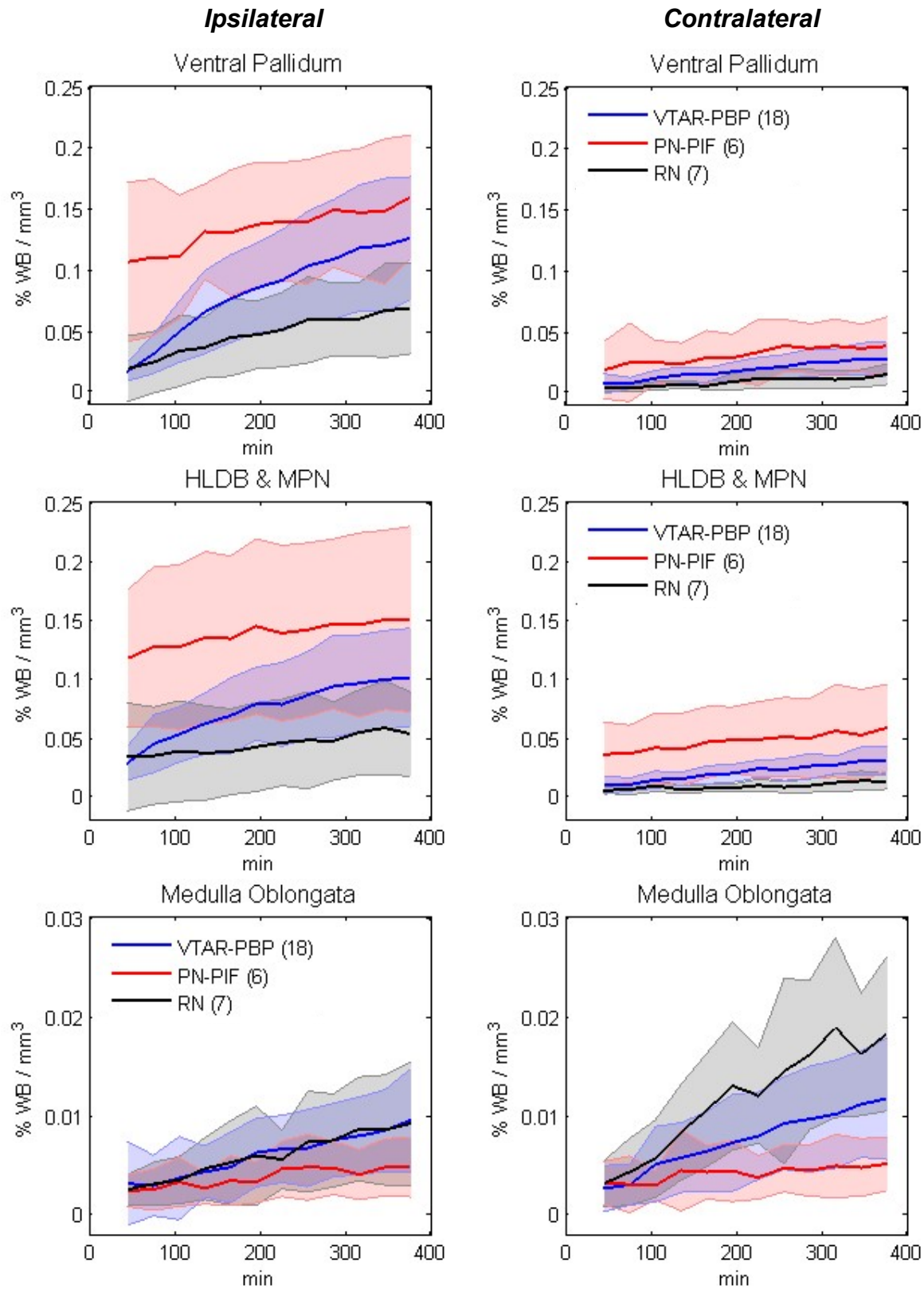


**Figure 23.12. <sup>52</sup>Mn transport to the VTA output regions in the rats grouped based on the injection location – part 3**

The thick lines represent the group means and the shaded areas are the standard deviations of the means.

present already in the first frame of the PET image, which was in line with the previously described qualitative evaluation of the PET images.

In addition, the high  $^{52}\text{Mn}$  concentration observed in the beginning in virtually all the VOIs of the *PN-PIF* group, only slightly fluctuated over time (especially in the ipsilateral AON and OB). In contrast, a gradual increase in the tracer amount was observed in the *VTAR-PBP* and *RN* groups. This rise was more rapid in the *VTAR-PBP* group than in the *RN* group in the ipsilateral ventral structures: NAc, OT, VP, and HLDB & MPN.

Finally, the only region with a lower content of  $^{52}\text{Mn}$  in the *PN-PIF* group than in the other two groups was the MO. In fact, the contralateral MO was also the only brain area characterized by a faster accumulation of the tracer in the *RN* group than in the *VTAR-PBP* group. This was a reflection of the  $^{52}\text{Mn}$  distribution visually identified in the PET images.

## 23.2 Dosimetry

The data from the first frames of the PET images of three *CTRL* rats injected into the *VTAR-PBP* were used to estimate the absorbed dose of the injected region, as well as of the entire brain. The first step of the analysis relied on modelling the relationship between the logarithmic values of the absorbed dose ( $\ln(D)$ ) and the mass of the brain tissue ( $\ln(m)$ ). The used 3rd order polynomial function provided a very good fit ( $R^2 = 0.998$ ) (Figure 23.13). The obtained equation was subsequently used to calculate the  $D_s$  for the masses of the two VOIs.

Under the assumption of no biological clearance of the PET tracer, the average dose rate at the injection time was 0.141 Gy/h for the *VTAR-PBP* and 0.001 Gy/h for the whole brain. Using these dose rates, the doses accumulated over different time periods could be

computed. Hence, the doses accumulated over 24 h would be 3.17 Gy for the VTAR-PBP and 0.03 Gy for the whole brain, while the respective doses accumulated over 4 weeks would be 26.40 Gy and 0.20 Gy. The doses for the injected region were much larger than those for the entire brain because of the much higher average concentration of the tracer.

Based on the above estimates, the doses absorbed over 4 weeks by the VTAR-PBP region in the rats in Study 3 injected with 170 kBq (Experiment 1) and 20 kBq (Experiment 3) of  $^{52}\text{Mn}$  could be also computed. They were 144.6 Gy and 17.1 Gy, respectively. Similarly, the absorbed doses accumulated over 90 min in the rats treated with 28 kBq or 149 kBq (Study 3, Experiment 2) could be compared. Those were 0.2 Gy and 1.0 Gy, respectively.

$$\ln(D) = -0.0047 * \ln(m)^3 + 0.0074 * \ln(m)^2 - 0.7620 * \ln(m) + 9.32$$

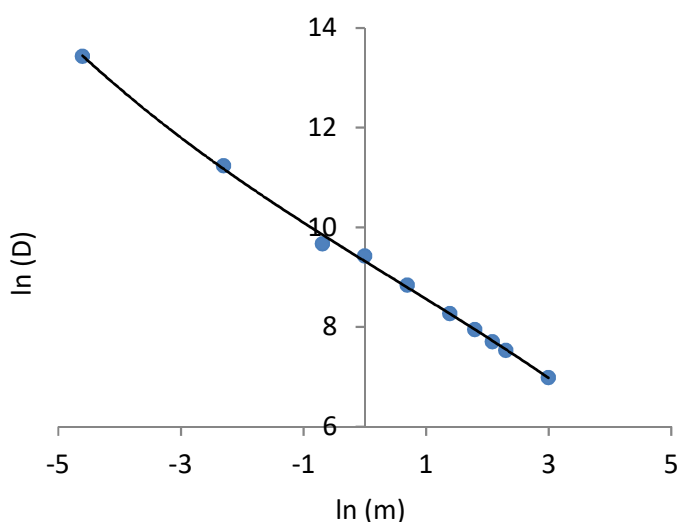


**Figure 23.13. First step of the dosimetry estimation**

The relationship between the  $\ln(D)$  and the  $\ln(m)$  for the mass range from 0.01 g to 20 g was modeled with a third order polynomial function.

## 24 PET with Online Recording of Blood Radioactivity

### 24.1 Evaluation of the experimental protocol

The sensitivity of the BS was exceptionally high,  $23 \pm 1 \%$  (mean  $\pm$  sd,  $n = 9$ ). The energy resolution was 19 % for the 511 keV photo peak with a timing resolution of 11.2 ns.

The physiological parameters of the animals were quite stable over the time of the experiment. A drop in the body temperature was observed in two rats when the flow in the shunt was initiated, but that was by only  $\sim 1^\circ\text{C}$  (Figure 24.1). The estimated flow rate in the shunt was  $1.2 \pm 0.1$  mL/min and in the MS catheter  $1.2 \pm 0.4$  mL/min.

The *wb* TACs recorded by MS, by the BS and derived from the PET images were, overall, in a

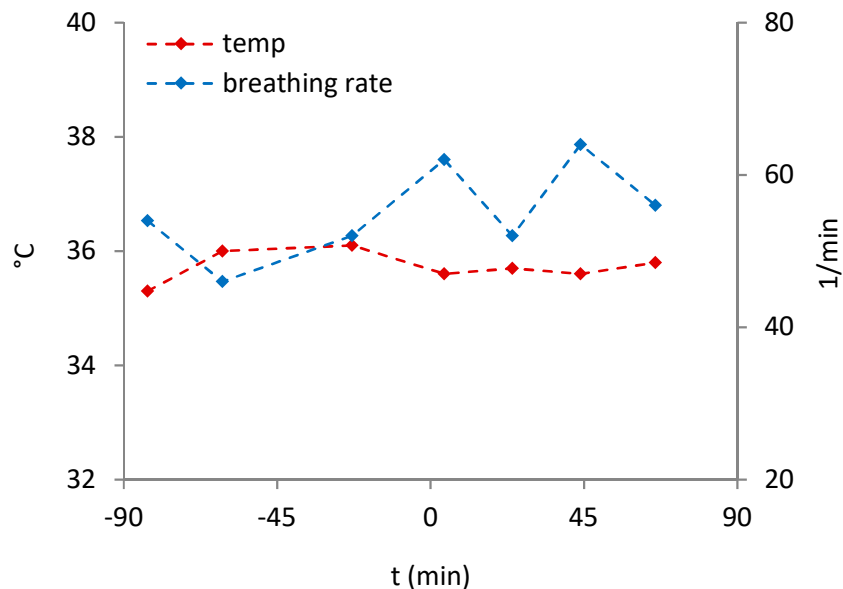


**Figure 24.1. Physiological parameters of a rat during the PET experiment with the BS measurement**

The body temperature and the breathing rate were monitored from the moment of anaesthetizing the animal until the end of the experiment. “0 min” indicates the time point of the tracer injection.

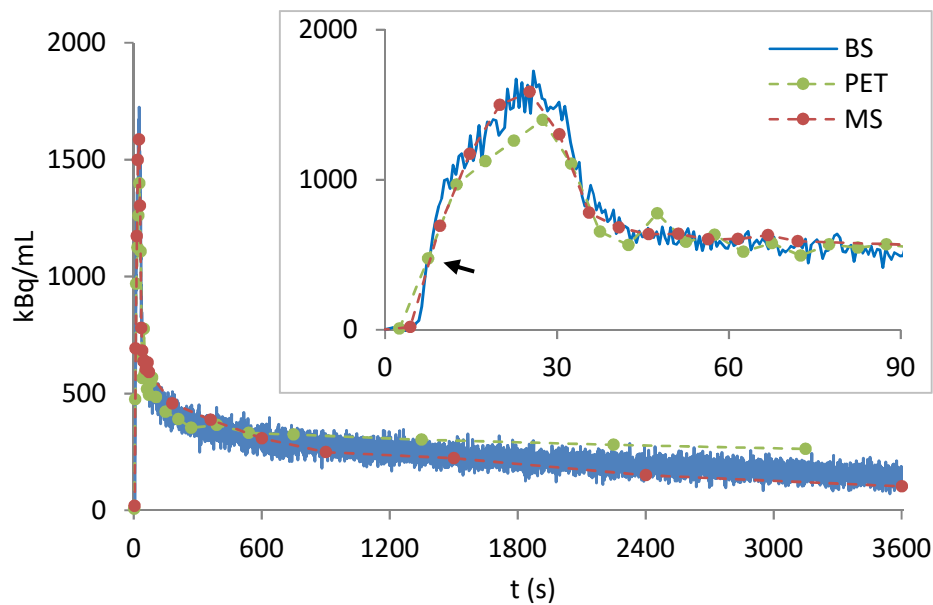


**Figure 24.2. Wb TACs recorded by the BS, MS, and PET in one rat**

The insert shows the first 90 s of the measurement. In order to correct for the delay, the MS- and BS-TACs were shifted on the time axis to match the first-above-baseline data point of the PET TAC (arrow).

good agreement (Figure 24.2). However, the PET-TAC was always the lowest during the first 30 s of the experiment. From approximately 10 min time point, it rose above the other two TACs. Additionally, the BS TAC tended to overestimate the MS TAC in the second half of the experiment.

This comparison was made after the MS and the BS TACs had been shifted on the time axis to match the first-above-baseline data point of the PET TAC. In this way, the delay in the shunt could be estimated. It was  $1.7 \pm 0.6$  s (mean  $\pm$  sd,  $n = 5$ ).

The dispersion factor,  $\tau$ , estimated in the step function measurements, was  $1.94 \pm 0.38$  (mean  $\pm$  sd,  $n = 4$ ). The mean value was used to model the IRF of the shunt system, which was required for the dispersion correction. However, in order to apply the correction by deconvolving the TACs by the IRF, the TACs had to be fitted in the first place. This

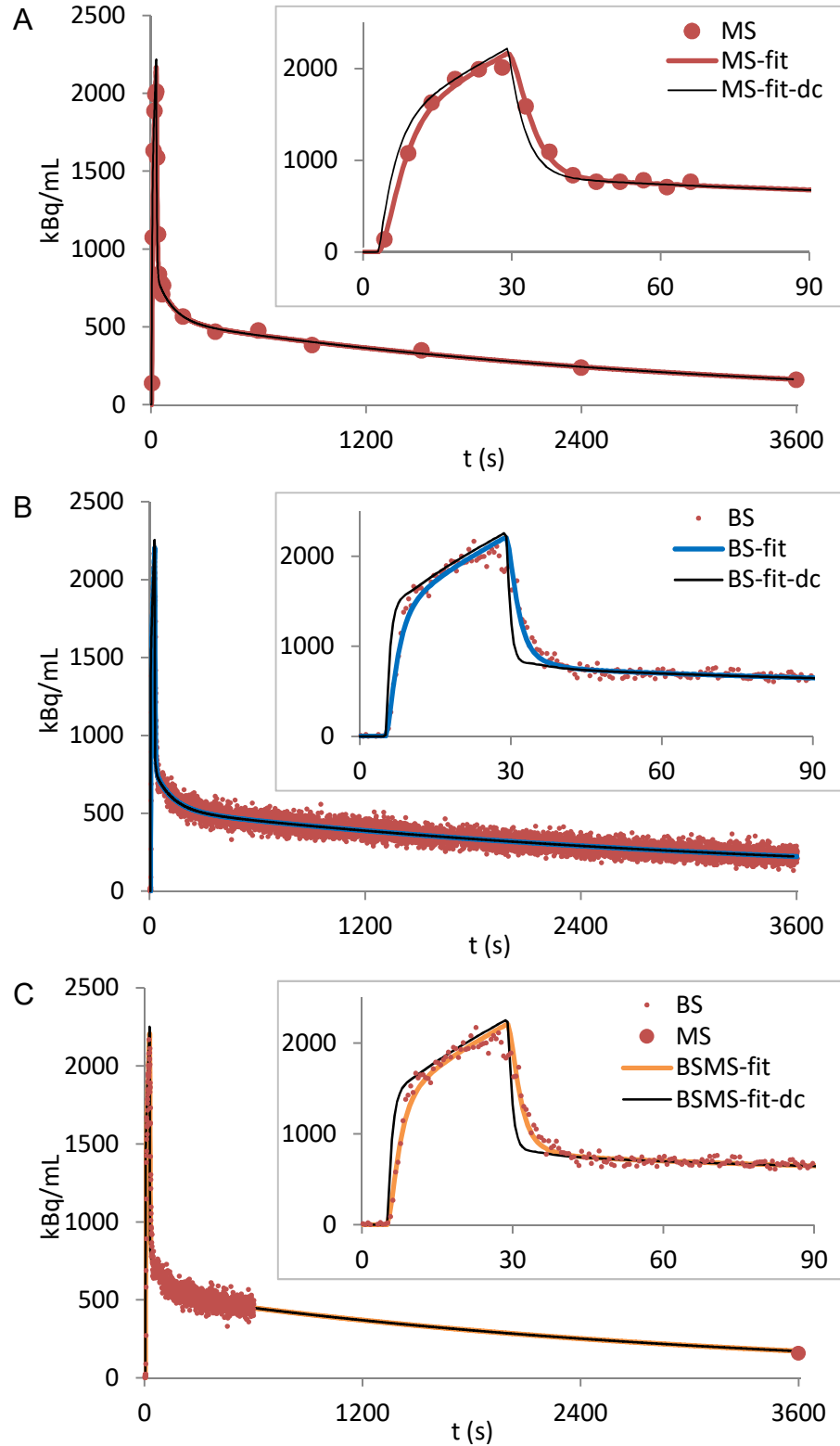


**Figure 24.3. The TACs fitting procedure and the dispersion correction**

**A.** An exemplar *wb* MS TAC, a fit to that data (MS-fit) and the dispersion-corrected fit (MS-fit-dc). **B.** The *wb* BS TAC from the same rat, a fit to that data (BS-fit) and the dispersion-corrected fit (BS-fit-dc). **C.** The combination of the BS recording with 1 manual sample, a fit to that data and the dispersion-corrected fit (BSMS-fit-dc). The inserts show the first 90 s of the measurement.

procedure allowed removing the noise from the data and it performed very well based on the visual inspection (Figure 24.3).

## 24.2 Impact of the technique of obtaining the AIF on 2TCM-KPs

The AIF includes the *wb* TAC as well as the *p* TAC of the PET tracer. In this study, the AIF was obtained in nine different ways from the same measurements. The effect of the technique used for deriving the AIF on the KPs estimated with the 2TCM is shown in Table 24.1 and Figure 24.4.

The true *wb* and *p* data, manually collected during the experiment, subsequently fitted and corrected for dispersion (MN-fit-dc) were used as the reference approach. The  $K_1$ ,  $k_2$ , and  $k_3$  estimated using this AIF were:  $0.17 \pm 0.04$  mL/min/ccm (mean  $\pm$  sd,  $n = 5$ ),  $0.34 \pm 0.08$  1/min, and  $0.048 \pm 0.009$  1/min, respectively. Comparing these values to the KPs estimated with the MS-fit approach, allows an estimation of the effect of the dispersion correction. When the correction was not applied, the KPs were almost 2-5 % overestimated, with the  $k_2$  being most affected.

**Table 24.1. KPs of the 2TCM**

estimated using the AIF obtained in nine different ways. The AIF obtained from the fitted and dispersion-corrected manual samples (MS-fit-dc) was considered the reference approach. The mean  $\pm$  sd of 5 rats are shown for  $K_1$ ,  $k_2$  and  $k_3$ . For each parameter, the % difference from the reference is shown in the neighboring column. Please refer to the text for explanation of the abbreviations.

Method of obtaining the AIF	$K_1$ (mL/min/ccm)	% diff. from ref.	$k_2$ (1/min)	% diff. from ref.	$k_3$ (1/min)	% diff. from ref.
MS	$0.19 \pm 0.04$	7.1	$0.37 \pm 0.09$	8.0	$0.048 \pm 0.009$	0.5
MS-fit	$0.18 \pm 0.04$	2.7	$0.36 \pm 0.08$	4.5	$0.049 \pm 0.009$	2.1
MS-fit-dc (ref.)	$0.17 \pm 0.04$	0.0	$0.34 \pm 0.08$	0.0	$0.048 \pm 0.009$	0.0
MS-fit-dc-calc	$0.18 \pm 0.03$	1.6	$0.35 \pm 0.07$	2.0	$0.052 \pm 0.010$	8.3
BS-calc	$0.19 \pm 0.03$	8.9	$0.35 \pm 0.06$	2.3	$0.041 \pm 0.010$	-13.4
BS-fit-calc	$0.19 \pm 0.03$	8.4	$0.34 \pm 0.05$	0.6	$0.042 \pm 0.007$	-12.4
BS-fit-dc-calc	$0.18 \pm 0.03$	5.4	$0.32 \pm 0.04$	-5.3	$0.039 \pm 0.008$	-18.9
ID-calc	$0.22 \pm 0.06$	24.1	$0.40 \pm 0.09$	16.7	$0.025 \pm 0.006$	-47.6
BSMS-fit-dc-calc	$0.18 \pm 0.03$	5.4	$0.33 \pm 0.05$	-4.8	$0.046 \pm 0.008$	-3.3

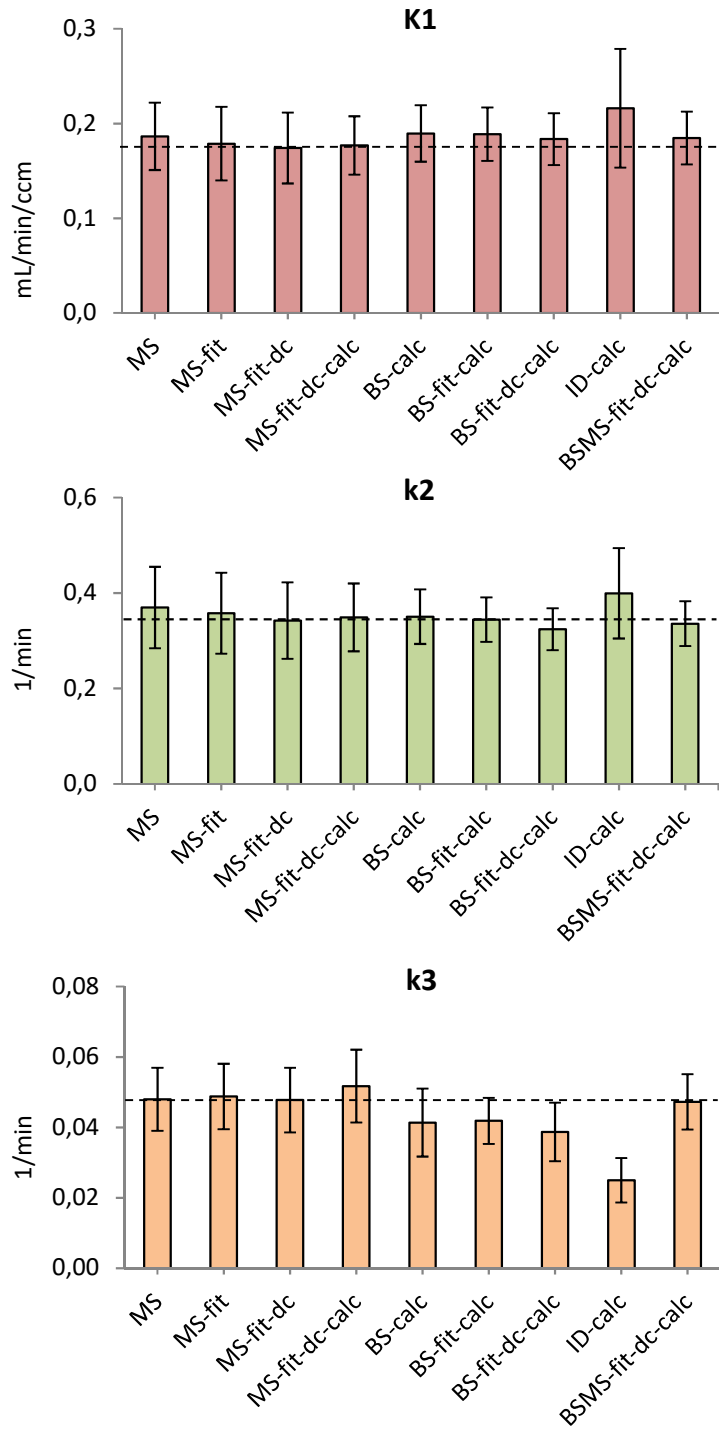


**Figure 24.4. KPs of the 2TCM**

The  $K_1$ ,  $k_2$ , and  $k_3$  were estimated using the AIF obtained in nine different ways. The AIF from the fitted and dispersion-corrected manual samples (MS-fit-dc) was the reference approach (dashed line). Using the AIF derived from the PET images (ID-calc) resulted in the highest deviations from the reference values. The BS-based approaches led to a reduced  $k_3$ . This could be recovered by combining the BS data with 1 manual sample (BSMS-fit-dc-calc).

When these overestimated values are compared to the KPs obtained with the original  $wb$  and  $p$  data, before the fitting step (MS), the impact of the fitting procedure can be assessed. The procedure led to the change in the  $K_1$  from  $0.19 \pm 0.04$  to  $0.18 \pm 0.04$  mL/ min/ccm, in the  $k_2$  from  $0.37 \pm 0.09$  to  $0.36 \pm 0.08$  1/min, and in the  $k_3$  from  $0.048 \pm 0.009$  to  $0.049 \pm 0.009$  1/min. Therefore, the effect was only minimal.

In the next step, the impact of using the  $\frac{p}{wb}$  ratio to extract the  $p$  values from the  $wb$  recording was assessed. Applying this approach to the MS data (MS-fit-dc-calc), resulted in only a small effect on the  $K_1$  and  $k_2$  values (they were overestimated by only approximately 2 %), but there was above 8 % overestimation of the  $k_3$ . Since using the  $\frac{p}{wb}$  ratio is unavoidable for deriving the AIF from the BS as well as from PET images, a similar effect is expected when these approaches are used.

In fact, when the BS-based techniques were applied the KPs were quite different from the references. When the original, *i.e.* not fitted and not corrected for the dispersion, BS data (BS-calc) were used, the  $K_1$  and  $k_2$  were overestimated by almost 9 % and more than 2 %, respectively. As discussed above, approximately 2 % of these errors could be attributed to the necessity of using the  $\frac{p}{wb}$  ratio. However, even taking this into account, the  $K_1$  would be still overestimated by almost 7 %. The deviation in the  $k_3$  was even higher; this KP was underestimated by more than 13 %.

When the fitted BS data (BS-fit-calc) were used to obtain the AIF, the differences in all three KPs were reduced by 0.5-2 %. This small change also indicates that the fitting procedure itself did not have a strong effect, similarly to the effect on the MS data.

Next, applying the dispersion correction to the fitted BS TAC (BS-fit-dc-calc) led to a further reduction in the deviation of the  $K_1$  from the reference value. It was now overestimated by slightly more than 5 %, which still incorporated 2 % resulting from using the  $\frac{p}{wb}$  ratio. However, the  $k_2$ , and especially the  $k_3$ , deviated more. They were underestimated by 5 and almost 19 %, respectively. This could be corrected for by combining the first 10 min of the BS recording with 1 manual sample collected at 60 min. When this combination was fitted and dispersion-corrected (BSMS-fit-dc-calc), the estimated  $K_1$  was  $0.18 \pm 0.03$  mL/min/ccm, the  $k_2$  was  $0.33 \pm 0.05$  1/min, and the  $k_3$  was  $0.046 \pm 0.008$  1/min. Therefore, the deviations from the respective reference values were within 5 % range.

For a comparison, the KPs were also estimated with the AIF derived from the PET images (ID-calc). This approach resulted in very high differences of the obtained values from the references. The  $K_1$  and  $k_2$  were overestimated by 24 and 17 %, respectively, while the  $k_3$  was almost 48 % underestimated.

# **DISCUSSION**

## 25 Mn<sup>2+</sup> for Tracing Neuronal Pathways with MEMRI vs Toxicity of the Metal

The first study conducted within the present work aimed to assess whether Mn<sup>2+</sup> doses required for MEMRI are safe for an intracerebral administration in rats. The results showed that 45 nmol of Mn<sup>2+</sup> applied directly into the VTA caused a dopaminergic lesion 4 weeks after the injection (Study 1). Furthermore, the 50 nmol dose administered into the STR affected GABA<sub>A</sub> receptors in the FC which was manifested as a reduction in the BPnd of [<sup>11</sup>C]flumazenil 2 days post-injection (Study 4).

The STR receives neuronal projections from most of the cortical areas, including the prefrontal and limbic cortices [213], and one day after the intrastrital injections of Mn<sup>2+</sup>, an increased signal intensity was observed in the FC in the T1W MR images. Therefore, the Mn ions were most probably transported from the STR to the FC where they interacted with the GABA<sub>A</sub> receptors. Although this would reflect the retrograde, rather than the most commonly observed with MEMRI anterograde transport, this direction of the intracellular movement of the Mn<sup>2+</sup> is also possible [214].

Interactions of Mn with the GABAergic system have been previously reported. Specifically, an increased accumulation of Mn in several brain regions, including the STR, GP, and HIP, in the iron-deficient rats was significantly correlated with reduced GABA levels [215]. However, an opposite effect, *i.e.* an increased GABA concentration, has been found in the CER of the rats exposed to a daily Mn dose of 20 mg/kg administered over 30 days [216]. Interestingly, in non-human primate studies, there was no impact of a 5-26 months long s.c.

treatment with manganese (IV) oxide ( $\text{MnO}_2$ ) on GABA, neither on glutamic acid decarboxylase (GAD), which converts glutamate to GABA [136, 143]. Therefore, the available literature is not fully consistent, although the observed discrepancies could be potentially attributed to the interspecies differences, as well as to the different experimental protocols used.

In Study 4, the BPnd of [ $^{11}\text{C}$ ]flumazenil was not significantly changed 30 days after the  $\text{Mn}^{2+}$  injection. Therefore, it is possible that following a single application of the metal in rats, the impact on the  $\text{GABA}_A$  receptors is only transient. This transient reduction in the availability of the receptors could potentially reflect an increased level of the endogenous GABA. In fact, it has been shown that Mn may increase the GABA concentration by interacting with GABA transporter (GAT) [217]. Nevertheless, this interpretation should be treated carefully, since GABA levels were not directly measured in Study 4.

Most importantly, regardless of the molecular mechanism underlying the observed effect of  $\text{Mn}^{2+}$  on the  $\text{GABA}_A$  receptors, this effect is highly undesired if  $\text{Mn}^{2+}$  shall be used as a tool for measuring neuronal activity. GABA is the main inhibitory neurotransmitter of the CNS and any change in its level may induce a direct impact on the neuronal activity.

In contrast to the results of [ $^{11}\text{C}$ ]flumazenil PET, neither short- nor long-term impact of  $\text{Mn}^{2+}$  on the BPnd of [ $^{11}\text{C}$ ]methylphenidate was observed in Study 4. Thus, a single intrastriatal administration of 50 nmol of the metal does not affect DAT in the STR. This is in contrast to the effects observed following a prolonged Mn exposure. For instance, a dose-dependent reduction in the striatal binding potential of [ $^{11}\text{C}$ ]nomifensine, which is another marker of the presynaptic DA reuptake, was observed in monkeys following a 16 months treatment with  $\text{MnO}_2$  [137]. Additionally, a transient decrease in the binding potential of

[<sup>11</sup>C]raclopride, a D<sub>2</sub> receptor antagonist, was also reported in that study. Furthermore, decreased levels of DA and its metabolite, 3,4-dihydroxyphenylacetic acid (DOPAC), have been found in the GP following a 5 months exposure to the total of 8 g of MnO<sub>2</sub> in monkeys [136], and an effect on the D1 receptors has been also reported [143].

In a more recent study, in which lower doses of Mn (*i.e.* total of 0.15-0.20 g) were applied, there was no effect of the metal on DAT and on D<sub>2</sub> receptors despite the prolonged exposure time, although the amphetamine-induced DA release was affected [218]. Hence, the Mn effect on the dopaminergic system most probably depends on the total accumulated dose [133]. While the 50 nmol of Mn<sup>2+</sup> used in Study 4 led to a reduction in the availability of the cortical GABA<sub>A</sub> receptors, it was apparently too low to exert a significant effect on the striatal DAT.

It is important to recognize that the 45-50 nmol doses used in Studies 1 and 4, are a reasonable representation of the doses commonly used in MEMRI investigations focusing on tracing neuronal pathways. In the studies of this type conducted over the recent years, between 1 and 400 nmol have been applied in rodents [125, 131, 146, 171, 219], birds [164], and monkeys [126, 166, 220]. However, the toxicity aspect was not always evaluated.

Due to the differences between the species and the neuronal systems under investigation, as well as between the MRI scanners used in different studies, it is not easy to define an exact dose of Mn<sup>2+</sup> which is sufficient for MEMRI and at the same time does not have a pharmacological or toxic effect. In rats, it has been shown that a direct injection of 40 nmol of Mn<sup>2+</sup> into the VTA significantly reduced the number of “normal-appearing neurons”. The 20 nmol dose also reduced this number, although the difference from the controls did not reach statistical significance [146].

However, in another study, performed in mice, even a lower dose led to functional disturbances in the neuronal activity. Specifically, 4 h after an intravitreal injection of 12.5 nmol of  $Mn^{2+}$ , reduced visual evoked potentials were recorded in the visual pathway. Although this effect was not present anymore at 24 h post-injection, the applied dose was anyway not detectable by the 11.7 T MR scanner [131], demonstrating that the potentially useful dose of  $Mn^{2+}$  was beyond the sensitivity of the MRI system.

Nevertheless, a detection of even lower doses of  $Mn^{2+}$  has been reported by other investigators. In monkeys, an 8 nmol dose was sufficient for MRI and did not cause a neuronal death. However, it resulted in astrogliosis in the surrounding tissue [147]. It is known that astrogliosis significantly affects neuronal activity and may even induce epileptic seizures [221]. Therefore, the 8 nmol dose would still be too high for functional neuroimaging with MEMRI. Moreover, the toxicity of this dose was assessed in the cortex, while other brain regions, particularly the basal ganglia, are more vulnerable to Mn.

Still lower doses of the contrast agent have been also used. Specifically, 2 and 3 nmol of  $Mn^{2+}$  were applied for tracing neuronal projections from the NAc to the VP [125] and from the Hb to the VTA [132]. However, neither the direct neurotoxicity nor the possible effect on the glial cells was assessed. Additionally, in all the mentioned studies utilizing the  $Mn^{2+}$  doses below 10 nmol, the MRI was carried out directly after the tracer administration. If an experimental protocol requires an additional time after the injection, the low amount of the administered  $Mn^{2+}$  may be partially washed out by the time of scanning.

In Study 1, 5 nmol of  $MnCl_2$  was administered in a bicine solution. Since the formed Mn-bicine is a low affinity chelate, 10 % of the molecules (0.5 nmol) are present as free ions [150]. These free Mn ions could have induced a degeneration of the dopaminergic neurons,

which did not happen. Therefore, the 0.5 nmol dose could be considered non-toxic, although several limitations of the study should be taken into account.

Firstly, only three rats per group were used which is not optimal for a proper toxicity evaluation. Secondly, potential short-term effects were not assessed, even though  $Mn^{2+}$  may affect the neuronal activity only temporarily [131]. Finally, only one method, the TH-staining, was used to investigate the possible side effects. Hence, some other aspects of the pharmacological action or toxicity of Mn, like impact on the  $GABA_A$  receptors or the mentioned astrogliosis, might have been undetected.

Nevertheless, even if 0.5 nmol was safe for a direct intracerebral application in rats, this dose was not sufficient for MRI at 24 h post-injection. The T1 values analyzed in the three main output regions of the VTA, where neuronal transport of  $Mn^{2+}$  was expected, were not changed as compared to the baseline values.

Thus, based on the results of Study 1, as well as on the available literature, it can be concluded that the  $Mn^{2+}$  doses required for MEMRI are either very close to the toxicity threshold of the metal, or even above it. This threshold lies possibly within the 1-5 nmol range, however, if only a few nmol of  $Mn^{2+}$  are used, MRI needs to be performed directly after the injection. Consequently, in order to use  $Mn^{2+}$  concentrations which are further away from the toxicity threshold, or to allow more flexible experimental protocols, a more sensitive method would be highly desired for tracing neuronal pathways with  $Mn^{2+}$ .

## 26 $^{52}\text{Mn}$ PET as an Alternative Method for Tracing Neuronal Tracts

### 26.1 Dosage

PET is a much more sensitive technique than MRI. While at least nanomols of  $\text{Mn}^{2+}$  are required for MEMRI, picomols of  $^{52}\text{Mn}$  used in the present work were completely sufficient for PET. Hence, the dose of the metal could be reduced by three orders of magnitude. It is worth noting that the Mn concentrations of the injected solutions were even lower than the physiological concentration of the metal in different regions of the rat brain [222]. Therefore, the toxicity effects were not expected. Surprisingly, the results of Experiment 1 in Study 3, in which as little as 38.3 pmol of  $\text{Mn}^{2+}$  were present in the injected volume of the  $^{52}\text{Mn}$  solution, were contrary to this expectation.

Four weeks after the injections into the VTA or the STR, approximately half of the animals exhibited an increased ratio of the ipsilateral vs contralateral rotations in the rotameter test, which indicated an imbalance of the motor control system. A similar effect had been observed previously, but it was always induced by hundreds of nmol of  $\text{Mn}^{2+}$  [223-225]. In one another study, an 8 nmol dose, but of  $\text{Mn}^{3+}$ , led to a significant impairment of a spontaneous motor activity and a conditioned avoidance response 2 weeks after an intranigral injection in rats [226]. However, that dose was still more than 200 times higher than the dose applied in Experiment 1. Moreover, toxicity of  $\text{Mn}^{3+}$  results from the relatively high reduction potential of the ion which causes oxidation of DA [226]. This effect would be much weaker for  $\text{Mn}^{2+}$  based on its lower reduction potential.

Additionally to the behavioral effect, the TH-staining performed on the brain tissue sections also suggested that the dopaminergic system was affected. A reduced staining intensity indicated that the level of TH in the neurons within the injected VTA (or in the SN ipsilateral to the injected STR) was lower compared to the level in the respective contralateral regions. However, the staining was only reduced, and not completely absent, suggesting that the neurons did not degenerate, but only their functionality (TH expression) was affected. This speculative claim may be supported by the shape of the neurons observed in the microscopic images. While necrotic cells would be characterized by cytoplasmic shrinkage, vacuolization, or mineralization in case of an advanced process [227], the neurons appeared completely normal.

As discussed above, changes in the neuronal morphology have been observed following the treatment with 20-40 nmol of  $Mn^{2+}$  [146], while lower doses (8-20 nmol) have been associated with functional effects [131, 147]. However, investigations of the consequences of a direct intracerebral administration of  $Mn^{2+}$  at the dose level lower than 1 nmol have not been reported. Thus, a direct comparison of the outcomes of the present results is not possible.

Nevertheless, as mentioned above, the physiological doses of the metal in different areas of the rat brain range from 50 to 600 nmol per 1 g of tissue, which corresponds to the 50-600  $\mu M$  concentrations [222]. The 38.3 pmol dose used in Experiment 1 was administered in 1  $\mu L$  volume and thus, the concentration of the solution was 38.3  $\mu M$ . Therefore, it is rather unlikely that the toxicity effects observed in Experiment 1 resulted from the metal dose. The radioactivity dose of  $^{52}Mn$  seems to be a more probable explanation.

In fact, the described behavioral as well as histological adverse effects were completely absent in the group of rats treated with the decayed solution. Although only four animals were used in that group, a total of eighteen rats were injected into the VTA with the reduced radioactivity dose (~20 kBq) of  $^{52}\text{Mn}$  in Experiment 3. The rotameter test was performed at 3, 14, and 28 days post-injection and the ipsilateral/contralateral rotations ratio was not different from the control group at any of the time points, suggesting no impact on the motor control system. Similarly, no differences in the staining intensity between the right and left VTAs were found in any of the evaluated tissue sections.

Experiment 2 of Study 3 was carried out to investigate further consequences of using different radioactivity doses for a direct intracerebral injection. DNA damage is one of the best known effects of ionizing radiation on biological tissues [228] and hence, it was chosen to evaluate this aspect.

Following a single or double DNA strand break caused by the radiation, the histone protein H2AX at the damage site is phosphorylated on the 139<sup>th</sup> serine residue [229]. This is an important molecular signal for the initiation of the DNA repair processes. The  $\gamma\text{H2AX}$  staining, which was used for the evaluation, detects the locations where the specific reaction has taken place. Therefore, what is actually imaged with this technique is the activation of the DNA repair machinery [230].

It was found that 90 min after the injection of ~150 kBq of  $^{52}\text{Mn}$  into the VTA, the DNA repair processes had been initiated at numerous foci. The ratio of the cells with foci vs the total number of cells was approximately seven times higher as compared to the control group within the injected VTA. The fact that the result of the 30 kBq group was hardly distinguishable from the controls strongly suggests that the radioactivity dose played a

crucial role. Interestingly, the “cells with foci/cells total” ratio was also elevated in the contralateral VTA of the 150 kBq group. This could be due to the possible transport or diffusion of the tracer along the VTA decussation. Since the VTAs are situated close to the midline of the brain, 90 min might have been sufficient for the transport of the tracer along this short distance.

At the second investigated time point, *i.e.* 24 h post-injection, the results of the three experimental groups were more homogenous. The “cells with foci” fraction in the ipsilateral VTA of the 150 kBq group had dropped as compared to the first time point, although it still remained the highest among the three groups. Why this reduction had occurred is not completely clear.

Due to the relatively long half-life of  $^{52}\text{Mn}$  (5.6 days) and the low clearance rate of the metal from the brain (7-8 days to wash out half of the intranasally-administered dose from trigeminal ganglia and spinal trigeminal nucleus [231]), the radiation level at 24 h post-injection was not much lower than at the 90 min time point. Therefore, a similar level of induction of the DNA damage would be expected. A possible explanation would be an adaptation of the cells to the ionizing radiation [232]. Alternatively, the phosphorylation processes initiating the DNA repair, which are visualized with the  $\gamma\text{H2AX}$  staining, might have become saturated.

However, to better understand the effects of radiation, the radiation doses should be taken into consideration. This aspect was investigated with the dosimetry analysis in Study 5. The results showed that 90 min after the administration of 30 kBq of  $^{52}\text{Mn}$  into the VTAR-PBP, the accumulated dose in this region was 0.2 Gy and that it was five times higher following the injection of 150 kBq. Interestingly, while the former value falls within the range of “low”

radiation doses, 1 Gy is often considered the border value between the “low” and “high” doses [233].

It is well documented that the responses of neural and glial cells to the low and high radiation doses are very distinct. For instance, an acute exposure of the hippocampal cells to the irradiation of 1 Gy or higher induces oxidative/nitrosative stress, increases DNA damage, promotes cell cycle arrest, and reduces the cells differentiation [234, 235]. The inhibition of the neurogenesis in the hippocampus, observed following an irradiation with 2-10 Gy doses, depends on the microglial activation which induces neuroinflammation [235]. Other cellular impairments, collectively referred to as the “radiation-induced injury”, include lipids peroxidation and microvascular damage and they can be induced by 2-6 Gy doses [236, 237]. Moreover, when a dose as high as 10 Gy was applied to different populations of the CNS cells in culture, an increased apoptosis and decreased cell survival were observed [238]. Finally, all these cellular and molecular effects may be manifested also at the cognitive level [235, 239].

As mentioned above, very different reactions of neurons and glia have been reported following an exposure to the low radiation doses, defined usually as  $< 1.0$  Gy, although less data are available regarding this dose range [233]. Specifically, it has been shown that 0.1 Gy may not affect gene expression, neither behavioral capabilities associated with learning and memory [240]. Furthermore, doses in the range of 0.05 to 0.5 Gy have been found to suppress the release of pro-inflammatory cytokines and reactive oxygen species leading to the attenuation of the inflammatory responses [241]. Finally, radioresistance and adaptation may occur after a treatment with doses below 0.3 Gy [232].

In summary, despite the difference in the experimental protocols, species of the experimental animals, and the applied doses, the available literature strongly suggests a distinction between the effects of the low and high radiation doses on the CNS [233]. The results of the dosimetry analysis from Study 5 seem to match this pattern very well. However, one methodological aspect should be emphasized. Namely, in the vast majority of the reported studies a single, acute radiation dose was followed by a period without the irradiation, before the effects were tested. In contrast, due to the long half-life of  $^{52}\text{Mn}$ , the exposure of the VTA in the present work continued uninterrupted from the moment of the tracer injection until the moment of the effects evaluation.

On one hand, under this condition of a constant irradiation, the cells may potentially not have sufficient time to properly initiate and maintain the repair processes. On the other hand, the dose rate is significantly lower than in other studies which may make the performance of the molecular repairs easier. Since these two factors act in opposite directions, possibly, they may cancel each other out.

However, in one study, the effects of a chronic radiation exposure of human neural progenitor cells to a low dose rate, have been examined *in vitro*. The cumulative doses ranged from 0.031 to 0.496 Gy but the radiation was delivered continuously over 72 h. The lowest dose resulted in alterations in the inflammatory pathways, the 0.124 Gy dose affected the DNA repair and cell adhesion molecules, while the highest dose affected DNA synthesis, cell metabolism, and neural differentiation [242]. Therefore, some of the effects known from the exposure to doses higher than 1 Gy have been observed. This might have been related to the relatively high sensitivity of the progenitor cells, as compared to the

matured cells, to radiation, but the chronic character of the irradiation could have played a role as well.

Although the continuous exposure of the VTA to  $^{52}\text{Mn}$  resembles this situation, the dose rate following the injection of approximately 30 kBq in Study 5 was only 0.141 Gy/h, which is three times lower than the lowest dose rate used in the study referenced above (0.42 Gy/h) [242]. Moreover, the 0.141 Gy/h dose rate was slowly, but continuously, decreasing, due to the  $^{52}\text{Mn}$  decay. Additionally, the accumulated doses calculated based on this dose rate were actually overestimated because of the assumption of no biological clearance of  $^{52}\text{Mn}$ . In fact, as already mentioned before, the time required for the clearance of the half of the intranasally administered Mn dose from the trigeminal system was 7-8 days [231]. Therefore, although the computed cumulative doses in the VTAR-PBP were: 0.2 Gy 90 min after the injection of 28 kBq (Experiment 2) and 17.10 Gy 4 weeks after the injection with the 20 kBq dose (Experiment 3) in Study 3, the true values were certainly lower. Consequently, the applied doses might have been low enough for the VTA cells to fully deal with. This conclusion would be supported by no increase in the DNA damage, no reduction in the TH expression, and no effect on the rotation behavior found in these experiments.

The dose rate calculated for the entire brain VOI in Study 5 was extremely low (0.001 Gy/h), resulting in very low accumulated doses of 0.03 Gy and 0.20 Gy at 24 h and at 4 weeks after the application of 30 kBq of  $^{52}\text{Mn}$ , respectively. Thus, the radiation-induced injury would be also unexpected in other parts of the brain. Nevertheless, possible bystander effects, *i.e.* the effects experienced by the cells not directly exposed to the radiation but receiving molecular signals from the neighboring irradiated cells [232], should be further verified.

## 26.2 Advantages of the method and potential applications

Tracing neuronal pathways with MEMRI has already proven to be a useful technique in the field of neuroscience and neurology, but the sensitivity of MRI systems poses limitations for some studies. Also using the method in primates is more restricted than in rodents due to their greater vulnerability to the Mn toxicity [243]. Hence, the present work proposes  $^{25}\text{Mn}$  as an alternative approach and demonstrates for the first time that tracing neuronal tracts with PET is feasible.

Specifically, following a unilateral  $^{52}\text{Mn}$  injection into the VTA, the mesolimbic and mesostriatal pathways were clearly visible in the images obtained 24 h later (Experiments 1 and 3 in Study 3). Together with the mesocortical pathway, these are the main rostral projections of the dopaminergic midbrain [9]. Although the mesocortical tract was not directly recognizable in the images, the quantitative analysis revealed a higher concentration of  $^{52}\text{Mn}$  in the ipsilateral than in the contralateral PFC, indicating that the tracer had reached that region. Moreover, a significantly higher concentration of  $^{52}\text{Mn}$  was found also in the ipsilateral NAc, OT, STR and AMG, which receive direct neuronal input from the injected VTA, as compared to the respective contralateral areas. Only the CER, used as a control region, showed no difference in the tracer accumulation between the right and the left side.

Similarly, after the injections into the STR, the ipsilateral GP, THL and SN accumulated significantly greater amounts of  $^{52}\text{Mn}$  compared to the respective contralateral areas, confirming the transport to the expected target regions of the STR. Once again, only the concentrations in both the hemispheres of the CER did not differ. In summary, these results

indicate that, similarly to non-radioactive  $Mn^{2+}$ ,  $^{52}Mn$  can be taken up and transported by neurons.

Also the results of Study 5 showed that the  $^{52}Mn$  transport visualized in, and quantified based on, the PET images, is in accordance with the known rat brain anatomy. Particularly grouping the experimental animals based on the injected subnucleus of the VTA allowed identification of the expected directions of the neuronal transport. Specifically, it was observed that when the tracer was injected into the VTAR-PBP region, its concentration was gradually rising in the ipsilateral dorsal and ventral striatal areas, including the STR NAc, OT, VP, and HLDB & MPN. These regions are known to receive the neuronal projections from the main nucleus of the VTA, the PBP [41].

In contrast, the  $^{52}Mn$  concentration in these areas was lower in the RN group. In fact, it is well established that the main output of the red nucleus in rodents is the rubrospinal tract which projects caudally and on the contralateral side into the spinal cord [244]. Accordingly, the MO was the only region analyzed in Study 5 in which the concentration of the tracer was higher on the contralateral side than on the ipsilateral side, and this was true only for the RN group. It is worth noting that the rubrospinal tract is a relatively thin bundle within the medulla oblongata, which was used as the VOI, and since the average concentration of the entire VOI was evaluated, the obtained value was most probably underestimated.

Interestingly, although smaller than in the rats injected into the RN, a gradual increase in the  $^{52}Mn$  content in the contralateral MO was also observed in the VTAR-PBP group. This could have possibly resulted from a partial diffusion of the tracer from the injections site to the RN. Similarly, a gradual increase in the  $^{52}Mn$  level in the regions which do not receive

the neuronal input from the RN (*e.g.* the NAc, the VP, or the STR) has been observed in these areas in the RN group. This was potentially due to the diffusion of a portion of the injected volume from the RN to the PBP. In fact, in all these VOIs, the mean values of the RN group were lower than in the VTAR-PBP group. Therefore, although it seems that depending on the exact location of the injection site a characteristic distribution pattern of  $^{52}\text{Mn}$  can be recognized, the distribution patterns could have potentially differed even more between the groups provided a smaller injection volume had been used.

Nevertheless, a very distinctive  $^{52}\text{Mn}$  distribution pattern could be recognized in the PN-PIF group. The mean concentration of the tracer in all the analyzed ipsilateral VOIs was highest among the three groups, and the differences from the VTAR-PBP and the RN groups were particularly apparent in the HLDB & MPN, AON, OT, and OB areas. In fact, these regions receive the neuronal input from the medial aspects of the VTA, including the PN, PIF, and the Li [41]. Since these subnuclei of the VTA are also situated rather ventrally, the distance to the RN, which is located in the dorsal portion of the midbrain, could be too large for a simple diffusion process. Consequently, the  $^{52}\text{Mn}$  transport along the contralateral rubrospinal tract would not be likely. In fact, the concentration of the tracer in the MO was approximately the same on both sides in the PN-PIF group and clearly lower than in the other two groups. Thus, the distribution of  $^{52}\text{Mn}$  observed in the PN-PIF group was, similarly to the first two groups, in agreement with the known neuronal connectivity of the rat brain.

Furthermore, the PET images of the PN-PIF group have provided perhaps the most intriguing result of Study 5. A clear signal of  $^{52}\text{Mn}$  was visible along the ipsilateral tract leading from the injection site, through the HLDB & MPN, AON, and up to the OB in the

images of almost all the rats from this group. The HLDB & MPN complex is recognized as the intermediate portion of the basal forebrain which, among other regions, prominently innervates the OB [11] (Figure 26.1). The direct neuronal projections from the VTA to the OB are rather sparse (compare Figure 1.2). Hence, the observed trace of  $^{52}\text{Mn}$  might be a reflection of the neuronal transport along two pathways: from the VTA to the basal forebrain and from the basal forebrain to the OB. Provided this is true, it could be concluded that  $^{52}\text{Mn}$  had crossed a synapse, which have been reported many times for  $\text{Mn}^{2+}$  [123, 127-130]. Unfortunately, the present study lacks a histological validation, and thus, an ultimate conclusion should not be drawn.

Another interesting characteristic of the images from the PN-PIF group was that the prominent transport of  $^{52}\text{Mn}$  to the OB had occurred within an hour from the injection of the tracer into the VTA. This indicates a rather fast transport rate and possibly reflects

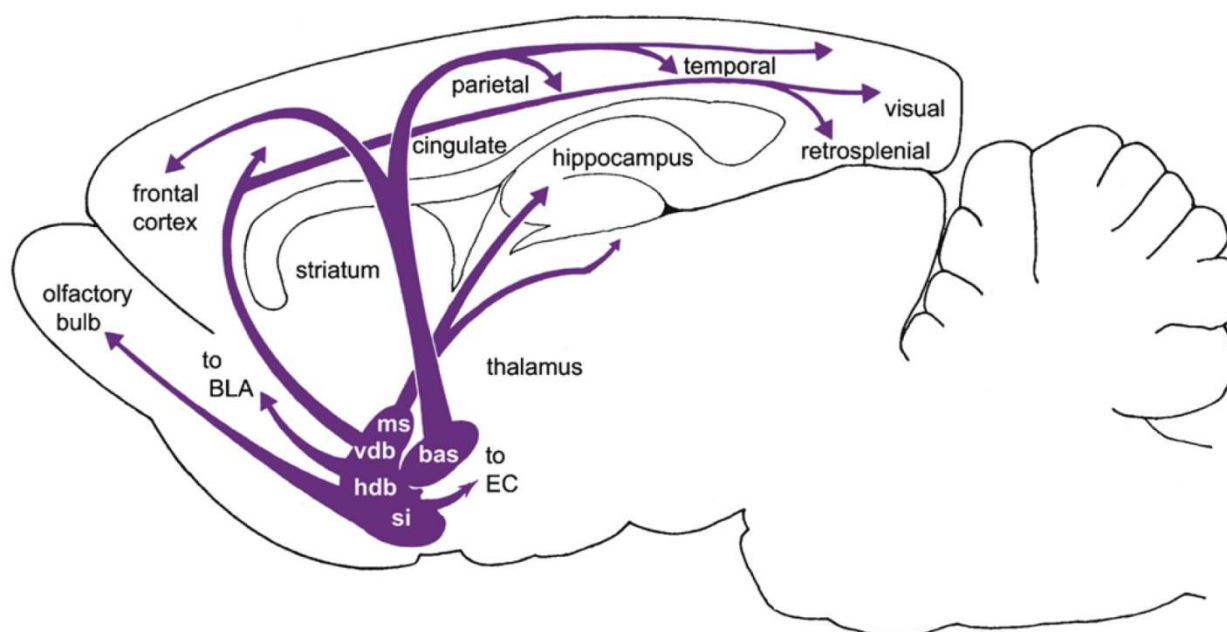


**Figure 26.1. The main neuronal projections of the rat basal forebrain**

The basal forebrain is composed of several, mostly cholinergic, nuclei: ms – medial septal nucleus, vertical and horizontal limbs of the diagonal band (vdb and hdb, respectively), substantia innominata (si), and nucleus basalis (bas), which project to many cortical areas, to the hippocampus, amygdala, and to the olfactory bulbs. BLA – basolateral amygdala, EC – entorhinal cortex. Adapted from [11].

some physiological properties of the neurons, apparently different from the properties of other neuronal pathways imaged in this study. For instance,  $^{52}\text{Mn}$  in the NAc was first observed approximately 2 h after the injection into the VTAR-PBP (Figure 23.3), although the distance from the injection site to the NAc is shorter than the distance to the OB. Additional experiments, potentially employing electrophysiological recording, should be conducted to verify whether the observed quick transport reflects an increased neuronal activity. Currently, this notion remains speculative.

One aspect of the  $^{52}\text{Mn}$  transport which the present work has not investigated in detail is the neuronal specificity. Since Mn divalent ion is taken up into the cells mostly by ion channels, ion exchangers or antiporters [114-117], which may be present on the cell surface of different neuronal types, the uptake should depend on the availability of the channels and the frequency as well as the duration with which they open. In fact, non-radioactive  $\text{Mn}^{2+}$  has been used to trace very different neuronal pathways, consisting of dopaminergic, noradrenergic, and other neurons [146, 159]. As long as the chemical form of the tracer is preserved (*i.e.* the oxidation state of +2), it should be possible to image the same pathways with  $^{52}\text{Mn}$  PET. The present work focused on the VTA, and thus, the imaged pathways were mostly dopaminergic. However, the rubrospinal tract originating from the RN is almost entirely glutamatergic [244], while the basal forebrain projection to the OB is composed mostly of cholinergic neurons [11]. Hence,  $^{52}\text{Mn}$  PET can be useful for imaging a variety of neuronal connections in the brain.

Assuming activity-dependence of the  $^{52}\text{Mn}$  transport, which has been already demonstrated for non-radioactive  $\text{Mn}^{2+}$  [119], it would be particularly interesting to use  $^{52}\text{Mn}$  PET for imaging the tracer distribution in the brain in relation to the animal's behavior. For

example, if the tracer is injected via a guide cannula previously fixed on the skull, the experimental animal may be engaged in a behavioral task while  $^{52}\text{Mn}$  is being taken up and transported by the involved neuronal circuits. Only after completing the task, the animal is anesthetized and the scanning procedure takes place to read out the distribution of the tracer.

This approach has been already used in one MEMRI study [125] and the main idea behind it is to remove the impact of anesthesia on the brain during the behavioral performance, when the involved brain pathways or areas are being “labeled”. This issue is currently the main drawback of other neuroimaging modalities, such as BOLD fMRI or DTI. Even though a few fMRI studies using the awake animal protocol have been reported [98, 245], a physical restraining had to be applied. This is not optimal not only because of a possible stress effect on the neural activity [246], but also because the restrained animal cannot perform active tasks, involving interactions with the environment (for example, pressing a lever or exploring a new territory), which are commonly used especially in rodent studies to assess the brain function.

Another possible application of  $^{52}\text{Mn}$  PET could be imaging of neurodegenerative processes in different animal models. For instance, an investigation of axonal transport in a mouse model of AD has been performed using MEMRI [172]. However, carrying it out with  $^{52}\text{Mn}$  PET would be burdened with a lower risk of metal intoxication. Furthermore, a reduced transport rate or total amount of the transported tracer would be expected in the affected neuronal pathways of the PD models or models of amyotrophic lateral sclerosis (ALS).  $^{52}\text{Mn}$  could be useful for monitoring the development and progression of these diseases as well

as the effects of experimental treatment strategies. This cannot be readily conducted with MEMRI since  $Mn^{2+}$  itself may evoke symptoms resembling parkinsonism [133].

Future applications could possibly also include imaging of visual, olfactory or peripheral neuronal pathways, where the stereotactic injection procedure might not be necessary. In fact, the usefulness of MEMRI in monitoring a sciatic nerve after a traumatic injury has been already tested in rats [214]. Due to the lower metal dose required,  $^{52}Mn$  PET could be more appropriate for this application.

Finally, it is worth mentioning that  $^{52}Mn$  production and separation methods have been largely advanced over the recent years [186-188, 191, 204], which is a prerequisite for any application. The relatively long half-life of  $^{52}Mn$  allows sufficient time for radiochemistry, as well as for a shipment of the tracer from a far situated production unit. Moreover, experiments with a complicated protocol can be easily conducted and a single injection might be sufficient for multiple measurements. Thus, first application studies have been already conducted [8, 189] and there is a potential for many further developments.

### **26.3 Activity-dependence of the $^{52}Mn$ neuronal transport**

One concern arising from the results of this work is that the tested pharmacological agents were not able to enhance or reduce the neuronal transport of  $^{52}Mn$  (Study 5). The only exception was non-radioactive  $Mn^{2+}$  whose effect was robust. AMPA, NMDA, AP-5 and TTX did not have any effect, despite the relatively high doses applied. Out of these substances, AMPA and TTX have been previously used to modulate the transport of  $Mn^{2+}$  from the injection site in the Hb to the interpeduncular nucleus (IPN) [132].

The authors found a significant increase in the longitudinal relaxation rate (R1, an inverse of the T1) in the group treated with 100  $\mu$ M AMPA, starting from approximately 2.5 h after the Mn<sup>2+</sup>/AMPA injection. The difference from the R1 of the control group, injected with the Mn<sup>2+</sup> solution alone, remained significant until the end of the measurement, 9.5 h post-injection. Thus, it was very surprising to find no difference between the *CTRL* and the *AMPA* groups in the <sup>52</sup>Mn PET study. However, several factors in the experimental protocols used in the present work and in the referred study, might have influenced the results.

## 26.4 Limitations and technical considerations

Besides the considerations raised in the previous section, several other limitations of  $^{52}\text{Mn}$  PET exist. Firstly, the relatively long half-life of the isotope, which allows sufficient time for the radiochemistry, shipment of the tracer, and convenient performance of complicated experiments, as already discussed, results in the relatively high radiation exposure for the experimental subject as well as for the researcher. The effects of different radioactivity doses on the brain tissue have been extensively discussed in Section 26.1. In regard to the scientific personnel, the dose exposure should be strictly monitored. Additionally, a prolonged storage of the radioactive waste would be necessary [180].

Another characteristic of  $^{52}\text{Mn}$  is the presence of numerous prompt  $\gamma$  rays in the decay scheme. These  $\gamma$  rays contribute to the issue of the radiation exposure discussed above, but additionally, they may have an effect on the PET images. As described in the Introduction (section 5.1), three types of the  $\gamma$  rays occur with a high probability and, if scattered, may be potentially captured by the detector system. In fact, a small artificial signal caused by this  $\gamma$  radiation has been reported in a phantom study utilizing the acquisition energy window of 450-600 keV [185]. The deviation from the true value of the image was in the 2 % range but could be reduced to -0.5 % by applying a cascade background correction.

The impact of the cascade  $\gamma$  rays on the PET images was investigated in Study 2. Without applying the cascade correction, the normalized profiles of the images of two phantoms did not differ depending on the energy window used for the acquisition (energy windows from 450-600 keV to 350-650 keV were tested). This apparently improved, as compared to the results obtained by Topping *et al.* [185], image quality might have resulted from a different

algorithm used for the image reconstruction. While the FBP algorithm was used in the cited work, the OSEM3D-MAP algorithm was applied in Study 2. Additionally, different PET scanners were used in both studies which might have also played a role.

Finally, the main drawback of  $^{52}\text{Mn}$  PET is its limited spatial resolution. In the image of the resolution phantom (Study 2), the smallest rod volumes which could be resolved had the diameter of 1.35 mm. Accordingly, it was possible to identify the brain regions as small as the rat SN in the images from the *in vivo* studies. Thus, currently, imaging of the neuronal pathways at the regional level is feasible in rats, but would be probably more challenging in mice. Nevertheless, possible improvements in the spatial resolution of PET scanners are currently under investigation. Results of simulation and experimental studies indicate that the resolution of 0.5-0.6 mm of the full width at half maximum (FWHM) may be achieved [247, 248]. If scanners with this high spatial resolution are available, the intrinsic limitation of  $^{52}\text{Mn}$  PET will be the positron range of the isotope, *i.e.* 0.63 mm [184].

## 27 Small Animal PET with Online Recording of the Blood Radioactivity using a Blood Sampler

As the final part of this PhD project, an experimental protocol for PET with online recording of the blood radioactivity level with a BS was established. The time course of the concentration of a PET tracer in the blood is required for full kinetic modeling, and the kinetic modeling, in turn, is very important for a detailed evaluation of pharmacokinetics of every novel tracer. Although the present work proposes  $^{52}\text{Mn}$  for tracing neuronal projections following a direct intracerebral administration, this isotope may be also used for labeling compounds which would be administered systemically. Therefore, the established experimental protocol may be potentially used for kinetic modeling of different PET tracers, including possible future  $^{52}\text{Mn}$ -labeled compounds.

The advantages of using a BS, rather than manual blood sampling, in small experimental animals include: (1) limiting the loss of the blood volume which may affect physiological parameters in rats [202] and be potentially lethal for mice; (2) accurate measurement of the peak activity after a bolus injection [249] which may be missed during MS due to the lower sampling rate; and (3) maintaining the entire amount of the tracer being under investigation in the body. Moreover, the MR-compatibility of the device used in this study provides additional benefits, as it potentially enables simultaneous PET-MRI measurements. This type of studies allows an acquisition of complementary structural and functional information in a reduced time [250, 251]. Additionally, the exceptionally high sensitivity of the BS (23 %) may be possibly sufficient also for human studies. In this case, the translation of research from the preclinical to the clinical level could be facilitated.

In the present study, there was a good agreement of the *wb* TACs measured with the BS and the MS, especially in the beginning of the experiments. Consequently, the mean  $K_1$  and  $k_2$  obtained with the BS-based approaches were very close to the reference values. However, the BS TACs were slightly overestimated in the second half of the recording. This was possibly due to an adhesion of the blood to the inner walls of the shunt tube and resulted in the underestimation of the mean  $k_3$ . In order to solve the problem, one manually collected blood sample was combined with the first 10 min of the BS recording. This approach, together with the used fitting procedure and the dispersion correction, allowed a full recovery of the  $k_3$  value and can be used in future studies. Alternatively, a different type of tubing may be used to reduce the adhesion of the blood and of the tracer itself, which will be particularly relevant for more lipophilic compounds. One possibility could be a Teflon® tube which has been recently proposed [252].

The main limitation of the BS recording technique is the necessity of applying the population-based approach to calculate the  $p$  values from the *wb* data. In the present study, using the mean coefficients of the  $\frac{p}{wb}$  ratio, rather than the measured  $p$  samples, to obtain the AIF in the same group of animals resulted in the 8 % difference of the  $k_3$  from the reference. If this  $\frac{p}{wb}$  ratio is used in a separate group, potentially even higher deviations may be expected. Hence, the differences in the KPs lower than 10 % should be interpreted carefully.

Finally, although the ID-AIF was not the main focus of the present work, this approach was also evaluated for comparison. The *wb* TACs obtained from the PET images largely overestimated the MS as well as the BS TACs, which resulted in the substantial underestimation of the  $k_3$ . This was most probably due to the gradual accumulation of

[<sup>18</sup>F]FDG in the myocardium which resulted in the spillover effect in the left ventricle [253] and led to the substantial underestimation (above 48 %) of the  $k_3$ . Therefore, if the AIF is derived from a PET image, it is critical to apply a correction for the spillover effect, but also for the partial volume effect [254, 255].

# **CONCLUSIONS AND OUTLOOK**

The present work demonstrates the feasibility of tracing neuronal pathways with  $^{52}\text{Mn}$  PET as an alternative method to MEMRI. The main advantage of  $^{52}\text{Mn}$  PET is the possibility to reduce the dose of the metal to the physiological level. This is important since doses of non-radioactive  $\text{Mn}^{2+}$  commonly used in MEMRI experiments may have pharmacological or even toxic consequences.

In fact, 50 nmol of  $\text{Mn}^{2+}$  administered into the rat striatum in Study 4 resulted in a reduced BPnd of [ $^{11}\text{C}$ ]flumazenil in the ipsilateral cortex, indicating that the contrast agent interacts with the GABAergic system. This effect is unacceptable if MEMRI shall be used for functional neuroimaging. Furthermore, although there was no effect of the intrastrially injected  $\text{Mn}^{2+}$  on the BPnd of [ $^{11}\text{C}$ ]methylphenidate, suggesting no impact on the DAT, the 45 nmol dose administered into the VTA did induce a dopaminergic lesion. This was manifested as a reduced intensity in the TH-stained brain tissue sections.

These data collectively indicate that  $\text{Mn}^{2+}$  interacts with the GABAergic as well as dopaminergic system, which is in agreement with the available literature. Since the neurotransmitter systems affected by Mn may influence each other, it will be important in future studies to investigate these interactions, and especially how they evolve in the course of Mn intoxication. The outcomes of such investigations should facilitate the development of treatment strategies for manganism.

Contrary to the  $\text{Mn}^{2+}$  doses required for MEMRI, the doses of the metal used in  $^{52}\text{Mn}$  PET were not harmful. Even with the nano-molar concentration and despite a lower spatial resolution of PET, known neuronal projections could be identified in PET images following a direct intracerebral administration of the tracer. Moreover, the reduced transport of  $^{52}\text{Mn}$  after its co-injection with  $\text{Mn}^{2+}$  showed that both isotopes use the same transport

mechanisms. Although the activity-dependence of the neuronal transport could not be confirmed in this work, these measurements should be repeated, possibly with a different anesthetic.

Additionally, the present results suggest that some physiological properties of different neuronal populations might be potentially observed with  $^{52}\text{Mn}$ , since the transport rate of the tracer appeared to depend on the specific sub-nucleus of the VTA into which the tracer was injected. Further studies, possibly utilizing electrophysiological recording or optogenetic methods, will be useful in untangling which specific mechanisms are responsible for the activity-dependent uptake and transport of  $^{52}\text{Mn}$ .

Although defining the most suitable applications of  $^{52}\text{Mn}$  PET will require further research, including the mentioned investigations of the exact molecular mechanisms, the present findings already provide a ground for many future developments. Besides employing the technique in animal neurological and neuroscientific studies,  $^{52}\text{Mn}$  may become an interesting PET isotope potentially applicable in the fields of oncology or infectious diseases. Given its long half-life,  $^{52}\text{Mn}$  may be particularly suitable for long-term studies.

However, the long half-life also implies that the exposure to the ionizing radiation will be prolonged compared to more traditional PET isotopes. Hence, although injecting 20-30 kBq of the tracer into the rat brain allowed avoiding the dopaminergic lesion, the effect on the motor control system, as well as inducing DNA breaks, monitoring of the possible consequences of the applied radioactivity doses will be very important. In addition, a possible impact of  $^{52}\text{Mn}$  on other cellular and molecular processes susceptible to irradiation should be assessed.

Finally, if  $^{52}\text{Mn}$  is used to label new PET tracers, the pharmacokinetics of these compounds in small animals may be examined using the experimental protocol established herein. Although the first measurement with a novel tracer always requires manual blood sampling for the collection of the plasma and evaluation of metabolites, subsequent studies may be based on the blood sampler recording, the estimated  $\frac{p}{wb}$  activity ratio, and the previously measured metabolite content. This approach ensures an accurate characterization of the peak activity and allows avoiding a blood loss which is critical in small animals. Thanks to the very high sensitivity, the blood sampler tested in the present work will be also suitable for studies with short-lived isotopes, such as  $^{11}\text{C}$  or  $^{15}\text{O}$ .

## Work Contribution and Acknowledgements

- **Dr Carsten Calaminus** supervised the present work. He taught the procedures of the free-floating histological staining and the stereotactic injection. He also helped to plan the experiments and to interpret the results. Moreover, he corrected the present thesis.
- **Dr Gregory W. Severin and Dr Jesper Fonslet** established  $^{52}\text{Mn}$  production and separation methods. They also produced the tracer for all the studies described in this work. After the production, they evaluated the purity of the solutions. Additionally, they participated in planning and discussing the results of the  $^{52}\text{Mn}$  toxicity study.
- **Dr Armin Kolb** contributed to the blood sampler study equally with the author of this thesis. He built the device, participated in designing and performance of the *in vivo* experiments, in data analysis and in the discussion of the results.
- **Dr Apostolos Menegakis** helped to plan and perform the experiment in which  $^{52}\text{Mn}$ -induced DNA damage was assessed. He also supported the data analysis and interpretation of the results in that study.
- **Dr Julia Mannheim** acquired the normalization PET data needed for the image reconstruction. She also advised on how to conduct and evaluate the phantom PET measurements.
- **Dr Salvador Castaneda-Vega** established the MRI sequences used to obtain anatomical images in Study 5. He also provided his expertise in the statistical analysis of the data in Study 3.

- **Matteo Tonietto** established and kindly shared the method of modeling the arterial input function which was used in the blood sampler study.
- **Prof Dr Martin Eichner** performed statistical analysis of the data from Study 4.
- **Jürgen Kupferschläger** performed the dosimetry calculations in Study 5.
- **Dr Andreas Maurer** supported the production of [ $^{11}\text{C}$ ]methylphenidate and [ $^{11}\text{C}$ ]flumazenil used in Study 4 and contributed to the design of the study evaluating the toxicity of  $^{52}\text{Mn}$ .
- **Sandro Aidone** provided technical assistant in Study 4 and in the experiments with the blood sampler.
- **Maren Harant** taught the procedure of arterial and venous catheter insertion and provided technical assistant in Study 4.
- **Ramona Stumm** produced [ $^{11}\text{C}$ ]methylphenidate and [ $^{11}\text{C}$ ]flumazenil used in Study 4. She also helped with the technical procedures used in the blood sampler study.

Additionally to the persons listed above, the author would like to acknowledge:

**Prateek Katiyar** for his support and advices during the analysis of the blood sampler data,

**Filippo Michelotti** for sharing his expertise and providing advice regarding T1 contrast enhancement and T1 mapping methods used in MRI,

**Dr Stefan Wiehr** and **Dr Anna-Maria Wild** for their contribution to planning and coordination of the  $^{52}\text{Mn}$  studies,

**Dr Michael Walker** for instructions and advice regarding the rotameter test,

**Dr Jonathan Cotton** and **Gregory Bowden** for their assistance and advice on chromatography methods,

**Dr Andreas Schmid** and **Dr Hans Wehrl** for their help during MRI measurements,

**Dr Jonathan Disselhorst** and **Dr Minhaz Ud-Dean** for their assistance in data analysis procedures,

**Dr Florian Maier** for the discussion about statistical tests and his contribution to the performance of trial experiments,

**Dr Geoffrey Warnock** for his advices regarding the experimental setup for the blood sampler study,

**Dr Kristina Herfert** for discussions about arterial input function and PET kinetic modeling,

**Prof Dr Adriaan Lammertsma** and **Dr Masqsood Yaqub** for the discussion about the dispersion correction,

and **Natalie Altmeyer** for her advice on histological staining procedures.

## Bibliography

1. Bailey, D.L., et al., *Positron emission tomography*. 2005: Springer.
2. Banerjee, S.R. and M.G. Pomper, *Clinical applications of gallium-68*. Applied Radiation and Isotopes, 2013. **76**: p. 2-13.
3. Conti, M. and L. Eriksson, *Physics of pure and non-pure positron emitters for PET: a review and a discussion*. EJNMMI Physics, 2016. **3**(1): p. 8.
4. database, N.M.-N.N.D.C.M.I.R.D. [cited 2017 27 July]; Available from: <http://www.nndc.bnl.gov/>.
5. Westbrook, C. and C.K. Roth, *MRI in Practice*. 2011: John Wiley & Sons.
6. Scuffham, J., et al., *A CdTe detector for hyperspectral SPECT imaging*. Journal of Instrumentation, 2012. **7**(08): p. P08027.
7. Silva, A.C. and N.A. Bock, *Manganese-enhanced MRI: an exceptional tool in translational neuroimaging*. Schizophrenia Bulletin, 2008. **34**(4): p. 595-604.
8. Napieczynska, H., et al., *Imaging neuronal pathways with <sup>52</sup>Mn PET. Toxicity evaluation in rats*. NeuroImage, 2017. **158**: p. 112-125.
9. Björklund, A. and S.B. Dunnett, *Dopamine neuron systems in the brain: an update*. Trends in Neurosciences, 2007. **30**(5): p. 194-202.
10. Turkington, T.G., *Introduction to PET instrumentation*. Journal of Nuclear Medicine Technology, 2001. **29**(1): p. 4-11.
11. Woolf, N.J. and L.L. Butcher, *Cholinergic systems mediate action from movement to higher consciousness*. Behavioural Brain Research, 2011. **221**(2): p. 488-498.
12. Tsao, C. *Basic MRI Physics*. [cited 2017 23.08]; Available from: [http://wikidoc.org/index.php/Basic\\_MRI\\_Physics](http://wikidoc.org/index.php/Basic_MRI_Physics).
13. Sanchez-Catalan, M., et al., *The antero-posterior heterogeneity of the ventral tegmental area*. Neuroscience, 2014. **282**: p. 198-216.
14. Verel, I., G.W. Visser, and G.A. van Dongen, *The promise of immuno-PET in radioimmunotherapy*. Journal of Nuclear Medicine, 2005. **46**(1 suppl): p. 164S-171S.
15. Morales, M. and E.B. Margolis, *Ventral tegmental area: cellular heterogeneity, connectivity and behaviour*. Nature Reviews Neuroscience, 2017. **18**(2): p. 73-85.
16. Paxinos, G. and C. Watson, *The Rat Brain in Stereotaxic Coordinates*. 6th ed. 2007: Academic Press.
17. Yetnikoff, L., et al., *An update on the connections of the ventral mesencephalic dopaminergic complex*. Neuroscience, 2014. **282**: p. 23-48.
18. German, D.C. and K.F. Manaye, *Midbrain dopaminergic neurons (nuclei A8, A9, and A10): three-dimensional reconstruction in the rat*. Journal of Comparative Neurology, 1993. **331**(3): p. 297-309.
19. Chuhma, N., et al., *Dopamine neuron glutamate cotransmission: frequency-dependent modulation in the mesoventromedial projection*. Neuroscience, 2009. **164**(3): p. 1068-1083.
20. Hnasko, T.S., et al., *Ventral tegmental area glutamate neurons: electrophysiological properties and projections*. Journal of Neuroscience, 2012. **32**(43): p. 15076-15085.
21. Tritsch, N.X., J.B. Ding, and B.L. Sabatini, *Dopaminergic neurons inhibit striatal output via non-canonical release of GABA*. Nature, 2012. **490**(7419): p. 262.
22. Stensrud, M.J., M. Puchades, and V. Gundersen, *GABA is localized in dopaminergic synaptic vesicles in the rodent striatum*. Brain Structure and Function, 2014. **219**(6): p. 1901-1912.
23. Yoo, J.H., et al., *Ventral tegmental area glutamate neurons co-release GABA and promote positive reinforcement*. Nature Communications, 2016. **7**: p. 13697.
24. Hnasko, T.S., et al., *Vesicular glutamate transport promotes dopamine storage and glutamate corelease in vivo*. Neuron, 2010. **65**(5): p. 643-656.

25. Zhang, S., et al., *Dopaminergic and glutamatergic microdomains in a subset of rodent mesoaccumbens axons*. *Nature Neuroscience*, 2015. **18**(3): p. 386-392.
26. Kim, J.-I., et al., *Aldehyde dehydrogenase 1a1 mediates a GABA synthesis pathway in midbrain dopaminergic neurons*. *Science*, 2015. **350**(6256): p. 102-106.
27. Seroogy, K., et al., *Further analysis of presence of peptides in dopamine neurons*. *Experimental Brain Research*, 1988. **72**(3): p. 523-534.
28. Szabo, B., S. Siemes, and I. Wallmichrath, *Inhibition of GABAergic neurotransmission in the ventral tegmental area by cannabinoids*. *European Journal of Neuroscience*, 2002. **15**(12): p. 2057-2061.
29. Margolis, E.B., et al.,  *$\kappa$ -Opioid agonists directly inhibit midbrain dopaminergic neurons*. *Journal of Neuroscience*, 2003. **23**(31): p. 9981-9986.
30. Margolis, E.B., et al., *Direct bidirectional  $\mu$ -opioid control of midbrain dopamine neurons*. *Journal of Neuroscience*, 2014. **34**(44): p. 14707-14716.
31. Kotecki, L., et al., *GIRK channels modulate opioid-induced motor activity in a cell type-and subunit-dependent manner*. *Journal of Neuroscience*, 2015. **35**(18): p. 7131-7142.
32. Fiorillo, C.D., P.N. Tobler, and W. Schultz, *Discrete coding of reward probability and uncertainty by dopamine neurons*. *Science*, 2003. **299**(5614): p. 1898-1902.
33. Tobler, P.N., C.D. Fiorillo, and W. Schultz, *Adaptive coding of reward value by dopamine neurons*. *Science*, 2005. **307**(5715): p. 1642-1645.
34. Schultz, W., *Behavioral dopamine signals*. *Trends in neurosciences*, 2007. **30**(5): p. 203-210.
35. Lammel, S., et al., *Unique properties of mesoprefrontal neurons within a dual mesocorticolimbic dopamine system*. *Neuron*, 2008. **57**(5): p. 760-773.
36. Roper, J., *Dissecting the diversity of midbrain dopamine neurons*. *Trends in Neurosciences*, 2013. **36**(6): p. 336-342.
37. Li, X., et al., *Heterogeneous composition of dopamine neurons of the rat A10 region: molecular evidence for diverse signaling properties*. *Brain Structure and Function*, 2013. **218**(5): p. 1159-1176.
38. Morales, M. and D.H. Root, *Glutamate neurons within the midbrain dopamine regions*. *Neuroscience*, 2014. **282**: p. 60-68.
39. Swanson, L., *The projections of the ventral tegmental area and adjacent regions: a combined fluorescent retrograde tracer and immunofluorescence study in the rat*. *Brain Research Bulletin*, 1982. **9**(1): p. 321-353.
40. Aransay, A., et al., *Long-range projection neurons of the mouse ventral tegmental area: a single-cell axon tracing analysis*. *Frontiers in Neuroanatomy*, 2015. **9**: p. 1-24.
41. Ikemoto, S., *Dopamine reward circuitry: two projection systems from the ventral midbrain to the nucleus accumbens-olfactory tubercle complex*. *Brain Research Reviews*, 2007. **56**(1): p. 27-78.
42. Schultz, W., P. Dayan, and P.R. Montague, *A neural substrate of prediction and reward*. *Science*, 1997. **275**(5306): p. 1593-1599.
43. Fiorino, D.F., et al., *Electrical stimulation of reward sites in the ventral tegmental area increases dopamine transmission in the nucleus accumbens of the rat*. *Behavioural Brain Research*, 1993. **55**(2): p. 131-141.
44. Karreman, M., B.H. Westerink, and B. Moghaddam, *Excitatory amino acid receptors in the ventral tegmental area regulate dopamine release in the ventral striatum*. *Journal of Neurochemistry*, 1996. **67**(2): p. 601-607.
45. Westerink, B. and H. Kwint, *The pharmacology of mesolimbic dopamine neurons: a dual-probe microdialysis study in the ventral tegmental area and nucleus accumbens of the rat brain*. *Journal of Neuroscience*, 1996. **16**(8): p. 2605-2611.
46. Wilson, C., et al., *Dopaminergic correlates of motivated behavior: importance of drive*. *Journal of Neuroscience*, 1995. **15**(7): p. 5169-5178.
47. Robinson, D.L., et al., *Sub-second changes in accumbal dopamine during sexual behavior in male rats*. *Neuroreport*, 2001. **12**(11): p. 2549-2552.

48. Di Chiara, G. and A. Imperato, *Drugs abused by humans preferentially increase synaptic dopamine concentrations in the mesolimbic system of freely moving rats*. Proceedings of the National Academy of Sciences, 1988. **85**(14): p. 5274-5278.
49. Brauer, L.H. and H. De Wit, *High dose pimozide does not block amphetamine-induced euphoria in normal volunteers*. Pharmacology Biochemistry and Behavior, 1997. **56**(2): p. 265-272.
50. Taber, M.T. and H.C. Fibiger, *Electrical stimulation of the prefrontal cortex increases dopamine release in the nucleus accumbens of the rat: modulation by metabotropic glutamate receptors*. Journal of Neuroscience, 1995. **15**(5): p. 3896-3904.
51. Legault, M., P.-P. Rompré, and R.A. Wise, *Chemical stimulation of the ventral hippocampus elevates nucleus accumbens dopamine by activating dopaminergic neurons of the ventral tegmental area*. Journal of Neuroscience, 2000. **20**(4): p. 1635-1642.
52. Stuber, G.D., et al., *Excitatory transmission from the amygdala to nucleus accumbens facilitates reward seeking*. Nature, 2011. **475**(7356): p. 377-380.
53. Stamatakis, A.M., et al., *A unique population of ventral tegmental area neurons inhibits the lateral habenula to promote reward*. Neuron, 2013. **80**(4): p. 1039-1053.
54. Gorelova, N., et al., *The glutamatergic component of the mesocortical pathway emanating from different subregions of the ventral midbrain*. Cerebral Cortex, 2011. **22**(2): p. 327-336.
55. Takahata, R. and B. Moghaddam, *Glutamatergic Regulation of Basal and Stimulus-Activated Dopamine Release in the Prefrontal Cortex*. Journal of neurochemistry, 1998. **71**(4): p. 1443-1449.
56. Carr, D.B. and S.R. Sesack, *GABA-containing neurons in the rat ventral tegmental area project to the prefrontal cortex*. Synapse, 2000. **38**(2): p. 114-123.
57. Albanese, A. and D. Minciacchi, *Organization of the ascending projections from the ventral tegmental area: a multiple fluorescent retrograde tracer study in the rat*. Journal of Comparative Neurology, 1983. **216**(4): p. 406-420.
58. Deniau, J., A. Thierry, and J. Feger, *Electrophysiological identification of mesencephalic ventromedial tegmental (VMT) neurons projecting to the frontal cortex, septum and nucleus accumbens*. Brain Research, 1980. **189**(2): p. 315-326.
59. Goeders, N.E. and J.E. Smith, *Cortical dopaminergic involvement in cocaine reinforcement*. Science, 1983. **221**(4612): p. 773-775.
60. Goeders, N.E., S.I. Dworkin, and J.E. Smith, *Neuropharmacological assessment of cocaine self-administration into the medial prefrontal cortex*. Pharmacology Biochemistry and Behavior, 1986. **24**(5): p. 1429-1440.
61. You, Z.-B., et al., *Electrical stimulation of the prefrontal cortex increases cholecystokinin, glutamate, and dopamine release in the nucleus accumbens: an in vivo microdialysis study in freely moving rats*. Journal of Neuroscience, 1998. **18**(16): p. 6492-6500.
62. Rushworth, M.F., et al., *Frontal cortex and reward-guided learning and decision-making*. Neuron, 2011. **70**(6): p. 1054-1069.
63. Ljungberg, T. and U. Ungerstedt, *Sensory inattention produced by 6-hydroxydopamine-induced degeneration of ascending dopamine neurons in the brain*. Experimental neurology, 1976. **53**(3): p. 585-600.
64. Abe, I., T. Watanabe, and H. Noguchi, *Enzymatic formation of long-chain polyketide pyrones by plant type III polyketide synthases*. Phytochemistry, 2004. **65**(17): p. 2447-53.
65. Yin, H.H. and B.J. Knowlton, *Contributions of striatal subregions to place and response learning*. Learning & Memory, 2004. **11**(4): p. 459-463.
66. Yin, H.H. and B.J. Knowlton, *The role of the basal ganglia in habit formation*. Nature Reviews. Neuroscience, 2006. **7**(6): p. 464-476.
67. Balleine, B.W. and J.P. O'doherty, *Human and rodent homologues in action control: corticostriatal determinants of goal-directed and habitual action*. Neuropsychopharmacology, 2010. **35**(1): p. 48-69.

68. McNamee, D., et al., *Characterizing the associative content of brain structures involved in habitual and goal-directed actions in humans: a multivariate fMRI study*. Journal of Neuroscience, 2015. **35**(9): p. 3764-3771.
69. Godwin-Austen, R., et al., *Effects of L-dopa in Parkinson's disease*. The Lancet, 1969. **294**(7613): p. 165-168.
70. Zapata, A., V.L. Minney, and T.S. Shippenberg, *Shift from goal-directed to habitual cocaine seeking after prolonged experience in rats*. Journal of Neuroscience, 2010. **30**(46): p. 15457-15463.
71. Kalivas, P.W., *Addiction as a pathology in prefrontal cortical regulation of corticostriatal habit circuitry*. Neurotoxicity Research, 2008. **14**(2): p. 185-189.
72. Tomasi, D. and N.D. Volkow, *Striatocortical pathway dysfunction in addiction and obesity: differences and similarities*. Critical Reviews in Biochemistry and Molecular Biology, 2013. **48**(1): p. 1-19.
73. Nestler, E.J. and W.A. Carlezon, *The mesolimbic dopamine reward circuit in depression*. Biological Psychiatry, 2006. **59**(12): p. 1151-1159.
74. Laviolette, S.R., *Dopamine modulation of emotional processing in cortical and subcortical neural circuits: evidence for a final common pathway in schizophrenia?* Schizophrenia Bulletin, 2007. **33**(4): p. 971-981.
75. Kapur, S. and G. Remington, *Dopamine D 2 receptors and their role in atypical antipsychotic action: still necessary and may even be sufficient*. Biological Psychiatry, 2001. **50**(11): p. 873-883.
76. Janowsky, D.S., et al., *Provocation of schizophrenic symptoms by intravenous administration of methylphenidate*. Archives of General Psychiatry, 1973. **28**(2): p. 185-191.
77. Laruelle, M. and A. Abi-Dargham, *Dopamine as the wind of the psychotic fire: new evidence from brain imaging studies*. Journal of Psychopharmacology, 1999. **13**(4): p. 358-371.
78. Grace, A.A., *Dysregulation of the dopamine system in the pathophysiology of schizophrenia and depression*. Nature Reviews. Neuroscience, 2016. **17**(8): p. 524-532.
79. Chang, C.-h. and A.A. Grace, *Amygdala-ventral pallidum pathway decreases dopamine activity after chronic mild stress in rats*. Biological Psychiatry, 2014. **76**(3): p. 223-230.
80. Valenti, O., K.M. Gill, and A.A. Grace, *Different stressors produce excitation or inhibition of mesolimbic dopamine neuron activity: response alteration by stress pre-exposure*. European Journal of Neuroscience, 2012. **35**(8): p. 1312-1321.
81. Mayberg, H.S., et al., *Deep brain stimulation for treatment-resistant depression*. Neuron, 2005. **45**(5): p. 651-660.
82. Viggiano, D., et al., *Behavioural, pharmacological, morpho-functional molecular studies reveal a hyperfunctioning mesocortical dopamine system in an animal model of attention deficit and hyperactivity disorder*. Neuroscience & Biobehavioral Reviews, 2003. **27**(7): p. 683-689.
83. Corral-Frias, N.S., et al., *Involvement of the ventral tegmental area in a rodent model of post-traumatic stress disorder*. Neuropsychopharmacology, 2013. **38**(2): p. 350-363.
84. Kessler, R.C., et al., *The global burden of mental disorders: an update from the WHO World Mental Health (WMH) surveys*. Epidemiology and Psychiatric Sciences, 2009. **18**(1): p. 23-33.
85. Vahle-Hinz, C. and O. Detsch, *What can in vivo electrophysiology in animal models tell us about mechanisms of anaesthesia?* British Journal of Anaesthesia, 2002. **89**(1): p. 123-142.
86. Long, M.A. and A.K. Lee, *Intracellular recording in behaving animals*. Current Opinion in Neurobiology, 2012. **22**(1): p. 34-44.
87. Mogenson, G., L. Swanson, and M. Wu, *Neural projections from nucleus accumbens to globus pallidus, substantia innominata, and lateral preoptic-lateral hypothalamic area: an anatomical and electrophysiological investigation in the rat*. Journal of Neuroscience, 1983. **3**(1): p. 189-202.
88. He, B., et al., *Electrophysiological imaging of brain activity and connectivity—challenges and opportunities*. IEEE Transactions on Biomedical Engineering, 2011. **58**(7): p. 1918-1931.
89. Burle, B., et al., *Spatial and temporal resolutions of EEG: Is it really black and white? A scalp current density view*. International Journal of Psychophysiology, 2015. **97**(3): p. 210-220.

90. Attal, Y. and D. Schwartz, *Assessment of subcortical source localization using deep brain activity imaging model with minimum norm operators: a MEG study*. PLOS One, 2013. **8**(3): p. e59856.
91. Gore, J.C., *Principles and practice of functional MRI of the human brain*. Journal of Clinical Investigation, 2003. **112**(1): p. 4-9.
92. Constable, R.T., *Challenges in fMRI and its limitations*, in *Functional Neuroradiology*. 2011, Springer. p. 331-344.
93. Hirsch, S., A. Dickenson, and L. Corradini, *Anesthesia influences neuronal activity and drug effectiveness in neuropathic rats*. PAIN, 2014. **155**(12): p. 2583-2590.
94. West, M.O., *Anesthetics eliminate somatosensory-evoked discharges of neurons in the somatotopically organized sensorimotor striatum of the rat*. Journal of Neuroscience, 1998. **18**(21): p. 9055-9068.
95. Huh, Y. and J. Cho, *Urethane anesthesia depresses activities of thalamocortical neurons and alters its response to nociception in terms of dual firing modes*. Frontiers in Behavioral Neuroscience, 2013. **7**: p. 1-9.
96. Yonezaki, K., et al., *Postanesthetic effects of isoflurane on behavioral phenotypes of adult male C57BL/6J mice*. PLOS One, 2015. **10**(3): p. e0122118.
97. Kenkel, W., et al., *Functional magnetic resonance imaging in awake transgenic fragile X rats: evidence of dysregulation in reward processing in the mesolimbic/habenular neural circuit*. Translational psychiatry, 2016. **6**(3): p. e763.
98. Harris, A.P., et al., *Imaging learned fear circuitry in awake mice using fMRI*. European Journal of Neuroscience, 2015. **42**(5): p. 2125-2134.
99. Table, E. and V. Table, *Dietary reference intakes for vitamin A, vitamin K, arsenic, boron, chromium, copper, iodine, iron, manganese, molybdenum, nickel, silicon, vanadium, and zinc*. 2001.
100. Fraga, C.G., *Relevance, essentiality and toxicity of trace elements in human health*. Molecular aspects of medicine, 2005. **26**(4): p. 235-244.
101. Law, N.A., M.T. Caudle, and V.L. Pecoraro, *Manganese redox enzymes and model systems: properties, structures, and reactivity*. Advances in inorganic chemistry, 1998. **46**: p. 305-440.
102. Wedler, F. and R. Denman, *Glutamine synthetase: the major Mn (II) enzyme in mammalian brain*. Current topics in cellular regulation, 1984. **24**: p. 153-169.
103. Prohaska, J.R., *Functions of trace elements in brain metabolism*. Physiological Reviews, 1987. **67**(3): p. 858-901.
104. Hurley, L.S., et al., *Influence of manganese on susceptibility of rats to convulsions*. American Journal of Physiology--Legacy Content, 1963. **204**(3): p. 493-496.
105. Papavasiliou, P.S., et al., *Seizure disorders and trace metals Manganese tissue levels in treated epileptics*. Neurology, 1979. **29**(11): p. 1466-1466.
106. Dupont, C. and Y. Tanaka, *Blood manganese levels in children with convulsive disorder*. Biochemical Medicine, 1985. **33**(2): p. 246-255.
107. Hostetler, C.E., R.L. Kincaid, and M.A. Mirando, *The role of essential trace elements in embryonic and fetal development in livestock*. The Veterinary Journal, 2003. **166**(2): p. 125-139.
108. Takeda, A., *Manganese action in brain function*. Brain Research Reviews, 2003. **41**(1): p. 79-87.
109. Murphy, V.A., et al., *Saturable Transport of Manganese (II) Across the Rat Blood-Brain Barrier*. Journal of Neurochemistry, 1991. **57**(3): p. 948-954.
110. Rabin, O., et al., *Rapid Brain Uptake of Manganese (II) Across the Blood-Brain Barrier*. Journal of Neurochemistry, 1993. **61**(2): p. 509-517.
111. Aschner, M. and M. Gannon, *Manganese (Mn) transport across the rat blood-brain barrier: saturable and transferrin-dependent transport mechanisms*. Brain Research Bulletin, 1994. **33**(3): p. 345-349.
112. Garrick, M.D., et al., *DMT1: a mammalian transporter for multiple metals*. Biometals, 2003. **16**(1): p. 41-54.
113. Fujishiro, H., et al., *Roles of ZIP8, ZIP14, and DMT1 in transport of cadmium and manganese in mouse kidney proximal tubule cells*. Metallomics, 2012. **4**(7): p. 700-708.

114. Narita, K., F. Kawasaki, and H. Kita, *Mn and Mg influxes through Ca channels of motor nerve terminals are prevented by verapamil in frogs*. Brain Research, 1990. **510**(2): p. 289-95.
115. Drapeau, P. and D. Nachshen, *Manganese fluxes and manganese-dependent neurotransmitter release in presynaptic nerve endings isolated from rat brain*. Journal of Physiology, 1984. **348**(1): p. 493-510.
116. Frame, M. and M. Milanick, *Mn and Cd transport by the Na-Ca exchanger of ferret red blood cells*. American Journal of Physiology-Cell Physiology, 1991. **261**(3): p. C467-C475.
117. Günther, T., J. Vormann, and E. Cragoe, *Species-specific Mn<sup>2+</sup>/Mg<sup>2+</sup> antiport from Mg<sup>2+</sup>-loaded erythrocytes*. FEBS Letters, 1990. **261**(1): p. 47-51.
118. Gavin, C.E., K.K. Gunter, and T.E. Gunter, *Manganese and calcium efflux kinetics in brain mitochondria. Relevance to manganese toxicity*. Biochemical Journal, 1990. **266**(2): p. 329-334.
119. Kikuta, S., et al., *Quantitative activation-induced manganese-enhanced MRI reveals severity of Parkinson's disease in mice*. Scientific Reports, 2015. **5**: p. 1-11.
120. Takeda, A., et al., *Manganese transport in the neural circuit of rat CNS*. Brain Research Bulletin, 1998. **45**(2): p. 149-152.
121. Bearer, E.L., X. Zhang, and R.E. Jacobs, *Live imaging of neuronal connections by magnetic resonance: Robust transport in the hippocampal-septal memory circuit in a mouse model of Down syndrome*. NeuroImage, 2007. **37**(1): p. 230-42.
122. Thuen, M., et al., *Manganese-enhanced MRI of the rat visual pathway: Acute neural toxicity, contrast enhancement, axon resolution, axonal transport, and clearance of Mn<sup>2+</sup>*. Journal of Magnetic Resonance Imaging, 2008. **28**(4): p. 855-865.
123. Pautler, R.G., A.C. Silva, and A.P. Koretsky, *In vivo neuronal tract tracing using manganese-enhanced magnetic resonance imaging*. Magnetic Resonance in Medicine, 1998. **40**(5): p. 740-748.
124. Tjalve, H., et al., *Uptake of manganese and cadmium from the nasal mucosa into the central nervous system via olfactory pathways in rats*. Pharmacological Toxicology, 1996. **79**(6): p. 347-356.
125. Inui, T., et al., *Activation of projective neurons from the nucleus accumbens to ventral pallidum by a learned aversive taste stimulus in rats: a manganese-enhanced magnetic resonance imaging study*. Neuroscience, 2011. **177**: p. 66-73.
126. Murayama, Y., et al., *Tracing neural circuits in vivo with Mn-enhanced MRI*. Magnetic Resonance Imaging, 2006. **24**(4): p. 349-358.
127. Tjälve, H., et al., *Uptake of manganese and cadmium from the nasal mucosa into the central nervous system via olfactory pathways in rats*. Basic & Clinical Pharmacology & Toxicology, 1996. **79**(6): p. 347-356.
128. Lindsey, J.D., et al., *Magnetic resonance imaging of the visual system in vivo: transsynaptic illumination of V1 and V2 visual cortex*. NeuroImage, 2007. **34**(4): p. 1619-1626.
129. Thuen, M., et al., *Manganese-enhanced MRI of the optic visual pathway and optic nerve injury in adult rats*. Journal of Magnetic Resonance Imaging, 2005. **22**(4): p. 492-500.
130. Watanabe, T., T. Michaelis, and J. Frahm, *Mapping of retinal projections in the living rat using high-resolution 3D gradient-echo MRI with Mn<sup>2+</sup>-induced contrast*. Magnetic Resonance in Medicine, 2001. **46**(3): p. 424-429.
131. Bearer, E.L., et al., *Role of neuronal activity and kinesin on tract tracing by manganese-enhanced MRI (MEMRI)*. NeuroImage, 2007. **37**: p. S37-S46.
132. Wang, L., et al., *Manganese-Enhanced MRI Reflects Both Activity-Independent and Activity-Dependent Uptake within the Rat Habenulomesencephalic Pathway*. PLOS One, 2015. **10**(5): p. e0127773.
133. Guilarte, T.R., *Manganese and Parkinson's disease: a critical review and new findings*. Environmental Health Perspectives, 2010. **118**(8): p. 1071-1080.
134. Groenewegen, H.J., *The basal ganglia and motor control*. Neural Plasticity, 2003. **10**(1-2): p. 107-120.

135. Neff, N.H., R. Barrett, and E. Costa, *Selective depletion of caudate nucleus dopamine and serotonin during chronic manganese dioxide administration to squirrel monkeys*. Cellular and Molecular Life Sciences, 1969. **25**(11): p. 1140-1141.
136. Eriksson, H., et al., *Effects of manganese oxide on monkeys as revealed by a combined neurochemical, histological and neurophysiological evaluation*. Archives of Toxicology, 1987. **61**(1): p. 46-52.
137. Eriksson, H., et al., *Manganese induced brain lesions in Macaca fascicularis as revealed by positron emission tomography and magnetic resonance imaging*. Archives of Toxicology, 1992. **66**(6): p. 403-407.
138. Olanow, C.W., et al., *Manganese intoxication in the rhesus monkey: a clinical, imaging, pathologic, and biochemical study*. Neurology, 1996. **46**(2): p. 492-498.
139. Chandra, S.V., R. Srivastava, and G.S. Shukla, *Regional distribution of metals and biogenic amines in the brain of monkeys exposed to manganese*. Toxicology Letters, 1979. **4**(3): p. 189-192.
140. Bird, E., A. Anton, and B. Bullock, *The effect of manganese inhalation on basal ganglia dopamine concentrations in rhesus monkey*. Neurotoxicology, 1984. **5**(1): p. 59-65.
141. Guilarte, T.R., et al., *Nigrostriatal dopamine system dysfunction and subtle motor deficits in manganese-exposed non-human primates*. Experimental Neurology, 2006. **202**(2): p. 381-390.
142. Struve, M.F., et al., *Basal ganglia neurotransmitter concentrations in rhesus monkeys following subchronic manganese sulfate inhalation*. American Journal of Industrial Medicine, 2007. **50**(10): p. 772-778.
143. Eriksson, H., et al., *Receptor alterations in manganese intoxicated monkeys*. Archives of Toxicology, 1992. **66**(5): p. 359-364.
144. Guilarte, T.R., et al., *Evidence for cortical dysfunction and widespread manganese accumulation in the nonhuman primate brain following chronic manganese exposure: a 1H-MRS and MRI study*. Toxicological Sciences, 2006. **94**(2): p. 351-358.
145. Eschenko, O., et al., *Mapping of functional brain activity in freely behaving rats during voluntary running using manganese-enhanced MRI: implication for longitudinal studies*. NeuroImage, 2010. **49**(3): p. 2544-2555.
146. Li, Y., et al., *Neuronal projections from ventral tegmental area to forebrain structures in rat studied by manganese-enhanced magnetic resonance imaging*. Magnetic Resonance Imaging, 2009. **27**(3): p. 293-299.
147. Canals, S., et al., *Magnetic resonance imaging of cortical connectivity in vivo*. NeuroImage, 2008. **40**(2): p. 458-472.
148. Alberts, B., *Molecular biology of the cell*. 2017: Garland Science.
149. Rogosnitzky, M. and S. Branch, *Gadolinium-based contrast agent toxicity: a review of known and proposed mechanisms*. Biometals, 2016. **29**(3): p. 365-376.
150. Seo, Y., et al., *Mn-bicine: A low affinity chelate for manganese ion enhanced MRI*. Magnetic resonance in medicine, 2011. **65**(4): p. 1005-1012.
151. Seo, Y., et al., *Mn-citrate and Mn-HIDA: intermediate-affinity chelates for manganese-enhanced MRI*. Contrast Media & Molecular Imaging, 2013. **8**(2): p. 140-146.
152. Gehl, H., et al., *Pancreatic enhancement after low-dose infusion of Mn-DPDP*. Radiology, 1991. **180**(2): p. 337-339.
153. Gehl, H., et al., *Mn-DPDP in MR imaging of pancreatic adenocarcinoma: initial clinical experience*. Radiology, 1993. **186**(3): p. 795-798.
154. Diehl, S.J., et al., *MR imaging of pancreatic lesions: comparison of manganese-DPDP and gadolinium chelate*. Investigative Radiology, 1999. **34**(9): p. 589-595.
155. Botsikas, D., et al., *Pancreatic magnetic resonance imaging after manganese injection distinguishes type 2 diabetic and normoglycemic patients*. Islets, 2012. **4**(3): p. 243-248.
156. Yang, Y., et al., *Dynamic manganese-enhanced magnetic resonance imaging can detect chronic cryoinjury-induced infarction in pig hearts in vivo*. Contrast Media & Molecular Imaging, 2011. **6**(6): p. 426-436.

157. Nordhøy, W., et al., *Manganese ions as intracellular contrast agents: proton relaxation and calcium interactions in rat myocardium*. NMR in Biomedicine, 2003. **16**(2): p. 82-95.
158. Hu, T.C.C., et al., *Manganese enhanced magnetic resonance imaging of normal and ischemic canine heart*. Magnetic Resonance in Medicine, 2005. **54**(1): p. 196-200.
159. Eschenko, O., et al., *Tracing of noradrenergic projections using manganese-enhanced MRI*. NeuroImage, 2012. **59**(4): p. 3252-3265.
160. Soria, G., et al., *Reproducible imaging of rat corticothalamic pathway by longitudinal manganese-enhanced MRI (L-MEMRI)*. NeuroImage, 2008. **41**(3): p. 668-674.
161. Watanabe, T., et al., *In vivo 3D MRI staining of the mouse hippocampal system using intracerebral injection of MnCl<sub>2</sub>*. NeuroImage, 2004. **22**(2): p. 860-7.
162. Yu, X., et al., *Thalamocortical inputs show post-critical-period plasticity*. Neuron, 2012. **74**(4): p. 731-742.
163. Bearer, E.L., et al., *Reward circuitry is perturbed in the absence of the serotonin transporter*. NeuroImage, 2009. **46**(4): p. 1091-1104.
164. Van der Linden, A., et al., *In vivo manganese-enhanced magnetic resonance imaging reveals connections and functional properties of the songbird vocal control system*. Neuroscience, 2002. **112**(2): p. 467-474.
165. Van der Linden, A., et al., *Applications of manganese-enhanced magnetic resonance imaging (MEMRI) to image brain plasticity in song birds*. NMR in Biomedicine, 2004. **17**(8): p. 602-612.
166. Saleem, K.S., et al., *Magnetic resonance imaging of neuronal connections in the macaque monkey*. Neuron, 2002. **34**(5): p. 685-700.
167. Yang, P.F., et al., *Functional tracing of medial nociceptive pathways using activity-dependent manganese-enhanced MRI*. Pain, 2011. **152**(1): p. 194-203.
168. Yu, X., et al., *Statistical mapping of sound-evoked activity in the mouse auditory midbrain using Mn-enhanced MRI*. NeuroImage, 2008. **39**(1): p. 223-230.
169. Bangasser, D.A., et al., *Manganese-enhanced magnetic resonance imaging (MEMRI) reveals brain circuitry involved in responding to an acute novel stress in rats with a history of repeated social stress*. Physiology & Behavior, 2013. **122**: p. 228-236.
170. Pelled, G., et al., *Manganese-enhanced MRI in a rat model of Parkinson's disease*. Journal of Magnetic Resonance Imaging, 2007. **26**(4): p. 863-870.
171. Serrano, F., et al., *Assessing transneuronal dysfunction utilizing manganese-enhanced MRI (MEMRI)*. Magnetic Resonance in Medicine, 2008. **60**(1): p. 169-175.
172. Minoshima, S. and D. Cross, *In vivo imaging of axonal transport using MRI: aging and Alzheimer's disease*. European Journal of Nuclear Medicine and Molecular Imaging, 2008. **35**(1): p. 89-92.
173. Zhang, X., et al., *Altered neurocircuitry in the dopamine transporter knockout mouse brain*. PLOS One, 2010. **5**(7): p. e11506.
174. Gallagher, J.J., et al., *Altered reward circuitry in the norepinephrine transporter knockout mouse*. PLOS One, 2013. **8**(3): p. e57597.
175. Pautler, R.G., R. Mongeau, and R.E. Jacobs, *In vivo trans-synaptic tract tracing from the murine striatum and amygdala utilizing manganese enhanced MRI (MEMRI)*. Magnetic Resonance in Medicine, 2003. **50**(1): p. 33-39.
176. Phelps, M.E., et al., *Application of annihilation coincidence detection to transaxial reconstruction tomography*. Journal of Nuclear Medicine, 1975. **16**(3): p. 210-224.
177. Brownell, G.L., *A history of positron imaging*. Physics Research Laboratory, Massachusetts General Hospital, MIT, 1999.
178. Levin, C.S., *New imaging technologies to enhance the molecular sensitivity of positron emission tomography*. Proceedings of the IEEE, 2008. **96**(3): p. 439-467.
179. Cherry, S.R. and M. Dahlbom. *PET: physics, instrumentation, and scanners*. in *PET*. 2006. Springer.
180. Topping, G.J., *Manganese imaging with positron emission tomography, autoradiography, and magnetic resonance*. 2014, University of British Columbia.

181. Mahajan, S. and C.R. Divgi, *The role of iodine-124 positron emission tomography in molecular imaging*. Clinical and Translational Imaging, 2016. **4**(4): p. 297-306.
182. Qi, J. and R.M. Leahy, *Iterative reconstruction techniques in emission computed tomography*. Physics in Medicine and Biology, 2006. **51**(15): p. R541-R578.
183. Alessio, A. and P. Kinahan, *PET image reconstruction*. Nuclear Medicine, 2006. **1**: p. 1-22.
184. Le Loirec, C. and C. Champion, *Track structure simulation for positron emitters of physical interest. Part II: The case of the radiometals*. Nuclear Instruments and Methods in Physics Research Section A: Accelerators, Spectrometers, Detectors and Associated Equipment, 2007. **582**(2): p. 654-664.
185. Topping, G.J., et al., *Manganese-52 positron emission tomography tracer characterization and initial results in phantoms and in vivo*. Medical Physics, 2013. **40**(4): p. 042502.
186. Buchholz, M., et al., *Cross-section measurements for the formation of manganese-52 and its isolation with a non-hazardous eluent*. Radiochimica Acta, 2013. **101**(8): p. 491-499.
187. Buchholz, M., I. Spahn, and H.H. Coenen, *Optimized separation procedure for production of no-carrier-added radiomanganese for positron emission tomography*. Radiochimica Acta, 2015. **103**(12): p. 893-899.
188. Graves, S.A., et al., *Novel Preparation Methods of (52)Mn for ImmunoPET Imaging*. Bioconjugate Chemistry, 2015. **26**(10): p. 2118-2124.
189. Lewis, C.M., et al., *(52)Mn production for PET/MRI tracking of human stem cells expressing divalent metal transporter 1 (DMT1)*. Theranostics, 2015. **5**(3): p. 227-239.
190. Wooten, A.L., B.C. Lewis, and S.E. Lapi, *Cross-sections for (p, x) reactions on natural chromium for the production of 52, 52m, 54 Mn radioisotopes*. Applied Radiation and Isotopes, 2015. **96**: p. 154-161.
191. Fonslet, J., et al., *Optimized procedures for manganese-52: Production, separation and radiolabeling*. Applied Radiation and Isotopes, 2017. **121**: p. 38-43.
192. Dayan, A. and A. Paine, *Mechanisms of chromium toxicity, carcinogenicity and allergenicity: review of the literature from 1985 to 2000*. Human & Experimental Toxicology, 2001. **20**(9): p. 439-451.
193. Kato, M., *Distribution and excretion of radiomanganese administered to the mouse*. Experimental Physiology, 1963. **48**(4): p. 355-369.
194. Kato, M., T. Hara, and Y. Koshida, *Autoradiographic observations of manganese in adult and embryo mice*. Experimental Physiology, 1963. **48**(4): p. 370-378.
195. Wooten, A.L., et al., *Biodistribution and PET Imaging of pharmacokinetics of manganese in mice using Manganese-52*. PLOS One, 2017. **12**(3): p. e0174351.
196. Hernandez, R., et al., *Radiomanganese PET Detects Changes in Functional  $\beta$ -cell Mass in Mouse Models of Diabetes*. Diabetes, 2017. **66**(8): p. 2163-2174.
197. McCormick, D.A., Z. Wang, and J. Huguenard, *Neurotransmitter control of neocortical neuronal activity and excitability*. Cerebral Cortex, 1993. **3**(5): p. 387-398.
198. Kalivas, P.W., *Neurotransmitter regulation of dopamine neurons in the ventral tegmental area*. Brain Research Reviews, 1993. **18**(1): p. 75-113.
199. Boellaard, R., et al., *Effects of noise, image resolution, and ROI definition on the accuracy of standard uptake values: a simulation study*. Journal of Nuclear Medicine, 2004. **45**(9): p. 1519-1527.
200. Takesh, M., *The potential benefit by application of kinetic analysis of PET in the clinical oncology*. ISRN Oncology, 2012. **2012**.
201. Huang, S.-C., *Role of kinetic modeling in biomedical imaging*. Journal of Medical Sciences, 2008. **28**(2): p. 57-63.
202. Weber, B., et al., *A femoral arteriovenous shunt facilitates arterial whole blood sampling in animals*. European Journal of Nuclear Medicine and Molecular Imaging, 2002. **29**(3): p. 319-323.
203. Breuer, J., et al., *Evaluation of an MR-compatible blood sampler for PET*. Physics in Medicine and Biology, 2010. **55**(19): p. 5883-5893.

204. Lahiri, S., D. Nayak, and G. Korschinek, *Separation of no-carrier-added  $^{52}\text{Mn}$  from bulk chromium: A simulation study for accelerator mass spectrometry measurement of  $^{53}\text{Mn}$* . Analytical Chemistry, 2006. **78**(21): p. 7517-7521.
205. Lammertsma, A.A. and S.P. Hume, *Simplified reference tissue model for PET receptor studies*. NeuroImage, 1996. **4**(3): p. 153-158.
206. Klumpers, U.M., et al., *Comparison of plasma input and reference tissue models for analysing [ $^{11}\text{C}$ ] flumazenil studies*. Journal of Cerebral Blood Flow & Metabolism, 2008. **28**(3): p. 579-587.
207. Ungerstedt, U. and G.W. Arbuthnott, *Quantitative recording of rotational behavior in rats after 6-hydroxy-dopamine lesions of the nigrostriatal dopamine system*. Brain Research, 1970. **24**(3): p. 485-493.
208. Dunnett, S.B., Torres, E. M., *Rotation in the 6-OHDA-Lesioned Rat*, in *Animal Models of Movement Disorders*, S.B.D. Emma L. Lane, Editor. 2011, Humana Press: New York. p. 299-315.
209. Munk, O.L., S. Keiding, and L. Bass, *A method to estimate dispersion in sampling catheters and to calculate dispersion-free blood time-activity curves*. Medical Physics, 2008. **35**(8): p. 3471-3481.
210. Iida, H., et al., *Error analysis of a quantitative cerebral blood flow measurement using  $\text{H}^{215}\text{O}$  autoradiography and positron emission tomography, with respect to the dispersion of the input function*. Journal of Cerebral Blood Flow & Metabolism, 1986. **6**(5): p. 536-545.
211. Sokoloff, L., *Mapping cerebral functional activity with radioactive deoxyglucose*. Trends in Neurosciences, 1978. **1**(3): p. 75-79.
212. Tonietto, M., et al. *A unified framework for plasma data modelling in dynamic positron emission tomography studies*. IEEE Transactions on Biomedical Engineering, 2018. **2018**.
213. Gerfen, C.R. and C.J. Wilson, *Chapter II The basal ganglia*. Handbook of Chemical Neuroanatomy, 1996. **12**: p. 371-468.
214. Matsuda, K., et al., *Retrograde axonal tracing using manganese enhanced magnetic resonance imaging*. NeuroImage, 2010. **50**(2): p. 366-374.
215. Erikson, K.M., et al., *Manganese accumulates in iron-deficient rat brain regions in a heterogeneous fashion and is associated with neurochemical alterations*. Biological Trace Element Research, 2002. **87**(1-3): p. 143-156.
216. Lipe, G.W., et al., *Effect of manganese on the concentration of amino acids in different regions of the rat brain*. Journal of Environmental Science & Health Part B, 1999. **34**(1): p. 119-132.
217. Fordahl, S.C., et al., *Manganese exposure inhibits the clearance of extracellular GABA and influences taurine homeostasis in the striatum of developing rats*. Neurotoxicology, 2010. **31**(6): p. 639-646.
218. Guilarte, T.R., et al., *Impairment of nigrostriatal dopamine neurotransmission by manganese is mediated by pre-synaptic mechanism (s): implications to manganese-induced parkinsonism*. Journal of Neurochemistry, 2008. **107**(5): p. 1236-1247.
219. Tang, Z., et al., *Manganese-enhanced magnetic resonance imaging combined with electrophysiology in the evaluation of visual pathway in experimental rat models with monocular blindness*. Brain and Behavior, 2017. **7**(7): p. e00731.
220. Simmons, J.M., et al., *Mapping prefrontal circuits in vivo with manganese-enhanced magnetic resonance imaging in monkeys*. Journal of Neuroscience, 2008. **28**(30): p. 7637-7647.
221. Robel, S., et al., *Reactive astrogliosis causes the development of spontaneous seizures*. Journal of Neuroscience, 2015. **35**(8): p. 3330-3345.
222. Anderson, J.G., P.T. Cooney, and K.M. Erikson, *Brain manganese accumulation is inversely related to  $\gamma$ -amino butyric acid uptake in male and female rats*. Toxicological Sciences, 2007. **95**(1): p. 188-195.
223. Parenti, M., et al., *Manganese neurotoxicity: effects of L-DOPA and pargyline treatments*. Brain Research, 1986. **367**(1-2): p. 8-13.
224. Ponzoni, S., et al., *Behavioral effects of intra-nigral microinjections of manganese chloride: interaction with nitric oxide*. Progress in Neuropsychopharmacology & Biological Psychiatry, 2000. **24**(2): p. 307-325.

225. Fernandes, A., et al., *Manganese neurotoxic time course is not influenced by L-deprenyl systemic treatment: influence of L-deprenyl in manganese neurotoxic time course*. Brain Research, 2010. **1317**: p. 277-285.
226. Diaz-Veliz, G., et al., *Behavioral effects of manganese injected in the rat substantia nigra are potentiated by dicumarol, a DT-diaphorase inhibitor*. Pharmacology, Biochemistry, and Behavior, 2004. **77**(2): p. 245-251.
227. Little Peter, R.D.B. *Nonneoplastic Lesion Atlas*. [cited 2017 10.09]; Available from: <https://ntp.niehs.nih.gov/nnl/nervous/brain/neurnecr/index.htm>.
228. Olive, P.L., *The role of DNA single-and double-strand breaks in cell killing by ionizing radiation*. Radiation Research, 1998. **150**(5s): p. S42-S51.
229. Rogakou, E.P., et al., *DNA double-stranded breaks induce histone H2AX phosphorylation on serine 139*. Journal of Biological Chemistry, 1998. **273**(10): p. 5858-5868.
230. Kuo, L.J. and L.-X. Yang,  *$\gamma$ -H2AX-a novel biomarker for DNA double-strand breaks*. In Vivo, 2008. **22**(3): p. 305-309.
231. Lewis, J., et al., *Trigeminal uptake and clearance of inhaled manganese chloride in rats and mice*. Neurotoxicology, 2005. **26**(1): p. 113-123.
232. Tang, F.R. and W.K. Loke, *Molecular mechanisms of low dose ionizing radiation-induced hormesis, adaptive responses, radioresistance, bystander effects, and genomic instability*. International Journal of Radiation Biology, 2015. **91**(1): p. 13-27.
233. Betlazar, C., et al., *The impact of high and low dose ionising radiation on the central nervous system*. Redox Biology, 2016. **9**: p. 144-156.
234. Acharya, M.M., et al., *Consequences of ionizing radiation-induced damage in human neural stem cells*. Free Radical Biology and Medicine, 2010. **49**(12): p. 1846-1855.
235. Mizumatsu, S., et al., *Extreme sensitivity of adult neurogenesis to low doses of X-irradiation*. Cancer Research, 2003. **63**(14): p. 4021-4027.
236. Ismail, A.F. and S.M. El-Sonbaty, *Fermentation enhances Ginkgo biloba protective role on gamma-irradiation induced neuroinflammatory gene expression and stress hormones in rat brain*. Journal of Photochemistry and Photobiology B: Biology, 2016. **158**: p. 154-163.
237. Gaber, M.W., et al., *An intravital microscopy study of radiation-induced changes in permeability and leukocyte-endothelial cell interactions in the microvessels of the rat pia mater and cremaster muscle*. Brain Research Protocols, 2004. **13**(1): p. 1-10.
238. Saeed, Y., et al., *Indirect effects of radiation induce apoptosis and neuroinflammation in neuronal SH-SY5Y cells*. Neurochemical Research, 2014. **39**(12): p. 2334-2342.
239. Raber, J., et al., *Radiation-induced cognitive impairments are associated with changes in indicators of hippocampal neurogenesis*. Radiation Research, 2004. **162**(1): p. 39-47.
240. Wang, B., et al., *Total body 100-mGy X-irradiation does not induce Alzheimer's disease-like pathogenesis or memory impairment in mice*. Journal of Radiation Research, 2013. **55**(1): p. 84-96.
241. Chien, L., et al., *Low-dose ionizing radiation induces mitochondrial fusion and increases expression of mitochondrial complexes I and III in hippocampal neurons*. Oncotarget, 2015. **6**(31): p. 30628-30639.
242. Katsura, M., et al., *Effects of chronic low-dose radiation on human neural progenitor cells*. Scientific Reports, 2016. **6**: p. 20027.
243. Aschner, M., K.M. Erikson, and D.C. Dorman, *Manganese dosimetry: species differences and implications for neurotoxicity*. Critical Reviews in Toxicology, 2005. **35**(1): p. 1-32.
244. Liang, H., G. Paxinos, and C. Watson, *The red nucleus and the rubrospinal projection in the mouse*. Brain Structure and Function, 2012. **217**(2): p. 221-232.
245. Schlegel, F., A. Schroeter, and M. Rudin, *The hemodynamic response to somatosensory stimulation in mice depends on the anesthetic used: implications on analysis of mouse fMRI data*. NeuroImage, 2015. **116**: p. 40-49.

246. Putnam, K.M., et al., *Neural activity and diurnal variation of cortisol: Evidence from brain electrical tomography analysis and relevance to anhedonia*. *Psychophysiology*, 2008. **45**(6): p. 886-895.
247. Park, S.J., W.L. Rogers, and N.H. Clinthorne, *Design of a very high-resolution small animal PET scanner using a silicon scatter detector insert*. *Physics in Medicine & Biology*, 2007. **52**(15): p. 4653-7467.
248. Yang, Y., et al., *A high resolution prototype small-animal PET scanner dedicated to mouse brain imaging*. *Journal of Nuclear Medicine*, 2016. **57**(7): p. 1130-1135.
249. Ashworth, S., A. Ranciar, and P. Bloomfield, *Development of an on-line blood detector system for PET studies in small animals*. *Quantification of Brain Function Using PET*, 1996: p. 62-66.
250. Maier, F.C., et al., *Longitudinal PET-MRI reveals [beta]-amyloid deposition and rCBF dynamics and connects vascular amyloidosis to quantitative loss of perfusion*. *Nature Medicine*, 2014. **20**(12): p. 1485-1492.
251. Wehrl, H.F., et al., *Preclinical and translational PET/MR imaging*. *Journal of Nuclear Medicine*, 2014. **55**(Supplement 2): p. 11S-18S.
252. Roehrbacher, F., et al., *Development and performance test of an online blood sampling system for determination of the arterial input function in rats*. *EJNMMI Physics*, 2015. **2**(1): p. 1-19.
253. Fang, Y.-H.D. and R.F. Muzic, *Spillover and partial-volume correction for image-derived input functions for small-animal 18F-FDG PET studies*. *Journal of Nuclear Medicine*, 2008. **49**(4): p. 606-614.
254. Park, M.-J., et al., *Assessment of partial volume effect in small animal cardiac PET imaging using Monte Carlo simulation*. *Journal of Nuclear Medicine*, 2013. **54**(supplement 2): p. 1638-1638.
255. Hsiao-Ming, W., et al., *Derivation of input function from FDG-PET studies in small hearts*. *Journal of Nuclear Medicine*, 1996. **37**(10): p. 1717-1722.

